Domain switching dynamics in ferroelastic and ferroelastic/ferroelectric perovskites

Giuseppe Viola

2009

A thesis submitted for the Degree of Doctor of Philosophy, at the School of Engineering and Materials Science, Queen Mary University of London

Abstract

A comprehensive study of domain switching process in different ferroelastic and ferroelastic/ferroelectric perovskite structured ceramics has been performed. The effects of thermal fluctuations on domain switching dynamics were investigated in the ferroelastic and in the ferroelectric case under static and dynamic electric and mechanical conditions.

In the ferroelastic case, domain switching behaviour was investigated for different compositions, using different types of mechanical tests. Compression tests were carried out to characterize the ferroelastic properties, such as coercive stress, hysteresis loop and irreversible strain. Creep experiments were performed to study the domain switching time dependence at different stress levels. Domain switching kinetics during creep was characterized by implementing a rate model, based on thermal activation rate theory, which allowed the activation volume to be estimated. A Rayleigh-type analysis was performed to study the effects of stress amplitude, loading rate, temperature and composition on ferroelastic switching. Rayleigh-type relationships were proposed to fit the results and the rate model developed was applied to quantify the effect of the loading rate on the Rayleigh loops. Alternative methodologies were developed to assess the effects of rate and temperature on the coercive stress, providing original sets of data. A further application of the rate model provided an estimation of the activation parameters (volume and enthalpy). In PZT 5A at the coercive field the activation volume was calculated to be 2.44 nm^3, with a reasonable consistency with the value obtained from creep tests (7.49 nm^3).

In the ferroelectric case, domain switching was studied by generating P-E and butterfly hysteresis loops and by analysing creep-relaxation curves. In creep experiments, the polarization and the strain were measured simultaneously, during the application of a constant electric field. An insight into the evolution of domain structure and on domain switching mechanisms was gained, highlighting analogies and differences with the ferroelastic case. Experiments at different frequencies, allowed the activation volume to be estimated at the coercive field (77 nm^3). The relatively large value indicates small rate dependence and suggests a domain structure with broad and mobile domain walls, being the preferred sites for the nucleation.

Acknowledgements

I am grateful to my supervisor Prof. Michael John Reece who patiently guided me during my study with stimulating discussions and important suggestions and ideas. I would like also to acknowledge all the other researchers and technicians who supported me, in particular Bill Godwin and John Caulfield. Special thanks go to Dr. Dmytro Verbylo for his friendship and significant support in the experimental work. Special regards to Dr. Frank Guiu for his significant support in the discussions. Thanks to Dr. Kok Boon Chong for friendship and valuable discussions. Thanks to Dr. Nina Orlovskaya for providing the different ferroelastic compositions I worked on and for the continuous proposals of new research work. Thanks to Dr. Haixue Yan for his ready availability in giving help and advice. Special thanks to EPSRC for financial support throughout my studies.

Special thanks to my dear parents to whom this work is dedicated and all my close friends who gave me moral support in the difficult moments.

Table of Contents

List of figures

List of tables

List of symbols

A_S: area swept by domain wall

$B(L)$: correlation function (avarage displacement of a domain wall)

C: interface stiffness

d: domain wall dimensionality

d_{ij}: piezoelectric coefficient

E: electric field

E_B: energy barrier

E_C: coercive electric field

E_{eff}: effective electric field

E_f: coercive electric field in the forward direction

E_{int}: internal electric field

E_r: coercive electric field in the reverse direction

f: frequency

F: applied force

F_C: critical force

F_P: pinning force

G: Gibbs free energy

H: enthalpy

H_m: magnetic field

$\hbar$: Plank constant

i_{max}: switching current

k_B: Boltzmann constant

L: domain wall length

L_L: Larkin length

M: magnetization vector

m: domain wall mobility

n: Avrami exponent

P: polarization vector

P_A: experimental constant

P_R: remanent polarization

P_S: saturation polarization

P_0: spontaneous polarization

$\dot{P}$: polarization rate

Q: electrical charge

S: mechanical compliance

S_e: entropy

S_{init}: initial compliance (first Rayleigh parameter)

S_{33}: mechanical compliance along the loading direction

$\overline{S}_{\text{int}}$: intrinsic compliance

T: temperature

T_L : experimental constant

t: time

t_f : time for the switching in the forward direction

t_{f0} : experimental constant

t_r : time for the switching in the reverse direction

t_{r0} : experimental constant

t_0 : characteristic time

U: internal energy

u: domain wall displacement

V_a: activation volume

V_R: random potential

V_s: fraction of switched volume

W: work done

$w(L)$: domain wall roughness

α_R : second Rayleigh parameter

β_f : experimental constant

Γ : rate of formation of activated nuclei

Γ_f : rate of formation of activated nuclei in the forward direction

Γ_{f0} : experimental constant

γ : shear strain

$\dot{\gamma}$: shear strain rate

ΔG : variation of Gibbs free energy (activation energy)

ΔH : variation of enthalpy (activation enthalpy)

ΔS_e : variation of entropy

ΔU : variation of internal energy

ΔH_m : magnetic field amplitude

$\Delta\varepsilon$: strain amplitude

$\Delta\sigma$: stress amplitude

δ_f : experimental constant

δ_r : experimental constant

ε : normal strain

ε_{cr} : normal creep strain

ε_{ext} : extrinsic strain

ε_{int} : intrinsic strain

$\dot{\varepsilon}$: strain rate

$\dot{\varepsilon}_0$: pre-exponential term

η : thermal noise

λ : rate sensitivity

μ : dynamical exponent

ν : characteristic frequency

θ : work hardening parameter

ϑ : pitting exponent

ρ : density of switching sites

σ : normal stress

σ_{app} : applied normal stress

σ_B : stress bias

σ_C : coercive stress

σ_{in} : internal normal stress

$\dot{\sigma}$: stress rate

τ : characteristic time

τ_{app} : applied shear stress

τ_{eff} : effective shear stress

τ_{in} : internal shear stress

χ : magnetic susceptibility

$\chi^{'}$: real part of magnetic susceptibility

$\chi^{''}$: imaginary part of magnetic susceptibility

χ_{init} : inital magnetic susceptibility (Rayleigh parameter)

χ_{L} : experimental constant

ω : angular frequency

ζ : roughness exponent

Chapter 1: Ferroelastic and ferroelectric materials

1.1 Introduction

The purpose of this chapter is to introduce the concept of ferroelasticity, presenting general definitions and classifications in terms of point group, ferroelastic phase transition and crystal structure/chemical composition of ferroelastic solids, to clarify the characteristics of this class of materials and to appreciate the analogies and differences at the microstructural level of different types of ferroic materials.

1.2 General definitions and classification of ferroelastic materials

"The ferroelasticity of a crystal consists in two main features:
1) a phase transition at certain temperature between the paraelastic and the ferroelastic phase, which produces a lattice distortion;
2) the possibility of reorientation of the lattice distortion by an external stress" [1].

Following K.Aizu, *"ferroelastic crystals"* belong to a more general category defined as *"ferroic crystals"*. A crystal is named *"ferroic"* when it has two or more orientation states in the absence of external applied fields, such as magnetic field, electric field and mechanical stress, and it can be shifted from to one to another of these states under the influence of the above mentioned applied fields. Any two of the orientation states are identical or enantiomorphous in the structure, but they present different arrangement of atoms [2].

Ferroelastic crystals are those ferroic crystals whose orientation states are characterized by different *spontaneous strain*, defined by a strain tensor of the second order. Any two of the orientation states are identical or enantiomorphous in the structure, but different in the *spontaneous strain tensor*, at null mechanical stress applied. The shift from a state to another in ferroelastic crystals can occur by applying a mechanical stress.

The process of the reorientation of the spontaneous strain is defined "*ferroelastic switching"*. The switching from a spontaneous strain state to another is a hysteretic process and the inherent hysteresis is named "*ferroelastic hysteresis*". A typical example of stress-strain loop is shown in Fig.1.1. The intersection of the two branches of the hysteresis curve identifies the *"critical stress"*, where significant changes in the domain pattern are induced. The stress at zero strain is defined as "*coercive stress*" (see Fig.1.1). Ferroelastic crystals with large ferroelastic hysteresis are classified as *"hard ferroelastics"* [1].

Some crystals present a "*spontaneous strain*" which cannot be reoriented because the "*critical stress*" is larger than their mechanical strength. Materials of this type are denominated "*potential ferroelastics*". Another class of materials is represented by those crystals that present a spontaneous strain, but there is no possibility to reorient it because the size of the crystal is too small to form domain patterns. These materials are called "*nanocrystals*". Examples of materials with large *spontaneous strain* in the ferroelastic phase, which cannot display ferroelastic hysteresis, are also known. They do not have two symmetrical equivalent ferroelastic states and they are named "*co-elastic crystals*". One of the most important is the calcite [1].

1.3 Aizu classification

Aizu proposed to classify *"ferroelastic crystals"* based on the following criterion [3]. On decreasing the temperature, a ferroelastic crystal undergoes to a phase transformation from a non-ferroelastic phase stable at high temperature (paraelastic phase), to a ferroelastic phase at low temperature. The former is referred as *"prototype phase"*. Paraelastic and ferroelastic phase have different crystallographic point of group and by knowing the point group of both the states, the number of the possible orientation states in the lower symmetry phase can be determined. The relationship between the ferroelastic phase and its prototype is given by the "*spontaneous strain tensor*". If all the possible orientation states have different spontaneous strain tensor, the species is classified as *"full ferroelastic"*. If at least two orientation states have identical spontaneous strain tensor, the species is defined *"partial ferroelastic"*. In the Aizu's formalism each species is represented with a

particular notation. For instance the notation $\bar{4}2mFm$, indicates a species having a prototype with point group $\bar{4}2m$ and a ferroelastic phase with point group *m*.

In Table 1 are listed all the possible ferroelastic species in terms of the point of group of the prototype and the ferroelastic phase. 94 "*full ferroelastic*" have been identified and 42 of them have been found to be also "*full ferroelectrics*". In crystals that are both fully ferroelectric and fully ferroelastic, any change in the polarization vector is always accompanied by a change in the strain tensor and vice-versa [3].

1.4 Ferroelastic phase transitions and spontaneous strain

Based on the Landau's theory of phase transitions, the ferroelastic phase transitions are characterized by a loss of symmetry from the paraelastic state (high symmetry and low microstructural order) to the ferroelastic state (lower symmetry and higher microstructural order). The broken symmetry is described by a thermodynamic variable called *"order parameter"*. The basic idea of Landau's theory is that the Gibbs free energy can be written as a power function of the order parameter. It is very frequent the case where different types of microstructural instabilities are involved in the phase transition. In this cases the order parameter coincides with the parameter describing the main instability and it will be coupled with other quantities (faint variables) associated with the other microstructural features.

In ferroelastic phase transitions where the only instability is the emergence of the spontaneous strain, the order parameter coincides with one of the component of the spontaneous strain tensor and the crystal is conventionally defined "*true-proper ferroelastic*" [4]. In cases where the appearance of the spontaneous strain is accompanied by other types of microstructural change, the spontaneous strain and the order parameter are coupled. If order parameter and the spontaneous strain are different parameters, but they have the same symmetry, the material is defined "*pseudo-proper ferroelastic*" and the coupling between the order parameter and the spontaneous strain is biquadratic [4]. All the materials where the order parameter and the spontaneous strain are different variables having also different symmetry are defined as "*improper ferroelastics*" [4].

The characteristic spontaneously deformed state is defined by a strain tensor, which relates the low-symmetry unit cell, to the high symmetry unit cell. In a linear approximation, the appearance of the spontaneous strain does not change the volume of the unit cell, leading to a trace strain tensor equal to zero.

1.5 Domain structure

A microscopic region in a ferroic material of a specific constant orientation state is called a "*domain*" and the boundary between two domains is called a "*domain wall*" or "*domain boundary*" [5]. Microstructural observations in the ferroelastic phase have shown domain patterns with twin structures [6]. The generation of a spontaneous strain due to the phase transition results in twin formation. Since all of the possible orientation states are energetically equivalent, different orientation states can coexist in the same crystal, which thus becomes twinned [7]. Actually, domain walls between adjacent domains can be seen as internal interfaces such that the lattice on either side of the wall corresponds to the other by a simple rotation. There is a correlation between the high symmetry phase and the twin structure formed below the transition temperature. In order to minimize the misfit along the boundary, two adjacent domains are locally stressed even in absence of external stress applied. The orientation of the domain walls and their shape after interacting with other domain walls can be determined by minimizing the strain energy and by applying strain compatibility criteria [1].

Another approach based on algebraic calculations has been introduced by J.Sapriel [7], and allows determining the orientation of the domain walls. Two types of domain walls can be distinguished: *W-walls* and *W'-walls*. The *W-walls* are crystallographic planes of fixed integer indices, independent on the temperature. The *W'-walls* are represented by irrational indices and their orientation depends on the relative spontaneous strain tensor and therefore is temperature dependent [7]. The interaction between different domain walls gives rise to different typical structures:

1) rounded junctions;
2) S-shaped walls;

3) needle twins.

From energy minimization and strain compatibility conditions, it can be shown that the interaction between two orthogonal domain walls produces a rounded junction, whose radius depends on the stiffness of the crystal [1]. In hard materials the radius is always bigger than in soft materials. S-shaped domain walls are formed when a non-intersecting domain wall bends into an S-shape because of the presence of a junction between two walls (Fig.1.2). Another frequent domain pattern is the needle shaped domains, with straight domain walls and a sharp tip at the end. Such pattern appears from the attraction of two corner twins walls with opposite curvature (Fig.1.3).

1.6 Dudnik-Kiosse classification of ferroelastic materials

Based on the crystallographic arrangement, 15 ferroelastic families have been identified. In addition, 8 other species that cannot be assigned to these 15 families have been found: H_3BO_3, Sb_5O_7I, KIO_2F_2, $Mg_2B_2O_3$, PtGeSe, $K_2Ba(NO_2)_4$, $ZnGeF_66H_2O$, $KClO_3$. H_3BO_3 and $KClO_3$ have very large spontaneous strain therefore its reorientation (ferroelastic switching) results quite difficult [4]. Most of the 15 families and some of the 8 species can be grouped in 5 crystal-chemical classes:

(1) ferroelastics with isolated anion complexes,
(2) ferroelastics with anion or cation complexes connected at the tips in continuous linear chains or layers,
(3) ferroelastics with anion complexes connected in continuous linear chains or layers through hydrogen bonds,
(4) ferroelastics with octahedral anion complexes connected at the tips in three-dimensional frames,
(5) ferroelastics forming ion molecular crystals.

The families belonging to Class 1 are seven: palmierites (e.g. $Pb_3(PO_4)_2$), fergusonites (e.g. $BiVO_4$), teilorites (K_2CrO_4), langbeinites ($LiTlSO_4$), complex cyanides ($K_2Mn_2(SO_4)_3$, double trigonal molybdates ($K_2Hg(CN)_4$), double trigonal tungstates $(NaFeMoO_4)_2$. Families belonging to Class 2 are four: pentophosphates (LaP_5O_{14}),

fresnoites ($BaTiGe_2O_8$), $M_4A(XO_4)_3$ ($K_4Zn(MoO_4)_3$, ditellurites ($SrTe_2O_5$). Species belonging to Class 3 are the alkali trihydro-selenites ($KH_3(SeO_3)_2$ and also H_3BO_3. Class 4 includes the perovskites group ABO_3 and Class 5 the calomel family (Hg_2Cl_2) [4].

1.7 Domain structures in ferroelectric materials

Ferroelelctric materials present a *spontaneous polarization* P_S below the transition temperature, which can be reoriented by applying an external electric field. Considering the polarization orientation in each domain, ferroelectric materials display two types of domain walls. Domain walls between domains with antiparallel polarization are defined "*180° walls*" and those which separate regions with mutually perpendicular polarization are named "*90° walls*" or more precisely "*non-180° walls*". In tetragonal structures for example, the angle formed by the polarization vector on each side of a 90° domain wall is slightly smaller than 90° (Fig.1.4). In contrast to a ferroelastic material, ferroelectrics experience the formation of a surface charge on the grain/domain boundary due to the appearance of the *spontaneous polarization* P_S at the transition temperature. This surface charge produces an electric field E_d, called "*depolarizing field*", which is oriented oppositely to the spontaneous polarization. The effect of the depolarizing field is to make the occurrence of single-domain state energetically not favourable. The appearance of a spontaneous strain at the phase transition produces mechanical stresses, which is an additional obstacle to the formation of single-domain structure. Therefore to minimize the electrostatic and elastic energy the ferroelectric crystal splits into domains. Both 90° and 180° walls reduce the effects of the depolarizing electric fields, while the elastic energy is minimized only through the formation of 90° walls (see Fig.1.5). Domains separated by 180° walls differ only in the direction of the polarization, so the 180° walls are often defined "*purely ferroelectric*". Domains across 90° walls while by differ in the orientation of the polarization vector and in the spontaneous strain tensor; hence 90° walls are both ferroelectric and ferroelastic. Applied electric fields are able to induce movement in both types of domain wall, while external mechanical field can act only on the 90° walls.

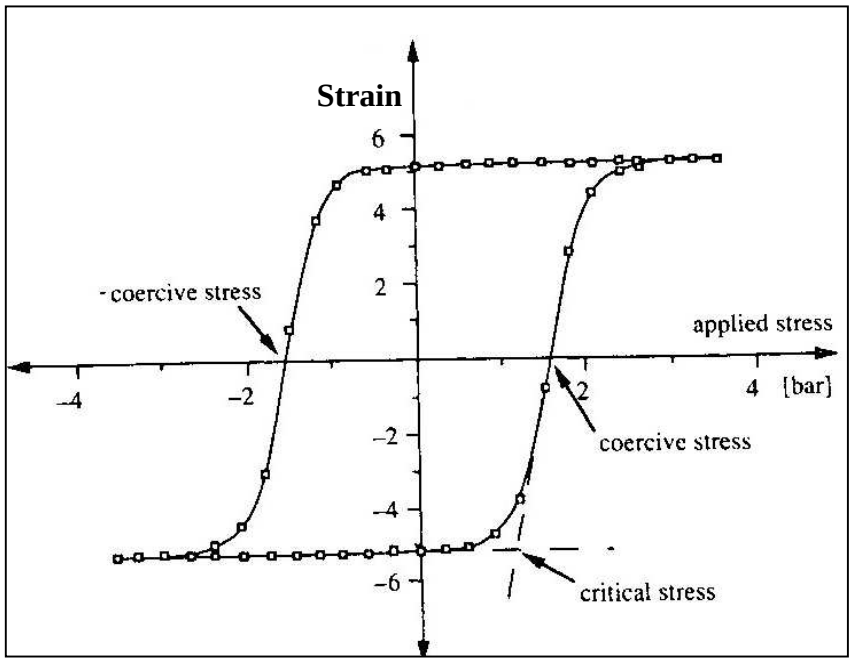

Fig.1.1: example of stress-strain hysteresis loop [1].

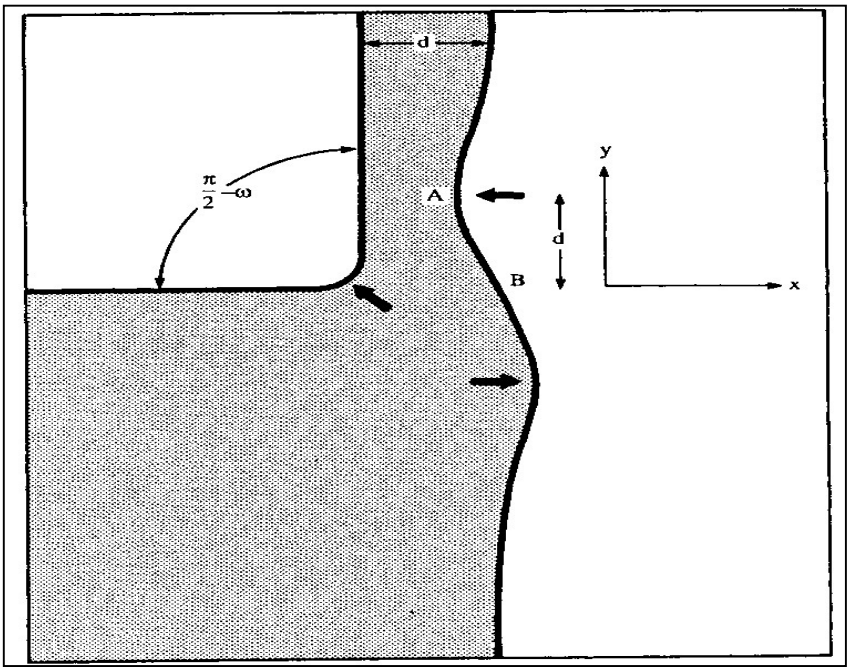

Fig.1.2: formation of S-shaped domain walls [1].

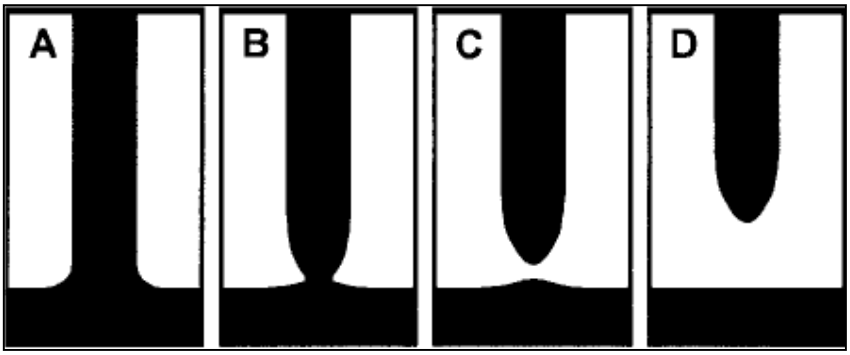

Fig.1.3: formation of needle-shaped domains [8].

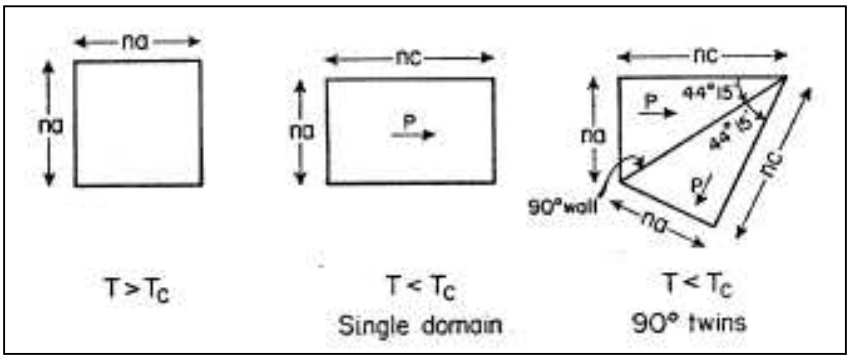

Fig.1.4: scheme of twinning [9].

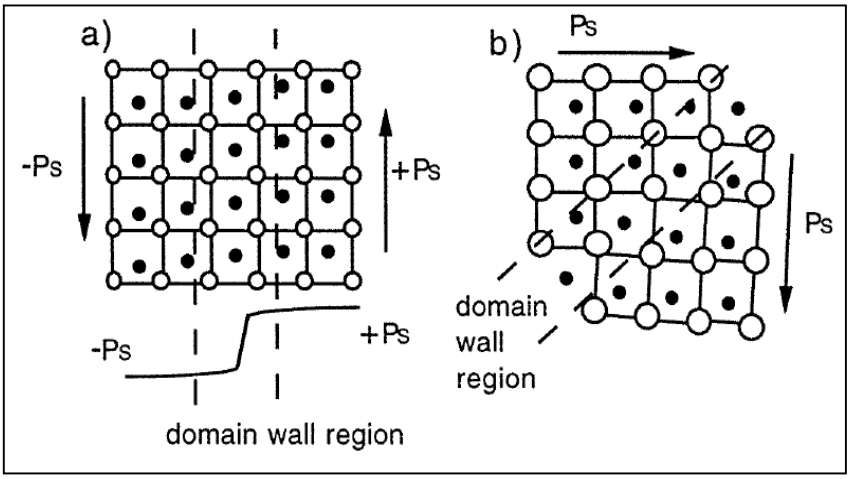

Fig.1.5: 90° and 180° domain walls [10].

Table 1.1: possible species of ferroelastics [3].

Ferroelastic species	Num. of states	Ferro-electric?	Ferroelastic species	Num. of states	Ferro-electric?	Ferroelastic species	Num. of states	Ferro-electric?
2F1	2	Yes	4/*mmm*F2/*m*(*p*)	4	—	6/*mmm*F*mmm*	3	—
*m*F1	2	Yes	4/*mmm*F*mmm*	2	—	23F1	12	Yes
2/*m*F$\bar{1}$	2	—	$\bar{3}$F1	3	Yes	23F2	6	Yes
222F1	4	Yes	$\bar{3}$F$\bar{1}$	3	—	23F222	3	—
222F2	2	Yes	32F1	6	Yes	23F3	4	Yes
*mm*2F1	4	Yes	32F2	3	Yes	*m*3F$\bar{1}$	12	—
*mm*2F2	2	—	3*m*F1	6	Yes	*m*3F2/*m*	6	—
*mm*2F*m*	2	Yes	3*m*F*m*	3	Yes	*m*3F*mmm*	3	—
*mmm*F$\bar{1}$	4	—	$\bar{3}$*m*F$\bar{1}$	6	—	*m*3F$\bar{3}$	4	—
*mmm*F2/*m*	2	—	$\bar{3}$*m*F2/*m*	3	—	432F1	24	Yes
4F1	4	Yes	6F1	6	Yes	432F2(*s*)	12	Yes
4F2	2	—	6F2	3	—	432F2(*p*)	12	—
$\bar{4}$F1	4	Yes	$\bar{6}$F1	6	Yes	432F222(*ss*)	6	—
$\bar{4}$F2	2	Yes	$\bar{6}$F*m*	3	Yes	432F222(*pp*)	6	—
4/*m*F$\bar{1}$	4	—	6/*m*F$\bar{1}$	6	—	432F422	3	—
4/*m*F2/*m*	2	—	6/*m*F2/*m*	3	—	432F32	4	—
422F1	8	Yes	622F1	12	Yes	$\bar{4}$3*m*F1	24	Yes
422F2(*s*)	4	Yes	622F2(*s*)	6	Yes	$\bar{4}$3*m*F2	12	—
422F2(*p*)	4	—	622F2(*p*)	6	—	$\bar{4}$3*m*F*m*	12	Yes
422F222	2	—	622F222	3	—	$\bar{4}$3*m*F222	6	—
4*mm*F1	8	Yes	6*mm*F1	12	Yes	$\bar{4}$3*m*F*mm*2	6	Yes
4*mm*F2	4	—	6*mm*F2	6	—	$\bar{4}$3*m*F$\bar{4}$2*m*	3	—
4*mm*F*m*	4	Yes	6*mm*F*m*	6	Yes	$\bar{4}$3*m*F3*m*	4	Yes
4*mm*F*mm*2	2	—	6*mm*F*mm*2	3	—	*m*3*m*F$\bar{1}$	24	—
$\bar{4}$2*m*F1	8	Yes	$\bar{6}$*m*2F1	12	Yes	*m*3*m*F2/*m*(*s*)	12	—
$\bar{4}$2*m*F2(*s*)	4	Yes	$\bar{6}$*m*2F2	6	—	*m*3*m*F2/*m*(*p*)	12	—
$\bar{4}$2*m*F2(*p*)	4	—	$\bar{6}$*m*2F*m*(*s*)	6	Yes	*m*3*m*F*mmm*(*ss*)	6	—
$\bar{4}$2*m*F*m*	4	Yes	$\bar{6}$*m*2F*m*(*p*)	6	Yes	*m*3*m*F*mmm*(*pp*)	6	—
$\bar{4}$2*m*F222	2	—	$\bar{6}$*m*2F*mm*2	3	Yes	*m*3*m*F4/*mmm*	3	—
$\bar{4}$2*m*F*mm*2	2	Yes	6/*mmm*F$\bar{1}$	12	—	*m*3*m*F$\bar{3}$*m*	4	—
4/*mmm*F$\bar{1}$	8	—	6/*mmm*F2/*m*(*s*)	6	—			
4/*mmm*F2/*m*(*s*)	4	—	6/*mmm*F2/*m*(*p*)	6	—			

Chapter 2: Domain wall dynamics

2.1 Introduction

The microstructural mechanisms of domain switching dynamics have been a matter of fundamental research for decades, but a universal theory is still missing. There is general agreement in the literature that domain switching involves two sub-processes: the nucleation of domain sites favourably orientated with the external field and the expansion of these sites by the movement of their walls. The expansion of the new domain sites produces a total change in the pre-existing domain configuration and it can occur once the domain nuclei have a critical size. Most of the published studies regard ferromagnetic and ferroelectric crystals, leaving the phenomenon of ferroelastic switching under mechanical loading less explored. The nucleation-growth mechanism is analogous for the different types of ferroic materials and it can be considered as a general framework in describing domain switching in various ferroic media. Relying on this analogy, some of the most significant achievements within the last 50 years on domain switching in ferroelectric systems are reviewed and experimental and theoretical approaches of general validity, which might be extended to the ferroelastic case, are summarized. The methodologies here reviewed, include empirical approaches, the development of kinetic models to describe domain switching dynamics, micromechanical and phenomenological models to simulate the macroscopic constitutive materials behaviour, random field theory to model the interactions between domain walls and pinning sites and thermal activation rate theory to estimate the effects of temperature and rate on the domain switching process. Furthermore, the most important achievements regarding the deformation and the creep behaviour in ferroeleastic and ferroelastic/ferroelectric materials are also mentioned and a brief summary on the Rayleigh-type behaviour and on the influence of rate and temperature on domain switching in ferroelectric media is also presented. The chapter is ended with a section on the aims and objectives of this work.

2.2 Experimental observations and empirical models

One of the first experimental observation of domain wall dynamics worthy of note was performed by W. Merz more than fifty years ago (1954) [11,12]. Merz studied the domain switching in ferroelectric poled $BaTiO_3$ single crystal by measuring the current produced by electrical pulses of different amplitude at different temperatures [11,12]. Domain switching was considered to occur in two stages: the nucleation of new domains with polarization opposite to the previous poling direction and expansion of these new domains under the action of the applied field. Merz described the trend with an empirical expression of the type:

$$i_{\max} \propto \exp\left(\frac{\alpha(T)}{E}\right) \tag{2.1}$$

where $i_{\max}$ is the switching current, $\alpha(T)$ is a coefficient temperature dependent and E is the applied electric field. In particular $\alpha(T)$ was found to be inversely proportional to the thickness of the sample [12]. Fitting of the results is shown in Fig.2.1. With increasing temperature it was possible to achieve the same switching current with a smaller electric field. Optical observations suggested that at higher temperatures the nucleation rate of reversed domains increased and the growth was faster. Compared with ferromagnetic systems, no sidewise motion of domain walls was found, but domain switching was observed occurring by the forward growth of many antiparallel new domains. The velocity at which the whole crystal switches was found to be eleven times smaller than the velocity of sound propagation and different mechanisms of nucleation-growth were proposed depending on the applied field level. At low field the switching time was considered to be primarily determined by the time necessary for the formation of new nuclei. At high applied fields the nucleation of new domain is very fast so the switching time is mainly due to the time that the new domains take to grow [12].

E.Little studied the nucleation and growth of 90º and 180º in barium titanate using an optical technique [13]. A single-domain crystal was employed to study 90º domain wall motion. The nucleation process is schematically illustrated in Fig.2.2. Wedges of opposite polarization are produced starting from the crystal boundaries. The

nucleation rate was found dependent on the applied field and on the time pulse. For the 180º domain switching, antiparallel domains formed with spike shapes at the crystal boundary and expanded along the polar axis. The dynamic of their growth is shown in Fig.2.3. The growth velocity increased with the applied field, but decreased in the last stage, when few domains remained still unswitched (blank wedges in Fig.2.3). The results suggested a fast forward movement and a slower sideways motion due to an increasing depolarizing field. A difference in the structure of the two types of walls was also proposed: 90º domain walls are thick as they were observed to split under certain switching conditions and 180º domain walls are thinner and they move through a mechanism of dipole flipping throughout the crystal. Interaction between 90º and 180º have been also studied and schematized in Fig.2.4. The results are in agreement with the trends found by Merz.

H.Stadler observed that in barium titanate the switching time decreased with increasing voltage and that at high voltages the switching time was half the time taken by a dilatational elastic wave to cross the crystal thickness [14].

Similar approaches for studying domain walls dynamic have been employed more recently with the advantage of more powerful microscopic observation techniques [15-17]. An increased use of AFM (Atomic Force Microscopy) and PFM (Piezoresponse Force Microscopy) has provided further insights in the domain switching kinetics [18-21].

V.Gopalan and T.E.Mitchell have studied the kinetics of 180º in $LiTaO_3$ finding similar trends already found previously in $BaTiO_3$ [15]. The effect of the internal field was also analyzed, whose microscopic origin is discussed in more detail in [16]. The presence of internal fields creates a large difference in the forward poling fields and reverse poling fields producing asymmetric P-E loops (Fig.2.5):

$$E_{\text{int}} = \frac{(E_f - E_r)}{2} \tag{2.2}$$

where E_f is the forward coercive field and E_r the reverse coercive field.

The switching time for the forward poling and the reverse poling were found to be dependent exponentially on the applied electric and internal field. A change in the activation field occurs from low to high electrical fields:

$$t_f = t_{f0} \exp\left(\frac{\delta_f}{E_f - E_{\text{int}}}\right), \qquad t_r = t_{r0} \exp\left(\frac{\delta_r}{E_f + E_{\text{int}}}\right) \tag{2.3}$$

The nucleation of new domains was not restricted only to the surface and the new nuclei had a dagger shape with polarization always opposite to the pre-existent domains, in the forward and reverse poling. The nucleation rate has been described with a function of the type:

$$\Gamma_f = \Gamma_{f0} \exp\left(-\frac{\beta_f}{E - E_{\text{int}}}\right) \tag{2.4}$$

where the parameter β_f assumes different values in the low and in the high field regime field. Sideways velocity was measured using transmitted light microscopy. Fig.2.6 shows the characteristic growth kinetics: triangles grow into larger triangles. Correspondence between domains is indicated with small arrows. It was concluded that in the low field regime the total switching time is limited by the sideways expansion of the domains and in the high regime field the nucleation of new domains and the sideways growth play approximately equal parts in determining the total switching time [15].

A direct observation of pinning and bowing of a single ferroelectric domain wall has been reported on $LiTaO_3$ using CMNSOM technique (Collection Mode Near-field Scanning Optical Microscope), showing that domain walls start moving under fields equal to a tenth of the coercive field [17].

AFM observation is a non-invasive technique to observe domain wall dynamic at nanometer scale [18]. Several measurements have been performed in lead zirconate titanate PZT thin films under constant electric pulses, showing an increasing domain radius with increasing time pulses (Fig.2.7). Domain wall velocity was measured

monitoring the lateral domain wall motion and the results were interpreted in terms of random field theory as explained in the next session [18,19].

PFM imaging performed by A.Gruvermar et al. on PZT thin films under constant electric fields has provided further insight regarding the kinetic of ferroelectric domain switching. At the beginning of the interval pulses the nucleation process is predominant; for longer time lateral domain expansion prevails. Nucleation process is enhanced at higher electric field applied (see Fig.2.8) and the nucleation rate changes during the time pulses: it reaches a maximum value after which it gradually decreases to zero [20]. Very recent analysis on PZT epitaxial thin films have used a combination of technique based on switching spectroscopy and PFM imaging for nucleation bias mapping [21].

2.3 Kinetic models

The kinetic of the domain switching process has often been studied using the Kolmogorov-Avrami approach, as proposed for the first time by Ishibashi and Takagi [22]. Based on fundamental assumptions [22], the fraction of volume switched under a constant applied field is expressed with a kinetic expression of the type:

$$V_S = 1 - \exp\left[\left(-\frac{t}{t_0}\right)\right]^n \tag{2.5}$$

where t_0 and n are used as fitting parameters. In particular n is related to the dimensionality of the domains and it has been found able to assume also non-integer values in contradiction with the original approach of the Kolmogorov-Avrami theory. Non-integer values of n have been proposed arising from the participation of domains with different dimensionality to the switching process [23]. Eq.2.5 is able to fit with good accuracy data for bulk materials, but it fails for domain switching in thin films [20,24].

A modified equation based on random field theory has been proposed for long-time tails to describe the evolution of the electric polarization in response to an electric field square wave in soft ferroelectrics [25]:

$$P(t) = P_A \exp\left\{-a\left[\ln\left(\frac{t}{\tau}\right)\right]^n\right\} \tag{2.6}$$

A rigorous kinetic theory for ferroelectric/ferroelastic switching was developed by Kukushkin et al. treating the domain switching process as a first order phase transition, showing that the kinetic can be described with analogue models of the liquid-solid phase transition [26,27]. The electric field/mechanical load plays the role of supercooling. Three different stages were identified. In the initial stage, thermal fluctuations produce the formation of a population of nuclei of the new phase, without causing any changes in the thermodynamic parameters of the system. In the second stage the process interests the main body, determining a significant variation of the thermodynamic state of the system, with a consequent variation of its thermodynamic parameters. The last stage was defined as "*Ostwald ripening*" and it is characterized by the mergence and the coalescence of small nuclei with larger ones. The theory developed allows deriving important characteristics of the process under constant field applied, such as an expression for the nucleation rate and growth rate, an expression for the evolution of the nucleus size distribution function and an expression which describes the volume fraction filled with nuclei [26,27].

2.4 Micromechanical models

Micromechanical models attempt the simulation of the macroscopic behaviour starting from the domain length scale. Macroscopic bodies are composed by grains containing domains randomly oriented. A switching criterion is a-priori assumed as threshold of non-linear behaviour. Homogenization techniques are used to simulate the continuum properties. The Reuss approximation represents the homogenization procedure and self consistent models the most sophisticated ones [28]. Reuss averaging is based on the assumption that stress and electric field are homogeneous throughout the polycrystal, whereas self-consistent models consider the crystal grains

as spherical inclusion in an infinite surrounding matrix. Two main categories of micromechanical models can be identified: models based on a complete switching and models based on incremental switching [29]. The main drawback of the micromechanical models is the huge number of internal variables, which causes significant difficulties for the implementation of such models in finite element computations.

2.5 Phenomenological models

The constitutive equations in phenomenological models are derived from a thermodynamic framework based on a Gibbs free energy or Helmotz free energy formulation, which are written as a function of internal variables of the system [29]. Cocks and McMeeking used remanent strain and remanent polarization as internal variables in the uniaxial case [30]. Later on, the model was extended in the multi-axial case by Landis [31]. The approach is based on the decomposition of the Helmotz free energy in a reversible part associated with the elastic, dielectric and piezoelectric energy per unit of volume and in an irreversible part related to the remanent strain and remanent polarization. Application of the Clasisus-Duhem inequality allows obtaining only the remanent states, which do not violate the thermodynamic principles: only non-negative increments in the energy dissipation are admitted. In agreement with the irreversible thermodynamics the remanent states are calculated through a flow rule, analogous to the J2 flow rule in metal plasticity, based on the concept of "*switching surface*". The switching surface analogously to crystal plasticity (yield surface) is a convex region of the space *electric field-stress* within which there is an absence of switching and the behaviour is linear piezoelectric [28]. The remanent states lie along the outward normal to the switching surface [28,31]. This thermodynamic framework requires several a-priori assumptions on the switching surface shape (switching criterion) and on the dependence of the linear properties and of the hardening moduli on the remanent strain and remanent polarization. Finite elements calculations enable the macroscopic material response to be simulated with a lower computational cost compared with the micromechanical models. The accuracy of the phenomenological approach in describing the experimental data has been compared with the accuracy of the micromechanical models for some of the most relevant ferroelectric compositions

[28]. However there are still no universal models to predict all the behaviour observed.

2.6 Models based on Domain Walls Pinning

A general approach has been developed to study domain wall dynamics in different types of ferroic systems, which treats the domain walls as elastic interfaces embedded in a potential environment, whose profile is perturbed by the presence of impurities acting as pinning points. In general, an external conjugate field produces a driving force on the interface, which interacts with the potential of the surrounding disordered medium in which the domain wall itself is placed. Random distributed impurities cause a random variation of the potential and consequently a slower domain walls motion. Disordering agents can produce two types of pinning effect, namely "*random bonds*" and "*random fields*" [19,21,32-35].

In the random bonds scenario, disordering agents keep the local symmetry of the order parameter, while in random fields disordering agents break this symmetry [21,32]. The effect of random bonds and random fields disorder on the potential landscape are shown in Fig.2.9: random bond disorder produces local variations in the depth of the double well potential (Fig.2.9a) keeping the symmetry of the function; random field disorder creates an asymmetrization of the ferroelectric double well potential (Fig.2.9b) [21,36].

Another distinction on the pinning nature is between "*weak*" and "*strong*" pinning. Pinning is considered "*weak*" (collective) when the interface is pinned on the fluctuations in the concentration of the disordering agents. Strong pinning occurs when the interface is pinned by many small isolated impurities [32]. At low temperatures there is a collective pinning and by increasing the temperature, the pinning effect becomes weaker and individual pinning becomes more and more frequent [37]. In the absence of thermal fluctuations and impurities the domain walls would assume a flat configuration. Disordering effects tend to roughen the domain wall and the resulting configuration arises from a competition between these disordering agents and the ordering effect of the interfacial elasticity [34-36].

The distorted configuration of the interface is defined through a displacement field $u(x)$ (Fig.2.10) whose correlation function *B(L)* quantifies the average displacement of the domain wall:

$$B(L) = < \overline{[u(x+L) - u(x)]^2} > \tag{2.7}$$

The symbol <…> denotes thermal averaging and $\overline{...}$ indicates disorder average; *L* indicates the length of the domain wall over which $B(L)$ is measured. The dependence of the correlation function $B(L)$ on *L* identifies two regimes: the so called "*Larkin regime*" where the dependence is of the type: $B(L) \propto L^{4-d}$ and the "*random manifold regime*" where $B(L)$ grows as $B(L) \propto \left(\frac{L}{L_L} \right)^{2\zeta}$ (Fig.2.11).

The exponent 2ζ depends on the nature of the disorder and on the dimensionality of the interface (fractal dimension). For a line (1-dimensional) in a random bond scenario, calculations have shown $\zeta = 2/3$. In case of a two-dimensional interface the roughness exponent has been estimated as $\zeta \approx 3/5$. In random field disorder the roughness exponent is given by: $\zeta = \frac{4-d}{3}$. The parameter ζ is defined "*roughness exponent*" [19,32,36]. The length threshold L_L is called "*Larkin length*" and it represents the smallest length at which the wall can be "*weakly pinned*". In the regime $L < L_L$ there is no metastability and no pinning occurs [32].

Often in the literature the correlation function $B(L)$ is replaced by the analogue function:

$$w(L) = < [u(x+L) - u(x)]^2 >^{1/2} \tag{2.8}$$

defined as "*domain wall roughness*".

In general the equations of the interface motion often used in the literature belong to two classes of equations: the *Edwards-Wilkinson equation* (linear approximation) and the *Kardar-Parisi-Zhang equation* (includes non-linear terms) [38]. A typical form of

the first class has been derived for the surface fluctuation in granular materials [39] and subsequently applied to the domain wall dynamic in disordered media [34,35]:

$$\frac{1}{k}\frac{\partial u}{\partial t} = C\nabla^2 u + F + F_P(x,u) + \eta(x,t) \tag{2.9}$$

where u is the average position of the domain wall, k and C are the "*mobility*" and the "*stiffness*" of the interface respectively. F is the external force applied and $\eta(x,t)$ represents the thermal noise. $F_P(x,u)$ is the pinning force arising from the random potential V_R:

$$F_P = -\frac{\partial V_R}{\partial u} \tag{2.10}$$

By solving Eq.2.9 the diagram "*interface velocity-applied force*" can be obtained at T=0 and at finite temperature, for static as well as dynamical external forces applied. A schematic diagram *velocity-applied force* is shown in Fig.2.12. At T=0 the interface does not move until the applied force reaches a critical value F_C. At finite temperatures, interface depinning can occur also in correspondence of subcritical forces, as effect of the thermal fluctuations. In the case $T = 0$, the thermal noise term $\eta(x,t)$ in Eq.2.9 is absent. The solution of Eq.2.9 for constant applied force shows that, in the hypothesis of *weak pinning*, the interface does not move until the applied force reaches a critical value F_C. At $T > 0$ and small forces applied the following expression for the domain wall creep velocity (under constant forces applied) has been derived:

$$v \propto \exp\left(-\frac{E_B}{k_B T}\right)\left(\frac{F_c}{F}\right)^{\mu} \tag{2.11}$$

where E_B is the energy barriers between different metastable states (pinning energy). The parameter $\mu = \frac{\vartheta}{2-\zeta}$, where $\vartheta = 2\zeta + d - 3$, is called the "*dynamical exponent*" and it takes into account both the dimension of the system *d* and the nature of the disorder [35]. The above expression can be seen as a generalization of the empirical Merz law (2.1) obtained from a physical basis and it takes into account the presence

of thermal fluctuations, the effect of a random potential, the nature of the disorder and the dimensionality of the domain wall [36]. The validity of this equation has been ascertained in different experimental situations and for different types of ferroic materials [19,40]. Regardless the temperature, for $F >> F_C$ the velocity is a linear function of the force applied [32-35].

Under an alternating applied field, domain wall motion is influenced by the frequency at which the external field is cycled. The macroscopic rate effects are represented by the dependence of the coercive field and the loop hysteresis on the frequency of the applied field [34,35]. Domain walls exhibit different modes depending on the frequency applied, which can be recognised in the so called "*Cole-Cole plot*", where the complex part χ'' of the dynamical susceptibility χ, is plot against its real part χ' (Fig.2.13). Note that the plot has absolutely a general character and it can be generated in different kinds of ferroic materials: the susceptibility becomes the magnetic susceptibility, the piezoelectric coefficient and the mechanical compliance in ferromagnetic, ferroelectric and ferroelastic systems respectively. The semicircle region indicated with R in Fig.2.13 corresponds to the highest frequency applied with a dispersive Debye-type function, which is reflected only in an oscillation between local energy minima, without net interface motion (Relaxation regime). For slightly lower frequencies, the Cole-Cole plot is linear and the range of frequencies is called "*creep regime*", where sideways motion of the domain walls can overlap to the nucleation of reversed domains. For smaller frequencies the susceptibility should be purely imaginary and ideally the slope χ'' / χ' becomes infinity as one can see in the schematic Cole-Cole diagram (Fig.2.13). This region is called "*viscous sliding*". In the range of even lower frequencies, the Cole-Cole plot appears as a quarter circles, half of the *relaxation* semicircle representing the "*switching region*" [35]. Characterization of domain wall dynamic in terms of Cole-Cole plot has been performed on ferromagnetic systems [35], ferroelectric materials [41] and more recently also in the ferroelastic case [37].

A general expression for the dependence of the susceptibility on the frequency of the applied field has been derived in the magnetic case [32]. It was shown that below a minimal length scale, domain walls move freely, hopping the pinning barriers. This

length scale depends logarithmically on the frequency of the applied field and leads also to a logarithmic dependence of the magnetic susceptibility. The functional dependence is given by:

$$\chi(\omega) = \chi_L \left[1 + \left(\frac{T}{T + T_L} \right) \ln \left(\frac{1}{\omega t_0} \right) \right]^{2/\vartheta} \tag{2.12}$$

where χ_L is the susceptibility at $T = T_L$. Analogous expressions have been applied to the piezoelectric coefficient [42] and to the mechanical compliance [37].

2.7 Models based on Rate Theory

Different mathematical treatments to describe the effect of the rate of the applied field on domain switching in different ferroic systems are based on the analogy with the dislocation motion in metals [43-45]. Domain switching is a thermally activated phenomenon and its driving force is partly supplied by the applied external field and partly supplied by the thermal fluctuation. Analogously to the dislocation case, the rate of switching can be expressed using an Arrhenius-type equation:

$$\dot{\varepsilon} = \dot{\varepsilon}_0 \exp \left[- \left(\frac{\Delta G}{k_B T} \right) \right] \tag{2.13}$$

where $\dot{\varepsilon}_0$ is the pre-exponential parameter depending on several microstructural factors [45], ΔG is the Gibbs free energy of the process, k_B the Boltzmann's constant and T the absolute temperature. The application of Eq.2.13 in appropriate experimental conditions, allows estimating the activation parameters of the domain switching process under static and dynamical applied fields [43,45]. The values of the activation parameters estimated for ferroelectric switching suggest that the energy required for the switching is mainly supplied by the external field [45]. Thermal fluctuations produce low amplitude and long wavelength undulation of domain walls and consequently nuclei with reverse polarization in shape of long protrusions and thickness in the order of the domain wall width are formed preferably on the domain walls [45].

2.8 Deformation behaviour

Ferroelastic and ferroelastic/ferroelectric materials exhibit a characteristic deformation behaviour when subjected to an external applied stress. The deformation response has been widely studied in different crystallographic structures and compositions under various loading conditions. Uniaxial compression is the most common test performed [46-58], but also studies involving tensile [59-62], bending [63-65] and torsion [66] loading conditions have been presented in the literature. Analyzing more specifically the behaviour under uniaxial compression loading, highly non linear deformation behaviour is observed in all the ferroelastic and ferroelastic/ferroelectric materials, usually attributed to the domain switching process.
In materials having solely ferroelastic characteristics, only a reorientation of the spontaneous strain occurs upon loading. In systems displaying ferroelastic and ferroelectric properties at the same time, the spontaneous strain reorientation is also accompanied by a rearrangement of the polarization domain configuration. In particular for the latter case, the mechanical response is also affected by the electrical boundary conditions [60,64]. These materials present higher stiffness in open circuit conditions than in short circuits [60].

Fig.2.14 shows an example of compressive stress-strain curve of a ferroelastic/ferroelectric material initially poled along the loading direction. The graph indicates a linear trend at small compressive loads (A-B path). This is just an ideal case, as most of ferroelastic materials present a non-linear behaviour even at very small loads. By increasing the load, non-180º domain switching occurs, which is reflected in a pronounced non-linear trend and in a decreasing tangent modulus. Mechanical loading produces plastic deformations due to the domain switching and a depolarization process, which is often named "*mechanical depolarization*" [51]. The spontaneous strain gets reoriented and the polarization of the domains switches in direction perpendicular to the load axis (B-D path), producing a depolarizing effect. At some stage, the domain switching becomes exhausted and no more domains are available to switch. The trend then appears again linear (D-E path). Stress-strain graphs do not display any distinct point correspondent to the onset of domain switching [50]. They rather present an inflection point, whose correspondent stress identifies the "*coercive stress*" of the material. The coercive stress represents the

stress at which the system has the highest switching rate [51]. The inflexion indicates the stress threshold where there is a transition from a softening process to a hardening process in the tangent modulus of the medium [50]. At the beginning of the unloading, the stress-strain trend is linear and its slope has been used by some authors to estimate the Young's modulus of the material (e.g. Ref. [54]). During unloading, a partial back switching occurs, leading to an irreversible strain and to a remanent polarization [47,51]. Such non-linear stress-strain behaviour can be observed in soft and hard compositions. The differences between those are evidenced by a lower coercive stress, a faster switching saturation, a higher depolarization and a higher strain irreversibility in the soft compositions compared with the hard ones [47,50]. Greater back switching in hard materials can be explained by higher internal stresses developed upon unloading, which facilitate the strain/polarization recovery [48].

For PZT compositions, the *Zr:Ti* ratio has been found to influence the mechanical properties and consequently the stress-strain trend. In more detail, at the morphotropic phase boundary (MPB) the remenent strain and the remenent polarization assume the maximum value and the coercive stress has a minimum [47].

2.9 Creep behaviour

The "*creep*" phenomenon is characterized by time dependent deformations occurring in different classes of materials, when subjected to constant loads for a certain period of time. In structural ceramics, creep is produced by the mechanism of vacancies diffusion, which is more significant at high temperature. In metals, creep deformation is mainly due to dislocation motion. Diffusional creep flow becomes more relevant at very high temperature. Three creep stages can be ideally identified under constant load, namely "*primary creep*", "*steady state creep*" and "*tertiary creep*" (Fig.2.15). During the first stage, the strain rate decreases with the time, due to a material's hardening, consequent to an increasing hindrance of dislocation movement. The strain rate decreases until it reaches a minimum, where it starts to be nearly constant, giving rise to a steady state creep, where the dislocations slide with constant low velocity. In the tertiary stage, microvoids are produced at the grain boundaries, which facilitate

grains sliding, producing an increasing strain rate and at the end the complete failure of the material [67].

Ferroelastic and ferroelectric ceramics exhibit mechanical and electrical creep also at room temperature, due to the thermally activated nature of the domain switching process. A number of studies regarding the creep phenomenon in this class of materials have already been performed [59,68-73], but a complete understanding of the inherent physical mechanisms is still missing.

Creep behaviour under tensile stress was performed by T.Fett and G.Thun [59]. D.Zhou and M.Kamlah performed mechanical and electrical creep tests on soft PZT at room temperature in poled and unpoled state [68]. A creep of the primary type, with a continuously decreasing strain rate, was found and described using an Andrade-type power law expression. The creep magnitude was observed to depend on the level of the applied mechanical load, with a maximum near the coercive field, due to the highest amount of domain switching in that region. The creep behaviour was attributed to a migration process of pinning defects under the action of the applied mechanical load, which produces a local unpinning effect on the domain walls. The diffusion character of the defects redistribution gives rise to the strain and polarization time dependence. The creep rate decay during time evidences that domain switching is locally consumable, implying the existence of saturation states [68]. In a separate study by the same authors, electrical creep behaviour was found to be also dependent on the electric loading history [69].

A more complicated power law expression was employed by Q.D.Liu and J.E.Huber to fit the uniaxial electrical creep observed in soft PZT-5H [70]. The model is able to describe a slow and stable creep below the coercive field and a rapid switching followed by gradual saturation above the coercive field.

J.S. Forrester and E.H. Kisi studied the mechanical creep behaviour of a soft composition of PZT doped with La and Sn in poled and unpoled state under compression loading. Poled samples showed a higher population of switchable domains compared with the unpoled ones. Creep strain was confirmed to be dependent on the level of the applied load, with a decreasing rate during time, which

denotes material's hardening. The results were described using an Andrade-type power law function, achieving good accuracy [71].

O.Guillon and coworkers simulated the creep behaviour of a soft PZT with a viscoplastic-type model, which was only able to reproduce the experimental data qualitatively. They also studied the influence of temperature, which was found to reduce the anelastic strain and the creep strain itself [72].

More recent studies were carried out in $LaCoO_3$ and $La_{0.8}Ca_{0.2}CoO_3$ based perovskites at room temperature [73], confirmed the trends previously described. An alternative phenomenological model was developed, which differently from the commonly used power laws, presents asymptotic values and therefore is mathematically able to describe saturation equilibrium strain states with high fitting accuracy. Differently from metals, creep in ferroic materials is an incremental exhaustion process of the finite number of switchable domains, which leads to a primary creep type and to the existence of strain saturation equilibrium states [73].

2.10 Rayleigh-type behaviour

Different types of ferroic systems exhibit similar hysteretic behaviour under the action of an applied external field. A particular manifestation of hysteretic characteristics is represented by the Rayleigh-type behaviour, observed for the first time in ferromagnetic materials in 1887 [74], characterized by hysteretic $M-H$ loops under weak applied fields and well described by the following empirical relationship, known as "*Rayleigh law*" [75]:

$$M = (\chi_{init} + \alpha_R H_{\max}) H_m \pm \frac{\alpha_R}{2}(H_{\max}^2 - H_m^2) \tag{2.14}$$

M is the magnetization, H_m is the applied magnetic field, $H_{\max}$ is the amplitude of the magnetic field, χ_{init} the initial magnetic susceptibility and α_R the Rayleigh parameter (Fig.2.16). There have been many attempts at deriving this equation from theoretical models, assuming that the Rayleigh hysteresis originates from the Barkausen jumps of the domain walls over pinning sites randomly distributed in the material [76-78].

Defects produce a significant perturbation of the potential energy of the medium in which the domain wall moves. Motion in such an environment leads to a magnetization field dependent which can be expressed with a reversible linear term and an irreversible quadratic component. The former is related to the vibrations and to small displacements of the domain wall around an equilibrium position, while the latter reflects the crossing of a local potential barrier by the domain wall, which reaches another equilibrium position (Fig.2.17) [79]. The magnetic susceptibility in weak field regime was found to be a linear function of the applied magnetic field and expressed as:

$$\chi = \chi_{init} + \alpha_R H_{\max} \tag{2.15}$$

Following these approaches, more recently, a Rayleigh type equation has been proposed also for ferroelectric systems, suggesting that the hysteretic behaviour of different types of ferroic materials can be described with analogous models [10,41,79-85]. A detailed review of ferroelectric hysteresis studies can be found in [10,41].

Ferroelectric systems show "*intrinsic*" and "*extrinsic*" contributions to the piezoelectric response. The intrinsic term reflects the change induced by the field within a domain, while the extrinsic is associated with domain wall movement [86]. Different experimental methods have been used to evaluate both contributions [84-91]. Particularly interesting is the procedure applied by Q.M.Zhang and coworkers based on the measurement of the hydrostatic piezoelectric coefficient, whose changes are due solely to variations of volume and definitely not related to domain walls movement, which is volume conserving [91]. It was found that at room temperature the extrinsic contribution is much higher than the intrinsic, in agreement with [87].

Both the reversible and irreversible components of the piezoelectric coefficient have show a dependence on the frequency of the external field applied [37,42,79,82,92,93], which has been described by employing a logarithmic expression proposed in [32], where a detailed treatment on the dynamic of interfaces (domain walls) has been presented and applied in particular to the magnetic susceptibility.

Rayleigh characteristics can be modified by doping, which influences the domain wall mobility. Interesting studies regarding the effect of dopants on the Rayleigh behaviour can be found in [83-85,90]. It can be generally summarized that donor species have a softening action, facilitating domain walls motion and acceptor agents produce a hardening of the material, hindering the domain walls movement. In particular the effect of donors was found to be much more significant in rhombohedral than in the tetragonal phase in PZT [90].

Deviations from the Rayleigh behaviour have been also observed and attributed to the presence of low disordered phases [10,79]. A harmonic analysis of the material's response under cyclic external fields gives the possibility to establish the conditions when a hysteretic non-linear systems behaves as a purely Rayleigh system. It was claimed that a purely Rayleigh behaviour is difficult to find in a real material and therefore it is convenient to replace the term "*Rayleigh behaviour*" with "*Quasi-Rayleigh behaviour*" [10].

A Rayleigh type analysis has been recently performed also on ferroelastic materials in bending conditions, monitoring the temperature dependence of the Rayleigh parameters on unpoled PZT [94]. The results were also used to obtain the activation energy of the Rayleigh process, displaying significantly larger values compared with the ones more recently presented in [45,95,96] for the ferroelectric case.

2.11 Rate and temperature effects

A number of studies regarding the influence of the rate of the applied electric field and of the temperature on domain switching have been performed in ferroelectric systems, by measuring P-E loops at different electric field frequency and temperatures, in bulk materials and thin films. Early work on barium titanate showed that the coercive field increases logarithmically with the frequency of the applied field [97,98]. A similar functional dependence was found also in $La_{0.5}Sr_{0.5}CoO_3/(Pb,La)(Zr,Ti)O_3/La_{0.5}Sr_{0.5}CoO_3$ thin film capacitors [99]. Increasing coercive field with increasing frequency was also measured in soft and hard PZT, doped respectively with Nb_2O_5 and Fe_2O_3 [100] and in $0.955Pb(Zn_{1/3}Nb_{1/3})O_3$-

$0.045PbTiO_3$ single crystal [101]. In [100] it was shown that the coercive field in the soft composition increases with the frequency up to 5 Hz and then it becomes almost constant. In the hard composition the saturation level was found to correspond to a much smaller frequency (400 mHz). The frequency dependence of the coercive field was justified as follows. The coercive field represents the effective field necessary to overcome the restoring forces and the viscous forces acting on the domain walls, during switching. At low frequency, the domain wall velocity is small and the viscous forces are reduced, determining a low coercive field. The saturation level occurs in a range of frequencies where the forces acting on the domain walls are not frequency dependent anymore. The difference in the upper limit between the soft and the hard composition has been attributed to a stronger pinning effect due to dipolar defects or space charges occurring in the hard composition. The rate dependence of switching and back switching was studied in virgin and fatigued (or depinned) state in the soft and the hard composition. Samples of the soft composition experienced a much smaller polarization in the fatigued state compared with the virgin specimens. The opposite behaviour was found in the hard composition. In virgin samples of the hard composition, dipolar defects aligned along the spontaneous polarization of the domains exert a pinning action on the domain walls, producing very small polarization and large backswitching. Decay in the saturation polarization with increasing frequency was also shown and imputed to a gradual decay of the 90º domain wall contribution, whose reorientation process is very slow, as also shown in [102]. The percentage of back switching was always found higher at lower frequencies, except in the virgin hard composition. Longer unloading time allows a higher degree of realignment of domains with the field. For fast electric field removal, domains tend to come back to their equilibrium position with high velocity. As a result, the viscous forces increase, limiting the backswitching [100].

J.Yin and W.Cao performed dynamic experiments, which allowed coercive field measurements at very low frequency (10^{-5} Hz), detecting a coercive field threshold, identified by a saturation value occurring for long time measurements (very low frequency), which represents an intrinsic switching barrier. This is in disagreement with random field models in which the coercive field can be arbitrarily small in correspondence of low enough frequencies [101].

Other studies in PZT 5H [45] and in PMN-PT [103], have shown that the coercive field decreases and the remanent polarization increases if the frequency is decreased.

The influence of temperature on ferroelectric switching has been analyzed in bulk materials as well as in thin films. In $BaTiO_3$ domain wall velocity was found to increase four orders of magnitudes when the temperature was increased of 75ºC [104]. Temperature dependence of stress-strain hysteresis was measured in $Pb_3(PO_4)_2$ single crystal at different loading rates and a decreasing strain with increasing temperature and loading rate was observed [105]. Ferroelectric P-E loop measurements in PZT 5H at various temperature showed a decreasing coercive field and remanent polarization with increasing temperature [45]. A linear decay in the coercive field and in the remanent polarization by increasing temperature was also found in PZT thin films [106]. Coercive field increased with decreasing temperature also in bismuth-layer structured thin films [107]. The lower coercitivity at higher temperature was explained based on the temperature-dependent effect of oxygen vacancies [108].

2.12 Aims and objectives

The main purpose of this work is to develop theoretical approaches and experimental methodologies of general validity in characterizing domain switching dynamics in ferroelastic and ferroelastic/ferroelectric materials. More precisely, the present study aims to achieve the following objectives:

- **Development of a general model in ferroelastic switching**

Based on the published literature, there is a significant lack of theoretical models describing domain walls dynamic stress induced in ferroelastic and ferroelastic/ferroelectric materials. The intention is to provide a general model which accounts for the intrinsic nature of the ferroelastic behaviour and therefore would be applicable to different ferroelastic compositions, avoiding the diversity of empirical expressions that would arise from fitting of the experimental data. In particular, in relation to the thermal activated nature of domain switching, the model aims to describe the deformation mechanisms in static and dynamic loading conditions, providing insightful parameters to quantify the rate dependence and the temperature effects on ferroelastic switching. The relationships between such parameters and materials crystal structure/composition would provide a more confident awareness on how microstructure and ferroelastic macroscopic behaviour are related.

- **Development of experimental methodologies to study rate and temperature dependence of ferroelastic switching**

In the literature there is almost a complete absence of experimental methodologies able quantify the effect of rate and temperature on domain switching mechanical stress induced. The present work aims to overcome this gap through the development of sensible experimental approaches for such purposes.

- **Evaluation of ferroelastic properties of different compositions**

The increasing use of ferroelastic materials in high technological applications, such as solid fuel oxide cells, oxygen separation membranes, sensors and catalysts, requires a detailed evaluation of the ferroelastic properties and a more clear understanding of the factors affecting them. For instance, the development of cracks in thin permeable membranes or the development of large creep deformation during working operations

would be undesirable and a detailed knowledge of the deformation behaviour of different ferroelastic compositions would eventually help in the choice of the most appropriate compositions and in understanding the relationships between composition (or doping) and deformation properties. This would overcome current technological problems, improving the performance of those materials in specific applications.

- **Ferroelectric switching mechanisms and role of thermal fluctuations**

The evolution of the domain configuration upon electrical loading has still not been satisfactorily described in the literature. The objective of this work is to gain further understanding in the domain switching dynamics by clarifying the domain switching mechanisms in the different regions of the hysteresis loops. The analysis will be carried out through a detailed inspection of the hysteresis curves (P-E and butterfly loops) and through an accurate study of the creep relaxation curves. The simultaneous measurement of polarization and strain during dwelling could provide the necessary information to understand the domain switching evolution along the loops. Creep tests, together with dynamic tests at different frequencies will be also useful to investigate the role of thermal fluctuation in ferroelectric switching, allowing further comparison with the ferroelastic case, in static and dynamic conditions.

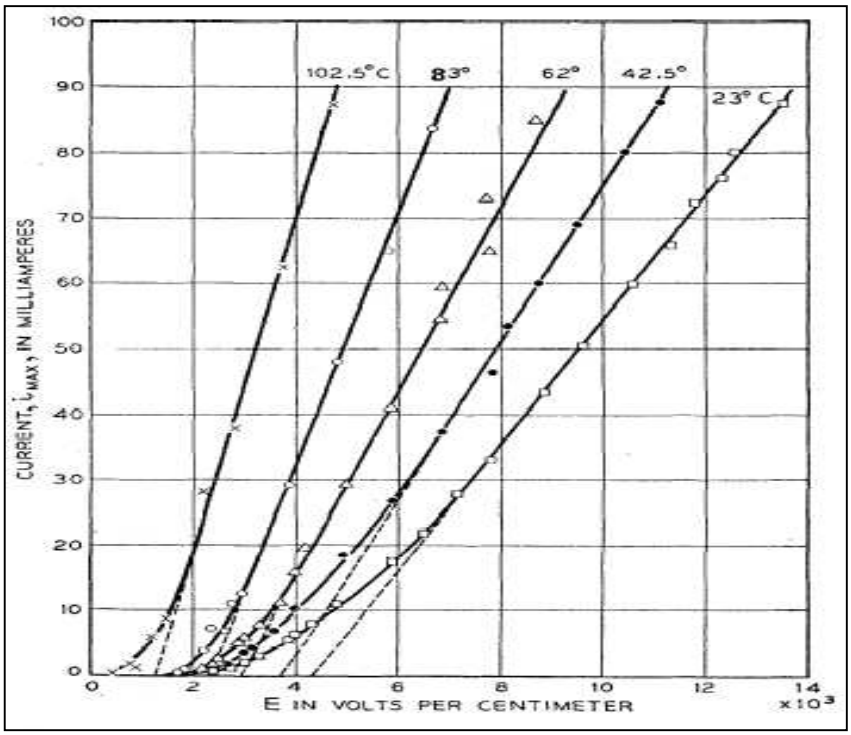

Fig.2.1: switching current-electric field [11].

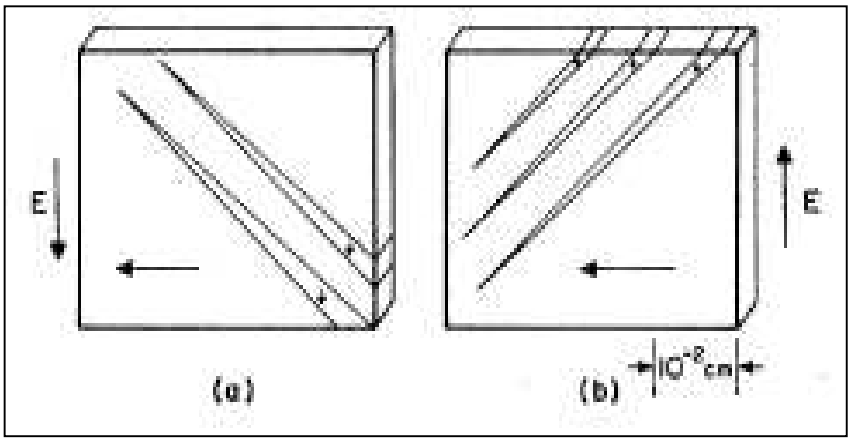

Fig.2.2: 90º domain switching nucleation [13].

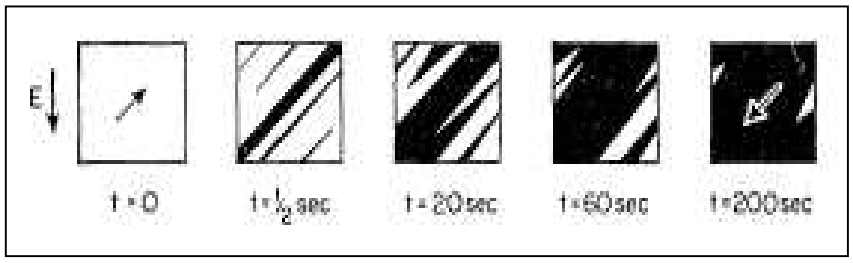

Fig.2.3: 180º domain switching kinetic [13].

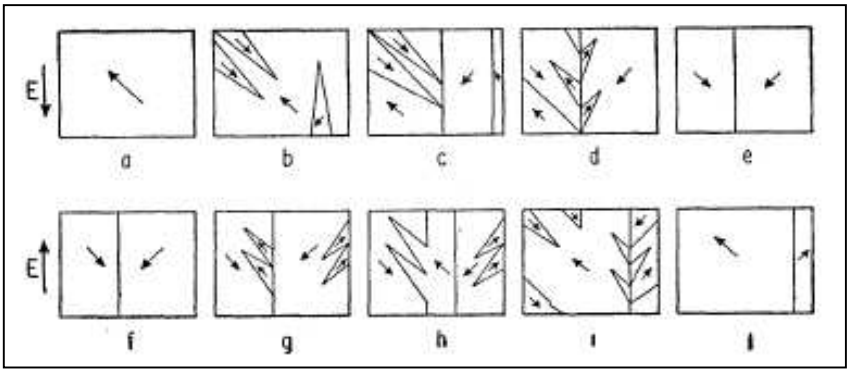

Fig.2.4: 90º and 180º domain walls interaction [13].

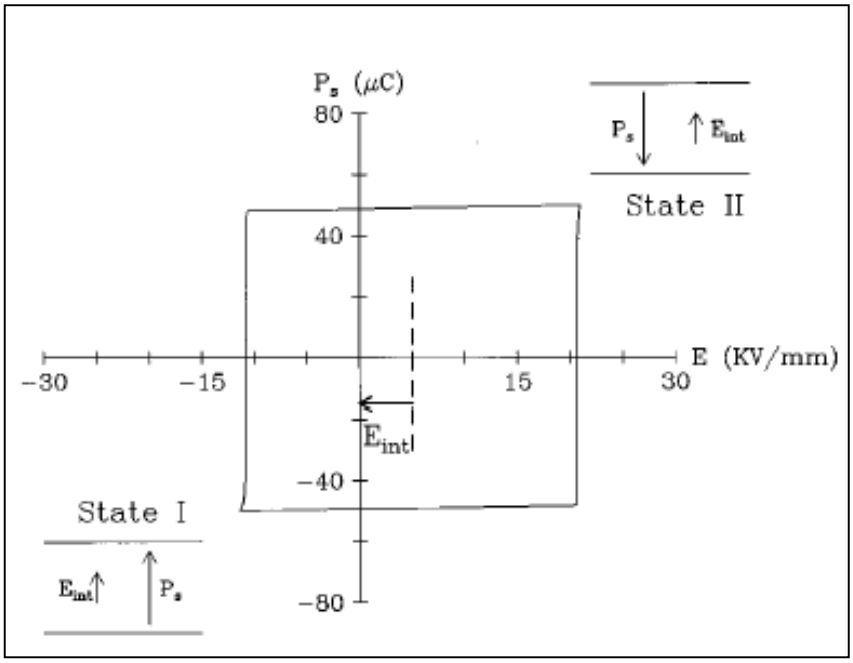

Fig.2.5: P-E loop asymmetry due to internal field in $LiTaO_3$ [15].

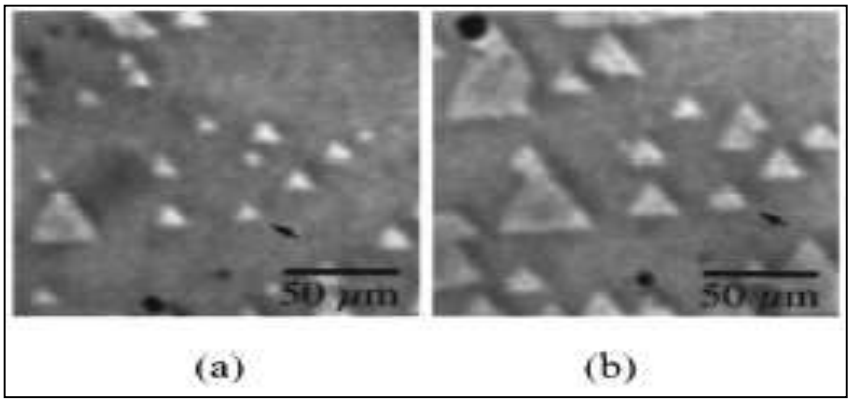

Fig.2.6: growth of 180º domains in $LiTaO_3$ [15].

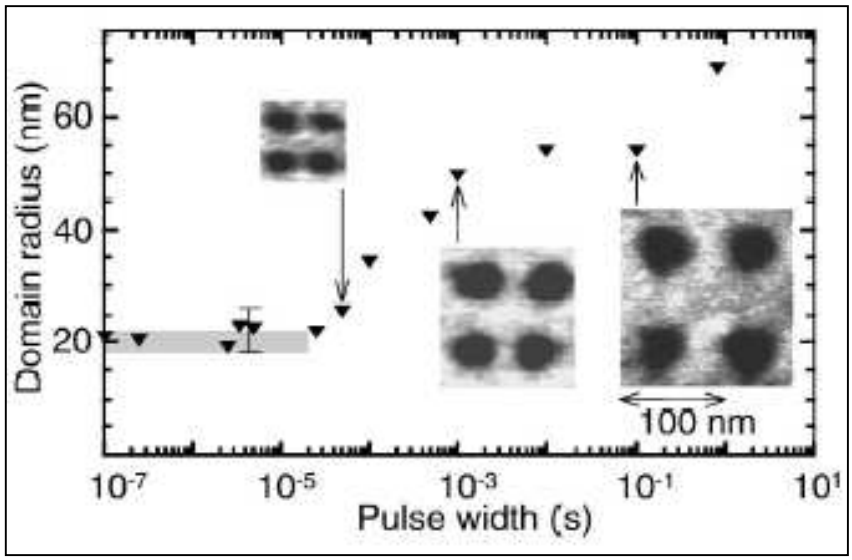

Fig.2.7: AFM image of domains as function of time pulse width in PZT thin films [18].

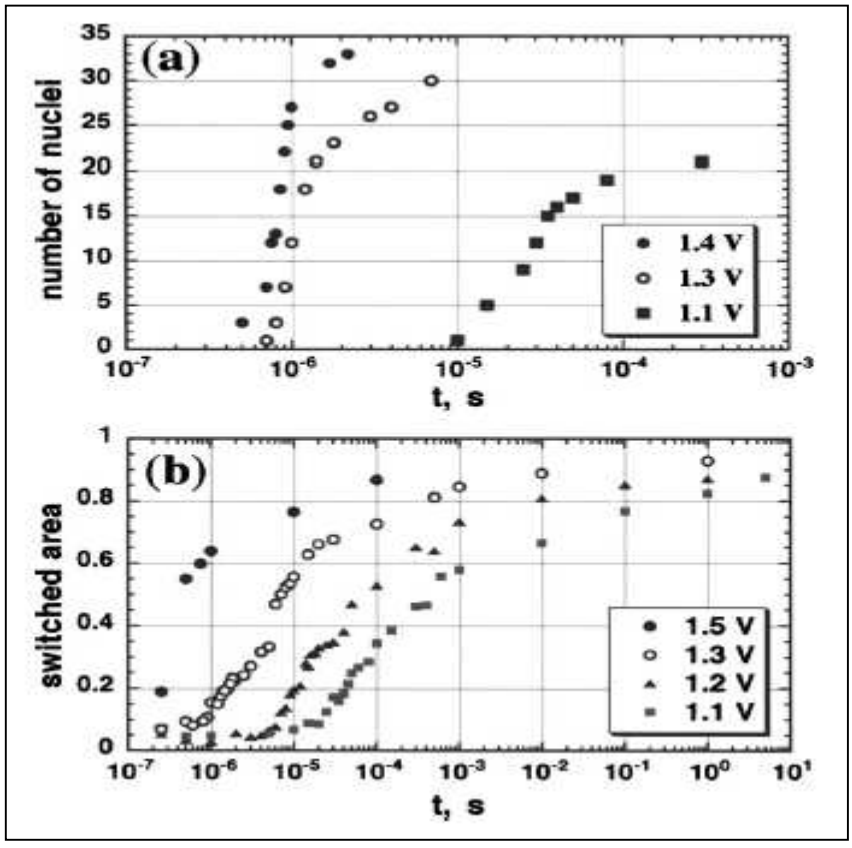

Fig.2.8: number of nuclei and switched area as function of time pulse width and applied electric field in PZT thin films [20].

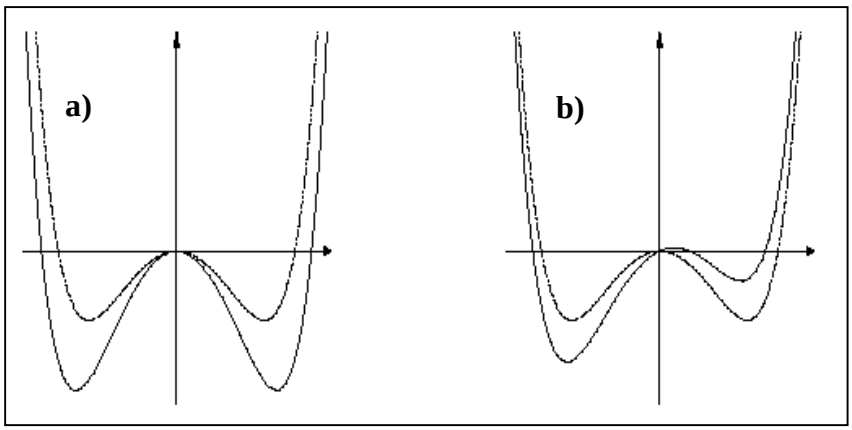

Fig.2.9: a) double well potential in random bond, b) random field [36].

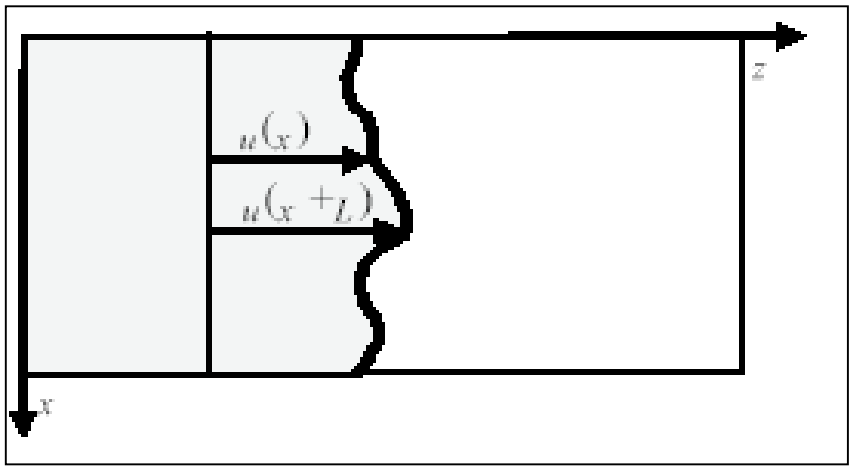

Fig.2.10: domain wall roughening [36].

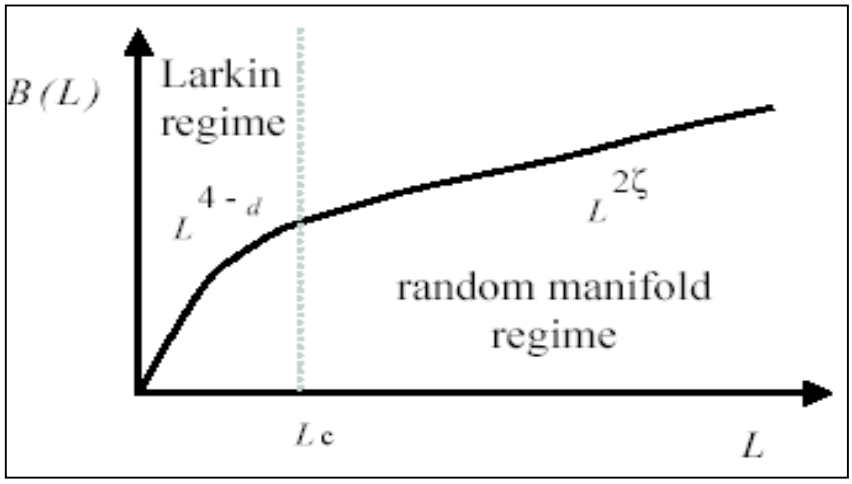

Fig.2.11: domain wall roughening regimes [36].

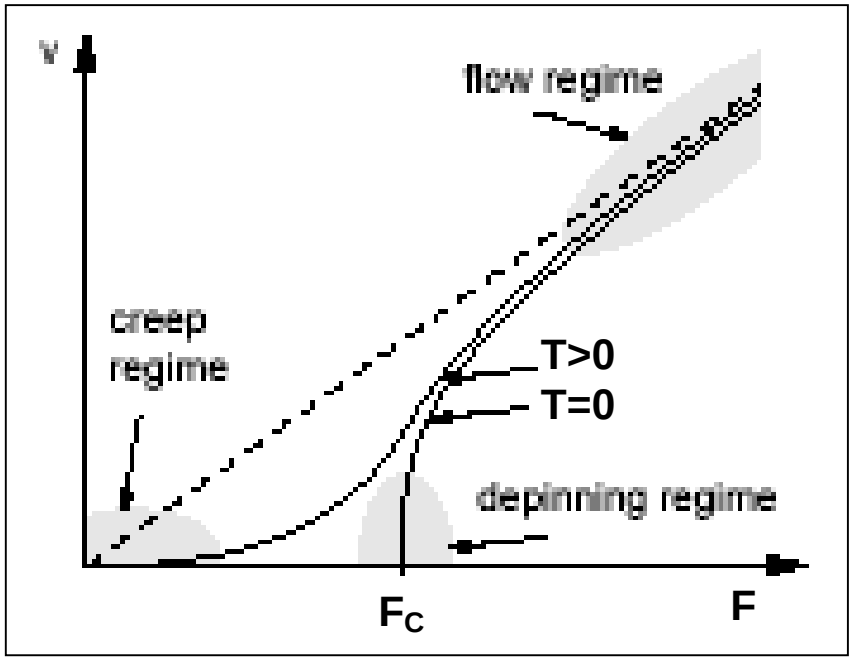

Fig.2.12: domain wall velocity-driving force at zero and finite temperature [34].

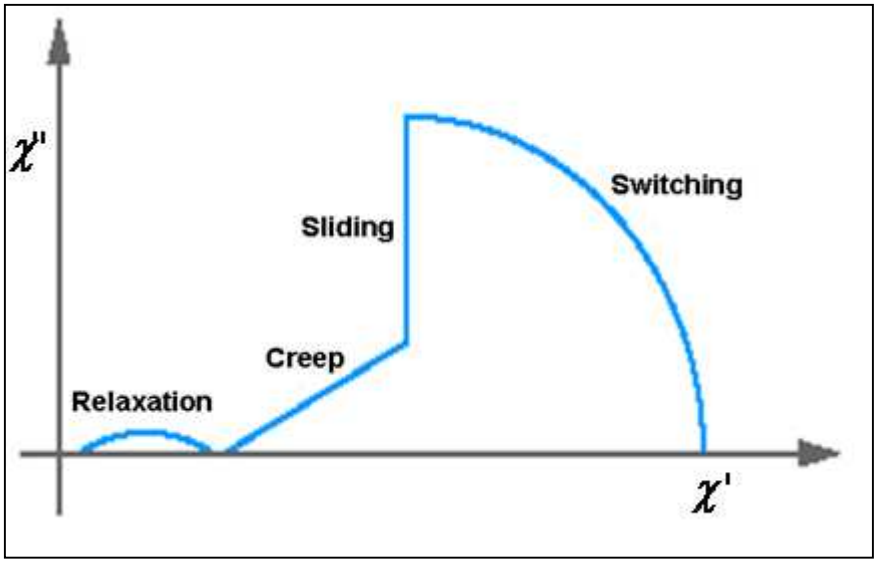

Fig.2.13: schematic Cole-Cole plot [35].

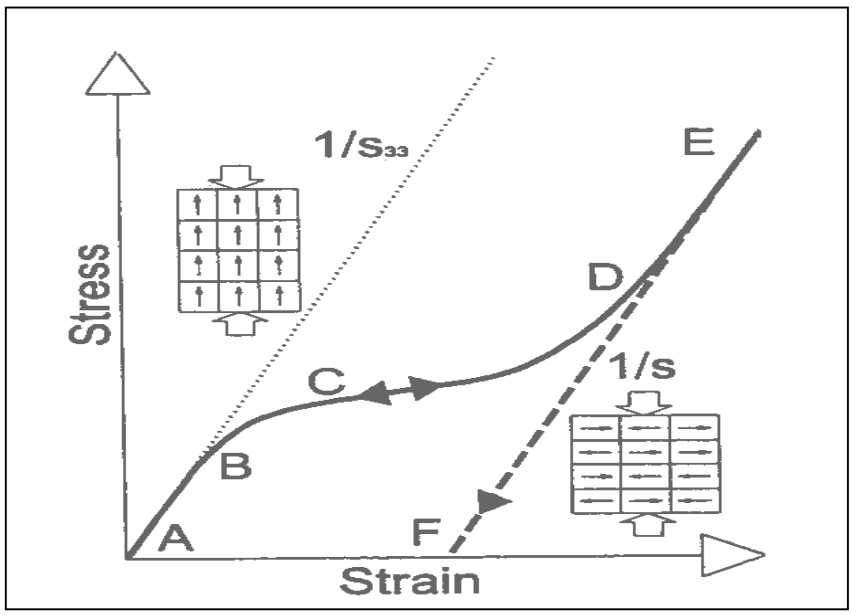

Fig.2.14: schematic stress-strain curve of ferroelastic/ferroelectric material [47].

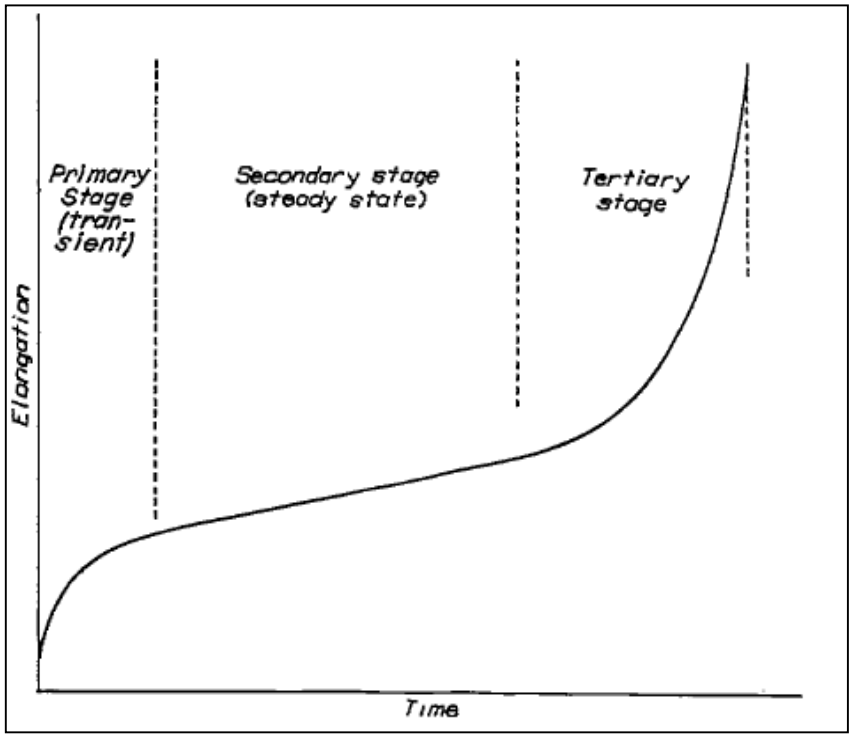

Fig.2.15: three stages of creep in metals [67].

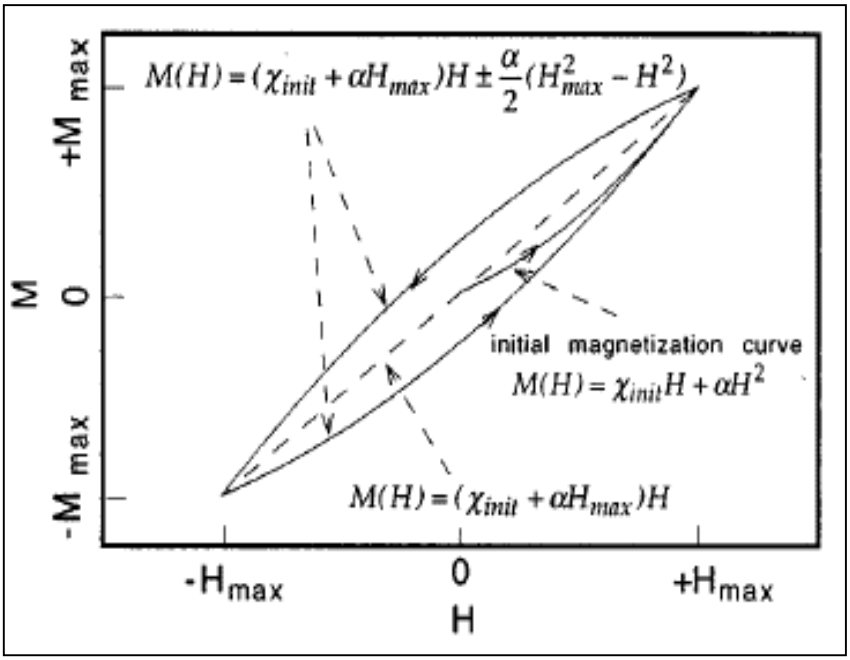

Fig.2.16: Rayleigh loops in magnetic materials [79].

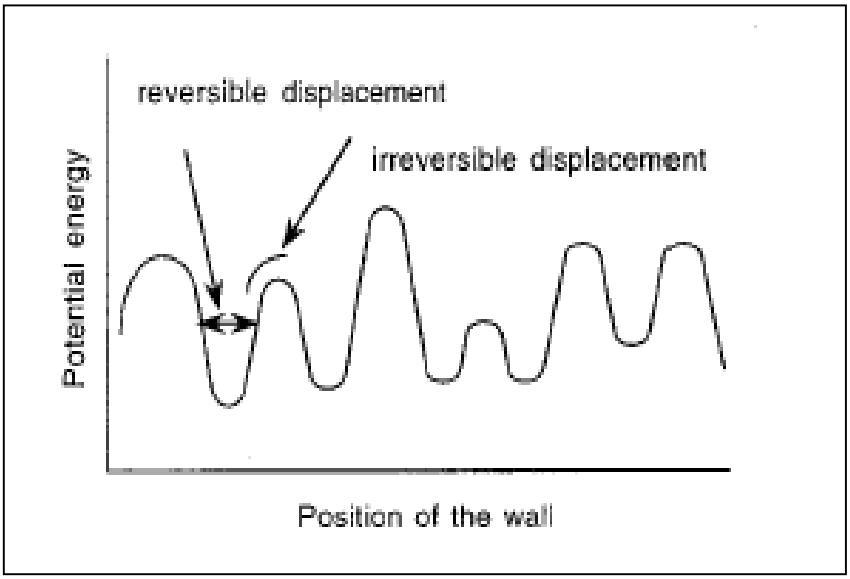

Fig.2.17: potential energy profile in ferroic materials [79].

Chapter 3: Rate model in ferroelastic switching

3.1 General framework

It is widely accepted in the literature and also confirmed by experimental observations that domain switching event occurs in two main key steps: the nucleation of new domain nuclei favourably orientated with the external field, and the subsequent expansion of these nuclei through the movement of their walls. Previous studies have demonstrated that the domain walls are the most favourite sites for the nucleation of the new domain nuclei, as also reviewed in [45]. Therefore it is reasonable to model the domain switching process as shown in Fig.3.1, where a volume *V* of material contains two pre-existing domains A and B. The domain A is supposed to be more favourably orientated than the domain B, with respect to the external field. The process of the switching of the domain B can be also seen as the expansion of the domain A to the expense of B, through the movement of the domain wall *d*. For the expansion of the domain A, one can imagine that the thermal fluctuations together with the applied field produce the nucleation of a new domain at the domain boundary. If this nucleus has a critical size, the domain wall jumps to the new equilibrium position, under the action of the effective shear stress τ_{eff} . Following the approach presented in [45], it is assumed that critical nuclei expand with no drag resistance, implying that the rate of nucleation is controlling the rate of the entire switching process. The critical volume of the new nucleus able to expand is called "*activation volume*", indicated in Fig.3.1 with V_a. Analogously to the dislocation case, the formation of activated complexes is a statistical process, resulting from the crossing of a potential energy barrier by molecules with high enough energy. Energy barriers are represented by long and short range interaction. Long range interactions are active throughout the material, while short range interactions are superimposed to the long ones and they act locally. Thermal fluctuations enable short range interactions to be surmounted under the application of an external field, driving the domain switching process.

According with the Eyring's rate theory [67,109,110], the rate of formation of critical nuclei Γ is given by:

$$\Gamma = \frac{k_B T}{\hbar} \exp\left[-\left(\frac{\Delta G}{k_B T}\right)\right] = \nu \exp\left[-\left(\frac{\Delta G}{k_B T}\right)\right] \tag{3.1}$$

where ν is the frequency at which the activated complexes overcome the energy barrier, G is the Gibbs free energy of the process, k_B is the Boltzmann constant and T the absolute temperature. The formation of nuclei produces a shear strain γ whose rate $\dot{\gamma}$ can be written as:

$$\dot{\gamma} = \gamma\Gamma = \gamma\nu \exp\left[-\left(\frac{\Delta G}{k_B T}\right)\right] = \gamma\nu \exp\left(\frac{\Delta S_e}{k}\right) \exp\left[-\left(\frac{\Delta H}{kT}\right)\right] \tag{3.2}$$

The shear strain γ depends on the density of nucleation sites ρ and on the area A_S swept by the domain wall (Fig.3.1), as shown in [45]. As the entropy change ΔS_e is very difficult to calculate especially in polycrystalline materials, it will be enclosed in the pre-exponential term, together with γ and ν, having:

$$\dot{\gamma} = \dot{\gamma}_0 \exp\left[-\left(\frac{\Delta H}{k_B T}\right)\right] \tag{3.3}$$

The term ΔH is given by the difference between the change in the internal energy ΔU and the work done W, leading to:

$$\dot{\gamma} = \dot{\gamma}_0 \exp\left[-\left(\frac{\Delta H}{k_B T}\right)\right] = \dot{\gamma}_0 \exp\left[-\left(\frac{\Delta U - W}{k_B T}\right)\right] = \dot{\gamma}_0 \exp\left[-\left(\frac{\Delta U - V_a \tau_{eff}}{k_B T}\right)\right] \tag{3.4}$$

The work done W has been expressed as the product between the activation volume V_a and the "*effective shear stress*" τ_{eff}, as already presented in [109,110].

It should be noted that in this model, the rate of activation of nuclei in the reverse direction has been neglected. In addition, for simplicity, the influence of the

depolarizing field in the ferroelastic/ferroelectric compositions has not been taken into account.

3.2 Creep deformations

Likewise to the case of dislocation movement [67,110], the effective shear stress τ_{eff} acting on the domain walls can be written as:

$$\tau_{eff} = \tau_{app} - \tau_{in} \tag{3.5}$$

where τ_{app} is the applied shear stress and τ_{in} the internal stress developed which oppose to the domain switching process.

In previous stress relaxation experiments on PZT, the influence of internal stress was shown [111]. It was argued that when the applied stress is higher than the internal stress, normal relaxation behaviour is observed, but when the internal stress exceeds the applied stress, negative stress relaxation occurs. When the internal stress is equal to the applied stress, no relaxation can be measured [111].

In ferroelastic and unpoled ferroelastic/ferroelectric compositions, the application of a mechanical load produces the generation of internal stresses due to the perturbation of the stable configuration of the domain structure developed below the phase transition temperature. In poled materials, the internal stresses arise by altering the stable configuration produced in the poling process. In both cases internal stresses oppose to the ferroelastic switching, as indicated in Eq.3.5.

It should be noted that the strain measured in the experiments is the normal strain ε, and it is related to γ by a numerical coefficient, which can be included in the pre-exponential term, having:

$$\dot{\varepsilon} = \dot{\varepsilon}_0 \exp\left[-\frac{\Delta U - V_a(\tau_{app} - \tau_{in})}{k_B T}\right] \tag{3.6}$$

It follows that:

$$\ln \dot{\varepsilon} = \ln \dot{\varepsilon}_0 + \frac{\Delta U}{k_B T} + \frac{V_a \tau_{app}}{k_B T} - \frac{V_a \tau_{in}}{k_B T} \tag{3.7}$$

In order to explain and describe the reason of the strain rate decay during creep, a differentiation respect with time can be made:

$$\frac{\partial}{\partial t}(\ln \dot{\varepsilon}) = \frac{\partial}{\partial t}(\ln \dot{\varepsilon}_0) - \frac{V_a}{k_B T}\frac{\partial \tau_{in}}{\partial t} \tag{3.8}$$

where the activation volume and the energy barrier have been considered time independent. In the first term at the second member of the previous equation, the only term which as been considered changing with time is the density of nucleation sites ρ. Eq.3.8 can be more conveniently rewritten as:

$$\frac{\partial}{\partial t}(\ln \dot{\varepsilon}) = A\frac{\partial \rho}{\partial \varepsilon}\frac{\partial \varepsilon}{\partial t} - \frac{V_a}{k_B T}\left(\frac{\partial \tau_{in}}{\partial \varepsilon}\frac{\partial \varepsilon}{\partial t}\right) \tag{3.9}$$

It is worthy realizing that the variation of ρ and τ_{in} during time are physically related; however the mathematical dependence is at the present unknown, therefore ρ and τ_{in} will be treated as independent each other. Integration of the Eq.3.9 respect with time gives:

$$\ln \dot{\varepsilon} = A\frac{\partial \rho}{\partial \varepsilon}\varepsilon - \frac{V_a}{k_B T}\theta\varepsilon \tag{3.10}$$

where $\theta = \frac{\partial \tau_{in}}{\partial \varepsilon}$.

In compression tests the maximum shear stress is half of the normal stress, therefore:

$$\theta = \frac{1}{2}\frac{\partial \sigma_{in}}{\partial \varepsilon} \tag{3.11}$$

It is assumed that the hardening produced during creep is the same as the hardening produced in monotonic loading. Therefore the hardening parameter can be evaluated as

the hardening of the stress-strain curve at every stress.

The second member of Eq.3.10 presents two terms associated with two possible causes of the strain rate decay during time. The first term is related to the exhaustion of the nucleation sites and the second term represents the build up of the internal stresses. By neglecting the exhaustion process, the Eq.3.10 predicts a linear trend $\ln\dot{\varepsilon}-\varepsilon$, whose slope can be used to estimate the activation volume V_a. Any deviations from linearity are attributed to the exhaustion mechanism.

3.3 Rate experiment

Domain switching is a time dependent process due to the effect of the thermal fluctuations on the domain wall movement. The longer the time during which thermal fluctuations can act, the higher the number of domains that may be switched. The influence of thermal fluctuations increases when the rate of the applied field is decreased. In the ferroelastic case, the applied stress needed to achieve a certain level of strain is higher in correspondence of higher loading rates. By generating stress-strain curve at different rates, the dependence of the applied stress on the loading rate can be determined for each strain state, by applying rate theory. At constant temperature the strain rate $\dot{\varepsilon}$ is expressed by Eq.3.6, from which one can obtain:

$$\ln\dot{\varepsilon} = \ln\dot{\varepsilon}_0 + \frac{\Delta U}{k_B T} + \frac{V_a \tau_{app}}{k_B T} - \frac{V_a \tau_{in}}{k_B T} \tag{3.11}$$

where the shear stress has been replaced with the normal stress as previously done for the creep case. Eq.3.11 can be rearranged as:

$$\left[\frac{k_B T}{V_a}\right]\ln\dot{\varepsilon} = \left[\frac{k_B T}{V_a}\right]\ln\dot{\varepsilon}_0 + \frac{\Delta U}{V_a} + \frac{(\sigma_{app} - \sigma_{in})}{2} \tag{3.12}$$

By assuming that a variation of the loading rate does not produce significant changes in the microstructure (constancy of the pre-exponential term) and in the internal stress σ_{in}, it follows that:

$$\left[\frac{k_B T}{V_a}\right] = \frac{1}{2}\frac{\partial \sigma_{app}}{\partial \ln \dot{\varepsilon}} \tag{3.13}$$

Plots $\sigma_{app} - \ln\dot{\varepsilon}$ can be generated for each level of strain and from the slope the activation volume can be estimated. The proposed model can be applied also in studying the influence of the temperature on the domain switching process, by calculating the activation enthalpy ΔH. From the rate equation (Eq.3.6) follows that:

$$\ln\dot{\varepsilon} = \ln\dot{\varepsilon}_0 - \frac{\Delta H}{k_B T} \tag{3.14}$$

The dependence of the strain rate on the loading rate and on the temperature is different for each strain (or stress) state. It is therefore needed to identify a parameter which is both rate and temperature dependent and that at the same it would represent the ideal physical conditions for the analysis. In the ferroelectric case [45], the coercive field has been proposed for such estimation, as it shows rate and temperature dependence, it guarantees comparable thermodynamical conditions for different rate and temperatures (always the highest switching rate for different rates and temperatures) and moreover it always occurs in correspondence of zero polarization, ensuring constancy of microstructure conditions. In analogy with the coercive field in P-E loops, the coercive stress has been identified as the most appropriate thermodynamical conditions for the analysis. By differentiating Eq.3.14 respect to $(1/T)$ at the coercive stress, one obtains:

$$\left(\frac{\partial \ln\dot{\varepsilon}}{\partial(1/T)}\right)_{\sigma_C} = -\frac{\Delta H}{k_B} \tag{3.15}$$

By determining the coercive stress at each loading rate and temperature, a master plot $\sigma_C - \ln\dot{\varepsilon}$ at different temperatures can be generated. For a constant value of σ_C then, another plot $\ln\dot{\varepsilon} - (1/T)$ can be obtained, whose slope is related to the activation enthalpy ΔH, through Eq.3.15.

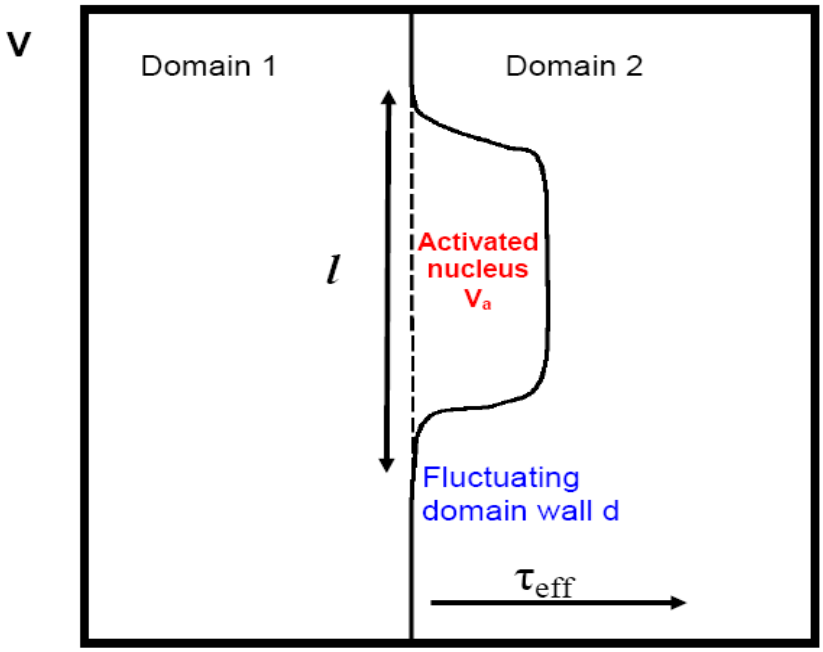

Fig.3.1: scheme of domain wall dynamic in domain switching.

Chapter 4: Materials and experimental methods

4.1 Introduction

Perovskite ceramics of the type ABO_3 are the object of this study. They belong to the Class 4 in the Dudnick-Kiosse classification (see Chapter 1). Compositions with ferroelectric and ferroelastic properties at the same time and compositions displaying only ferroelastic behaviour were selected for the experimental studies. The choice of the compositions selected has been motivated by a considerable scientific and industrial interest in these materials [48,49,56,57,112]. In this chapter, details regarding the compositions studied, the experimental equipment and methods are presented and described.

4.2 Materials

4.2.1 Ferroelectric/Ferroelastic Perovskites: PZT-4D, PZT-5A

Hard PZT-4D and soft PZT-5A samples poled along two different directions were supplied by Morgan Matroc Transducer Division (Southampton, UK) and in particular two different batches of PZT 5A have been received from the company. Due to commercial confidentiality, details on the dopants are unknown. General properties and previous characterizations are given in [44].

PZT solid-solution ceramics display excellent dielectric, pyroelectric and piezoelectric properties and they are widely used in different types of applications, such as sensors, actuators and transducers. They exhibit ferroelastic and ferroelectric properties at the same time. The PZT phase diagram is shown in Fig.4.1. The morphotropic phase boundary in the middle of the diagram separates the tetragonal and the rhombohedral ferroelectric phases. The subscripts A and F stand for antiferroelectric and ferroelectric phase and the letters C, T, R and O for cubic, tetragonal, rhombohedral and orthorhombic phases respectively. At the morphotropic phase boundary (which occurs for compositions $PbZrO_3$:$PbTiO_3$ close to 1:1), most of the properties, such as dielectric constant, piezoelectric coefficients and electromechanical coupling

coefficients, are maximized. It is rare to find PZT in a chemically pure form. By doping, '*hard*' and '*soft*' PZT compositions can be obtained. '*Hard*' compositions are produced using acceptor dopants in the A-site, for instance K^{+1}, or by replacing (Zr,Ti) in the B-site with acceptors like Fe^{+3}. As a result, oxygen vacancies are introduced, which stabilize the domain structure, increasing the coercive field and making the process of poling-depoling more difficult. Acceptor doping increases electrical conductivity and reduces dielectric loss, due to a hindered domain-wall motion.

"*Soft*" compositions are generated by doping PZT with donor species. They exhibit high dielectric losses, low conductivity, low coercive field and high piezoelectric coefficients. The process of poling-depoling is much easier compared with "*hard*" compositions.

Due to their simultaneous ferroelectric/ferroelastic nature, there is interest to understand the mechanical response of PZT in different poling states. PZT 4D and PZT 5A samples of cylindrical and square shape were mechanically tested with dimensions mentioned in each experimental condition in the following chapters. Piezoelectric coefficients were measured before every experimental test and the numerical values are reported in each experimental chapter. In order to also study the behaviour also in the unpoled state, specimens were depoled in a furnace up to temperatures 50ºC above the Curie point for two hours.

In order to study analogies and differences on the domain switching behaviour induced by mechanical stress and electric field, electrical experiments such as P-E loop, butterfly hysteresis and electrical creep were also carried out on PZT 5A.

4.2.2 Ferroelastic Perovskites

Five different compositions having only ferroelastic characteristics have been analyzed:

- $LaCoO_3$ (LC)
- $La_{0.8}Ca_{0.2}CoO_3$ (LCC)

- $(La_{0.7}Sr_{0.3})_{0.98}MnO_3$ (LSM)
- $(La_{0.9}Sr_{0.1})_{0.95}Cr_{0.85}Ni_{0.05}Mg_{0.1}O_3$ (LSCNM)
- $La_{0.6}Sr_{0.4}Fe_{0.8}Co_{0.2}O_3$ (LSFC)

The powders were provided by Praxair Specialty Ceramics (USA) and the samples were processed through a succession of calcination, dry milling, uniaxially pressing, cold isostatically pressure and sintering. Calcination temperature, uniaxial and isostatic pressure, sintering temperature and time were different for the different compositions. Samples were machined at PremaTech Inc. (USA).

$LaCoO_3$ (LC) and $La_{0.8}Ca_{0.2}CoO_3$ (LCC)

Lantanum cobaltites are ABO_3 perovskites (see Fig.4.2) and they represent very promising materials for solid oxide fuel cells and for oxygen separation membrane, because of their high ionic conductivity. Although they present excellent electrochemical and thermal properties, the possibility of their use is determined by their mechanical properties, which are of great interest [56,112].

Lantanum cobaltites undergo a ferroelastic phase transition from a cubic phase (stable at high temperature) to a rhombohedral phase (stable at low temperature) with space group $R\bar{3}c$ [56,112-114]. The phase transition produces four different variants. The spontaneous strain is represented by a stretching along the (111) direction (Fig.4.3) The rhombohedral distortion is described using the angle ά (Fig.4.3). Pure LC has the largest distortion of the cobaltite compounds. The rhombohedral distortion can be reduced by substituting divalent cations on the A site. The distortion disappears for doping with Sr^{2+} above x=0.5 [114].

The transition temperature is very high (>1100ºC) and can be lowered with A^{2+} cation substitution. Such doping produces a conversion to a metallic phase [114]. The substitution of calcium produces an increase in the thermal conductivity by three orders of magnitude for 10mol% and four orders of magnitude for 20mol% Ca [114].

Different types of microstructural features have been observed in LC, such as twins, antiphase domains, stacking faults and dislocations. Details can be found in [113,114]. Information on the processing conditions are given elsewhere [115].

$(La_{0.7}Sr_{0.3})_{0.98}MnO_3$ (LSM)

Strontium substituted lanthanum manganite are of interest for solid fuel cell cathodes with due to their high chemical stability and electronic conductivity [116]. In addition, they present interesting magnetoresistance properties, which make them useful in magnetic memory devices [117]. Tailored properties can be obtained via different amounts of doping. The $La_{1-x}Sr_xMnO_{3+\delta}$ system has a pseudo-perovskite structure, having orthorhombic symmetry of the type $Pbnm$, rhombohedral $R\bar{3}c$ and monoclinic $P2_1/c$ [118].

$(La_{0.9}Sr_{0.1})_{0.95}Cr_{0.85}Ni_{0.05}Mg_{0.1}O_3$ (LSCNM)

Pure $LaCrO_3$ materials are widely used in solid fuel cells, oxygen separation membranes and sensors. They experience a first order phase transition from an orthorhombic structure $Pbnm$ (stable at low temperature), to a rhomboedral $R\bar{3}c$ (stable at higher temperature). The phase transition starts around 250ºC and finishes roughly at 268ºC. Such transitions can be driven also by applying mechanical stress.

At higher temperatures these systems undergo another phase transition of the second order from the rhombohedral phase to a cubic phase. Addition of Sr^{2+} stabilizes the presence of the rhombohedral phase at room temperature [119]. Substitution of Cr with Ni produces the precipitation of metallic Ni nanoparticles. There is considerable scientific and technological interest in the study of the stress induced phase transition, which will be subject of the next chapters. Details about the processing condition are given in [119].

$La_{0.6}Sr_{0.4}Fe_{0.8}Co_{0.2}O_3$ (LSFC)

LSFC composition has very good electrical conductivity between 600ºC and 800ºC, high oxygen surface exchange and high oxygen self diffusion coefficient. It does not react with ceria-based electrolytes and it presents a compatible coefficient of thermal expansion. In terms of crystal structure, this system shows different distortion from

the perfect cubic lattice depending on the level of Sr^{2+} doping. For *x* below 0.2, it presents an orthorhombic structure. The most studied composition is $La_{0.6}Sr_{0.4}Fe_{0.8}Co_{0.2}O_3$, which has a rhombohedral symmetry at room temperature and a phase transition to cubic between 400ºC and 500ºC [120].

4.3 Experimental equipment

4.3.1 Measurements of piezoelectric constants

The d_{33} piezoelectric coefficient of the PZTs was measured with a Berlincourt piezometer (model ZJ-3B) produced by the Institute of Acoustic Chinese Academy of Science. The device applies small dynamical forces F parallel to the polarization direction and it measures the resulting charge, ΔQ, obtaining the piezoelectric constant as:

$$d_{ij} = \frac{\Delta Q}{\Delta F}$$

4.3.2 Mechanical tests

Mechanical tests were performed using a servo-hydraulic testing machine (Instron 8511) with a load cell of 20 kN. Compression loads were applied along the sample maximum dimension using a metal push rod (Fig.4.4) and the strain was measured using three strain gauges, placed on the lateral faces of the specimen, along the loading direction. The actual strain was calculated by averaging the values given by the three different strain gauge signals. Strain gauges (model FLA-3-11-1L), with a strain gauge factor of 2.14, were purchased from Tokyo Sokki Kenkyujo Co.Ltd and supplied by Techni Measure. A mechanical jig was used to optimize the alignment of the sample along the loading axis, minimizing bending effects (Fig.4.4). The alignment of the specimen was improved upon small load ramps and by adjusting the position of the sample after each ramp, in order to get strain signals as similar as possible in all the strain gauges. The experimental data was acquired using Labview software (version 6.1) with a rate of sampling dependent on the loading rate of the

test. In particular, compression tests on poled samples were carried out in closed circuit conditions, using metal plates on the top and at the bottom of the sample.

The sensitivity of the equipment was estimated using a sample of alumina which displays linear elastic behaviour. By generating its stress-strain curve (Fig.4.5), the absence of artefacts during stress-strain measurements was ensured and the validity of the stress-strain results of all the other materials tested was proved. The noise and eventual drift in the load and strain signals were evaluated by holding a constant stress of 100 MPa for ten minutes on the alumina sample, which at room temperature does not experience any creep strain. The noise in the signals was calculated as the difference between the peak to peak values and it was estimated as $\pm 5N$ for the load signal which did not show significant drift (Fig.4.6). For the strain signal the drift was quantified as $1*10^{-8}/s$ (Fig.4.7). The maximum appropriate loading frequency was estimated to be 0.5 Hz. At higher frequencies, the phase lag between the load and the strain signals produced an apparent hysteresis, which is not an actual feature of linear elastic materials such as alumina.

4.3.3 Temperature chamber

A heating chamber was built to carry out experimental tests in a controlled temperature environment. Samples were tested within a square chamber made up of superwool, which is a very good thermal insulator. The temperature regulation was achieved with a system of two Peltiers (ThermaTec^{TM}) and four fans, placed in the chamber and heated by a power supply (Manson SPS9602). The temperature was measured with a thermometer (Testo 935) directly in contact with the sample and controlled by adjusting the voltage set on the power supply. The maximum range of temperature that could be achieved was from room temperature up to 140ºC.

4.4 Compression tests

Rectangular samples (5x5x10 mm) of PZT 4D and PZT 5A have been ground in order to obtain flat bases, ensuring a uniform stress distribution throughout the whole sample during compression loading. Compression tests up to 400 MPa were performed at room temperature and the stress-strain trend of each composition was

obtained. In order to investigate how the direction of the polarization influences the mechanical properties, the experiments on PZTs were performed in three different poling states: poling parallel to load axis; poling perpendicular to the load axis and unpoled state. Each test was performed using a pre-compression load of 10 N and a loading rate of 1 MPa/s. Cyclic incremental tests were also carried out in order to analyze the deformation mechanisms under cyclic loads. Eight loading-unloading cycles of 50 MPa increments were applied and the corresponding compressive stress-strain curves were generated.

All of the other ferroelastic compositions were received with cylindrical shape of 6 mm diameter and 12 mm height. Their higher compressive strength compared with the PZTs allowed compression tests up to 700 MPa at room temperature to be performed. A loading rate equal to 4900 N/min (approximately 2.88 MPa/s), for consistency with previous experiments and a pre-load of 10 N were used in testing all the ferroelastic compositions.

4.5 Tension-Compression tests

Servo-hydraulic Instron 8511 was also used to carry out tension-compression experiments. A mechanical jig was produced to allow tension-compression loading conditions. Two metal rings were glue at the two ends of the sample, using araldite. A magnetic V-block was used to minimize any misalignments that could have occurred during the gluing process. Four metal grips having an L-shape were mounted on the rods of the machine in a way that when the metal rod was moving upward, two grips were holding the bottom ring and the other two were pulling the upper one, exerting a tensile loading on the sample (Fig.4.8). Compression load was applied as usually done in a normal compression test. A good level of alignment was achieved once again by checking the strain signals upon small load ramps and by adjusting the position of the sample to get closer strain response from the three strain gauges.

Rectangular samples of unpoled PZT 5A and LC with dimensions 7x7x14 mm were used for tension-compression experiments. Tensile tests on ceramics are always quite difficult to carry out due to their brittleness, which usually causes failure at the

gripping area. Different experimental set ups and different sample shapes were previously used to perform such tests [59-62]. In this work the gripping problem has been avoided by gluing the samples in metal rings (Fig.4.8). The edges of the specimen were rounded by fine grinding in order to avoid stress concentration at the sample edges and premature failure. Cyclic incremental tests of 250 N increments starting from a minimum of 750 N were performed and the consequent tension-compression loops were produced.

4.6 Mechanical creep tests

Creep tests were performed at room temperature in load control mode using the Instron 8511 testing machine. Each sample was loaded and unloaded in steps, holding the load at different stress levels.

Square samples (5x5x10 mm) of PZT 4D and PZT 5A with flat bases were tested in three different poling states up to 400 MPa, using a pre-compression load of 10 N and a loading rate of 1 MPa/s. Cylindrical samples of all the other ferroelastic compositions accurately machined (6 mm diameter and 12 mm height) were tested with a pre-load of 10 N and a loading rate equal to 4900 N/min (approximately 2.88 MPa/s), for consistency with previous experiments.

4.7 Rayleigh Analysis

A Rayleigh-type analysis was performed on rectangular samples (5x5x10 mm) of three different compositions: PZT 5A poled parallel, $LaCoO_3$ (LC) and $La_{0.8}Ca_{0.2}CoO_3$ (LCC). Stress-strain loops were generated by applying a static compressive load and then superimposing cyclic compressive loads of different amplitudes, frequencies and loading rate at room temperature. A series of additional tests were performed at six different temperatures, with constant stress amplitude, in order to study the combined effect of temperature and frequency.

At room temperature, the specimens were subjected to a static compressive stress of 12 MPa and to a sinusoidal dynamical compressive load, superimposed on the static

one. Five different amplitudes ($\Delta\sigma$=2, 4, 6, 8, 10 MPa) and four different frequencies (f=0.01, 0.05, 0.1, 0.5 Hz) were used for the dynamic loading. Another batch of data was generated using a triangular dynamical loading in order to have a continuously constant loading rate for all the stress amplitudes. The combined effect of the frequency and the temperature was studied by keeping the amplitude constant at 4 MPa and performing the tests at six different temperatures: 25, 30, 40, 50, 60 and 70°C. Eight frequencies were selected for the triangular dynamical load: 0.004, 0.008, 0.016, 0.032, 0.064, 0.128, 0.256, 0.512 Hz. For 4 MPa stress amplitude, those frequencies correspond to a loading rate of 0.064, 0.128, 0.256, 0.512, 1.024, 2.048, 4.096, 8.192 MPa/s respectively.

For every stress amplitude $\Delta\sigma$, the actual compressive stress that the specimens experienced along the loops varied in the range [12+Δσ, 12-Δσ]. The static stress bias was chosen within the subcoercive field region in all the compositions tested. Other experiments were performed on PZT 5A poled parallel with the static bias stress at the coercive stress. Closed loops could be obtained only after a stress-aging of the sample for one hour under the applied load. Therefore, it was preferable to carry out the Rayleigh-type analysis well below the coercive stress, where the shorter characteristic times allow generating closed loops (in the range of frequency/loading rate used), without any aging process, which would produce significant changes in the microstructure of the material.

4.8 Rate experiments

The best experimental approach to study the stress rate and temperature dependence of ferroelastic switching is by tension-compression testing, which allows complete strain (microstructure) recovery and gives the possibility of using only one sample for several rates and temperatures tests, minimizing data scatter. The difficulties in performing such tests determined the necessity of developing an alternative experimental approach. Compression tests on different samples at different rates produced highly scattered data with inconsistent trends. Compression stress-strain curves at different loading rate have been generated in load control mode using only one sample with the two procedures described below (Procedure 1 and Procedure 2).

Procedure 1 was used to study the effect of different loading rate to some specified maximum stress. The maximum stress was then increased and the procedure repeated (see Fig.4.9). The data was used to generate the stress-strain curves for different loading rates. More precisely, Procedure 1 involves the following steps:

1) Loading the sample until stress level 1 at stress rate 1;
2) Total unloading at stress rate 1;
3) Loading the sample until stress level 1 at stress rate 2;
4) Total unloading at stress rate 2;
5) Repeating the previous steps for other rates at stress level 1;
6) Repeating the previous steps at stress levels higher than stress level 1.

The load-time ramp is shown in Fig.4.9. With this procedure several loading rates can be applied. The stress-strain curves were constructed by measuring the strain at each stress level and at each rate and by fitting the data points collected. Cubic polynomial functions were used for the fitting, providing very high accuracy.

In Procedure 2 the loading was done in segments alternating two loading rates. The transfer from one rate to the other was done by partial unloading and then reloading at the new rate (Fig.4.10). This was used to generate stress-strain curves at two different rates also during the unloading. Procedure 2 is based on the following steps:

1) Loading the sample until stress level 1 at stress rate 1;
2) Partial unloading at stress rate 1;
3) Dwell for 1 minute;
4) Loading the sample until stress level 2 at stress rate 2;
5) Partial unloading at stress rate 2;
6) Dwell for 1 minute;
7) Loading the sample until stress level 3 at stress rate 1;
8) .....

The load-time ramp is shown in Fig.4.10. Stress-strain curve were assembled from the (strain, stress) data points collected. The main advantage of the second procedure is the possibility of generating also the unloading portion at the two rates employed, which would be more difficult using Procedure 1.

An additional experimental procedure (Procedure 3) was developed in order to generate stress-strain curves at different temperature. Procedure 3 follows the steps listed below:

1) Loading the sample until stress level 1 at temperature 1;
2) Total unloading;
3) Increasing the temperature at temperature 2;
4) Loading the sample until stress level 1 at temperature 2 higher than temperature 1;
5) Repeating steps 2), 3), 4) at stress level 1, for temperature higher than temperature 2;
6) Cooling at temperature 1;
7) Loading the sample until stress level 2 higher than stress level 1 at temperature 1;
8) Repeating steps 2), 3), 4), 5) at stress level 2, for higher temperatures.
9) .....

Once again the stress-strain curves were obtained from the (strain, stress) data points at the different stress levels and different temperatures. Steps 1-4 of Procedure 1 can replace steps 1-2 in Procedure 3 to analyze stress rate and temperature effect on the same sample.

Procedure 1 was applied in poled PZT 5A (square samples 7*7*12 mm) and LSFC (cylindrical samples 6mm diameter and 12 mm height). Measurements using Procedure 2 and 3 have been performed only in PZT 5A poled parallel. Compressed air spray was used to speed up the cooling process. A pre-compression load of 10N was used in all the tests.

4.3 Electrical experiments

4.3.1 P-E loops and Butterfly hysteresis

Tests were performed on a "*soft*" PZT 5A with a morphotropic boundary composition, provided by Morgan Matroc Transducer. Samples were in the form of disks with a diameter of 10 mm and 1 mm thickness. Experiments were carried out in a silicon oil bath on the same sample due to the high stability and reproducibility of the loops. The

apparatus used in shown in Fig.4.11. Electrical voltage waveform was applied using a HP33120A function generator, software controlled. A TREK 609E-6 voltage amplifier was used to amplify 1000 times the applied voltage signal. A low-noise current-voltage converter Model SR570 with different types of filtering functions was used. The purpose of filtering was to reduce the background noise produced by the main power supply, the electrical circuit and the surrounding instruments. A special probe for simultaneous measurement of polarization and strain was built in collaboration with NPL, consisting of a pair of NXB2-AL nanosensors, which convert mechanical displacement into a voltage, with a sensitivity in the order of nanometers. The sensor is driven by a single channel NS2000 controller. The output from the NS2000 is sent to a digital voltmeter for data acquisition. Data of electric field, current, polarization and strain were directly acquired via LabView software. P-E and butterfly loops were generated up to E=4 kV/mm, which produced loops fully saturated. Triangular ramps of different frequencies in the range 0.1-5 Hz were used to study the rate dependence of the coercive field.

4.9.2 Electrical creep

Electrical creep experiments were performed using the same circuit shown in Fig.4.11 with the exception of the waveform generator and the data acquisition method. The electrical voltage waveform was applied using a HP33220A function generator, which allows voltage signals of arbitrary forms to be generated. An Agilent digital oscilloscope model 54624A was used to capture the data for electric field, current and strain. In particular, the current data was integrated with respect to time, to obtain the resultant polarization. The type of waveform applied with the voltage generator is shown in Fig.4.12. Ramp frequency was 1 Hz and the creep dwelling time was three seconds. A series of electric fields were held: 0, 0.4, 0.8, 1, 1.2, 1.4, 1.5, 1.68, 1.8, 2, 2.5 kV/mm in the loading branch of the hysteresis loops and 3, 2, 1, 0 kV/mm in the unloading branch. Each unloading after creep was followed by two more ramps at the same frequency, applied with a HP33120A voltage generator and acquired by the PC using Labview program. The reason of cycling before creep was to condition the materials to obtain reproducible microstructures and properties.

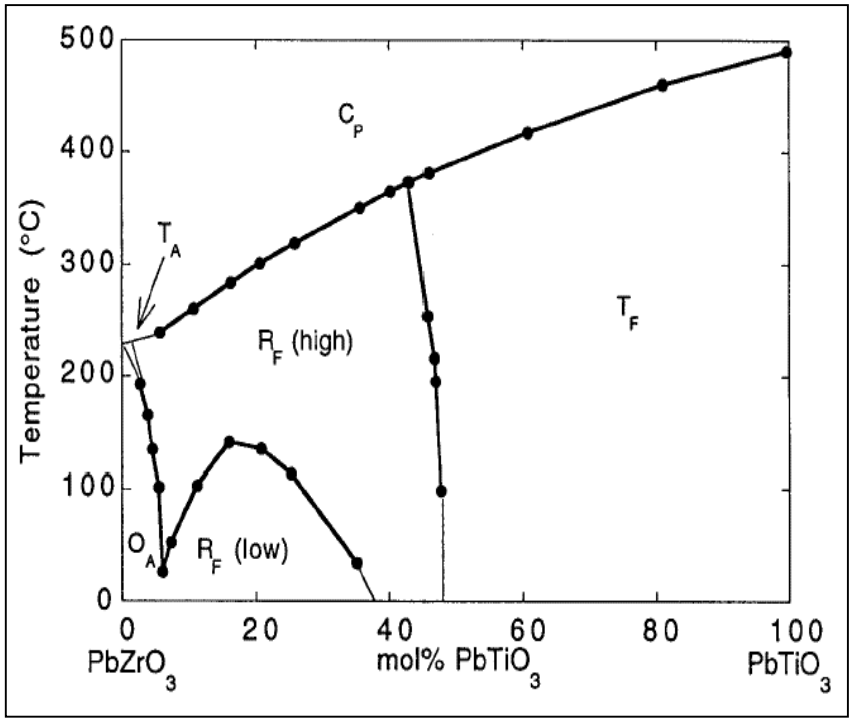

Fig.4.1: PZT phase diagram [41].

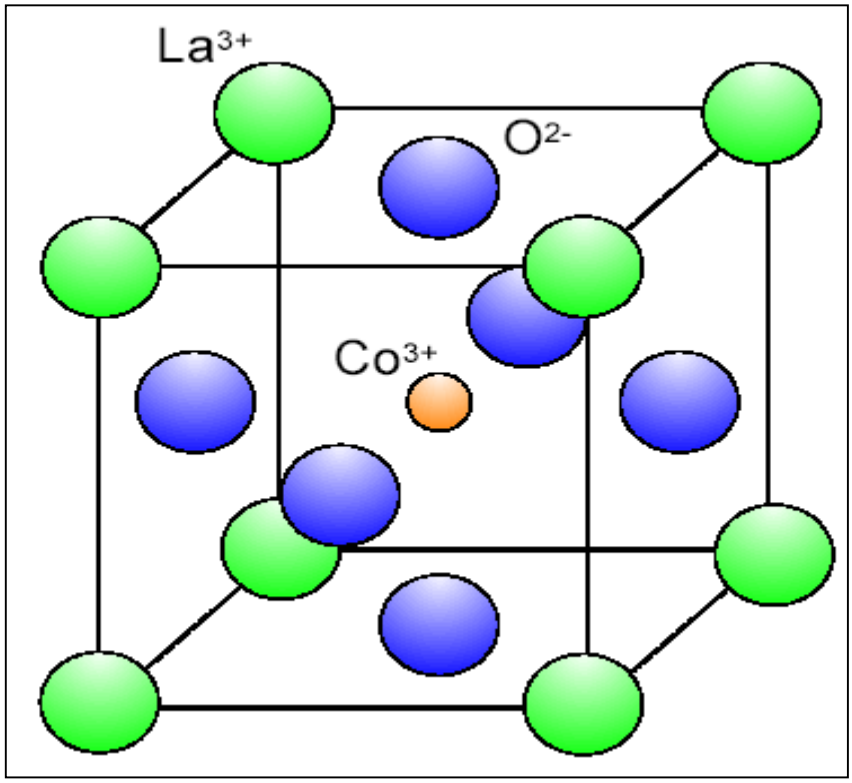

Fig.4.2: $LaCoO_3$ perovskite structure [120].

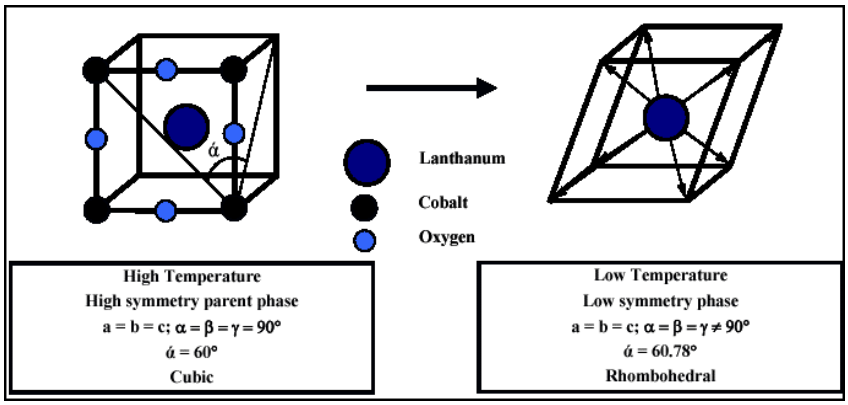

Fig.4.3: rhombohedral distortion in $LaCoO_3$ [114].

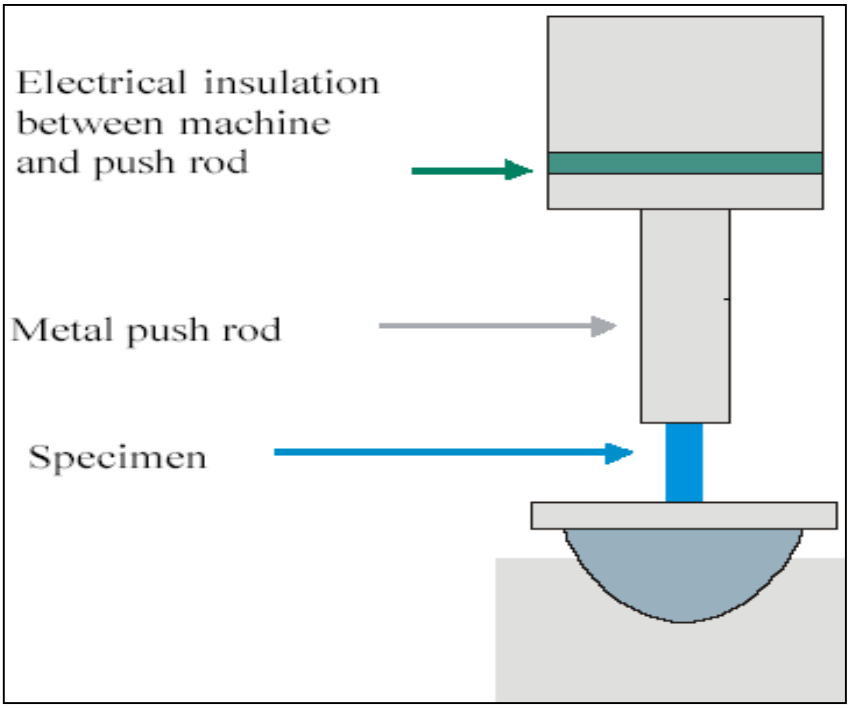

Fig.4.4: servo-hydraulic compression testing machine [44].

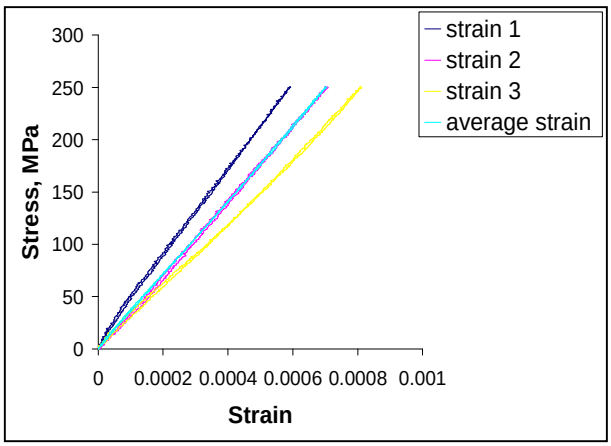

Fig.4.5: stress-strain curve of alumina.

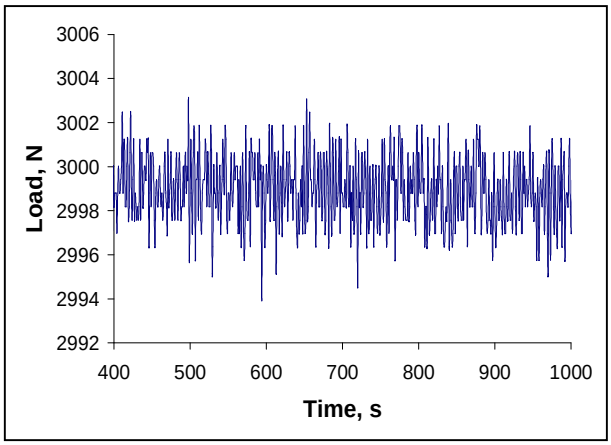

Fig.4.6: level of noise in the load signal.

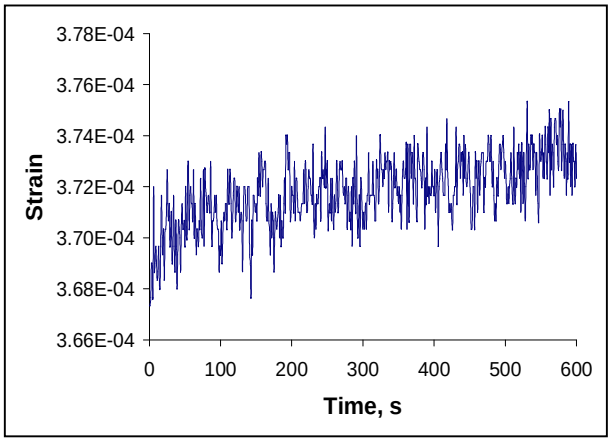

Fig.4.7: level of noise and drift in the strain signal.

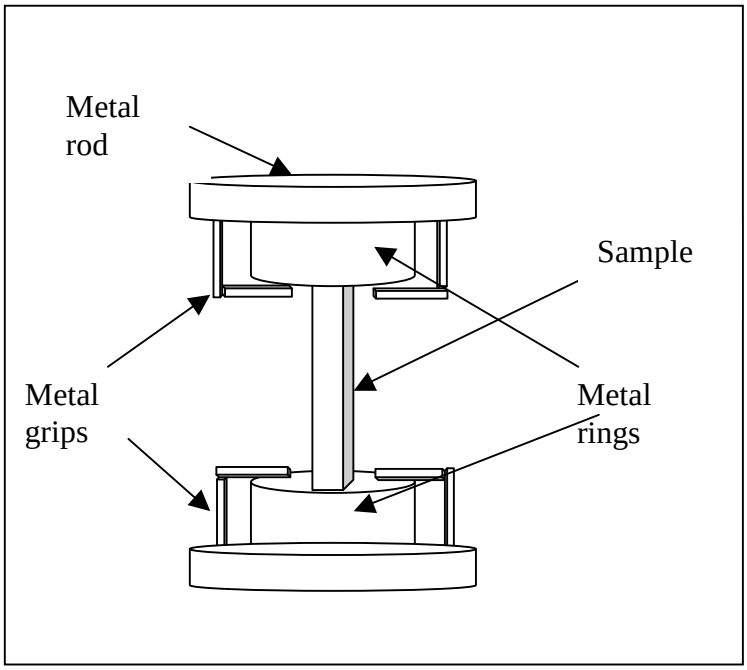

Fig.4.8: mechanical jig for tension-compression experiments.

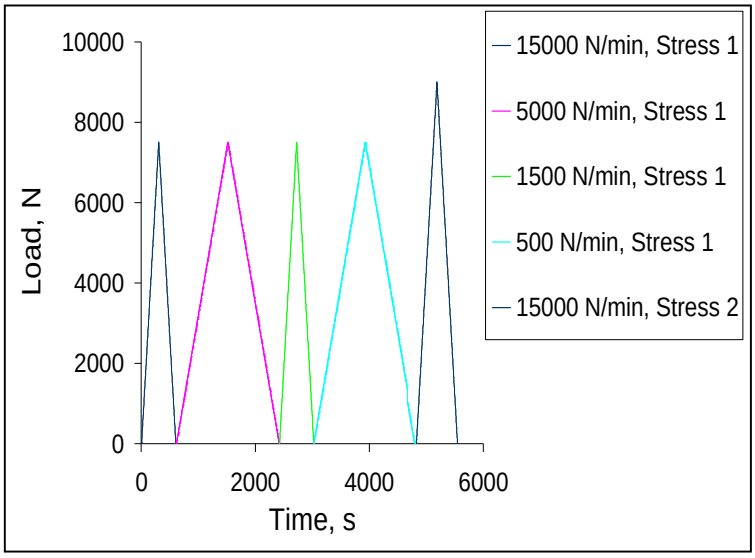

Fig.4.9: example of load ramps in Procedure 1.

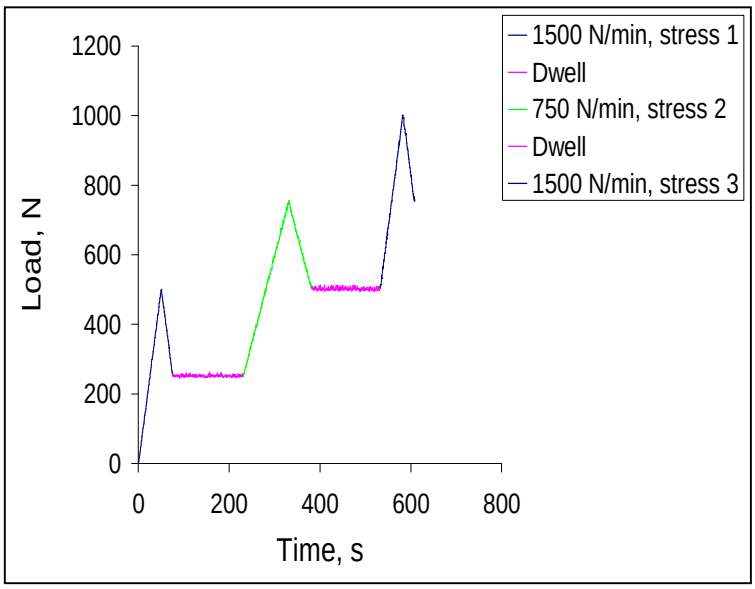

Fig.4.10: example of load ramps in Procedure 2.

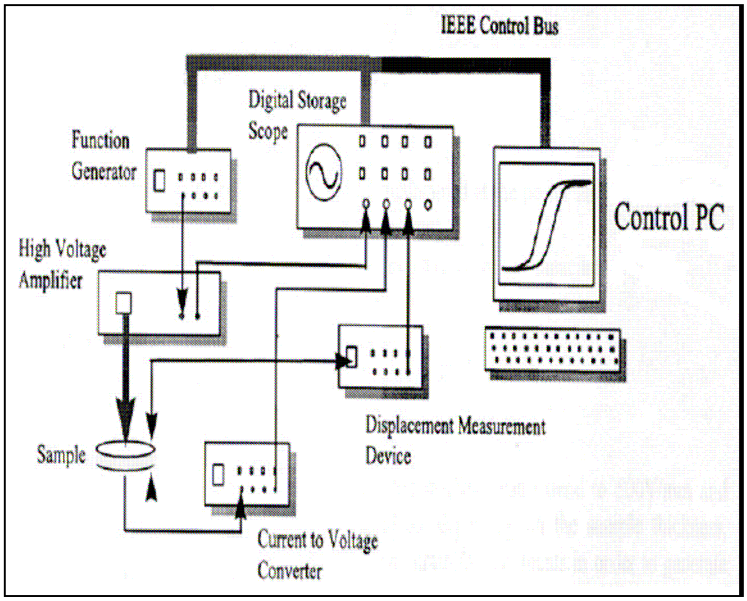

Fig.4.11: equipment for electrical experiments [121].

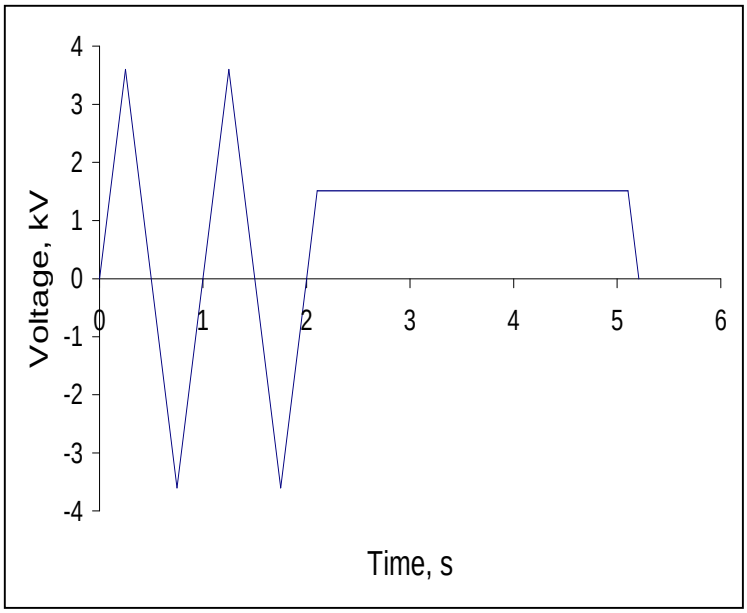

Fig.4.12: voltage waveform in electrical creep experiments.

Chapter 5: Deformation behaviour

5.1 Introduction

The deformation behaviour of all the compositions was studied in compression loading using the equipment and the procedures described in Chapter 4. The purpose was to characterize the ferroelastic properties, identifying important parameters such as coercive stress, saturation strain and remanent strain and to understand the physical origin of the trends observed based on the materials structure and composition.

Incremental cyclic compressive tests were performed on the polar perovskites in order to gain further insights regarding the mechanisms of deformation and the non-linear and hysteretic behaviour. In addition, tension-compression test is more useful means of studying ferroelasticity, since it allows complete strain recovery by reversing the loading direction. The generation of saturated $\sigma - \varepsilon$ loops has been attempted in PZT 5A and LC that displayed a low coercive stress in compression. Results are presented and discussed in detail.

5.2 Compression tests

The stress-strain plots for all the compositions show the characteristic trend of ferroelastic materials: non-linear behaviour from the beginning; inflection point corresponding to the coercive stress (see also Fig.2.14), a restricted linear part at the beginning of unloading followed by a non-linear portion and pronounced irreversible strains (Fig.5.1-5.6). Following J.Fan et al. [50] and D.Zhou et al. [51], the coercive stress has been identified as the stress where the tangent modulus, calculated from the numerical first differentiation of the stress-strain diagram, assumes its minimum value (minimum work hardening). The highest compliance at the coercive stress determines also a maximum in the strain rate, confirming high microstructural mobility.

However, the values of the coercive stress calculated have a relative validity as they are strongly dependent on the rate of the applied load. The dependence on the loading rate will be analyzed in more details in Chapter 8.

Soft PZT 5A has shown lower coercive stress, lower hysteresis area and less pronounced recovery during unloading than the hard PZT 4D. It is likely that the higher recovery in the harder material is due to the development of higher internal stresses during the domain reorientation upon loading, as also proposed in [48].

The poling state significantly influences the mechanical response of the ferroelastic/ferroelectric materials (Fig.5.1, 5.2), in agreement with previous studies [48]. Samples initially poled parallel to the loading direction show larger saturation and irreversible strain compared with the other poling states (Fig.5.1, 5.2), due to the higher number of switchable domains. The application of a compressive load parallel to the poling direction produces a depoling process of the material, through 90° domain switching. During the unloading, only some of the domains switch back under the action of the internal stresses. The large deformations developed during the loading process and the only partial back switching leads to large irreversible strains. The back switching becomes more significant at the last stage of the unloading, where the strain recovery increases because the applied load is not sufficient to oppose the action of the internal stresses. The higher initial stiffness and the higher coercive stress shown by the samples initially poled parallel compared to the unpoled ones (see Fig.5.1) is probably due to a more stable configuration of the domains produced by the poling process.

Non-linear compressive behaviour of LC and LCC arise from ferroelastic domain switching as confirmed also by previous XRD analysis [56, 57]. Details on the evolution of the domain structure in LCC during compression loading have been provided via in situ synchrotron X-ray diffraction [57]. It was shown that during compression loading the volume fraction of domains having the distortion axis parallel to the loading direction increase, at the expenses of the domains whose distortion axis is perpendicular to the direction of applied stress [57].

By comparing the stress-strain diagrams of the two compositions, the effect of the acceptor calcium doping on the ferroelastic behaviour can be observed. Although previous studies [114] have shown that the calcium decreases the distortion (as already mentioned in Chapter 4), the present results suggest that macroscopically, the calcium has the effect of increasing the coercive stress, hysteresis and irreversible strain (Fig.5.3). The smaller hysteresis observed in LC has been attributed to higher samples porosity, which has a pinning effect on the inelastic hysteretic behaviour [56]. The higher coercive stress despite a smaller distortion can be attributed to the pinning effect on domain walls due to the oxygen vacancies generated by acceptor doping. In Fig.5.4 the compressive stress-strain curve is shown.

Stress-strain diagram of LSFC (Fig.5.5) confirms its ferroelastic nature previously observed in four point bending conditions [122]. The large coercive stress and the large hysteresis area denote hard ferroelasticity.

Particularly interesting is the behaviour of LSCNM, which shows three inflection points, as also visible from the work hardening and strain rate curves (Fig.5.7, 5.8). The first inflection point corresponds to the first local minimum of the work hardening as function of the stress applied. This stress represents the coercive stress of the *Pnma* ferroelastic phase at room temperature. Upon loading the material experiences a structural phase transition from the *Pnma* orthorhombic phase to the $R\bar{3}c$ rhombohedral phase [119]. The latter is also ferroelastic and its coercive stress corresponds to the third inflection point, identified by the second local minimum in the work hardening curve. The second inflection point, distinguished by a local maximum in the tangent modulus (Fig.5.7), is a transitional point, which indicates the point where the amount of $R\bar{3}c$ is more dominant in the system [119].

5.3 Incremental cyclic compression tests

The mechanical response upon incremental cyclic compressive loading of PZT 5A reproduces very closely the stress-strain shape obtained from single cycle experiments. Cyclic tests are plotted with the single cycle test (Fig.5.9-5.11), confirming previous observations on $La_{0.6}Sr_{0.4}FeO_3$ [56] and $LaFeO_3$ [55]. A memory

strain effect was also observed; during successive cycles the materials experience the same level of strain corresponding to loads equal to the maximum load of the previous compressive cycle. Analogue features were also shown by $LaFeO_3$ [55].

5.4 Tension-compression tests

Cyclic tension-compression experiments were carried out on PZT 5A unpoled and LC, from a minimum load of 750 N and by increasing the load by 250 N every cycle. All the specimens had a quite low tensile strength (<40MPa), which did not allow saturated tension-compression loops to be achieved. The low tensile strength was the main reason of performing cyclic tests with small load increments, in order to generate stress-strain loops at least for small applied loads. The highest tensile strength has been shown by LC (38 MPa). The response to cyclic loads is analogous to the case of uniaxial compression, as the cyclic incremental tests resemble the single cycle experiment (Fig.5.14, 5.17). Fig. 5.13 and 5.16 show the strain response to the load applied (Fig.5.12, 5.15) for PZT 5A unpoled and LC respectively.

Tension-compression tests on PZT unpoled and poled perpendicular to the load, have been performed also by other research groups with a similar experimental arrangement [59]. They reported non-symmetric stress-strain behaviour under tension and compression, with higher plastic strains under tensile loading, especially in samples poled perpendicular to the load axis. Similar asymmetries have been published also for $BaTiO_3$ obtained from bending tests [63].

By testing materials with a smaller coercive stress and smaller stress to saturation, well saturated stress-strain loops, analogous to ferroelectric P-E loops, could be generated and clearer conclusion regarding the mechanisms of deformation under tensile and compressive stress could be drawn.

5.5 Conclusions

The deformation behaviour of different ferroelastic/ferroelectric perovskites compositions under uniaxial compression was studied in detail. The results obtained

identified trends common to all the compositions analyzed, as well as particular features regarding some of the materials tested. In the ferroelectric compositions poling state significantly influences the stress-strain characteristics. Incremental cyclic compression tests evidenced a strain memory effect. Tension-compression experiments represent a more informative way of characterization, but are much more difficult to carry out compared with the compression tests. The generation of complete saturation loops is often limited by a tensile strength lower than the coercive stress of these materials.

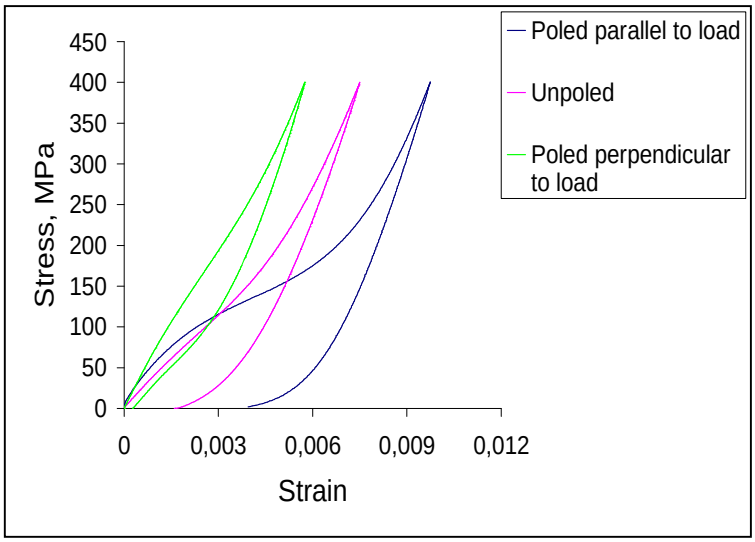

Fig.5.1: stress-strain curve of PZT 4D in three different poling states at 1 MPa/s.

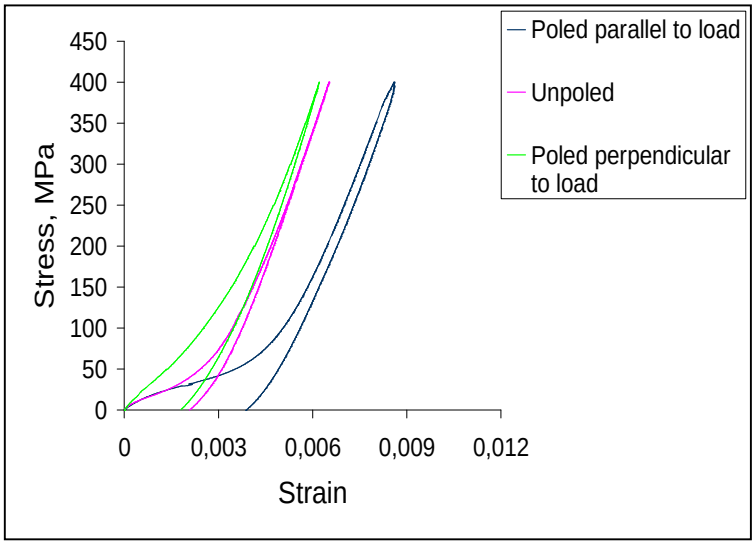

Fig.5.2: stress-strain curve of PZT 5A in three different poling states at 1 MPa/s.

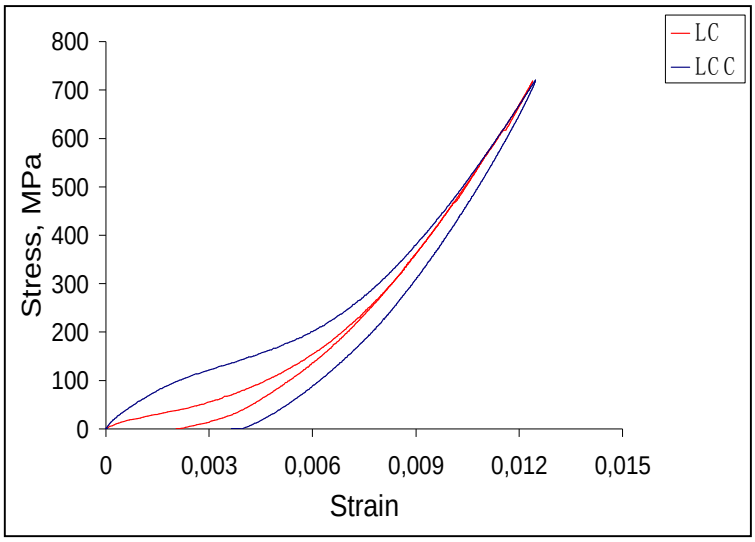

Fig.5.3: stress-strain curve of LC and LCC at 4900 N/min.

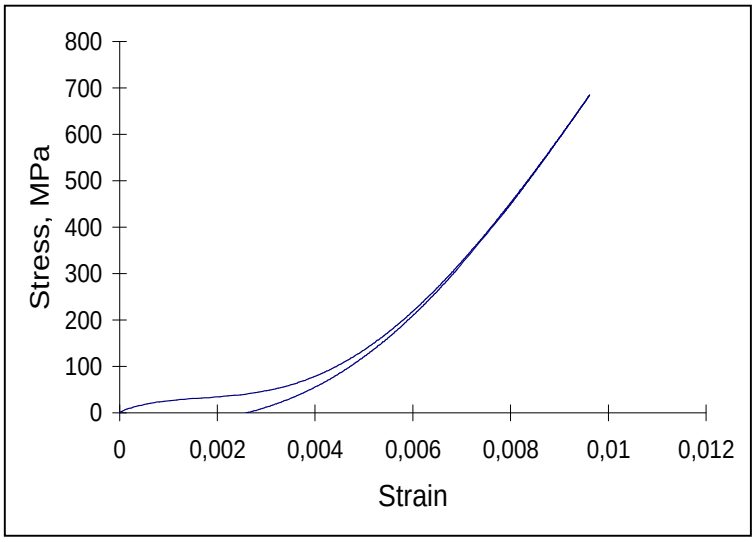

Fig.5.4: stress-strain curve of LSM at 4900 N/min.

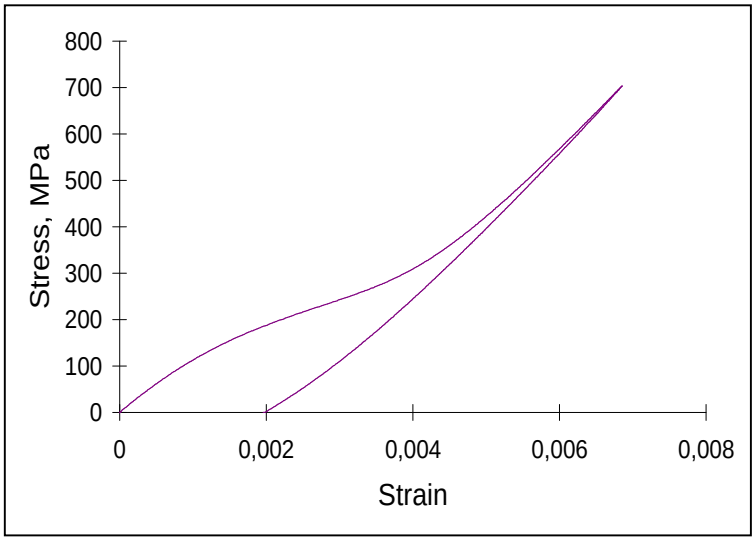

Fig.5.5: stress-strain curve of LSFC at 4900 N/min.

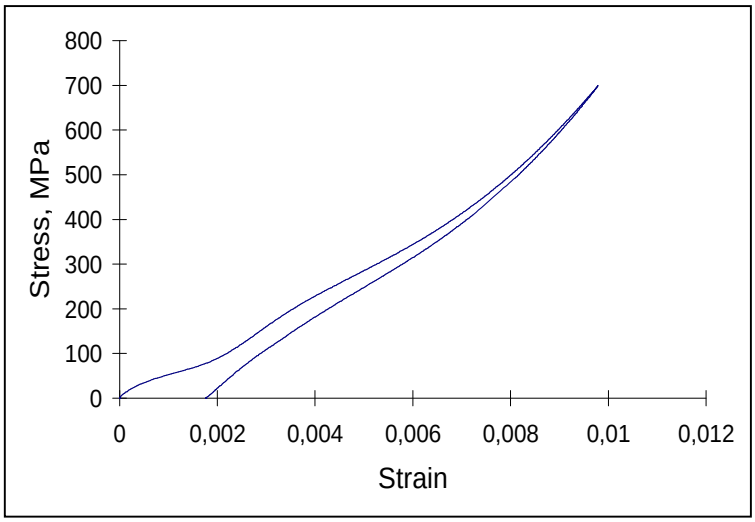

Fig.5.6: stress-strain curve of LSCNM at room temperature at 4900 N/min.

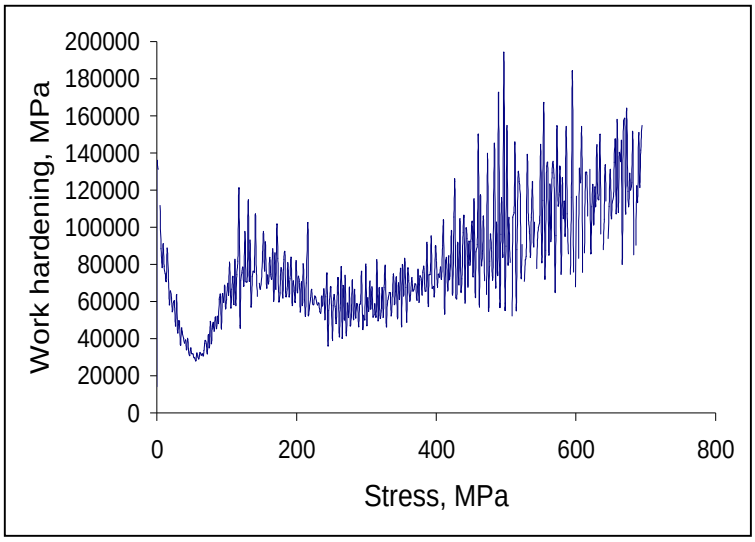

Fig.5.7: work hardening as a function of stress in LSCNM.

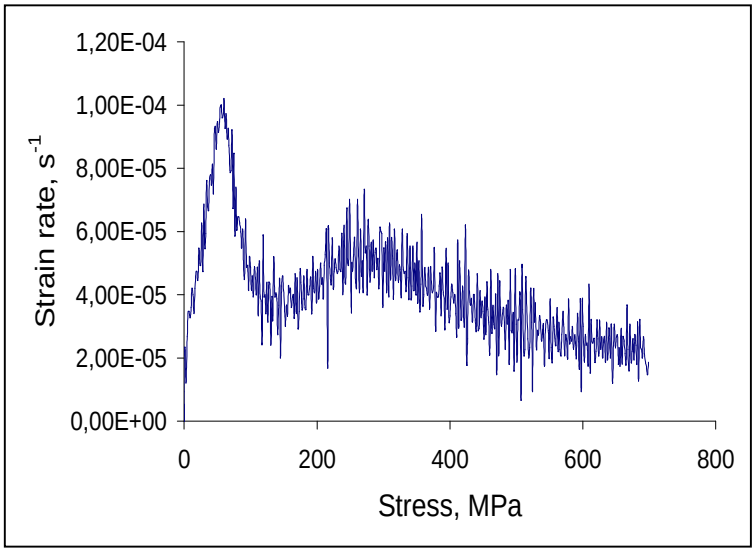

Fig.5.8: strain rate as a function of stress in LSCNM.

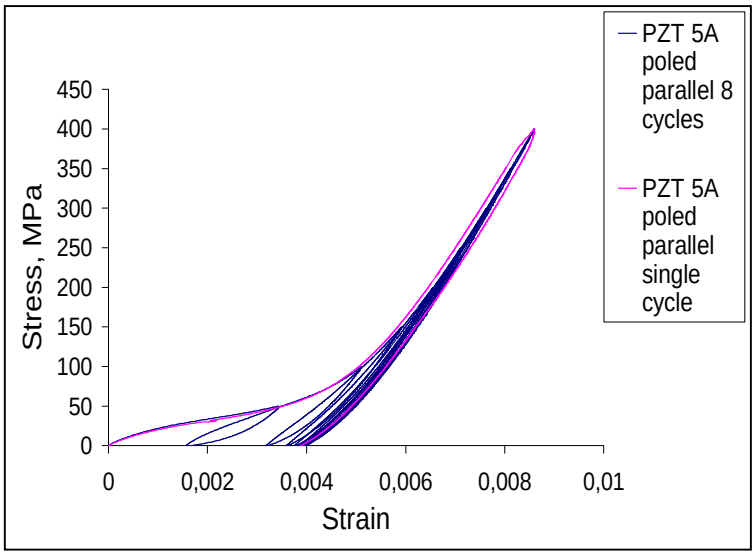

Fig.5.9: cyclic compression test in PZT 5A poled parallel.

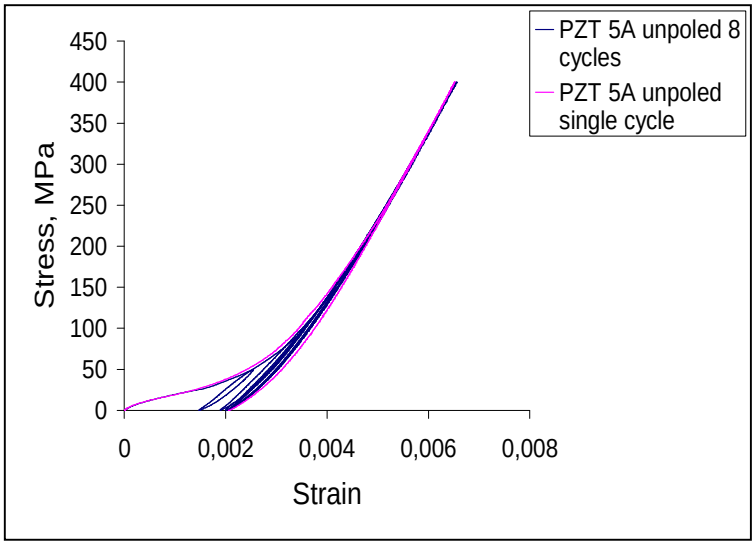

Fig.5.10: cyclic compression test in PZT 5A unpoled.

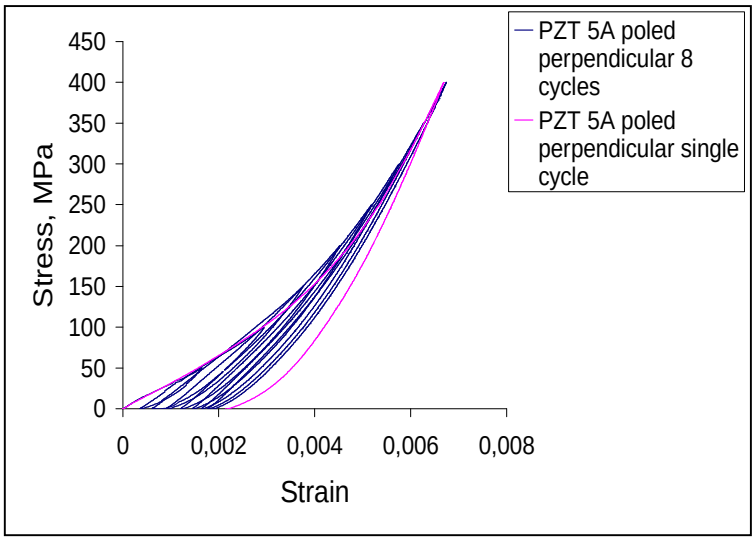

Fig.5.11: cyclic compression test in PZT 5A poled perpendicular.

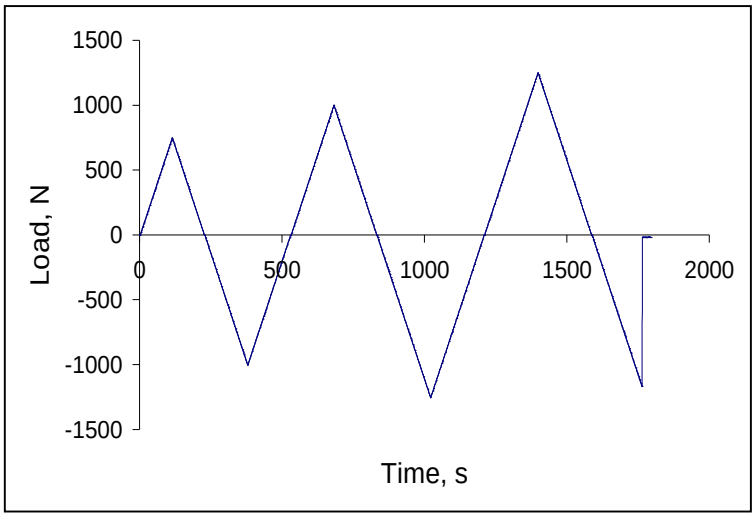

Fig.5.12: incremental load ramps in tension-compression experiments at room temperature in PZT 5A unpoled.

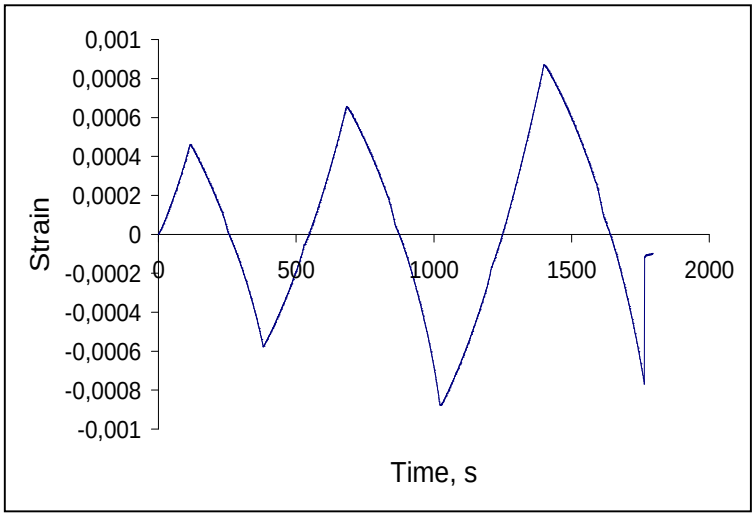

Fig.5.13: strain response to incremental loading in tension-compression experiments at room temperature in PZT 5A unpoled.

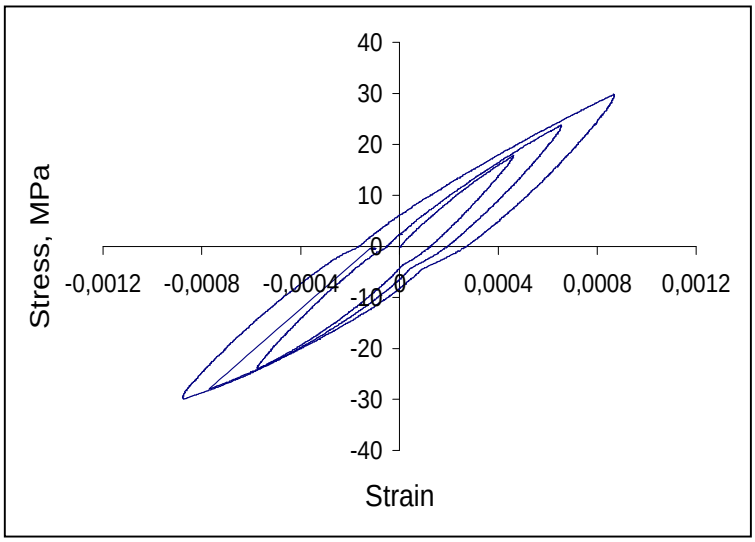

Fig.5.14: tension-compression incremental loops at room temperature in PZT 5A unpoled.

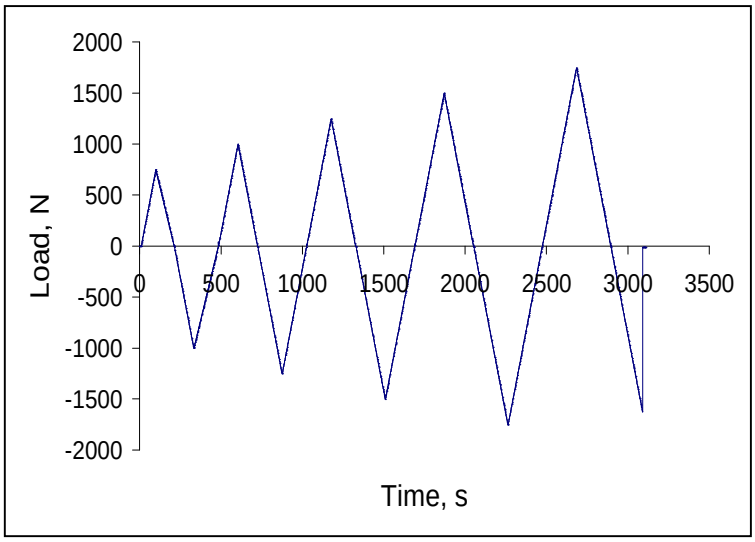

Fig.5.15: incremental load ramps in tension-compression experiments at room temperature in LC.

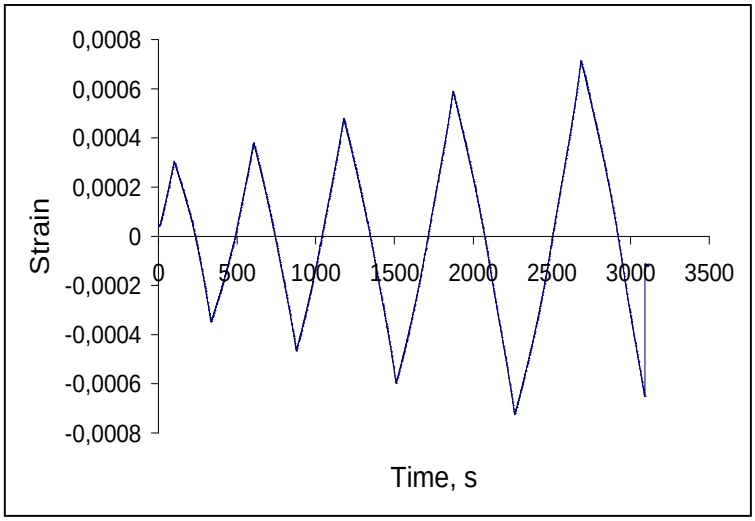

Fig.5.16: strain response to incremental loading in tension-compression experiments at room temperature in LC.

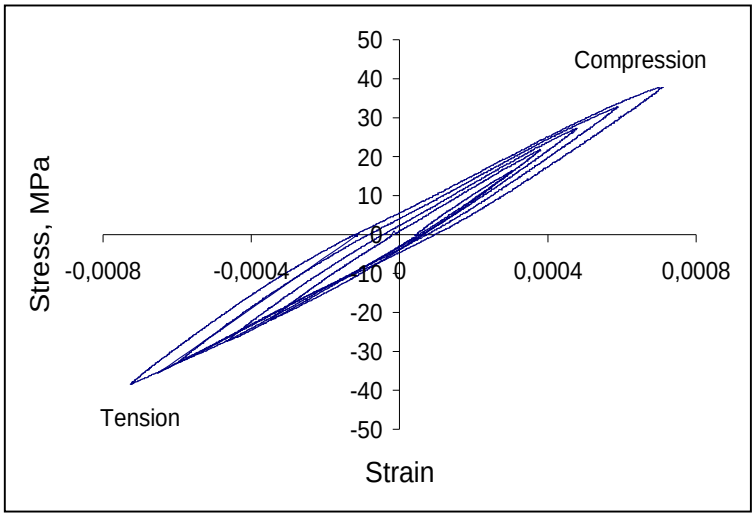

Fig.5.17: tension-compression incremental loops at room temperature in LC.

Table 5.1: coercive stress in ferroelastic/ferroelectric compositions.

Ferroelastic/ferroelectric compositions	Coercive stress (MPa)
PZT 4D poled parallel	140
PZT 4D unpoled	90
PZT 4D poled perpendicular	170
PZT 5A poled parallel	30
PZT 5A unpoled	20
PZT 5A poled perpendicular	Not detectable

Table 5.2: coercive stress in ferroelastic compositions.

Ferroelastic compositions	Coercive stress (MPa)
LC	65
LCC	130
LSM	30
LSFC	220
LSCNM	60

Chapter 6: Mechanical creep behaviour

6.1 Introduction

Most of the papers presented in the literature so far have provided only a phenomenological description of the creep phenomenon and physical models able to describe the observed creep behaviour have not yet been developed. Despite an excellent fitting capability, most of the empirical expressions previously used present serious limits in reflecting the underlying physical mechanisms, driving the present study towards the achievement of a fundamental understanding.

In this chapter, experimental results showing the creep phenomenology of different ferroelastic/ferroelectric ceramics are presented and a physical model based on the rate theory of thermally activated phenomena was implemented to elucidate the possible physical processes involved and to estimate the parameters controlling the ferroelastic creep behaviour. Knowledge of the physical mechanisms behind the strain time evolution under constant stress applied could provide a better understanding of the ferroelastic switching process under static conditions and support the design of sensors and actuators, especially in working conditions where constant loads are involved.

6.2 Creep deformations

All the compositions examined have shown common experimental trends. A creep of the primary type with decreasing rate was observed by holding the load in the loading part of the stress-strain diagram (see for example Fig.6.1, 6.3, 6.5, 6.7, 6.9, 6.11, 6.13-6.17). When loads were held in the unloading part of the stress-strain curve, a visible strain recovery was found (see for example Fig.6.2, 6.4, 6.6, 6.8, 6.10, 6.12). The creep strain ε_{cr} has been defined as the difference between the strain at last instant of the creep ε_f and the strain at the first instant of the creep ε_0:

$$\varepsilon_{cr} = \varepsilon_f - \varepsilon_0 \tag{6.1}$$

In agreement with previous studies [68-73], the creep strain depends on the magnitude of the applied load, displaying a maximum at the coercive stress, where the driving force of the domain switching process is highest. At each stress, the creep strain rate decreases with the time, showing a significant decay.

The strain recovery observed during the unloading steps is attributed to the back switching, driven by the internal stresses. The highest recovery occurs where the slope of the unloading part of stress-strain diagram is minimum. This normally occurs at the smallest applied stress (0.2 MPa). An exception is represented by PZT 4D poled perpendicular, where the largest strain recovery is observed around 50 MPa (Fig.6.6). For smaller stresses the slope becomes higher (see Fig.5.1 Chapter 5) and the strain recovery, lower (Fig.6.6).

Significant differences in the creep strain magnitude were also observed in LC and LCC (Fig.6.13, 6.14). The differences in the creep behaviour between these two compositions can be framed in a more general picture noting that hard compositions always show more significant creep strain than the soft ones. It seems that soft compositions can be easily switched upon monotonic loading, showing smaller effects upon static loading, while hard compositions need more assistance by the thermal fluctuations in order to drive the process.

6.3 Application of rate theory

All the compositions examined showed common experimental trends. A logarithmic fitting expression has been engaged to describe the creep strain as a function of the time:

$$\varepsilon_{cr} = P1\ln(t + P2) + P3 \tag{6.2}$$

where *P1*, *P2*, and *P3* are fitting parameters. *P1* determines the total creep strain, *P2* is related to the characteristic time and *P3* represents the strain offset. Since the strain values have been normalized using Eq.6.1, *P3* is practically zero as shown in Fig.6.18-6.38.

Eq.6.2 has been derived in the dislocation case from the rate model expressed by Eq.6.3, which takes into account the net rate of generation of positive dislocations [67,109]:

$$\dot{\gamma} = A\left\{\exp\left[-\left(\frac{V(\tau_{eff} - M\gamma)}{k_B T}\right)\right] - \exp\left[-\left(\frac{V(\tau_{eff} - M\gamma)}{k_B T}\right)\right]\right\} = 2A\sinh\left[\frac{V(\tau_{eff} - M\gamma)}{k_B T}\right] \tag{6.3}$$

where $\dot{\gamma}$ is the shear strain rate, V the activation volume, τ_{eff} the effective shear stress, M the relaxation modulus and γ the shear strain. The solution was reported in [109], which was used to fit the results:

$$\gamma = P1\ln(t + P2) + P3 \tag{6.4}$$

The fitting expression (6.2) always provides a quite high accuracy as shown in Fig.6.18-6.38.

In the rate model presented in Chapter 3, the mathematical formulation has been simplified, by neglecting the rate of generation of the activated complex in the reverse direction, as already suggested in [43-45]. In the model developed, a rate equation that identifies two possible factors determining the observed strain rate decay during the time has been derived (see Chapter 3):

$$\ln \dot{\varepsilon}_{cr} = A\frac{\partial \rho}{\partial \varepsilon}\varepsilon_{cr} - \frac{V_a}{k_B T}\theta\varepsilon_{cr} \tag{6.5}$$

The two mechanisms above mentioned are expressed by the two terms at the second part of Eq.6.5: the exhaustion of the nucleated sites represented by the first term, and the development of the internal stresses due to the formation of activated nuclei in the unswitched regions of the material, described by the second term.

By assuming that the process is controlled by the build up of the internal stresses, the exhaustion term can be neglected and from the slope of the plot $\ln\dot{\varepsilon}_{cr} - \varepsilon_{cr}$, the activation volume V_a can be estimated:

$$\ln \dot{\varepsilon}_{cr} = -\frac{V_a}{k_B T}\theta \varepsilon_{cr} \tag{6.6}$$

It is worthwhile to underline that the volume of the activated nuclei has been assumed to be constant with time during the creep test, (and location within the sample), determining a constant work hardening rate θ, calculated from the stress-strain curve as:

$$\theta = \frac{1}{2}\frac{\partial \sigma_{app}}{\partial \varepsilon} \tag{6.7}$$

In this calculation it has been assumed that the hardening produced during creep at certain applied stress is equal to the hardening produced by applying the monotonic loading (see Chapter 3).

Examples of the $\ln\dot{\varepsilon}_{cr} - \varepsilon_{cr}$ plot are shown in Fig.6.39-6.42 for PZT 5A poled parallel, where the term ε_{cr} represent the creep strain defined in Eq.6.1 and $\ln\dot{\varepsilon}$ has been calculated from the fitting using Eq.6.2. The graphs show behaviour very close to linearity, except for small creep strain where small deviations can be observed (Fig.6.39-6.42).

The activation volume has been evaluated in all the compositions at different stress levels, showing values between few nanometers^3 (PZT 4D poled parallel, LCC, LSFC) and 150 nm^3 (LSM) (Fig.6.43, 6.44), consistent with previous estimations in PZTs [44,45,111]. A characteristic trend with the applied stress was found (Fig.6.43, 6.44) and its interpretation is not straightforward.

In general, by comparing the values of the activation volume of the ferroelastic compositions (see Fig.6.44) it can be concluded that hard compositions (LCC and LSFC) present low values of the activation volume, suggesting a greater rate dependence compared with the soft ones (LC and LSM). Data regarding LSCNM are more difficult to interpret due to the phase transition stress induced (see Chapter 5).

6.4 Conclusions

The creep behaviour of ferroelastic/ferroelectric ceramics was studied under mechanical compression loading at room temperature. Typical common features were observed in all the materials studied, also in agreement with previous studies. An efficient fitting expression, derived from the dislocation rate theory was proposed to describe the time dependent deformations under constant applied loads. In analogy with thermally assisted dislocation motion, a rate model was developed to justify the reasons behind the observed trends. Two possible sources of strain rate decay have been identified, namely exhaustion and hardening. Based on the fundamental assumptions that these two phenomena are uncoupled and that the build up of the internal stresses is the main factor causing the rate decay during creep, the activation volume of the ferroelastic creep was estimated and used as a key parameter in determining the domain switching rate under constant load. Based on the model developed it was found that in hard compositions domain switching occurs through the nucleation and the expansion of small activated nuclei, whereas in soft compositions domain switching is characterized by the nucleation and the expansion of large activated nuclei. Higher creep strains in hard ferroelastic compositions evidence a significant difference in the amount of domain switching that can be produced in monotonic loading (without creep) and in stepwise loading (with creep). This suggests that hard compositions need more help from thermal fluctuation to drive the switching process, evidencing higher rate dependence and a domain switching process characterized by nucleation and expansion of small activated nuclei.

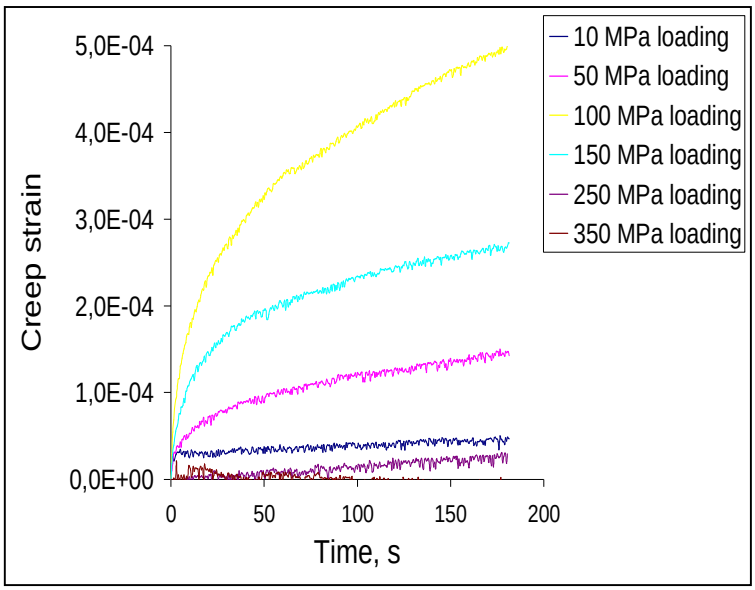

Fig.6.1: creep strain at different stress levels in PZT 4D poled parallel to load during loading.

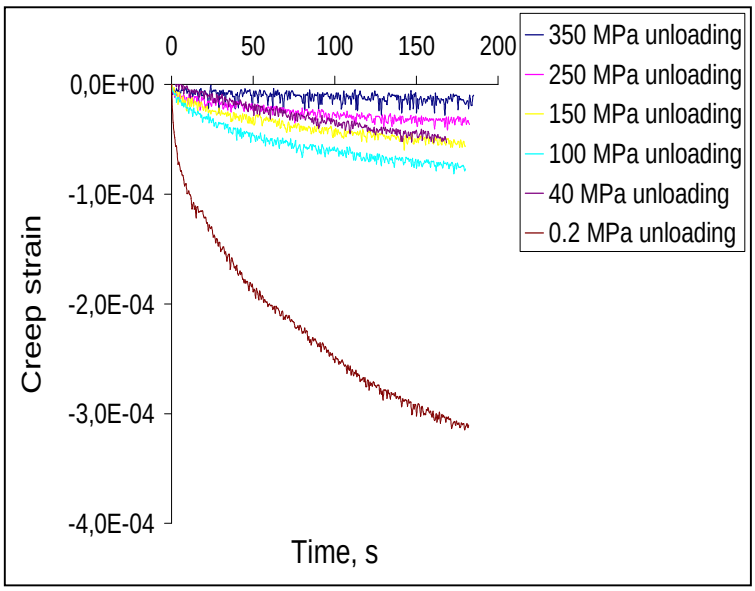

Fig.6.2: creep strain at different stress levels in PZT 4D poled parallel to load during unloading.

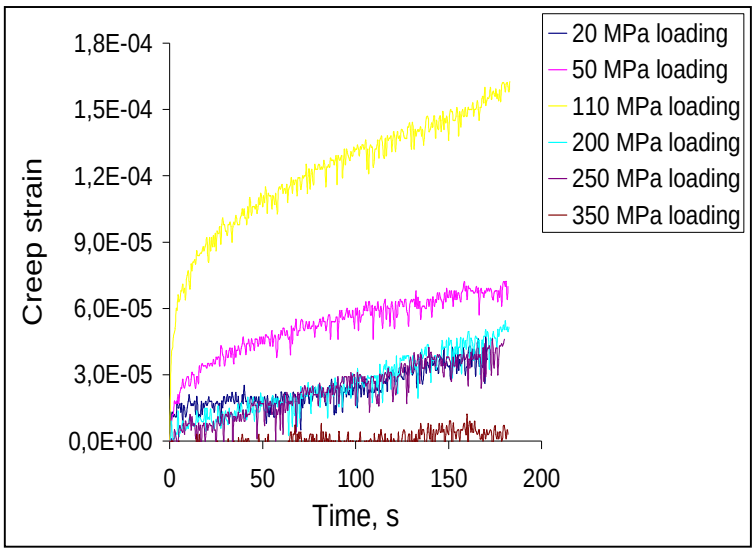

Fig.6.3: creep strain at different stress levels in PZT 4D unpoled during loading.

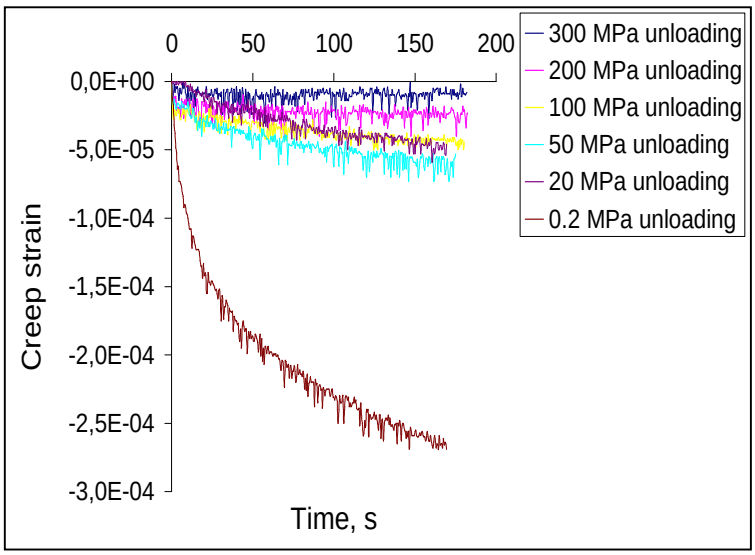

Fig.6.4: creep strain at different stress levels in PZT 4D unpoled during unloading.

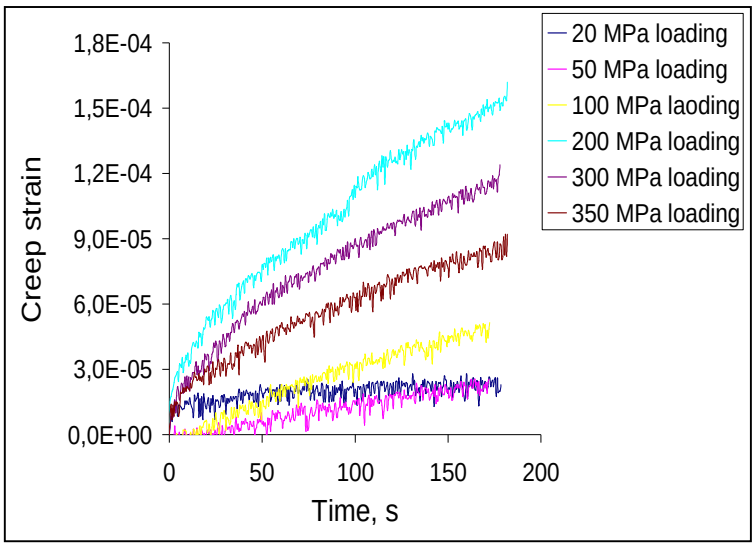

Fig.6.5: creep strain at different stress levels in PZT 4D poled perpendicular to load during loading.

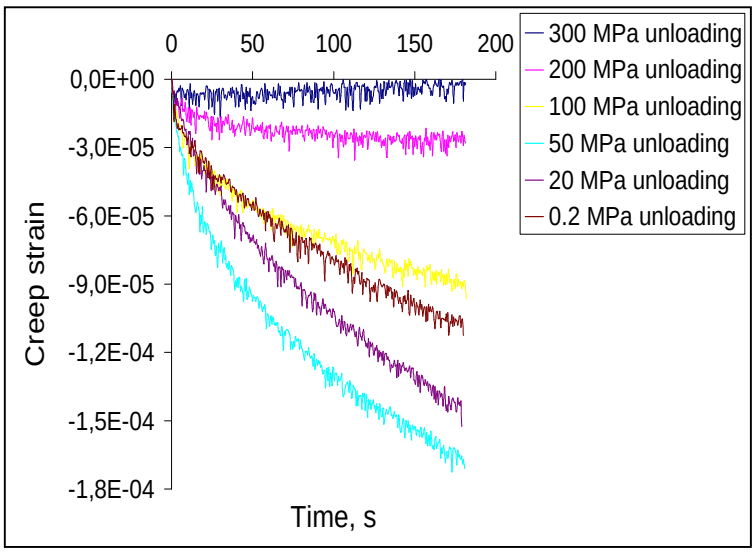

Fig.6.6: creep strain at different stress levels in PZT 4D poled perdendicular to load during unloading.

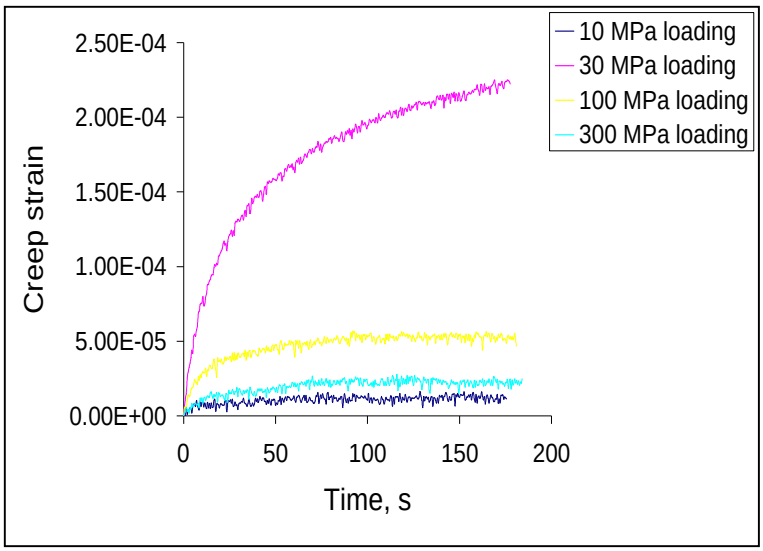

Fig.6.7: creep strain at different stress levels in PZT 5A poled parallel to load during loading.

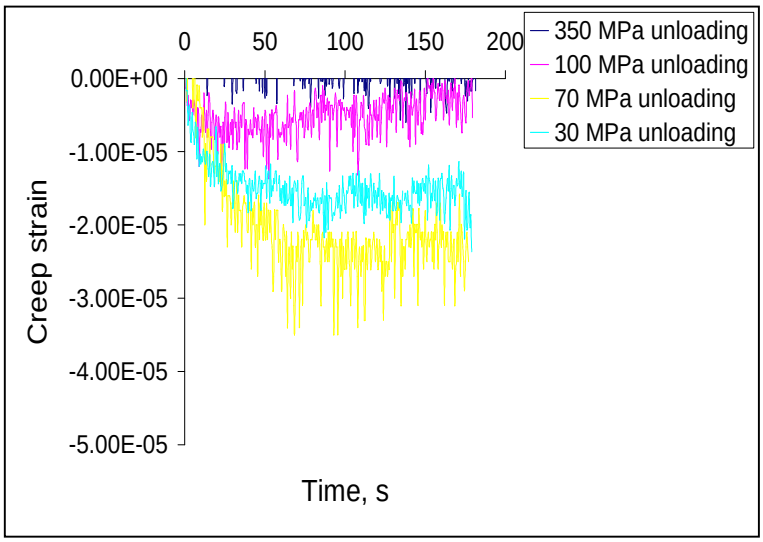

Fig.6.8: creep strain at different stress levels in PZT 5A poled parallel to load during unloading.

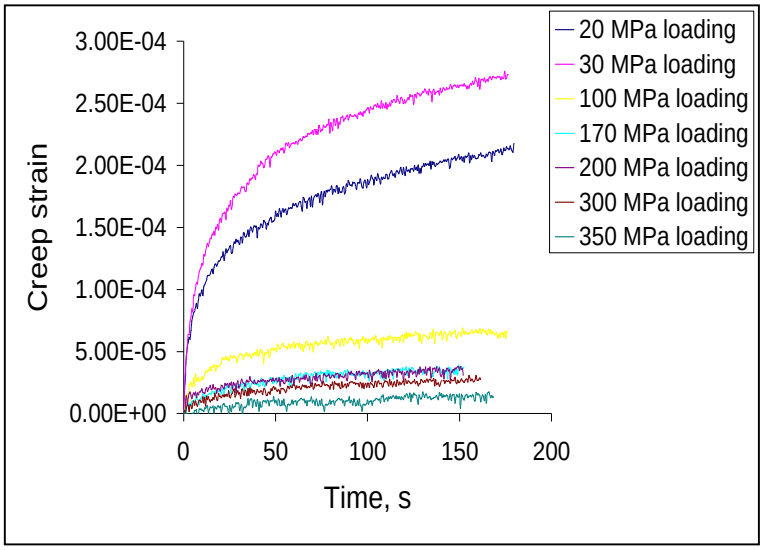

Fig.6.9: creep strain at different stress levels in PZT 5A unpoled during loading.

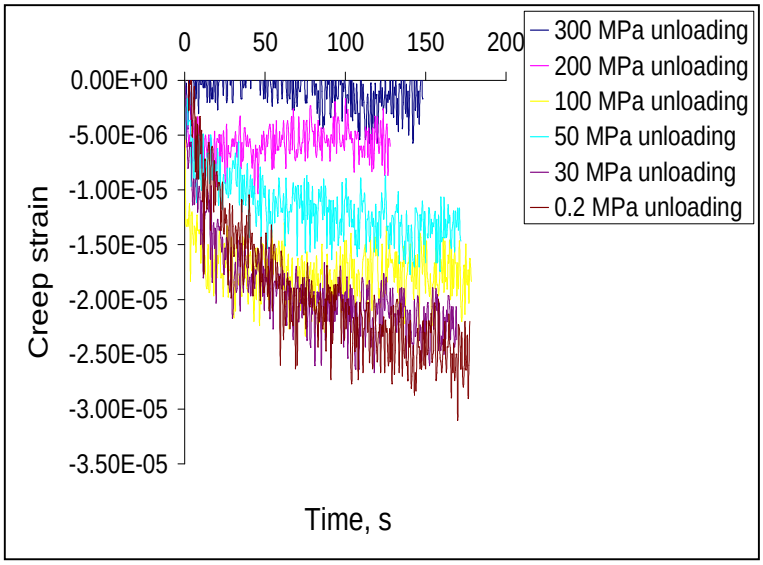

Fig.6.10: creep strain at different stress levels in PZT 5A unpoled during unloading.

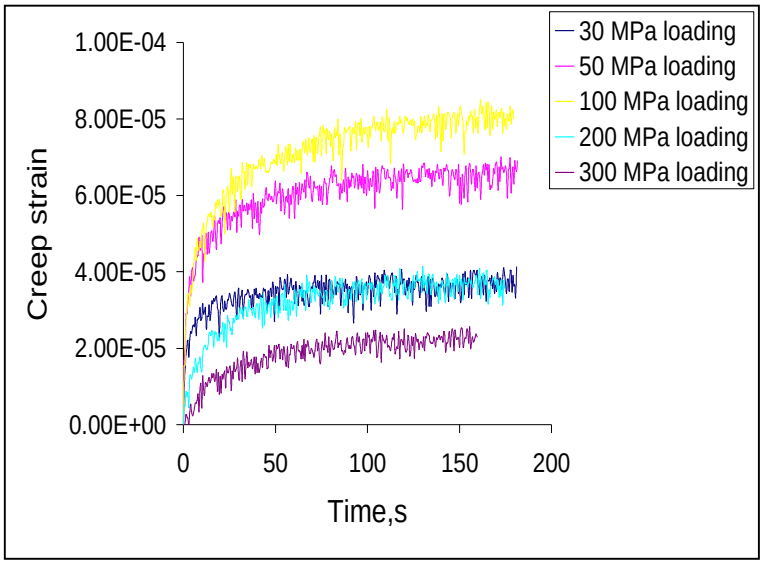

Fig.6.11: creep strain at different stress levels in PZT 5A poled perpendicular to load during loading.

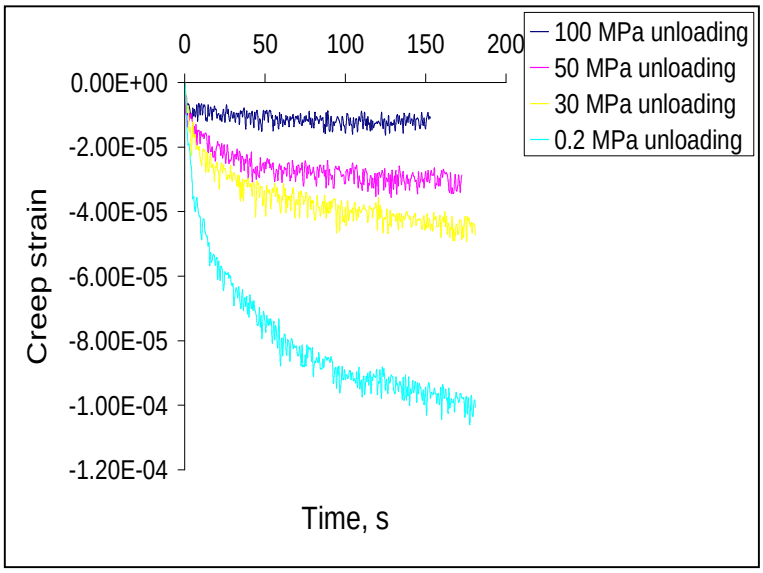

Fig.6.12: creep strain at different stress levels in PZT 5A poled perpendicular to load during unloading.

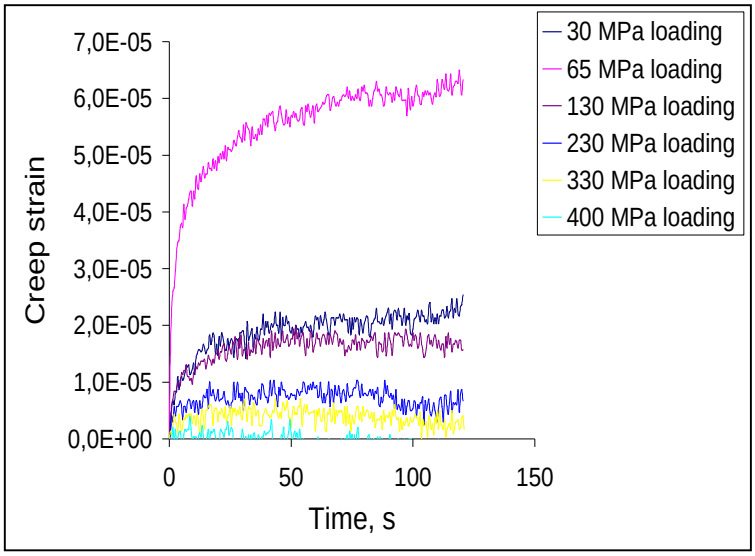

Fig.6.13: creep strain at different stress levels in LC during loading.

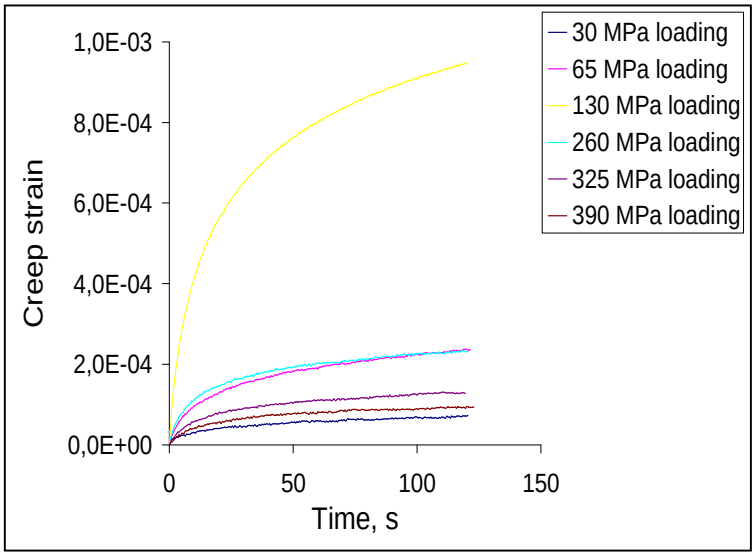

Fig.6.14: creep strain at different stress levels in LCC during loading.

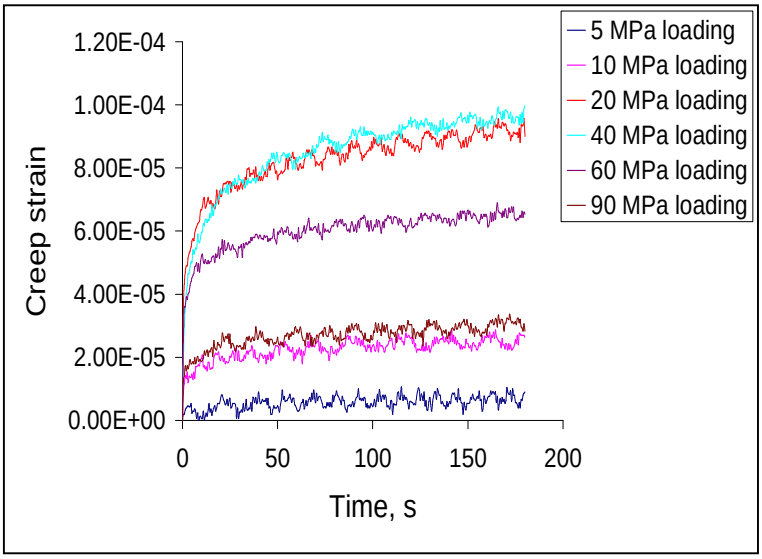

Fig.6.15: creep strain at different stress levels in LSM during loading.

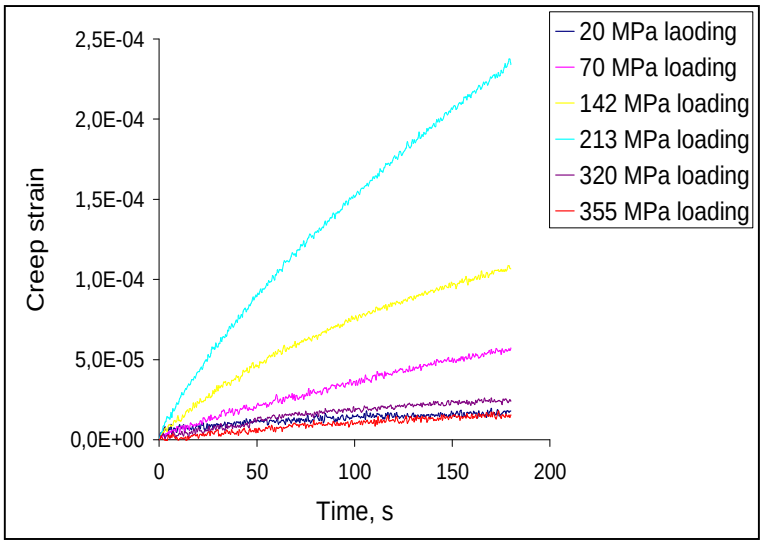

Fig.6.16: creep strain at different stress levels in LFSC during loading.

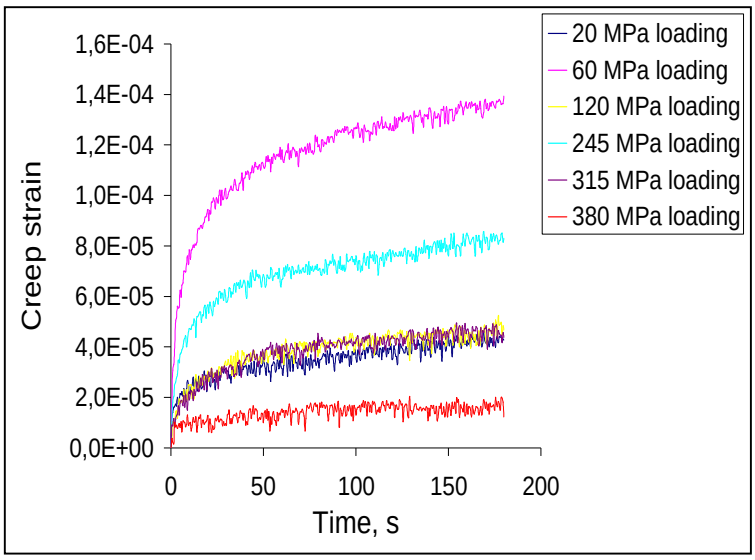

Fig.6.17: creep strain at different stress levels in LSCNM during loading.

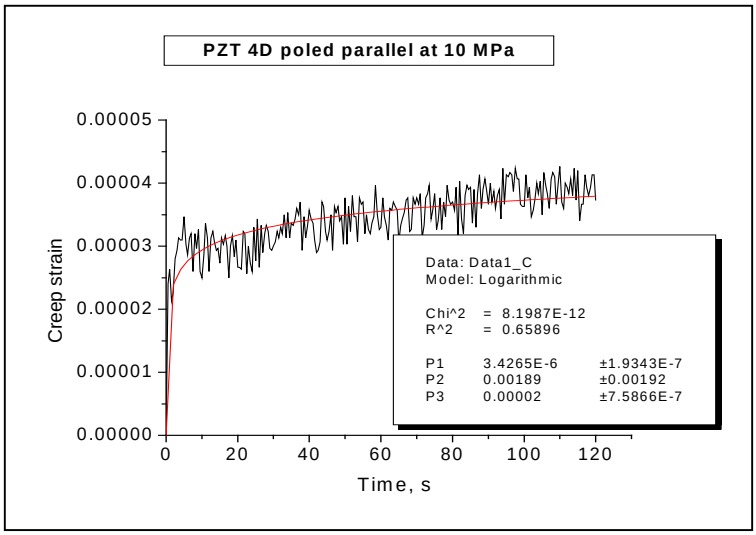

Fig.6.18: logarithmic fitting of creep strain in PZT 4D poled parallel at 10 MPa.

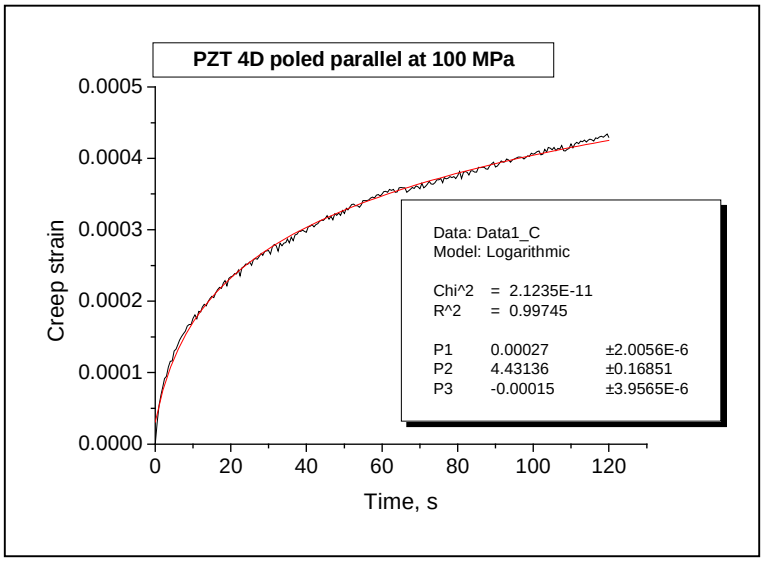

Fig.6.19: logarithmic fitting of creep strain in PZT 4D poled parallel at 100 MPa.

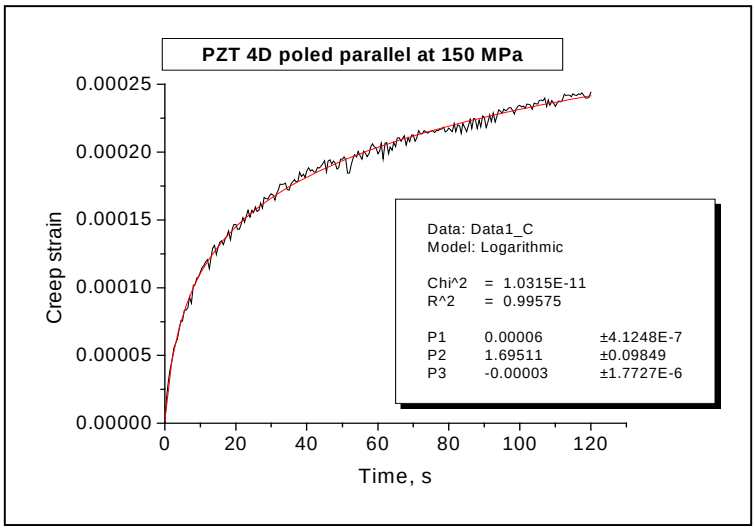

Fig.6.20: logarithmic fitting of creep strain in PZT 4D poled parallel at 150 MPa.

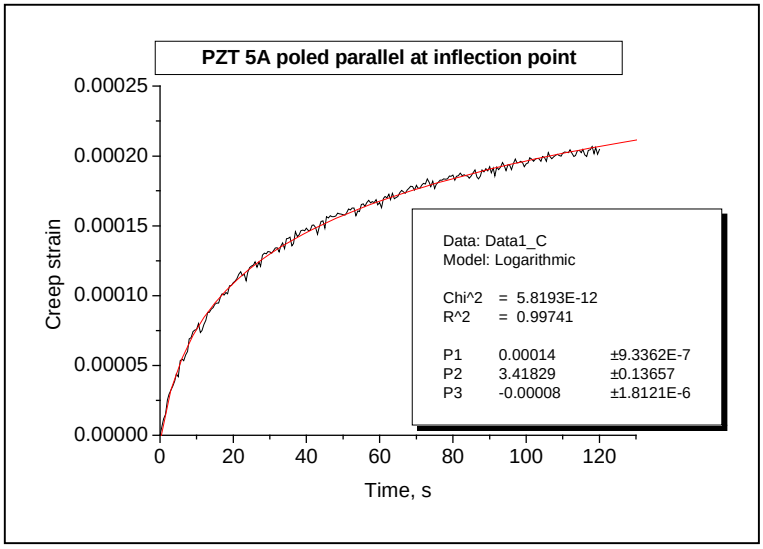

Fig.6.21: logarithmic fitting of creep strain in PZT 5A poled parallel at 30 MPa (coercive stress).

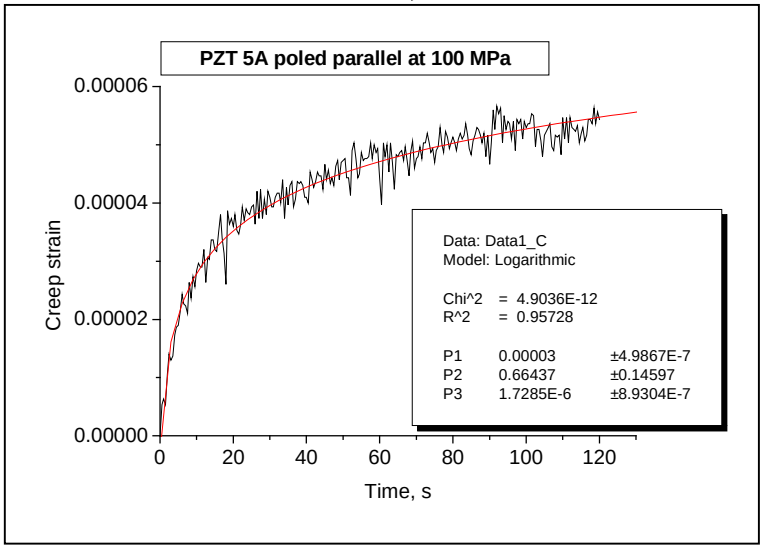

Fig.6.22: logarithmic fitting of creep strain in PZT 5A poled parallel at 100 MPa.

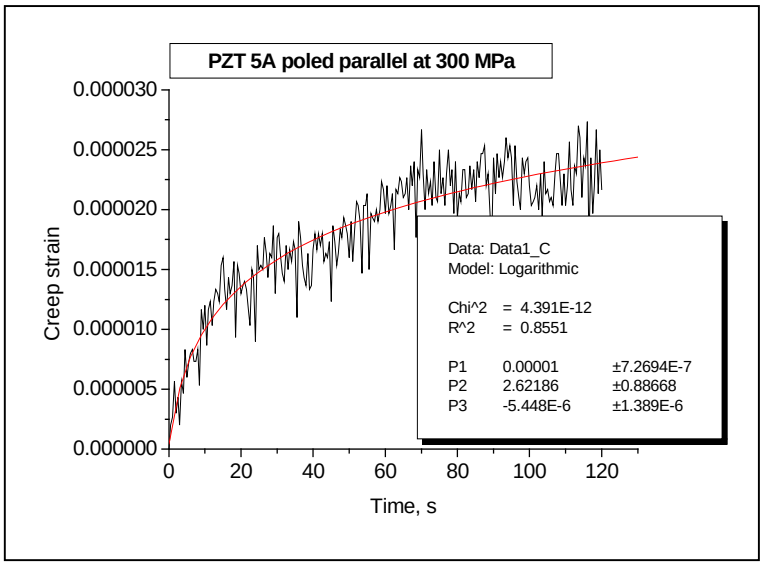

Fig.6.23: logarithmic fitting of creep strain in PZT 5A poled parallel at 300 MPa.

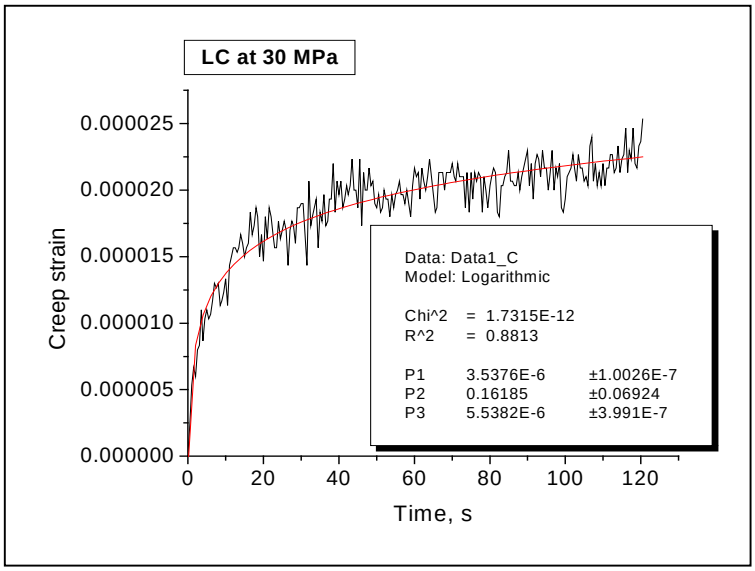

Fig.6.24: logarithmic fitting of creep strain in LC at 30 MPa.

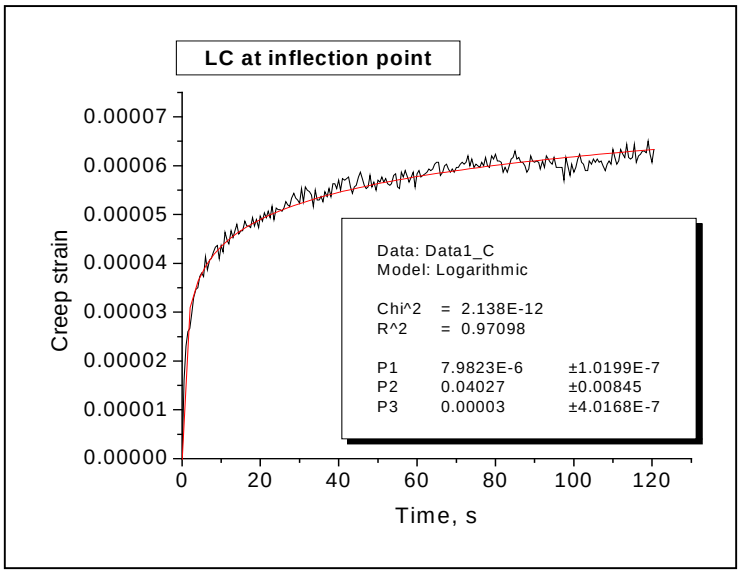

Fig.6.25: logarithmic fitting of creep strain in LC at 65 MPa (coercive stress).

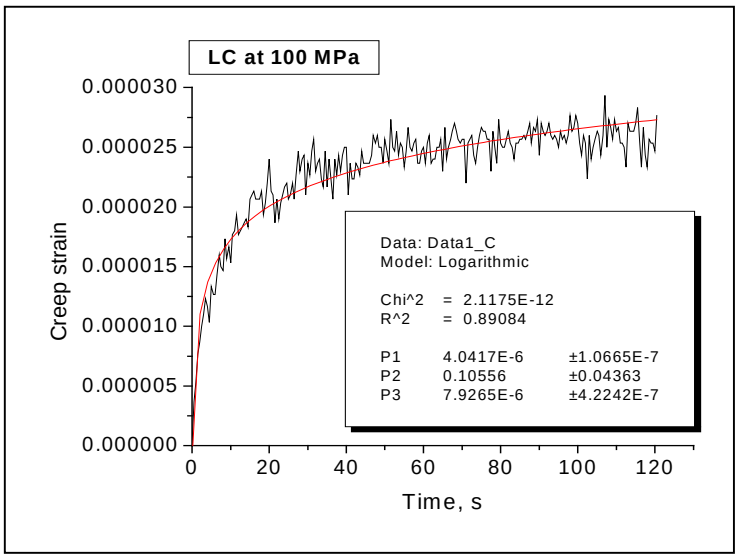

Fig.6.26: logarithmic fitting of creep strain in LC at 100 MPa.

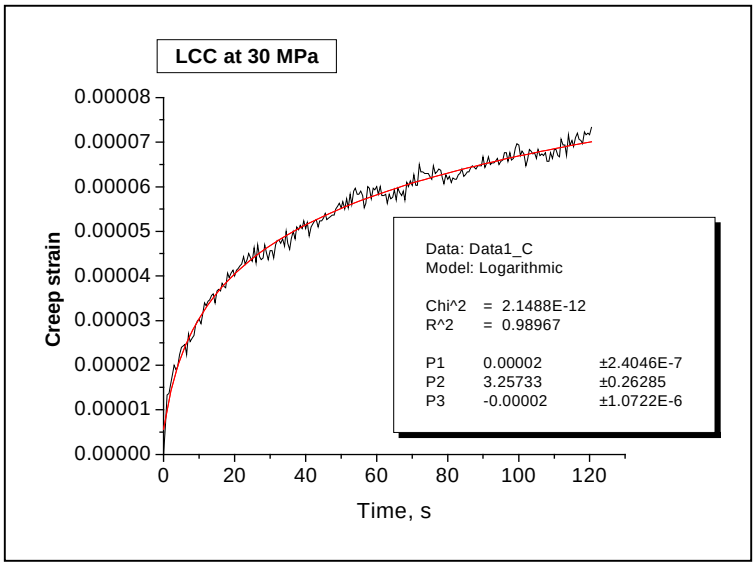

Fig.6.27: logarithmic fitting of creep strain in LCC at 30 MPa.

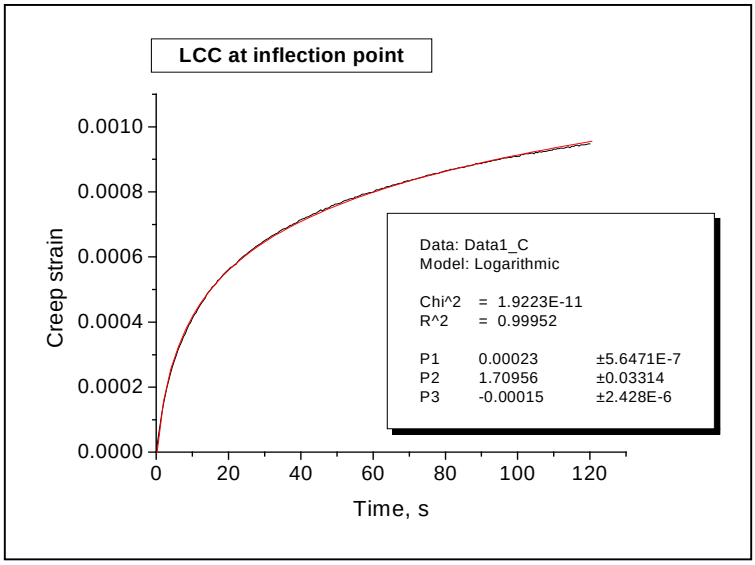

Fig.6.28: logarithmic fitting of creep strain in LCC at 130 MPa (coercive stress).

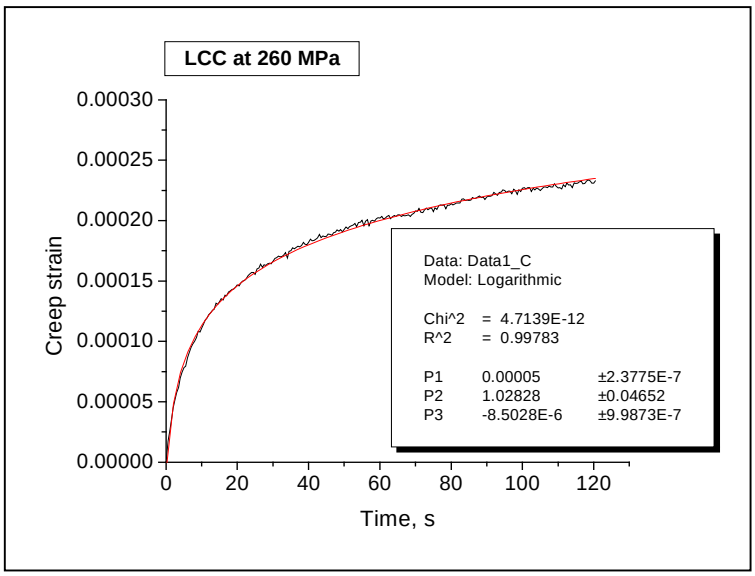

Fig.6.29: logarithmic fitting of creep strain in LCC at 260 MPa.

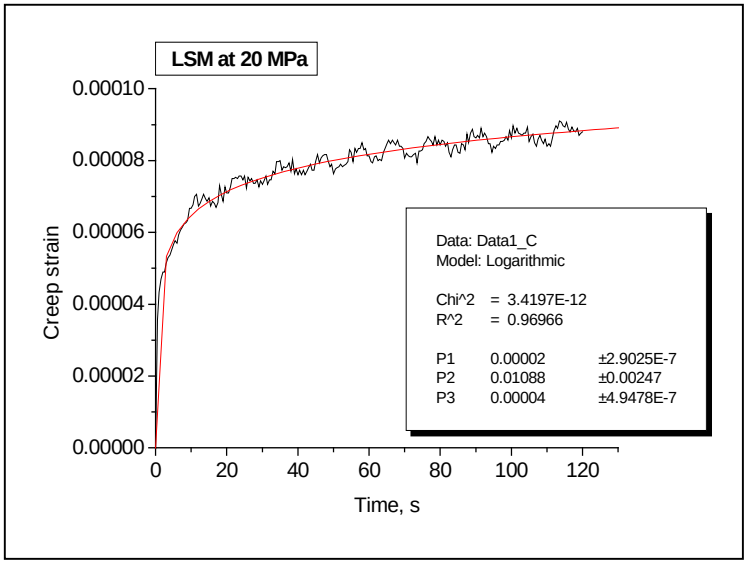

Fig.6.30: logarithmic fitting of creep strain in LSM at 20 MPa.

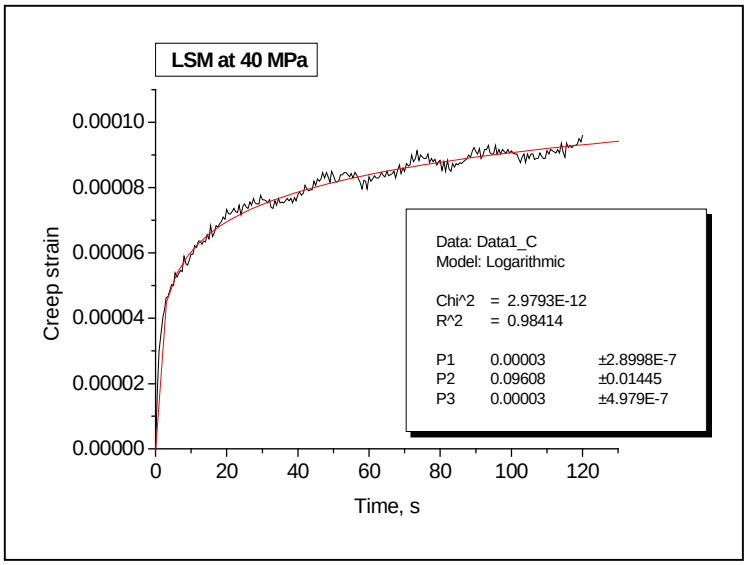

Fig.6.31: logarithmic fitting of creep strain in LSM at 40 MPa.

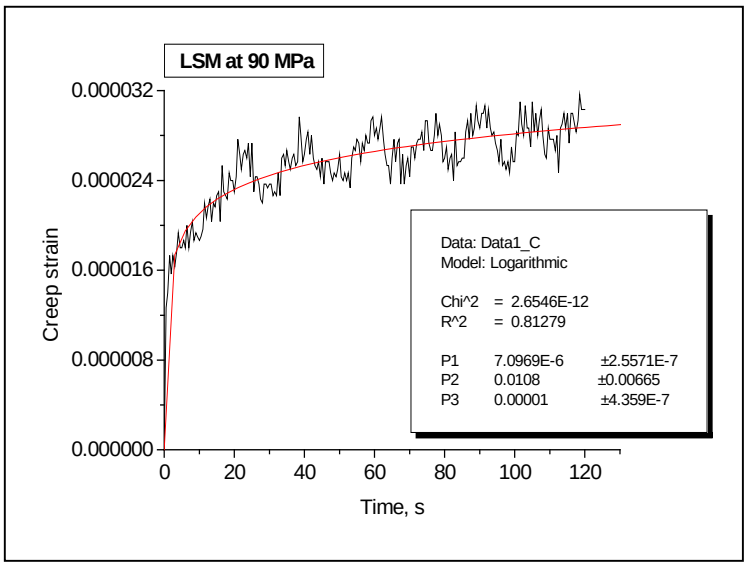

Fig.6.32: logarithmic fitting of creep strain in LSM at 90 MPa.

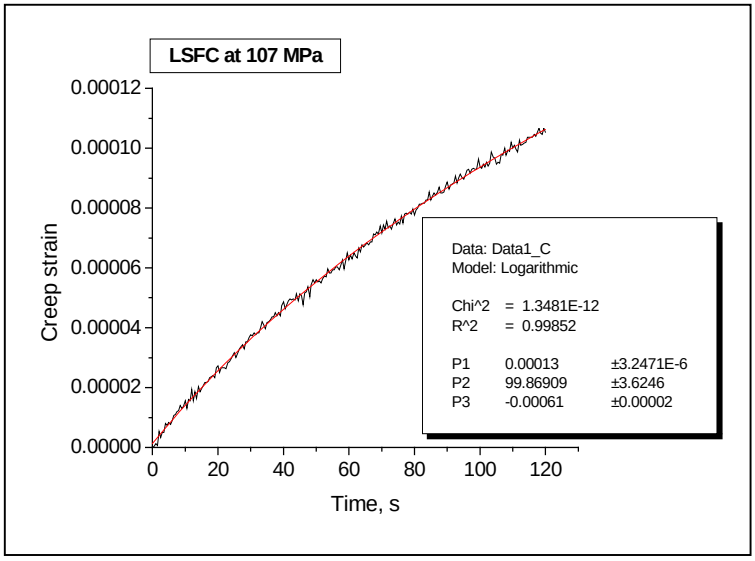

Fig.6.33: logarithmic fitting of creep strain in LSFC at 107 MPa.

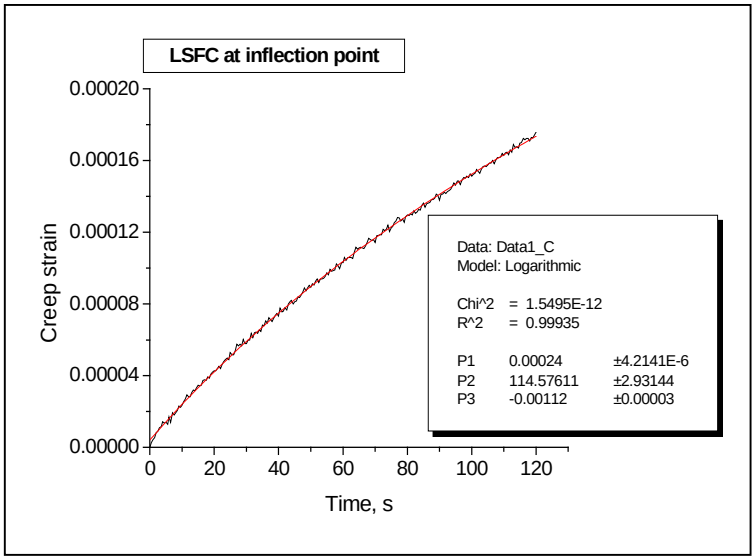

Fig.6.34: logarithmic fitting of creep strain in LSFC at 210 MPa (coercive stress).

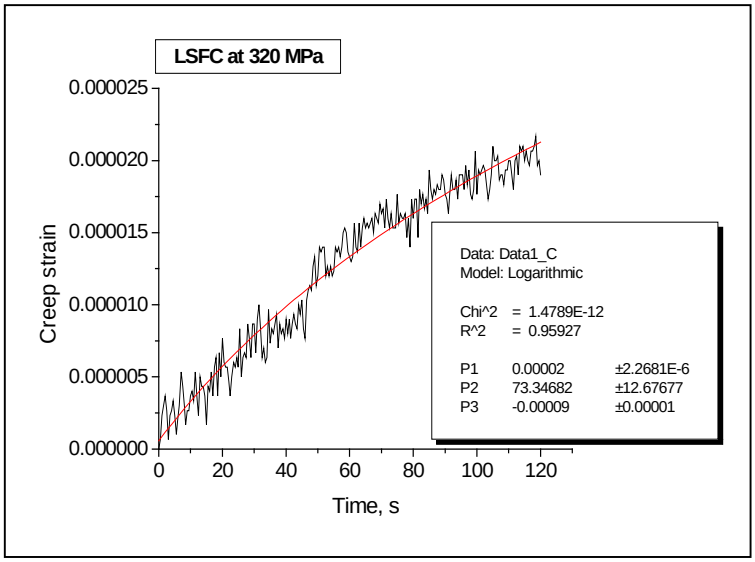

Fig.6.35: logarithmic fitting of creep strain in LSFC at 320 MPa.

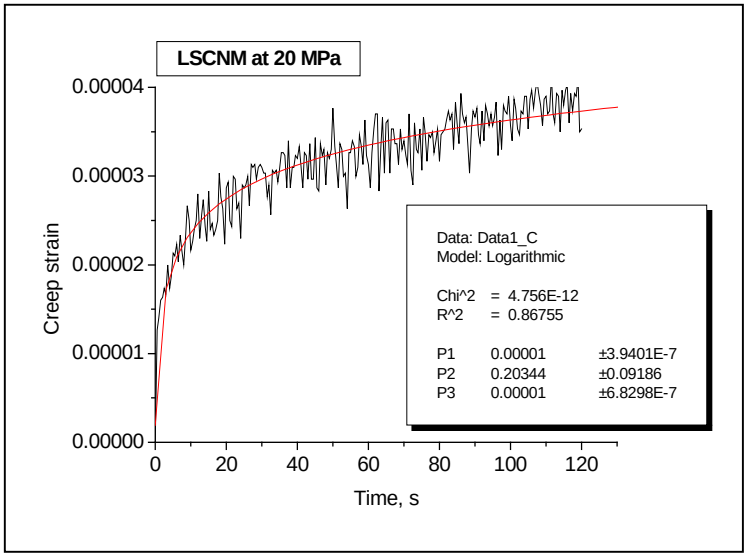

Fig.6.36: logarithmic fitting of creep strain in LSCNM at 20 MPa.

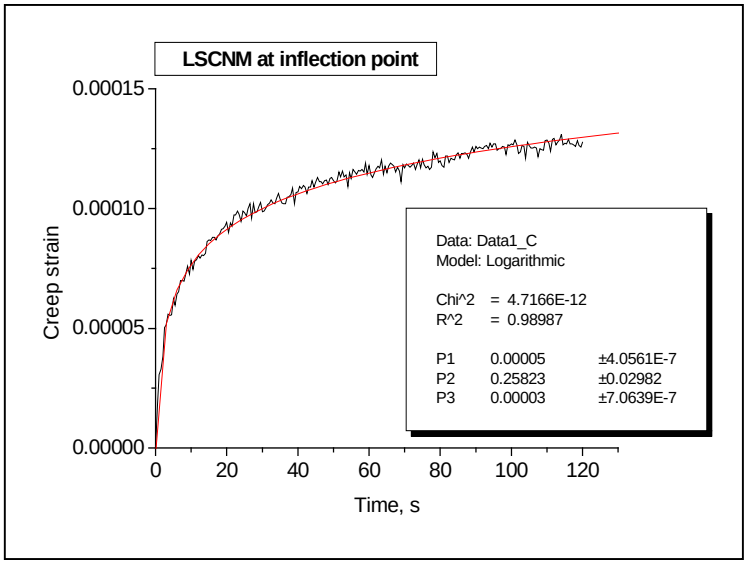

Fig.6.37: logarithmic fitting of creep strain in LSCNM at 60 MPa (coercive stress).

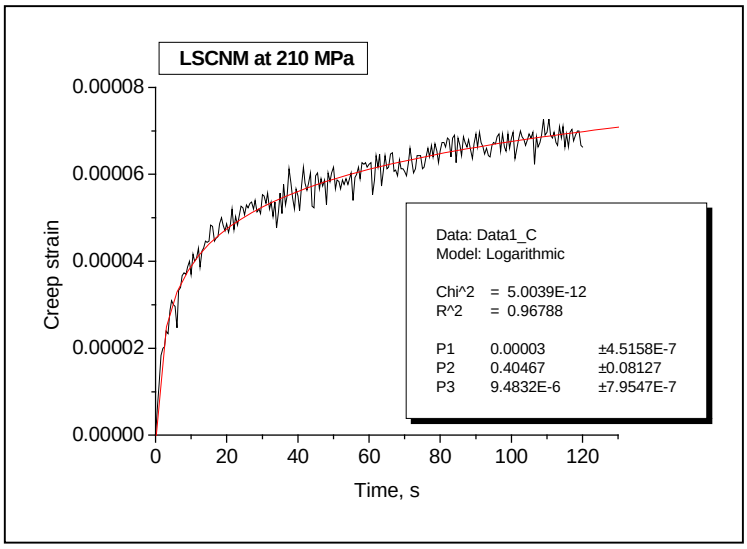

Fig.6.38: logarithmic fitting of creep strain in LSCNM at 210 MPa.

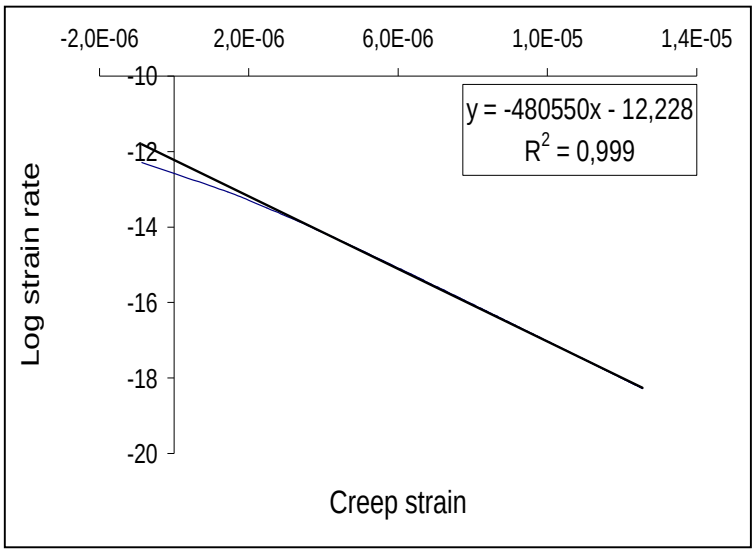

Fig.6.39: logarithmic strain rate-creep strain in PZT 5A poled parallel at 10 MPa during loading.

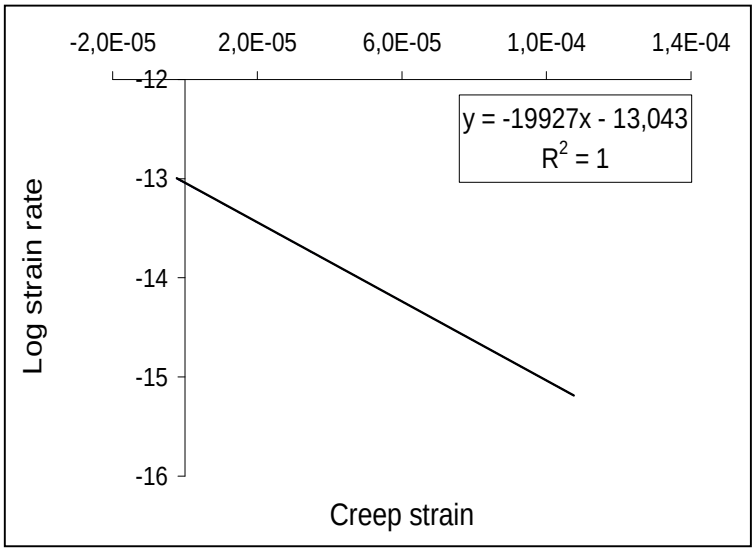

Fig.6.40: logarithmic strain rate-creep strain in PZT 5A poled parallel at 40 MPa during loading.

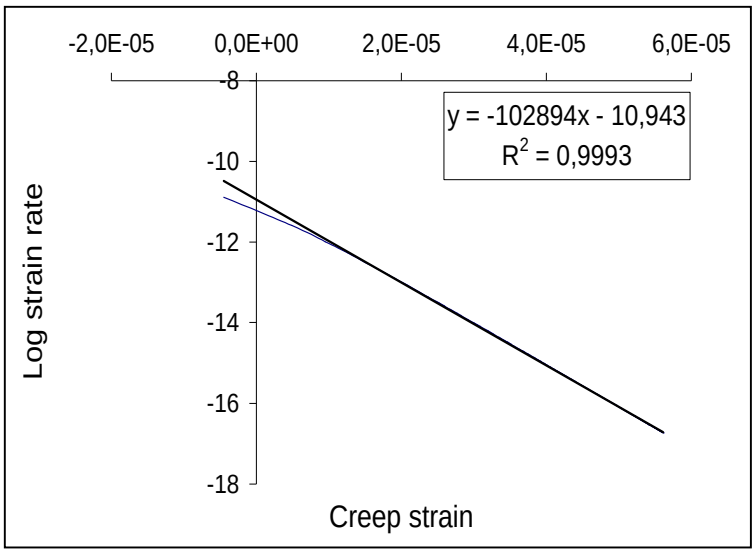

Fig.6.41: logarithmic strain rate-creep strain in PZT 5A poled parallel at 100 MPa during loading.

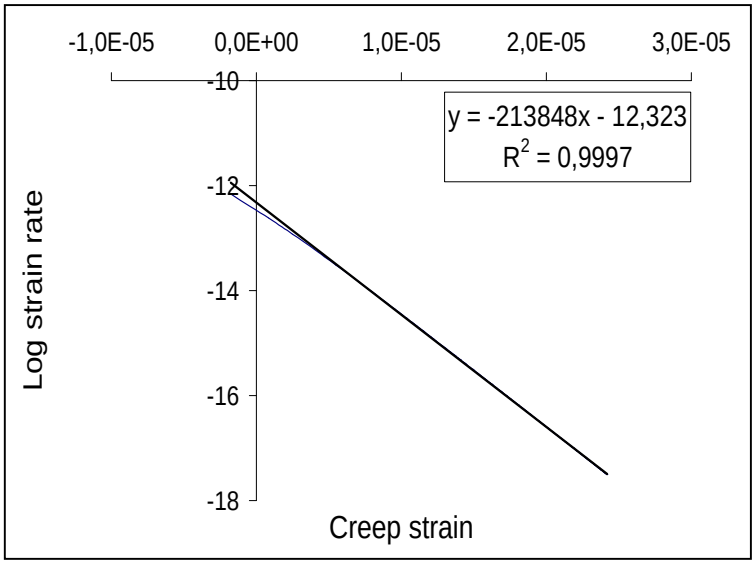

Fig.6.42: logarithmic strain rate-creep strain in PZT 5A poled parallel at 300 MPa during loading.

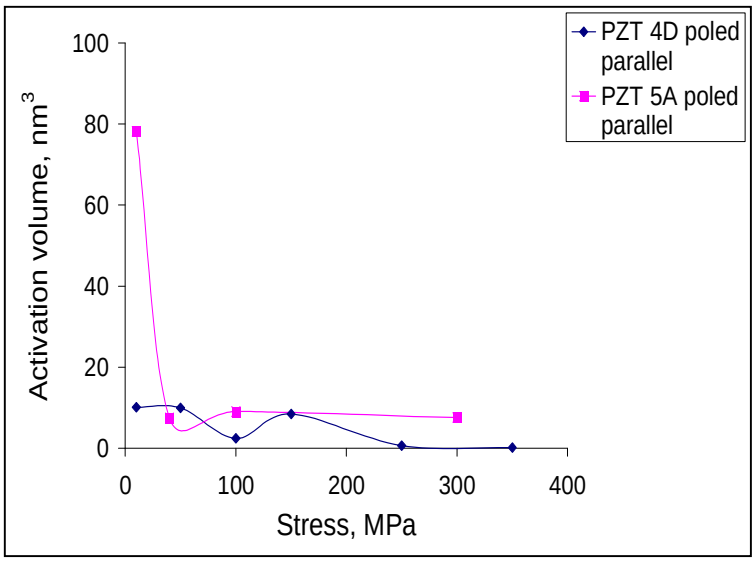

Fig.6.43: activation volume at different stress level in PZT 5A poled parallel and PZT 4D poled parallel.

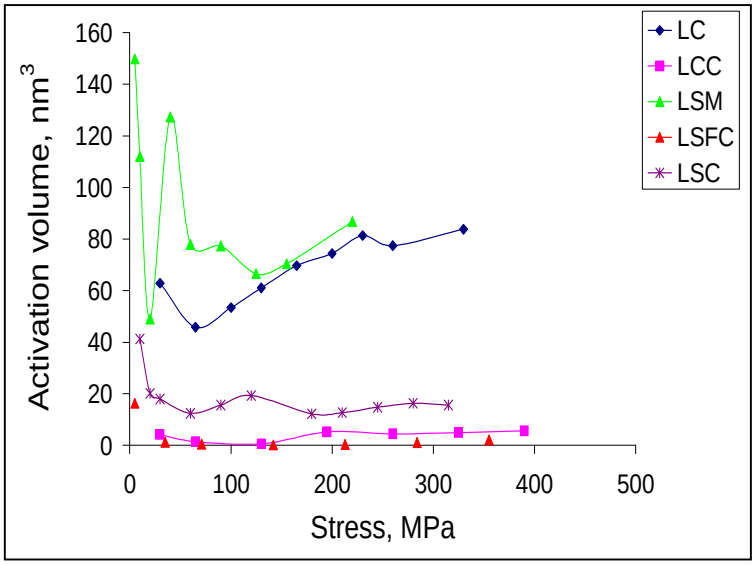

Fig.6.44: activation volume comparison in all the ferroelastic compositions.

Chapter 7: Rayleigh-type behaviour

7.1 Introduction

In this chapter, the effects of rate and the temperature on ferroelastic switching were investigated, by studying the stress-strain hysteresis loops under weak applied stress (Rayleigh loops), in different perovskite ceramics. A simplified procedure was developed to separate "*intrinsic*" and "*extrinsic*" contributions to the strain, showing that the former is dominant in the Rayleigh loops generated. The results were interpreted in terms of thermal activation and the rate model proposed was applied to estimate the effect of loading rate on the extrinsic strain. The model developed may be regarded as a valid alternative to the empirical approaches currently used. In addition, the combined effects of frequency and temperature on the Rayleigh loops was studied by keeping the stress amplitude constant in order to estimate mechanical and thermal contribution to ferroelastic switching in the Rayleigh loops. The results could be useful in the design of ferroelastic/ferroelectric devices subjected to cyclic weak applied fields, based on a more detailed knowledge of the effects of rate, temperature and dopants on the strain response.

7.2 Rayleigh loops

Although an harmonic analysis would be necessary to establish whether the material behaves as a proper Rayleigh system as discussed in [13], such an analysis has not been performed, and regardless, the hysteretic loops have been named "*Rayleigh loops*", without considering eventual deviations from the pure Rayleigh behaviour. Three different batches of data have been generated and the results will be presented in the following order:

1) at room temperature using sinusoidal dynamic loading,
2) at room tempearature using triangular dynamic loading,
3) at different temperatures.

7.2.1 Rayleigh loops at room temperature using sinusoidal dynamic loading

Hysteretic loops were generated by applying a sinusoidal stress wave of five different amplitudes ($\Delta\sigma = 2,4,6,8,10 MPa$) and four different frequencies ($f = 0.01, 0.05, 0.1, 0.5 Hz$), around a static stress bias of 12 MPa. In an analogous manner to the magnetic susceptibility χ_{ij} (see Eq.2.15 Chapter 2) and the piezoelectric coefficients d_{ij} [10,41,79-85], the mechanical compliance S_{33} was found to be linearly dependent on the stress amplitude and expressed as:

$$S_{33} = S_{init} + \alpha_R \Delta\sigma \tag{7.1}$$

where S_{init} and α_R are the Rayleigh parameters and $\Delta\sigma$ the stress amplitude.

The term S_{init} practically represents the value of the mechanical compliance extrapolated to $\Delta\sigma = 0$, indicating the value of S_{33} corresponding to the bias stress of 12 MPa. It is worthwhile noting that this parameter coincides with the "*elastic compliance*" only in the case of linear elastic materials. In the present situation this condition is observed only in LCC (Fig.7.1-7.5). PZT 5A poled parallel and LC exhibit highly non-linear behaviour from the very beginning of the stress–strain curves (see chapter 5) and hysteretic loops at the bias stress applied. The parameter α_R quantifies the domain walls displacement along the loops. Rayleigh hysteretic loops were fitted using the following equation:

$$\varepsilon = (S_{init} + \alpha_R \Delta\sigma)\sigma \pm \frac{\alpha_R}{2}(\Delta\sigma^2 - \sigma^2) = S_{33}\sigma \pm \frac{\alpha_R}{2}(\Delta\sigma^2 - \sigma^2) \tag{7.2}$$

The sign "+" describes the upper branch of the loop and the sign "-" the lower one. Examples of fittings are shown in Fig.7.1, where, for simplicity, the origin of the coordinates system has been placed in the centre of each compressive loop. In general, the mechanical compliance S_{33} increases monotonically with the amplitude of the dynamical applied stress $\Delta\sigma$ and decreases with increasing frequency (Fig.7.2-7.5). The trends obtained are in agreement with previous studies [37,83,85].

The Rayleigh parameters, S_{init} and α_R were evaluated by fitting the data using Eq.7.1. Hysteretic Rayleigh behaviour is clearly more significant in PZT 5A and LC, which have larger Rayleigh coefficients than LCC (Fig.7.6, 7.7). In LCC, the compliance S_{33} is constant in all the range of the amplitudes and of the frequencies examined. Its variability is confined within the scatter of the experimental data, showing analogies with a pure linear elastic material, by displaying non-hysteretic compressive loops, with $\alpha_R = 0$ (Fig.7.1-7.7).

A comparison between LC and LCC, suggests that under the particular static stress bias imposed, the calcium inhibits the domain switching and reduces the hysteresis. Even though the calcium produces a reduction of the distortion, it increases the domain switching stress threshold, evidenced also by a higher coercive stress in LCC (see also Chapter 5). A similar effect of calcium doping was observed in Ca-doped $KMnF_3$ [37]. Analogous trends have also been found in Fe-doped barium titanate [83] and in Nd-doped $Pb(Zr,Ti)O_3$ [85]. This is probably due to the generation of oxygen vacancies in acceptor-doped perovskites, which act as pinning sites for the domain walls.

The parameter S_{init} has a dependence on the frequency of the applied stress in PZT 5A and LC, whereas it is constant in LCC, representing its "*elastic compliance*" (Fig.7.6, 7.8). A dependence on the frequency was also observed in previous studies for the piezoelectric coefficient [42,79,92] and for the mechanical compliance [37]. In Fig.7.8 the trend is plotted for PZT 5A for a wider range of frequencies. Following Damjanovic [42,79] and Schranz et al. [37], an analogous expression derived for the magnetic susceptibility [32] (introduced in paragraph 2.6 in Chapter 2) has been used to fit the results:

$$S_{init} = P_1\left(1 + P_2 \ln\left(\frac{P_3}{f}\right)\right)^{P_4} \tag{7.3}$$

where f is the frequency of the dynamical load.

Eq.7.3 describes with reasonable accuracy the observed trend. The physical meaning of the fitting parameters is explained in [32]. In particular the parameter P_4 is related

to the roughness of the domain walls and it is in very good agreement with the other values presented in the literature [37,42]. The meaning of its numerical value is still under discussion and it could provide further insights into the nature of domain wall pinning and the geometry of domain walls, as it has already been shown by Paruch et al. through the direct measurement of the roughness exponent in PZT epitaxial thin films [123]. Based on the analogy between Eq.7.3 and Eq.2.12 in Chapter 2 and on the accuracy of Eq.7.3 in fitting the data, it can be concluded that the Rayleigh-type behavior is governed by domain wall pinning and thermally activated hopping, which influence the ferroelastic properties and determine their characteristic rate dependence.

7.2.2 Rayleigh loops at room temperature using triangular dynamic loading

Hysteretic loops were generated at 26 different frequencies in PZT 5A poled parallel in order to obtain Rayleigh loops at constant frequencies and constant loading rate on the same sample. A triangular stress wave of five different amplitudes ($\Delta\sigma = 2, 4, 6, 8, 10 MPa$) was used and loops at eight different frequencies (f=0.004, 0.008, 0.016, 0.032, 0.064, 0.128, 0.256, 0.512 Hz) and eight different loading rates ($\dot{\sigma} = 0.064,\ 0.128,\ 0.256,\ 0.512,\ 1.024,\ 2.048,\ 4.096,\ 8.192$ MPa / s), around the static stress bias of 12 MPa, were chosen for the study. The strain amplitude was measured and the mechanical compliance and the Rayleigh parameters were estimated. Similar trends with the data obtained with sine loading waves (section 7.2.1) were found. Examples of loops at different loading rates are shown in Fig.7.9. The strain amplitude and the mechanical compliance obey the Rayleigh laws, presenting a parabolic and a linear dependence on the stress amplitude respectively. They both increase as the frequency and the loading rate are decreased (Fig.7.10-7.13). Rayleigh parameters have shown rate dependence (Fig.7.14-7.17). A particular feature, whose origin is still unclear, is the non-monotonic trend of the parameter α_R as a function of the loading rate (Fig.7.17). Different from the experiments at constant frequency, where α_R decreases monotonically with increasing frequency (Fig.7.16), there is a particular loading rate where α_R assumes a local maximum.

7.2.3 Application of rate theory

In the literature, Rayleigh-type behavior is commonly attributed to the interaction of domain walls with defects acting as pinning sites. It was proposed that domain wall motion in Rayleigh loops involves several steps: pinning in an equilibrium position, bowing, unpinning, displacement, repining in a new equilibrium position and debowing [124].

As part of the overall ferroelastic phenomenology, Rayleigh-type behavior can be modeled by assuming that domain wall movement in the Rayleigh-type deformations occurs through the nucleation and the expansion of activated nuclei, with the nucleation being the rate limiting step of the overall process. The nucleation of activated nuclei is characterized by an energetic barrier, which can be surmounted by supplying thermal energy $k_B T$ (k_B=Boltzmann constant) and/or via the application of an external field, and a by time constant, that gives rise to the observed rate dependence. Therefore it is physically reasonable considering the Rayleigh-type behavior as a thermally activated process and to describe its rate dependence in terms of thermal activation rate theory. According to the model developed in Chapter 3, the rate of the strain produced by domain wall movement ("*extrinsic strain*") is given by:

$$\dot{\varepsilon}_{ext} = \dot{\varepsilon}_0 \exp\left(-\frac{\Delta H}{k_B T}\right) \tag{7.4}$$

Differently from the creep process, where the strain is mainly due to domain wall movement, in the Rayleigh loops the strain has two contributions: the "*elastic strain*", which does not involve domain wall motion and the "*ferroelastic strain*" due to domain wall movement. The separation of the two components is not straightforward and a simplified procedure is proposed to estimate both.

It should be noted that Eq.7.1 cannot be used in such evaluation, because the parameter S_{init} is rate dependent and cannot be considered as the "*elastic compliance*", as already pointed out in the section 7.2.1. The "*intrinsic contribution*" can be determined exactly only at zero absolute temperature, where domain walls are frozen, because of the absence of thermal energy [82]. However, it can be observed

that as the loading rate increases, the parameter S_{init} decreases to an asymptotic value $\overline{S}_{init}$, which can be considered as the "*intrinsic compliance*", with reasonable accuracy. By accepting the asymptotic value of S_{init} as physically sensible for the "*intrinsic compliance*", the "*intrinsic strain*" $\Delta\varepsilon_{\text{int}}$ can be estimated as:

$$\Delta\varepsilon_{\text{int}} = \overline{S}_{init}\Delta\sigma \tag{7.5}$$

where $\Delta\sigma$ is the stress amplitude. The elastic modulus calculated from $\overline{S}_{init}$ is around 80 GPa, which is higher than the value provided by the manufacturer Morgan Matroc (61 GPa), suggesting that the value estimated from the Rayleigh-type loops is less affected by extrinsic contributions.

The "*extrinsic strain*" can be then derived by subtracting the "*intrinsic strain*", from the experimental values of the measured "*total strain amplitude*". Results are shown in Fig.7.18, evidencing that the "*intrinsic deformations*" are dominant in the conditions examined, in agreement with analogous Rayleigh-type analysis performed on relaxor PZN-8PT, where "*intrinsic contributions*" to the piezoelectric response were found larger than the "*extrinsic*" ones [125].

It is assumed that the experimental conditions used to carry out the tests (weak applied field and small stress amplitudes) do not produce dramatic changes in the microstructure of the samples, ensuring small variations in the pre-exponential parameter $\dot{\varepsilon}_0$, which, for simplicity, can be considered constant, without leading to significant inaccuracies.

Theoretically, the extrinsic strain amplitude under conditions of constant microstructure can be obtained from Eq.7.4 as:

$$\Delta\varepsilon_{ext} = \dot{\varepsilon}_0 \int_0^{\frac{\Delta\sigma}{\dot{\sigma}}} \exp\left(-\frac{\Delta U - V_a \dot{\sigma}_{app} t}{k_B T}\right) dt \tag{7.6}$$

Eq.7.6 can be rewritten in a more convenient form:

$$\Delta\varepsilon_{ext} = \dot{\varepsilon}_0 \int_0^{\frac{\Delta\sigma}{\dot{\sigma}}} \exp(A + Bt)dt \tag{7.7}$$

where:

$$A = -\frac{\Delta U}{k_B T} \text{ and } B = \frac{V_a \dot{\sigma}_{app}}{k_B T} \tag{7.8}$$

The integral in Eq.7.6 can be analytically calculated, having:

$$\Delta\varepsilon_{ext} = \frac{\dot{\varepsilon}_0}{B}\left[\exp(A + Bt)\right]_0^{\frac{\Delta\sigma}{\dot{\sigma}}} = \frac{\dot{\varepsilon}_0}{B}\left[\exp\left(A + B\frac{\Delta\sigma}{\dot{\sigma}}\right) - \exp A\right] \tag{7.9}$$

Let us indicate with $\Delta\varepsilon_{ext1}$ and $\Delta\varepsilon_{ext2}$ two strain amplitudes obtained with the same stress amplitude, but with different loading rates, $\dot{\sigma}_1$ and $\dot{\sigma}_2$ respectively. The ratio will be given by:

$$\frac{\Delta\varepsilon_{ext1}}{\Delta\varepsilon_{ext2}} = \frac{\frac{k_B T\dot{\varepsilon}_0}{V_a\dot{\sigma}_1}\left[\exp\left(A + \frac{V_a\dot{\sigma}_1}{k_B T}\frac{\Delta\sigma}{\dot{\sigma}_1}\right) - \exp A\right]}{\frac{k_B T\dot{\varepsilon}_0}{V_a\dot{\sigma}_2}\left[\exp\left(A + \frac{V_a\dot{\sigma}_2}{k_B T}\frac{\Delta\sigma}{\dot{\sigma}_2}\right) - \exp A\right]} \tag{7.10}$$

Although the pre-exponential parameter is unknown, constant microstructure conditions are reflected in a coincident value of $\dot{\varepsilon}_0$ for $\Delta\varepsilon_{ext1}$ and $\Delta\varepsilon_{ext2}$. Therefore the previous ratio leads to:

$$\frac{\Delta\varepsilon_{ext1}}{\Delta\varepsilon_{ext2}} = \frac{\dot{\sigma}_2}{\dot{\sigma}_1} \tag{7.11}$$

In Fig.7.19-7.23 both the ratios were plotted as a function of the loading rate at the different stress amplitudes. The highest accuracy was obtained for 2 MPa stress amplitude (Fig.7.19), which is the experimental situation that guarantees smaller changes in the microstructure and consequently it represents the most appropriate condition to apply the model expressed by Eq.7.4.

7.2.4 The effect of temperature

The strain amplitude $\Delta\varepsilon$ of the Rayleigh loops is a function of the type:

$$\Delta\varepsilon = \Delta\varepsilon(\sigma_B, \Delta\sigma, f, T) \tag{7.12}$$

where σ_B is the static bias applied, $\Delta\sigma$ is the stress amplitude of the dynamical load, f is the frequency of the dynamical load applied and T the temperature. In order to minimize creep effects, facilitating the generation of closed loops, the analysis was performed by choosing only one stress bias, within the sub-coercive field region in all the materials tested. The specimens were subjected to a static compressive load of 12 MPa and to a triangular dynamic load superimposed on the static one. In order to analyze solely the effect of the temperature and frequency, the stress amplitude of the dynamical load was kept constant ($\Delta\sigma = 4MPa$) and the frequency (f=0.008, 0.016, 0.032, 0.064, 0.128, 0.256 *Hz*) and the temperature (T=25, 30, 40, 50, 60, 70 *ºC*) varied. Hysteretic stress-strain loops were generated and the measured loop-strain was plotted as a function of frequency and temperature. In Fig.7.24 stress-strain loops of PZT 5A poled parallel (Δσ=4 MPa, f=0.064 Hz) are shown for three different temperatures. Increasing the temperature, the loop-compliance increases and larger strain is produced. Analogous trends were observed also on LC and LCC, in agreement with recently published data on PZT thin films [126]. The strain amplitude increased with increasing the temperature and decreasing frequency in all the compositions examined (Fig.7.25-7.27). The trend is more pronounced in PZT 5A poled parallel, due to a larger domain wall motion under the conditions studied. The overlapping of data in LC and LCC (Fig.7.26, 7.27) is due to the prevalence of "*intrinsic deformations*" in the considered circumstance that have small rate and temperature dependence, precluding the observation of clear trends. By increasing the stress amplitude a greater number of domain can switch and more clear trends can be observed (Fig.7.28, 7.29), confirming the functional dependence (7.12). A comparison between LC and LCC, once again suggests that under the static stress bias imposed and for Δσ=4 MPa, the calcium has a hindering action on the domain wall movement, probably due to the formation of oxygen vacancies which act as pinning sites for the domain walls.

7.3 Conclusions

Rayleigh-type analysis is a powerful tool to study the rate and the temperature dependence of the mechanical response of ferroelastic materials under weak applied mechanical stresses. The results confirmed that hysteretic behaviour and domain wall mobility are influenced by doping. Rayleigh-type equations (7.1), (7.2), and (7.3) have been successfully applied to ferroelastic materials, proving that different ferroic systems can be described using analogous models. The rate dependence of the Rayleigh loops was attributed to the thermally activated nature of the ferroelastic switching process. A simplified procedure was proposed for the separation of the intrinsic and the extrinsic strain, suggesting that the former is predominant in the Rayleigh loops generated. Rate theory is able to predict the effect of the change in rate on the extrinsic strain, representing a sensible physical model to describe the effect of rate on Rayleigh-type deformations. The accuracy of the prediction is higher for small stress amplitudes, where the assumptions of the model hold more reasonably. The effect of temperature was found to increase the strain amplitude of the Rayleigh loops reconfirming that thermal energy represents an additional driving force for the ferroelastic switching process.

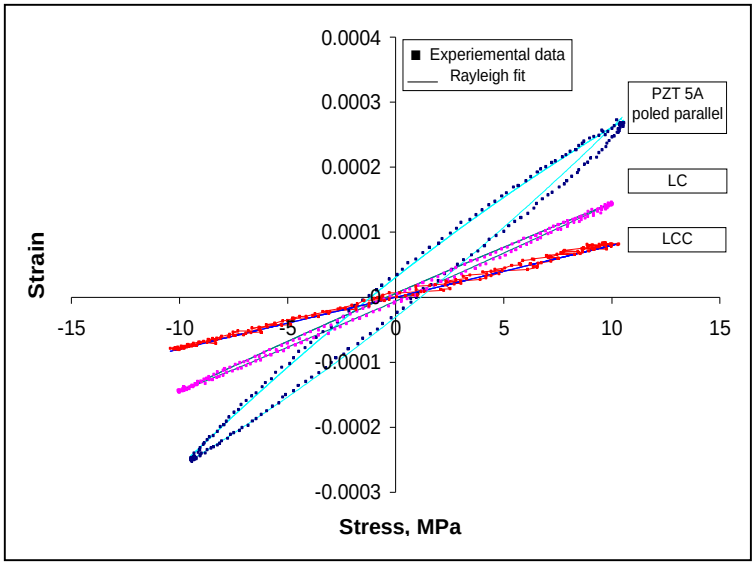

Fig.7.1: fitting of Rayleigh loops generated using sinusoidal stress waves with Δσ=10 MPa and f=0.01 Hz.

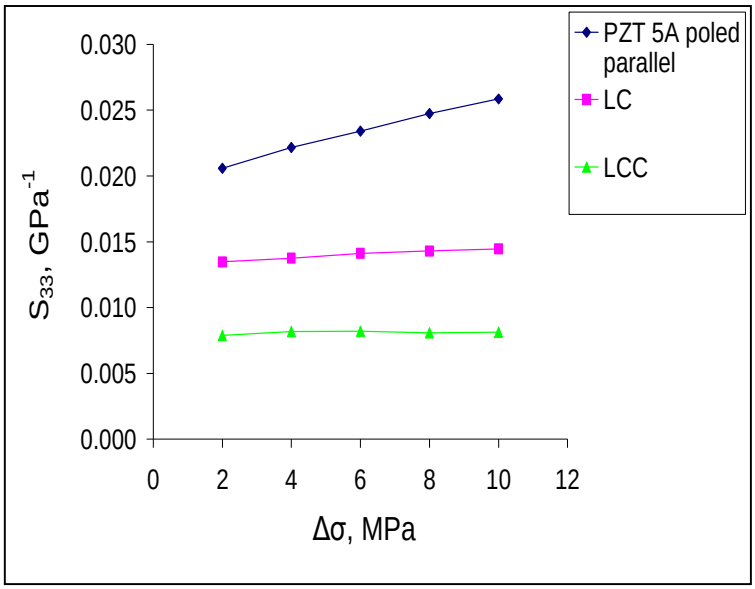

Fig.7.2: S_{33}-Δσ from loops generated using sinusoidal stress waves with f=0.01 Hz.

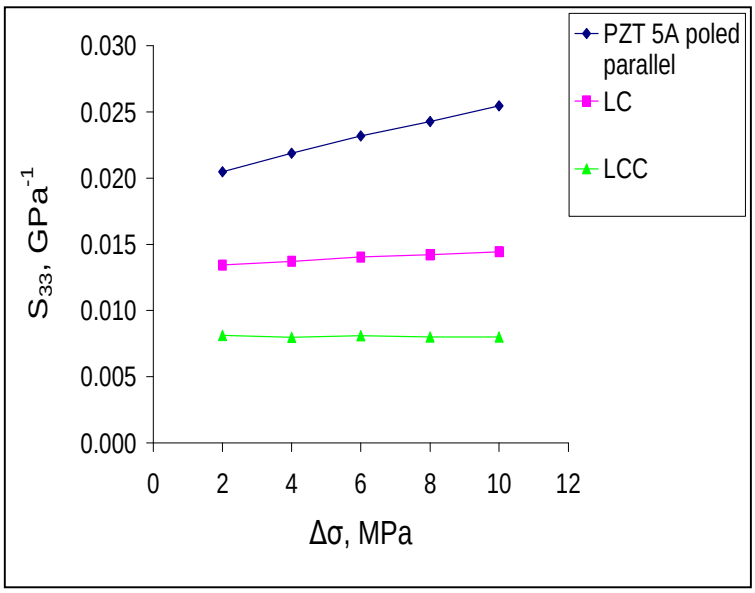

Fig.7.3: S_{33}-Δσ from loops generated using sinusoidal stress waves with f=0.05 Hz.

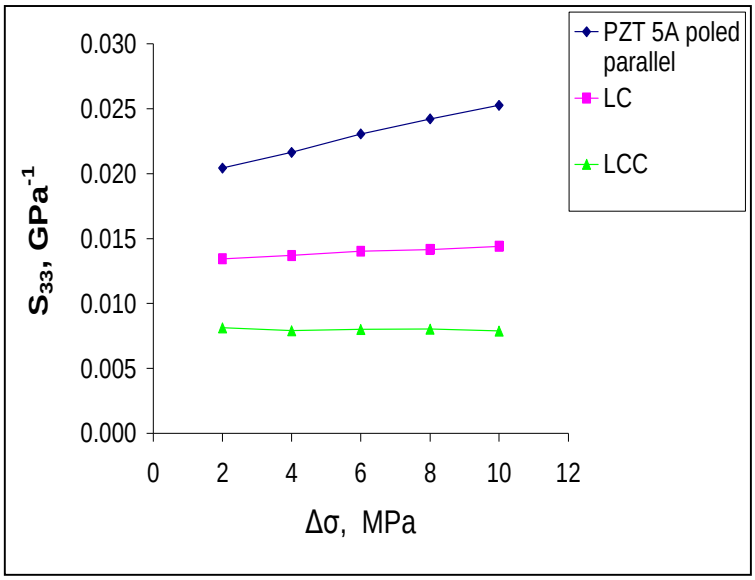

Fig.7.4: S_{33}-Δσ from loops generated using sinusoidal stress waves with f=0.1 Hz.

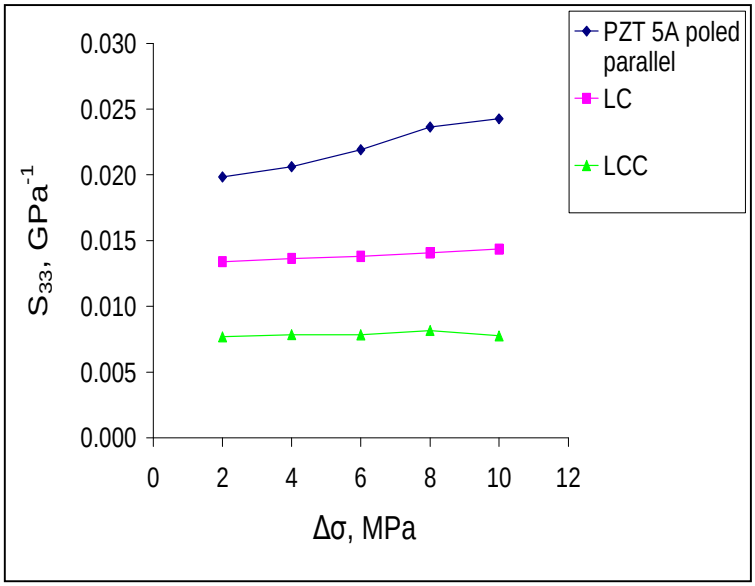

Fig.7.5: S_{33}-Δσ from loops generated using sinusoidal stress waves with f=0.5 Hz.

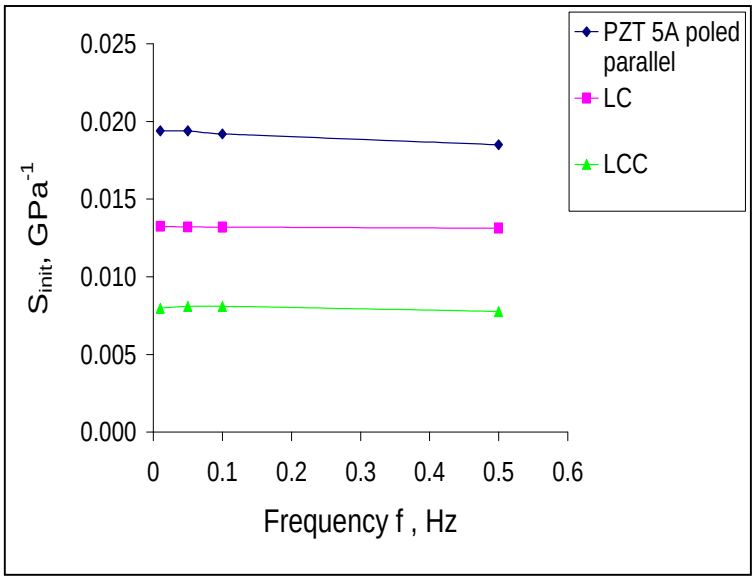

Fig.7.6: comparison of the Rayleigh parameter S_{init} (from loops generated using sinusoidal stress waves).

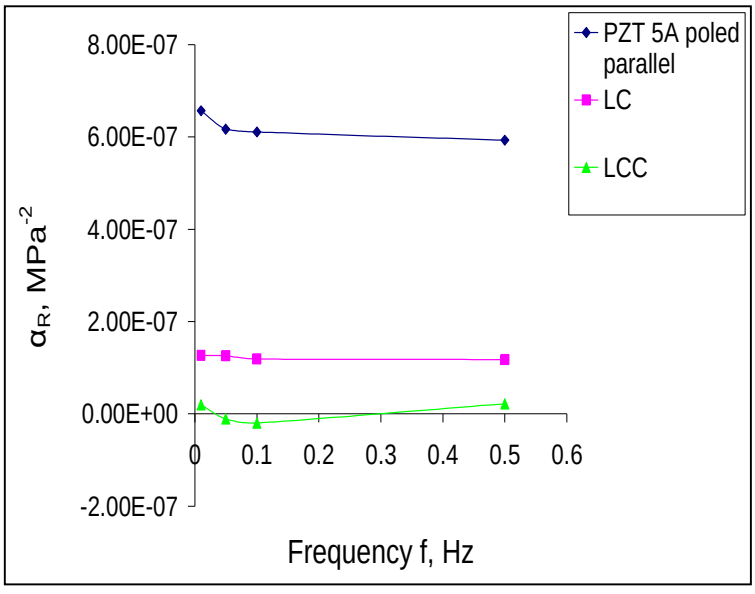

Fig.7.7: comparison of the Rayleigh parameter α_R (from loops generated using sinusoidal stress waves).

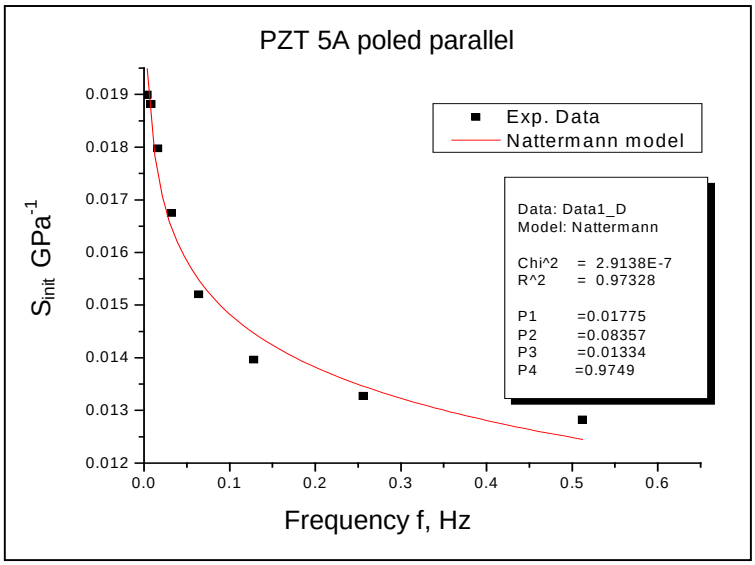

Fig.7.8: frequency dependence of the Rayleigh parameter S_{init}.

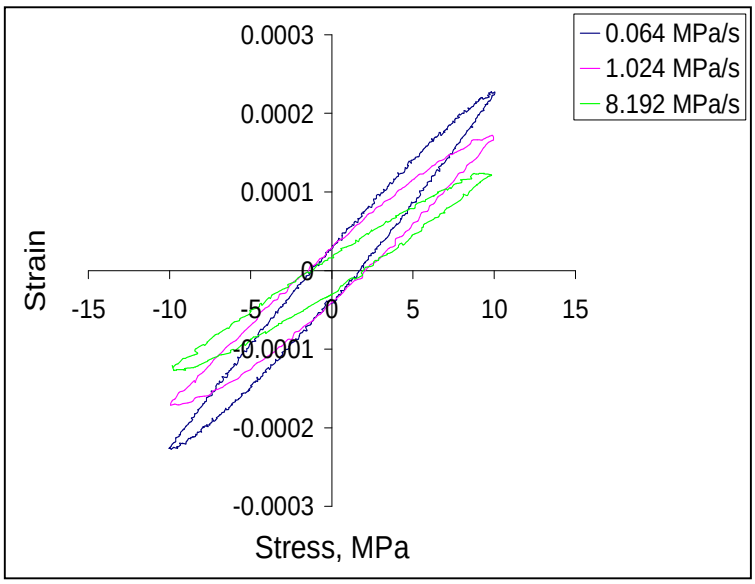

Fig.7.9: example of stress-strain loops generated using triangular stress waves with different loading rates in PZT 5A poled parallel.

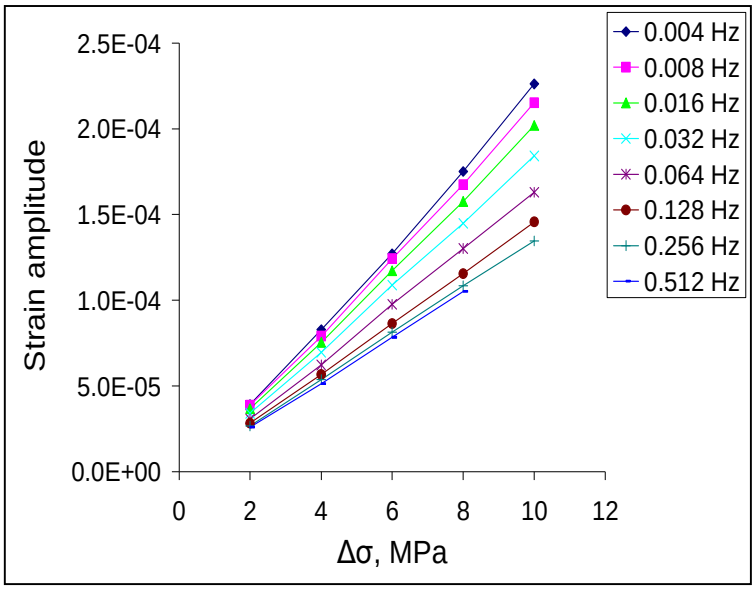

Fig.7.10: strain amplitude-Δσ from loops generated using triangular stress waves at eight different frequencies in PZT 5A poled parallel.

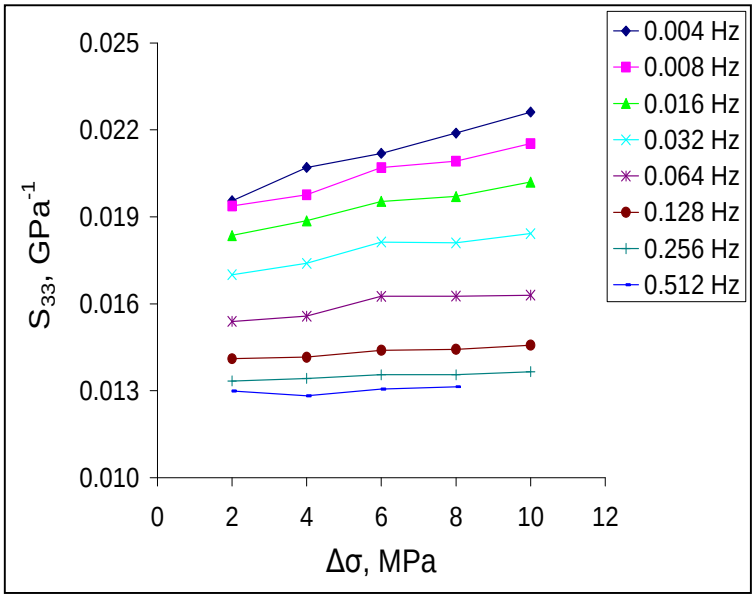

Fig.7.11: S_{33}-Δσ from loops generated using triangular stress waves at eight different frequencies in PZT 5A poled parallel.

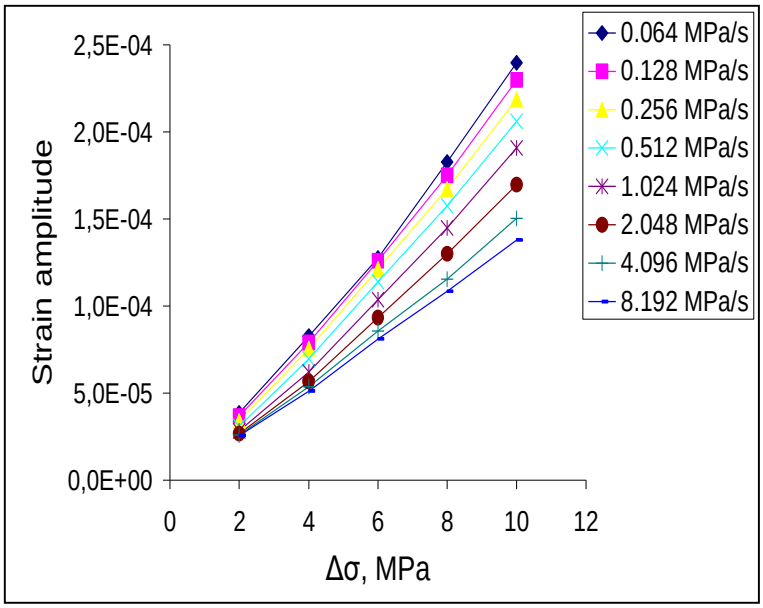

Fig.7.12: strain amplitude-Δσ from loops generated using triangular stress waves at eight different loading rates in PZT 5A poled parallel.

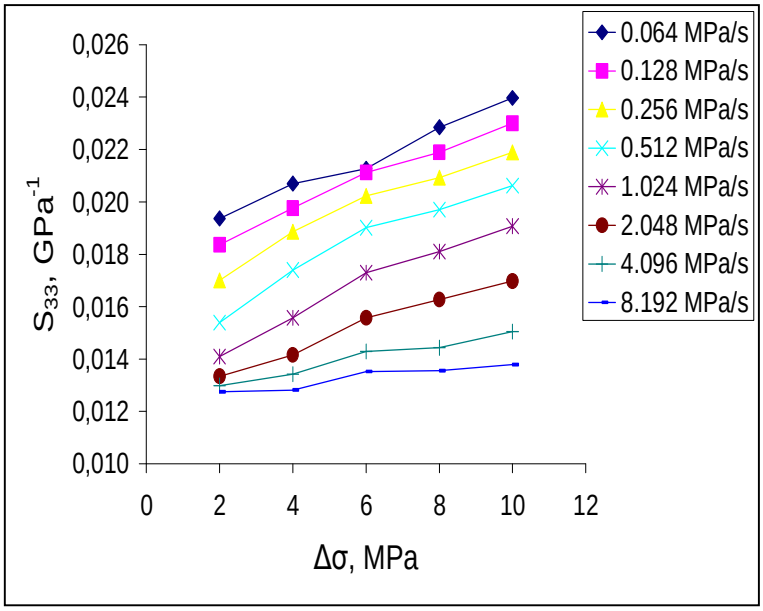

Fig.7.13: S_{33}-Δσ from loops generated using triangular stress waves at eight different loading rates in PZT 5A poled parallel.

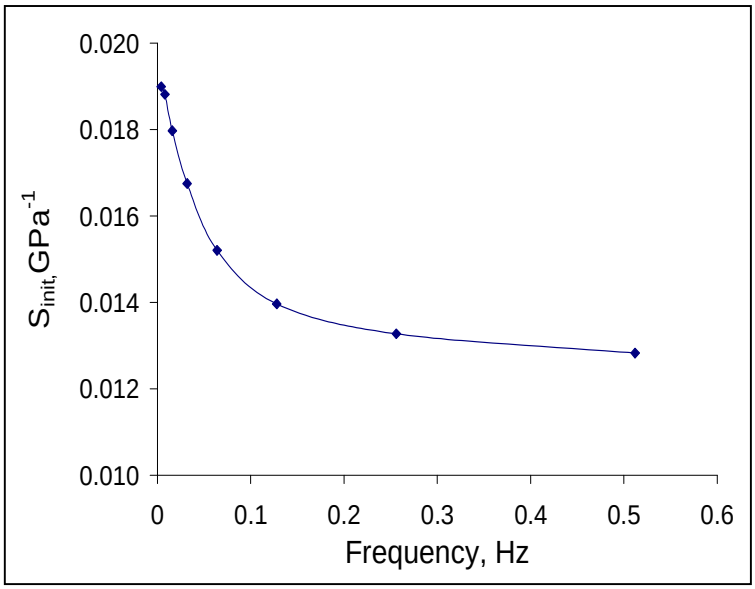

Fig.7.14: the Rayleigh parameter S_{Init} as a function of frequency in PZT 5A poled parallel (from loops generated using triangular stress waves).

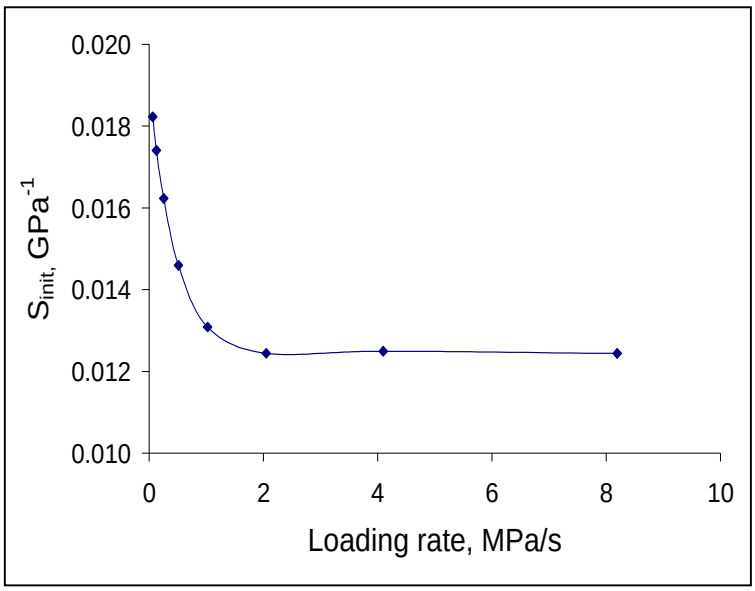

Fig.7.15: the Rayleigh parameter S_{Init} from loops generated as a function of loading rate in PZT 5A poled parallel (from loops generated using triangular stress waves).

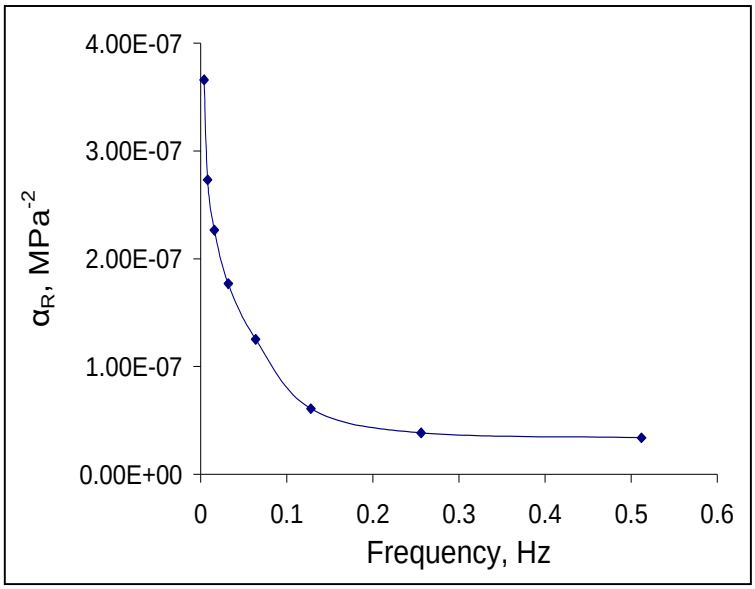

Fig.7.16: the Rayleigh parameter α_R as a function of frequency in PZT 5A poled parallel (from loops generated using triangular stress waves).

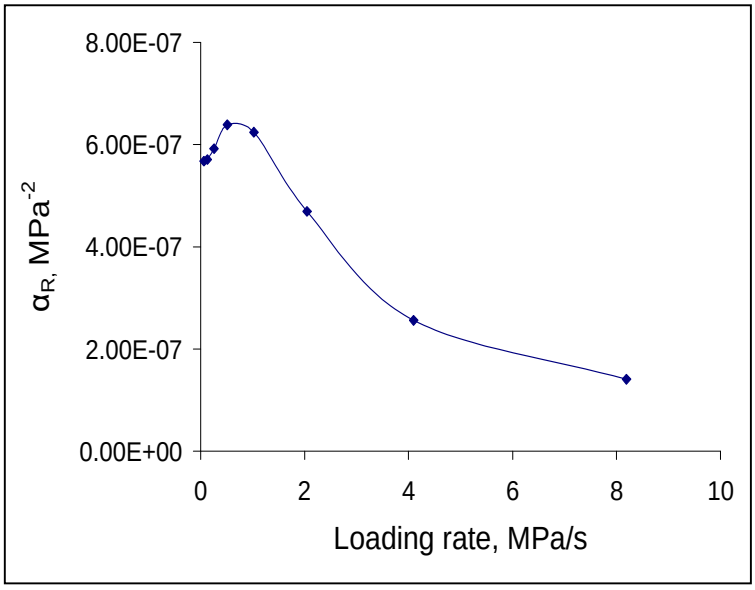

Fig.7.17: the Rayleigh parameter α_R as a function of loading rate in PZT 5A poled parallel (from loops generated using triangular stress waves).

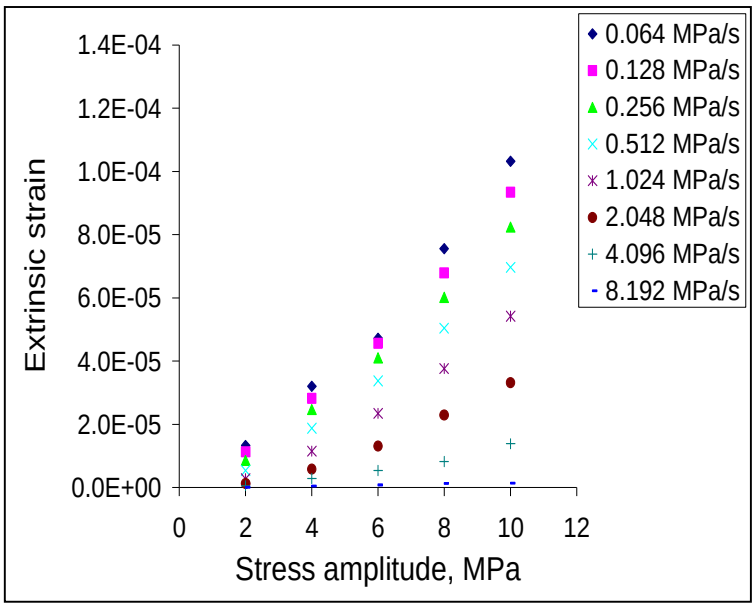

Fig.7.18: extrinsic strain at different stress amplitudes and different loading rates in PZT 5A poled parallel.

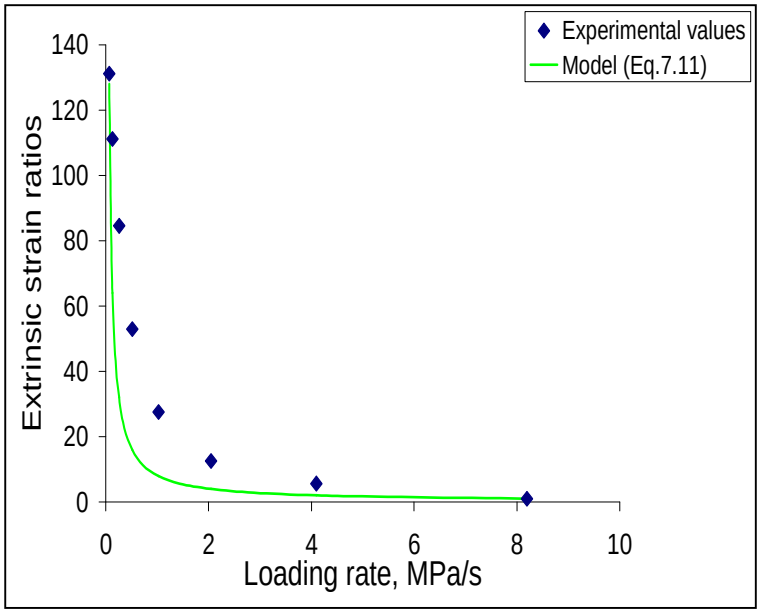

Fig.7.19: comparison experimental values-model at 2 MPa stress amplitude in PZT 5A poled parallel.

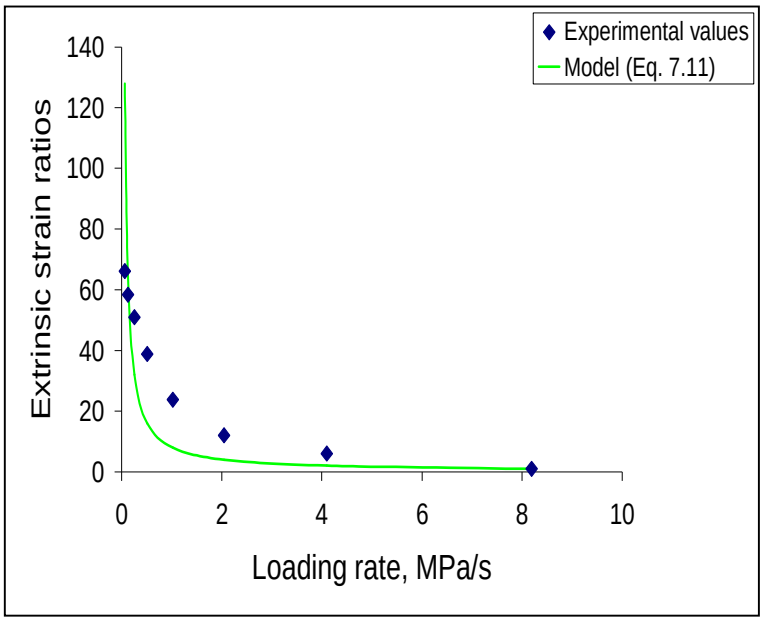

Fig.7.20: comparison experimental values-model at 4 MPa stress amplitude in PZT 5A poled parallel.

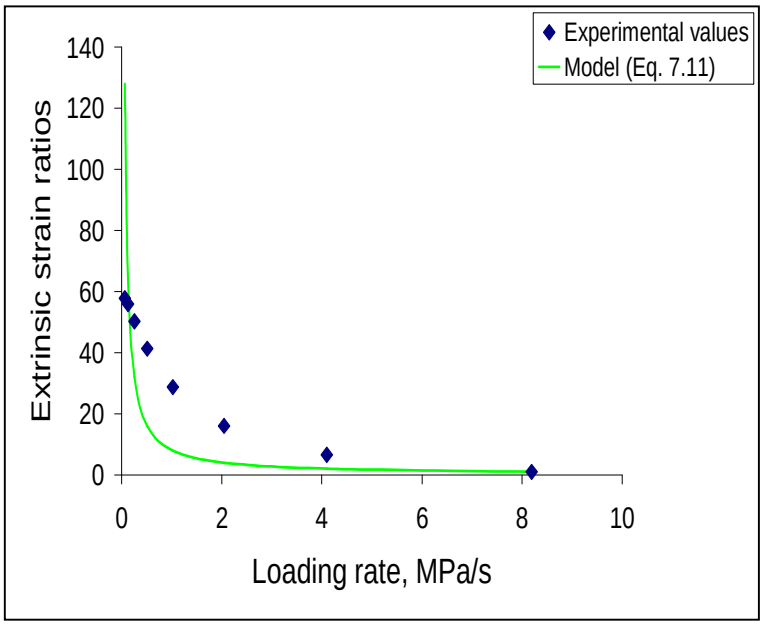

Fig.7.21: comparison experimental values-model at 6 MPa stress amplitude in PZT 5A poled parallel.

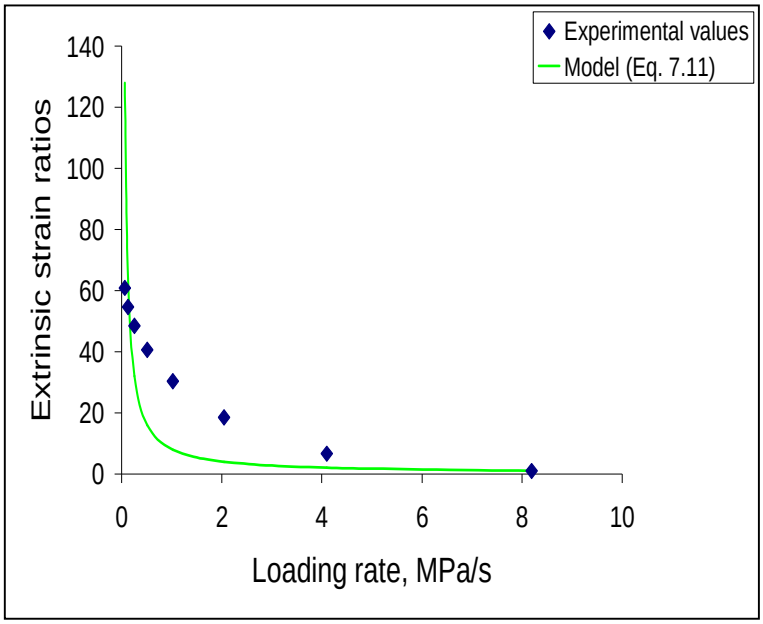

Fig.7.22: comparison experimental values-model at 8 MPa stress amplitude in PZT 5A poled parallel.

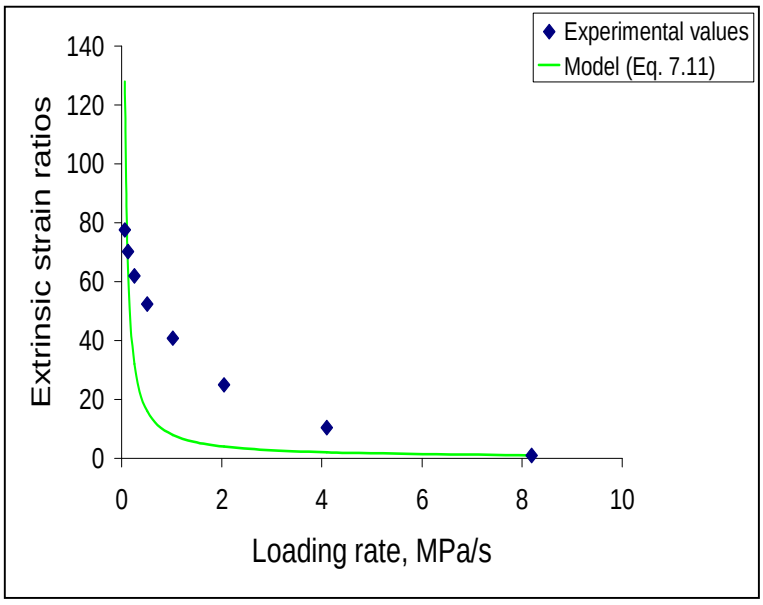

Fig.7.23: comparison experimental values-model at 10 MPa stress amplitude in PZT 5A poled parallel.

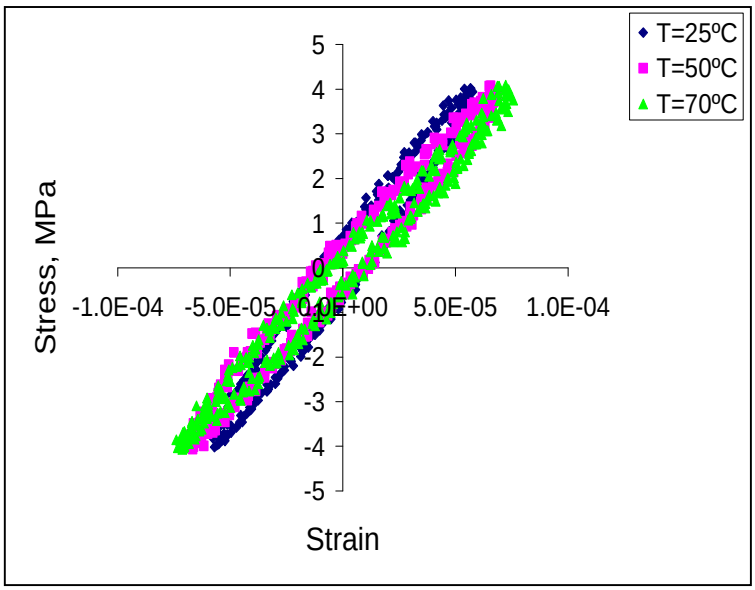

Fig.7.24: examples of loops generated using triangular stress waves at 0.064 MPa/s and different temperature in PZT 5A poled parallel.

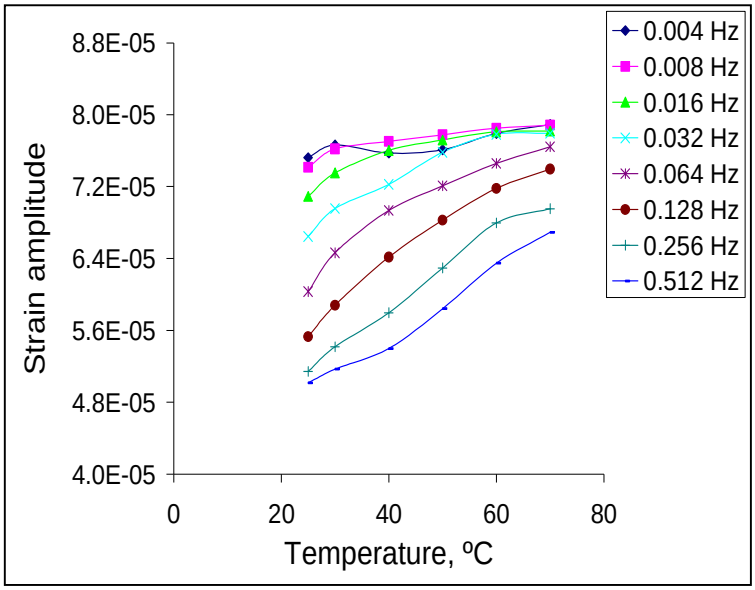

Fig.7.25: strain amplitude of loops generated using triangular stress waves with 4 MPa amplitude and eight different frequencies, at different temperatures in PZT 5A poled parallel.

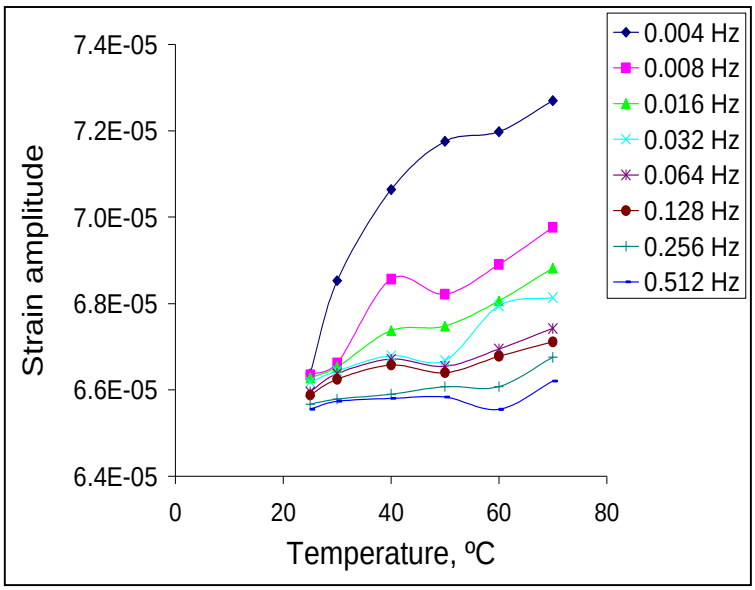

Fig.7.26: strain amplitude of loops generated using triangular stress waves with 4 MPa amplitude and eight different frequencies, at different temperatures in LC.

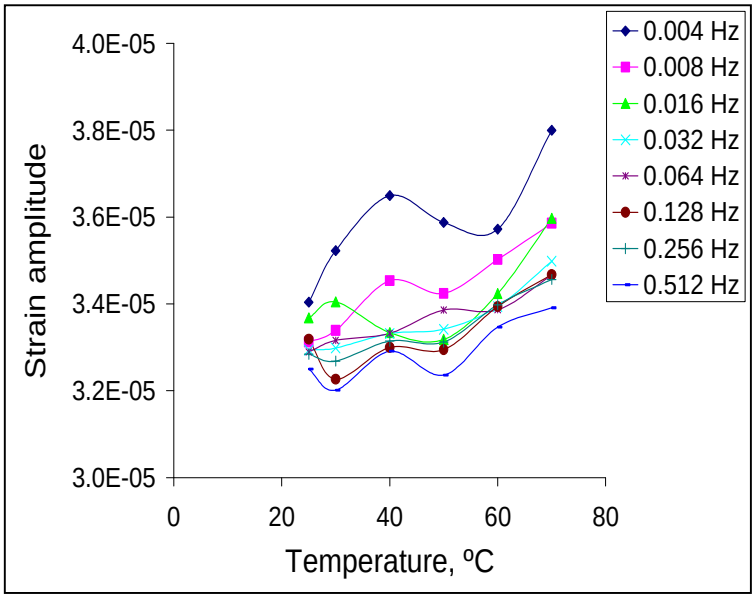

Fig.7.27: strain amplitude of loops generated using triangular stress waves with 4 MPa amplitude and eight different frequencies, at different temperatures in LCC.

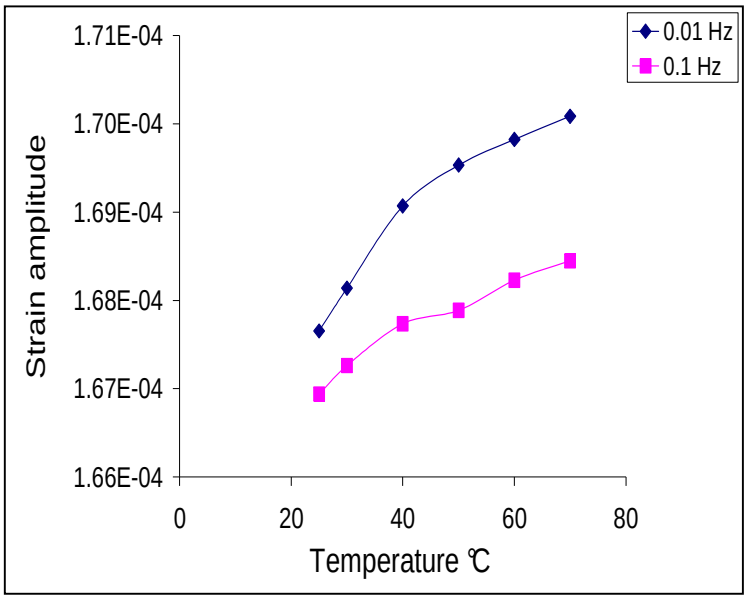

Fig.7.28: strain amplitude of loops generated using triangular stress waves with 10 MPa amplitude and different frequencies, at different temperatures in LC.

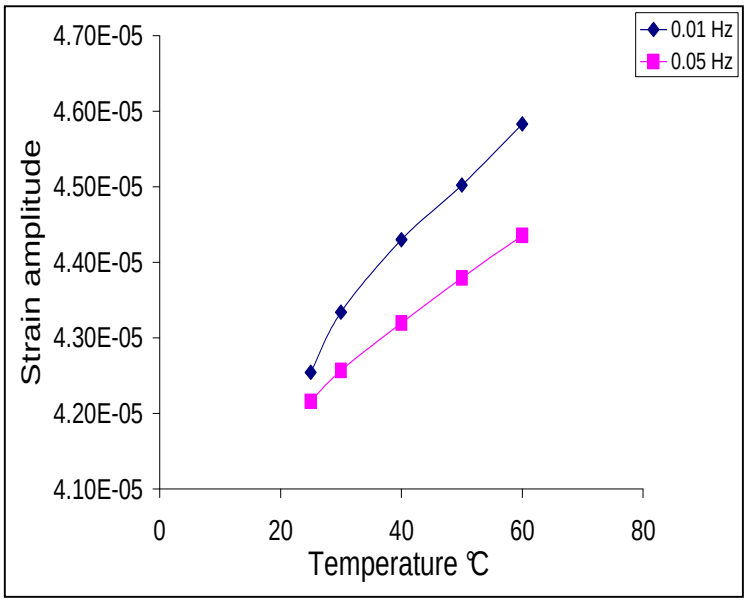

Fig.7.29: strain amplitude of loops generated using triangular stress waves with 10 MPa amplitude and different frequencies, at different temperatures in LCC.

Chapter 8: The effects of loading rate and temperature on compression stress-strain curve

8.1 Introduction

In this chapter the influence of loading rate and temperature on the compression stress-strain curve of ferroelastic/ferroelectric materials is presented. The analysis is based on an alternative experimental technique, which involves studying the compression stress-strain curve at different loading rates and temperatures on the same sample, avoiding data scatter arising from using different specimens. The variations of the coercive stress with loading rate and temperature were measured, identifying a logarithmic and linear functional relationship in the respective cases. The data generated were then used to estimate the activation volume and enthalpy, by applying rate theory. The method could represent an efficient characterization approach in ferroelasticity, where rate and temperature dependence under mechanical loading can be hardly found in the literature.

8.2 Experimental procedure

Compressive stress-strain curve at different loading rates were generated using the Procedure 1 and Procedure 2, while the curves at different temperatures were obtained applying Procedure 3 (see section 4.8 in Chapter 4).

8.2.1 Loading rate dependence

In Fig.8.1 the complete incremental cycles generated by using Procedure 1 (see Chapter 4 for details) are shown for PZT 5A poled parallel at four different loading rates. By considering the maximum points of each cycle and by fitting the data points using a cubic polynomial expression, the stress-strain curves at the four loading rates applied were obtained using only one sample (Fig.8.2). The same procedure was applied on LSFC and the curves shown in Fig.8.3 were generated. The region near the coercive stress shows the highest rate sensitivity (Fig.8.2, 8.3). The

assembled curves show smaller deformation for higher loading rates (Fig.8.2, 8.3). A very good agreement between the stress-strain curve generated incrementally and the ones measured from a single monotonic compression test (see Chapter 5) was observed for LSFC (see Fig.8.4), demonstrating the efficiency of the implemented experimental procedure.

The fitting functions allowed the work hardening to be estimated as a function of the applied stress (Fig.8.5-8.6), in order to get the coercive field at each loading rate, as the stress at which correspond a minimum in the tangent modulus (minimum work hardening). Very similar coercive stress values to the ones obtained from a single test were measured in LSFC (see Fig.5.5 in Chapter 5). In agreement with previous studies [97, 98], the dependence of the coercive stress on the loading rate was found to be of the logarithmic type, in both the compositions (Fig.8.7, 8.8).

A further proof of the validity of the experimental methodology comes from the results shown in Fig.8.9, where it can be observed that the stress-strain trends at different loading rates are totally reproducible upon repeated cycles. A good match is verified also in the unloading portion and in the irreversible strain. Along with [102], higher strain recovery (back switching) can be observed at slower rates, leading to smaller irreversible strains corresponding to lower loading rates.

An interesting phenomenon related to the presence of the back stresses (never reported in the literature) can be observed again in Fig.8.9. After the cycle indicated in the graph as "15000 N/min 1st", the loading rate was reduced again to 1500 N/min, to check the reproducibility with the previous cycle at the same rate (1500 N/min 1st). A strain recovery was observed at the beginning of the loading portion, determining a negative slope (negative tangent modulus) at the beginning of the stress-strain curve, (see Fig.8.9 test indicated with "1500 N/min 2nd"). This effect happened also in the following tests, labelled in Fig.8.9 with "1500 N/min 3rd", where the reproducibility at 1500 N/min was checked again. The curves generated with the same loading rate are completely superimposed, evidencing a strong memory effect. The validity of the developed technique relies on the described reproducibility.

Results obtained with Procedure 2 are shown in Fig.8.10-8.12. The difference between the two curves in Fig.8.12 is not clearly detectable, as the loading rates used were very close each other. The advantage of this procedure is represented by the possibility of generating also the unloading portion at different rates. The main drawback comes from the difficulty in using more than two different loading rates.

All the results obtained confirm that domain switching is enhanced at small loading rates. The reason for such behaviour arises from the thermally activated nature of domain wall movement. It is therefore appropriate to apply a rate model based on thermally activated phenomena in order to quantify the loading rate sensitivity. The procedure developed in [45] for the ferroelectric case and formulated in Chapter 3 for the ferroelastic case will be followed.

8.2.2 Application of rate theory

The curves obtained at different rates on only one sample are considered to be obtained by testing identical samples at different loading rates, assuming that a variation of the loading rate does not produce significant changes in the microstructure (constancy of the pre-exponential term) and in the internal stress σ_{in}. Based on these assumptions, the model developed in Chapter 3 has provided the following expression:

$$\left[\frac{k_B T}{V_a}\right] = \frac{1}{2}\frac{\partial \sigma_{app}}{\partial \ln \dot{\varepsilon}} \tag{8.1}$$

It should be noted that the most appropriate way of generating stress-strain curve at different rates would have been performing the experiments in strain control mode, which was not possible in the experimental equipment available. Therefore, the only way of obtaining the strain rate was from the differentiation of the strain-time curves shown in Fig.8.13, 8.17, generated using Procedure 1. The strain rate as a function of strain is plotted in Fig.8.14 and Fig.8.18 for PZT 5A and LSFC respectively.

Plots $\tau_{app} - \ln \dot{\varepsilon}$ were generated at different strain levels, using the strain rate extrapolated at each strain using the plots in Fig.8.14 and Fig.8.18. In compression

loading conditions, the maximum shear stress τ_{app} is half of the normal stress σ_{app}. Plots $\tau_{app} - \ln\dot{\varepsilon}$ show a linear trend (Fig.8.15, 8.19) and from the slopes the activation volume was estimated for the entire range of strain in the curves generated in both the compositions tested (Fig.8.16, 8.20).

Minimum value of the activation volume occurs in the coercive stress region, where the materials exhibit the highest rate sensitivity. The values calculated in this region are in a very good agreement with the ones obtained from the creep tests (Fig.8.16, 8.20). In PZT 5A at the coercive stress, activation volume was estimated as 7.49 nm^3 from creep test and 2.44 nm^3 from the rate experiment. In LSFC at the coercive stress activation volume was found to be 0.81 nm^3 in creep experiments and 0.91 nm^3 in rate experiments. Significant discrepancy with the creep tests can be observed at very small strain in both the compositions, arising probably from the different character of the two tests performed. The increasing of the activation volume above the coercive stress is higher compared with the creep tests, probably because the curves were generated using odd functions (cubic power functions) having an inflection point at the coercive stress, determining symmetric values of the activation volume for smaller and higher stresses than the coercitivity (clearly visible in Fig.8.20). The comparison between the two compositions (Fig.8.21) confirms the results shown in Chapter 6. Higher activation volume indicates smaller characteristic times and faster domain switching kinetic.

8.2.2 Temperature dependence

The effect of temperature has been studied in PZT 5A poled parallel by applying the Procedure 3 (see Chapter 4). Stress-strain curves have been generated on the same sample at five different temperatures (T=30, 40, 50, 60, 70ºC). Room temperature was not included in order to speed up the cooling process. The curves in Fig.8.22, 8.23 were generated using only one loading rate (5000 N/min), in order to study solely the effect of temperature.

In general, with increasing temperature, the ferroelastic phase transition temperature is approached and the distortion of the unit cell reduces, producing compressive

deformations in poled samples with prevalence of tetragonal structure such as PZT 5A. In Fig.8.22 the origin of the curve at 30ºC was placed at (0,0) for practical reason. The curves at higher temperatures start at the strain values experienced by the samples at the different temperatures, before the load was applied. For simplicity the origin of all the stress-strain curves have then been placed at (0,0) as shown in Fig.8.23.

It can be observed that at higher temperature the saturation strain becomes smaller, in analogy with the electrical case, where the P-E loops show a decreasing of saturation polarization with increasing temperature [45]. All the curves cross in a particular point (σ_{cross}, ε_{cross}), whose strain can be produced with the same applied stress at all the temperatures (Fig.8.23). Below the crossing point, the temperature reduces the stress needed to achieve a fixed amount of strain. Above the crossing point, if the temperature is increased, higher stresses are needed to produce a certain level of strain (Fig.8.23). This is reflected also in the work hardening and in the strain rate curves, evidencing the influence of the temperature on domain switching kinetic (Fig.8.24, 8.25). Referring to the latter, it is worth noting at stresses below σ_{cross}, increasing the temperature the strain rate increases, while in correspondence of stresses higher than σ_{cross}, the strain rate decreases by increasing the temperature (Fig.8.25). The ranges of the applied field where the nucleation (or the growth) prevails have not been clearly established yet. The effect noticed in the strain rate is probably related to the predominance of one of the two mechanisms mentioned, which may change below and above the crossing point.

By increasing the temperature a linear decay of the coercive stress was measured (Fig.8.26) in agreement with previous studies [106]. This is due to a reduction in the spontaneous distortion of the unit cell at higher temperatures. It is evident that the temperature significantly influences the deformation behaviour of ferroelastic materials, supplying part of the energy necessary for the domain switching process. In previous investigations it was shown that the energy required for the formation of critical nuclei is mainly provided by the work done by the applied electric field [45]. In order to quantify the amount of energy supplied by the thermal fluctuations, the activation enthalpy can be estimated. The approach presented in [45] has been adapted for the ferroelastic case developing the model presented in Chapter 3.

From the relationship:

$$\dot{\varepsilon} = \dot{\varepsilon}_0 \exp\left[-\left(\frac{\Delta H}{k_B T}\right)\right] \tag{8.2}$$

it follows that:

$$\ln\dot{\varepsilon} = \ln\dot{\varepsilon}_0 - \frac{\Delta H}{k_B T} \tag{8.3}$$

The effect of the temperature can be quantified by estimating the activation enthalpy ΔH under conditions of constant microstructure. In P-E loops, constancy of microstructure conditions at the coercive field are more readily verified by a constantly null value of the polarization in correspondence of the coercive field for every frequency and temperature at which the P-E loops are generated [45]. The difficulty of generating tension-compression loops in the mechanical case determines the impossibility of producing experimental plots, where the coercive stress occurs always at the same value of the strain, as shown in Fig.8.27. Regardless, it is assumed that the density of nuclei is constant at the coercive stress, for all the temperatures and the loading rates applied. Therefore, by partially differentiating Eq.8.3 respect with $(1/T)$ at constant coercive stress value, the following relationship can be obtained:

$$\left(\frac{\partial \ln\dot{\varepsilon}}{\partial(1/T)}\right)_{\sigma_C} = -\frac{\Delta H}{k_B} \tag{8.4}$$

The previous equation states that the activation enthalpy can be obtained by measuring the variation of the strain rate consequent to a change in temperature at the coercive stress σ_C, which is assumed to be the most appropriate thermodynamical conditions to perform the analysis, as for all the possible loading rates all the compositions display a minimum work hardening and/or a maximum strain rate.

Because the coercive stress and the strain rate both change with the loading rate and temperature, from the stress-strain curves obtained at the different temperature with five different loading rates (Fig.8.28-8.32), a master plot $\sigma_C - \ln\dot{\varepsilon}$ at different temperatures was generated (Fig.8.33). Once again the strain rate was not externally

controlled, but obtained indirectly from the derivation of the strain-time curves. The proposed method allowed also the activation volume to be estimated at different temperature.

From the master plot, the activation enthalpy was estimated through Eq.8.4 for six values of the coercive stress (Fig.8.33), obtaining higher activation enthalpy in correspondence of smaller coercive stresses (Fig.8.34). The highest value of the activation enthalpy measured (0.88 eV) is 5.5 times higher than the ones measured in the ferroelectric case (0.16 eV) [45]. This mentioned discrepancy, the dependence of the activation enthalpy on the choice of the coercive stress, the dubious constancy of microstructure in the present experimental conditions and the particular strain rate dependence on the temperature (Fig.8.25) are all factors of uncertainty for the value of ΔH measured.

8.3 Conclusions

Alternative experimental procedures were developed to study the influence of loading rate and temperature on ferroelastic switching. Compression stress-strain curves at different rates and temperatures were generated, evidencing similar trends previously found in the literature for the analogous ferroelectric case. By applying rate theory, the rate dependence was quantified by estimating the rate sensitivity and the activation volume for different strain levels. A reasonably good agreement with the values obtained from the creep experiment was found in the coercive stress region, identifying the activation volume as a fundamental physical parameter, which controls the domain switching time dependence. The influence of the temperature was quantified by calculating the activation enthalpy, whose estimation requires an improved experimental technique to reduce the uncertainty on the values obtained.

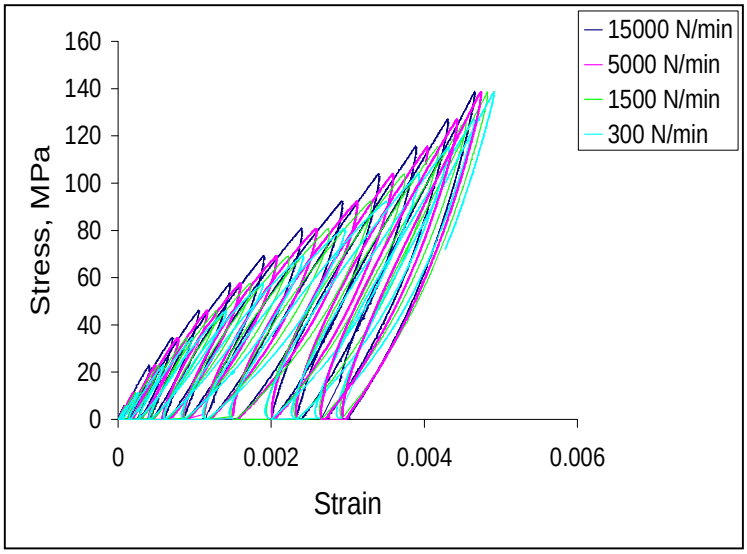

Fig.8.1: incremental cycles at different loading rate in PZT 5A poled parallel using Procedure 1.

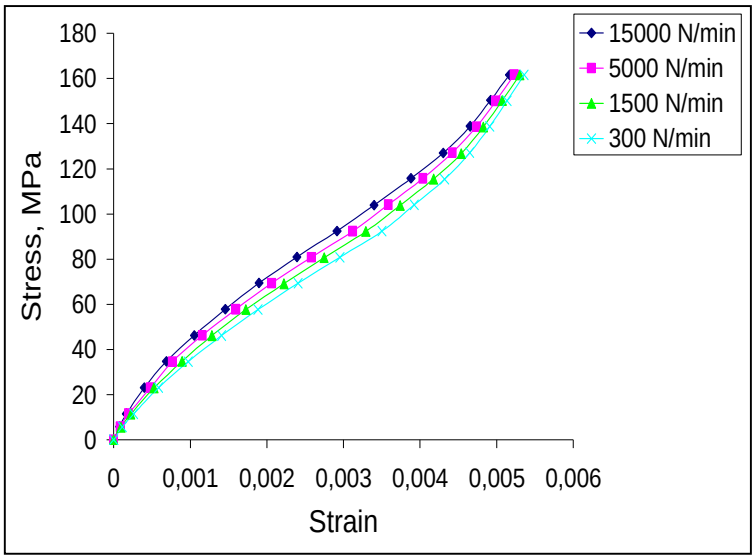

Fig.8.2: fitting of data points at different loading rate generated by fitting the data obtained using Procedure 1 in PZT 5A poled parallel.

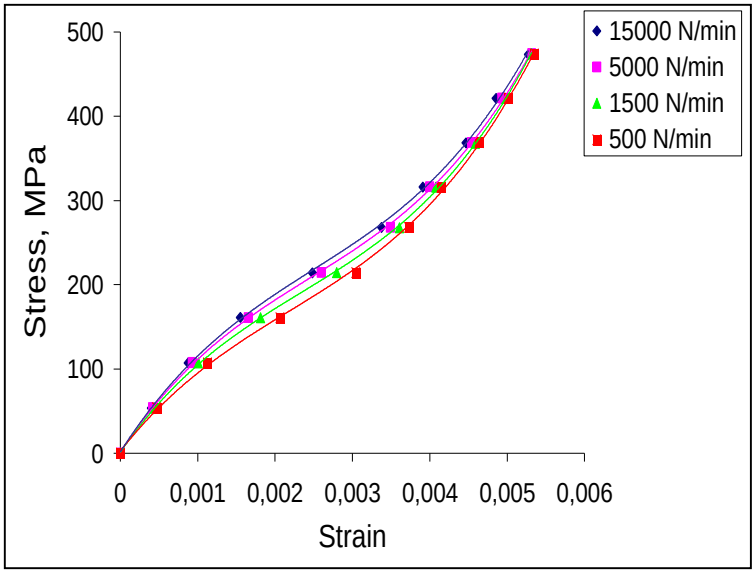

Fig.8.3: fitting of data points at different loading rate generated by fitting the data obtained using Procedure 1 in LSFC.

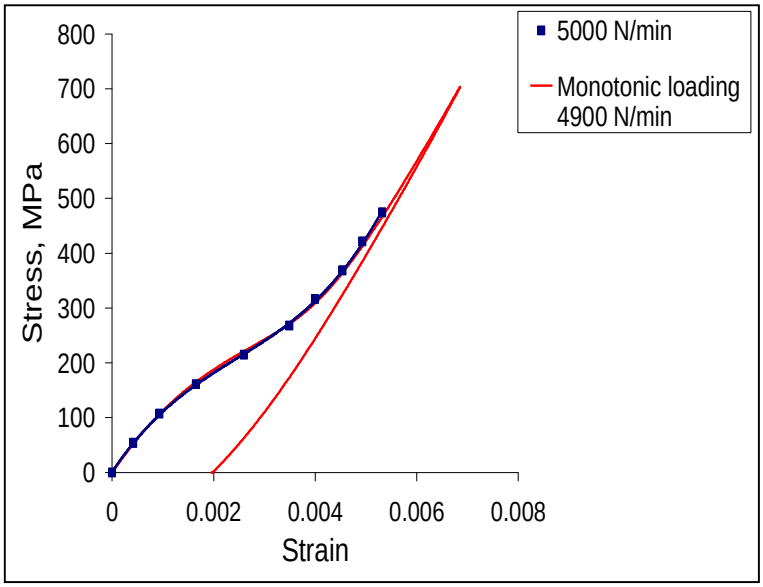

Fig.8.4: comparison between stress-strain curves generated with Procedure 1 and with monotonic loading in LSFC.

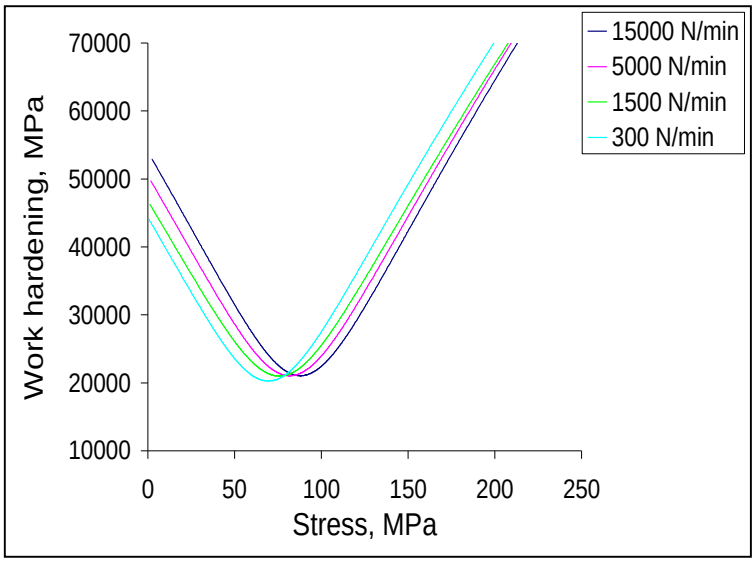

Fig.8.5: work hardening as a function of stress at different loading rate in PZT 5A poled parallel.

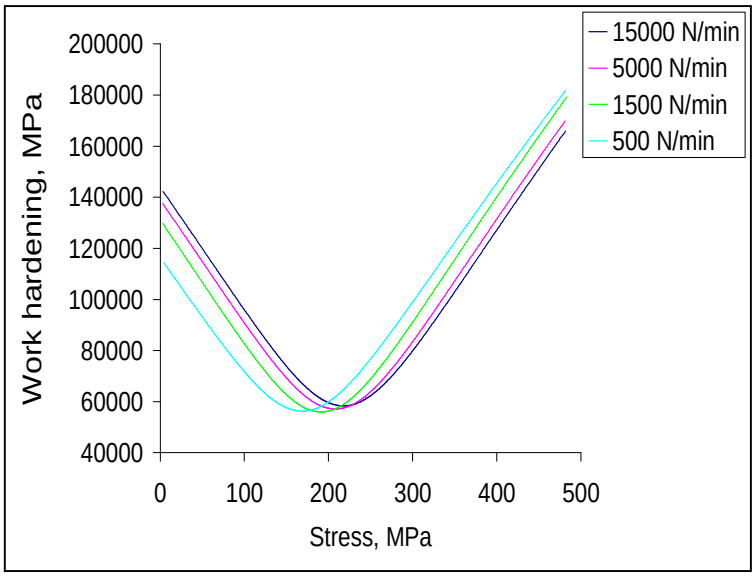

Fig.8.6: work hardening as a function of stress at different loading rate in LSFC.

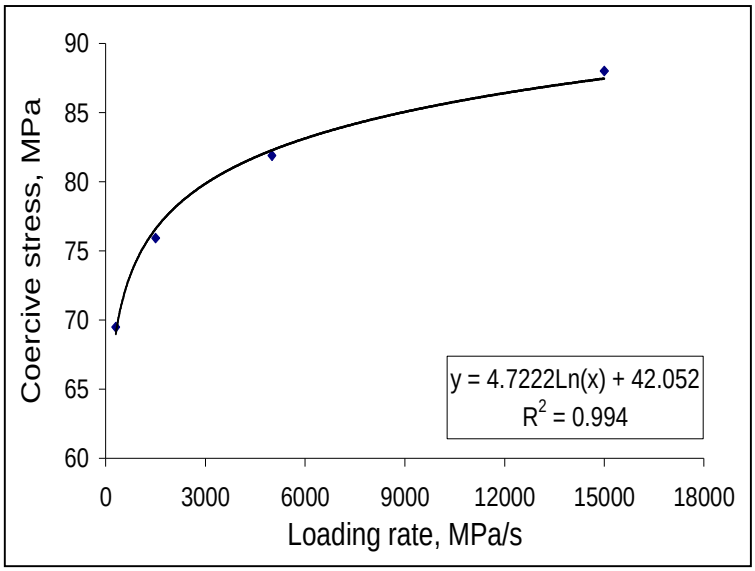

Fig.8.7: coercive stress as a function of loading rate in PZT 5A poled parallel.

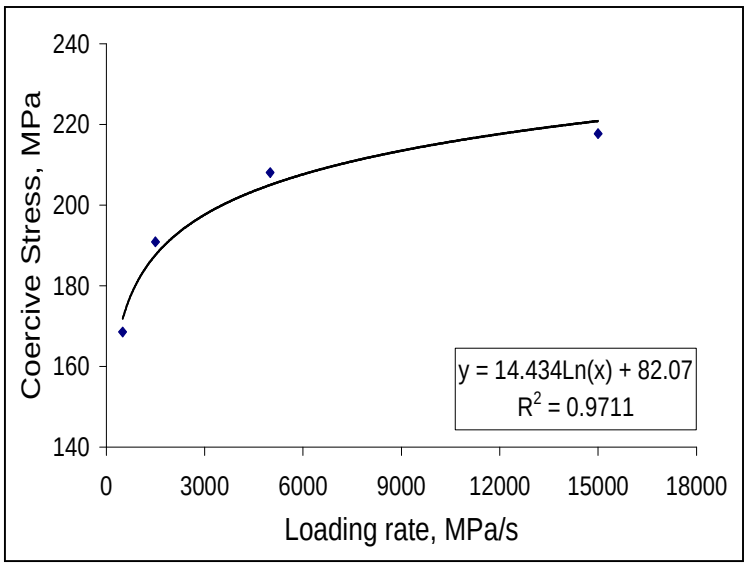

Fig.8.8: coercive stress as a function of loading rate in LSFC.

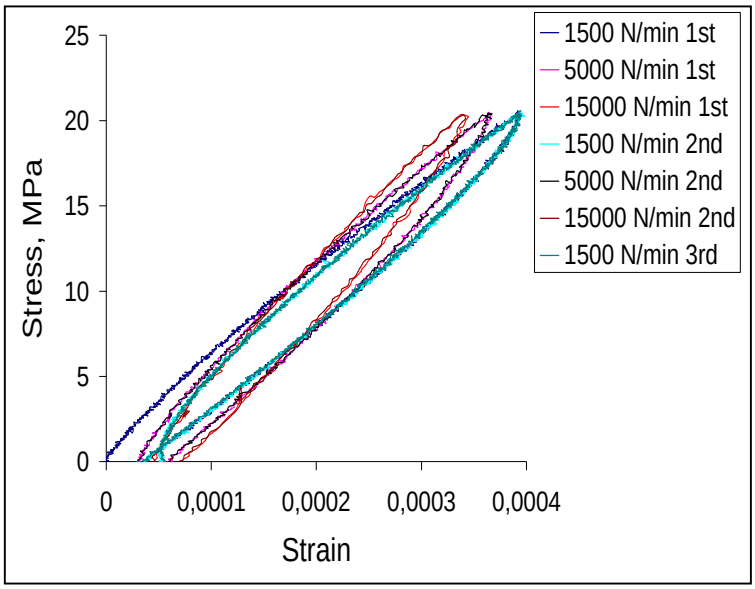

Fig.8.9: reproducibility at different loading rate in PZT 5A poled parallel (Procedure 1).

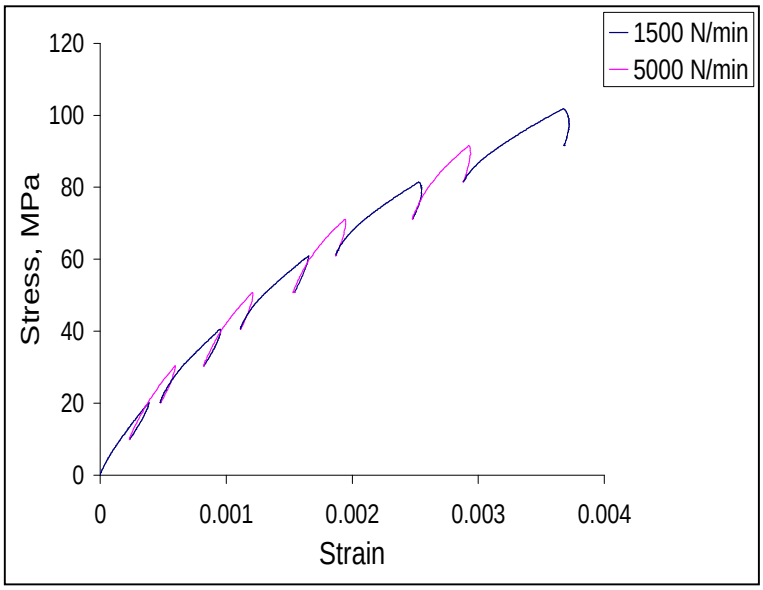

Fig.8.10: stress-strain loading rate dependence in PZT 5A poled parallel using Procedure 2.

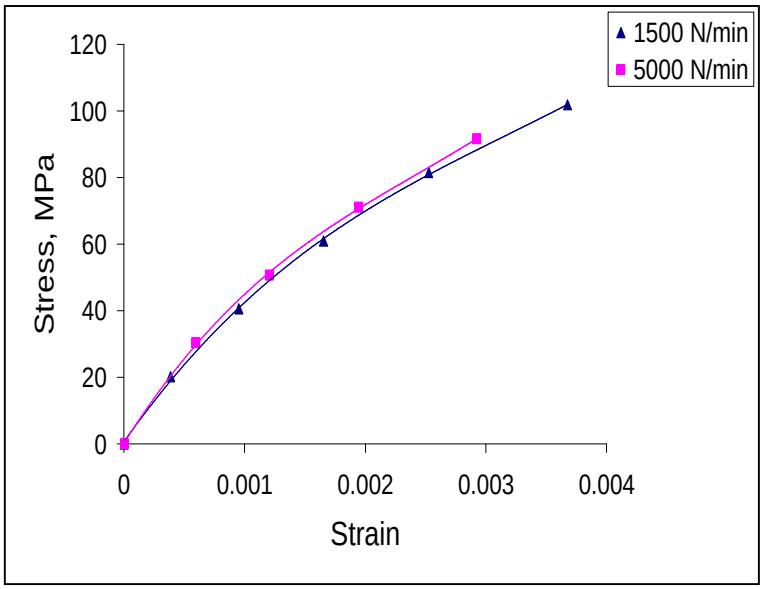

Fig.8.11: stress-strain data points at two different loading rates in PZT 5A poled parallel using Procedure 2.

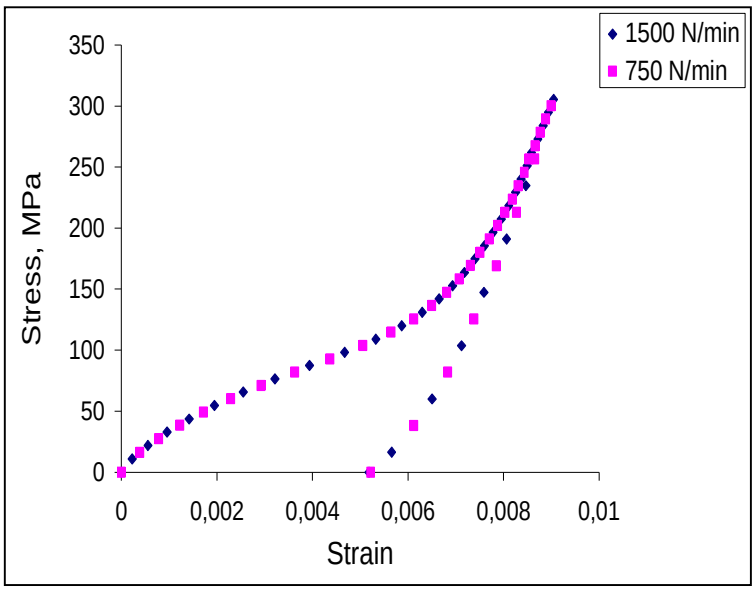

Fig.8.12: stress-strain data points at two different loading rates in PZT 5A poled parallel using Procedure 2.

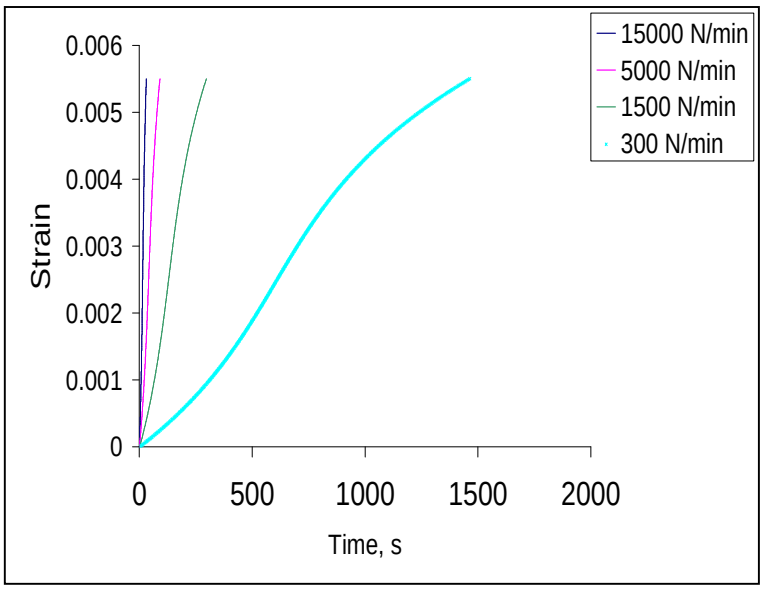

Fig.8.13: strain –time plots at different loading rates in PZT 5A poled parallel using Procedure 1.

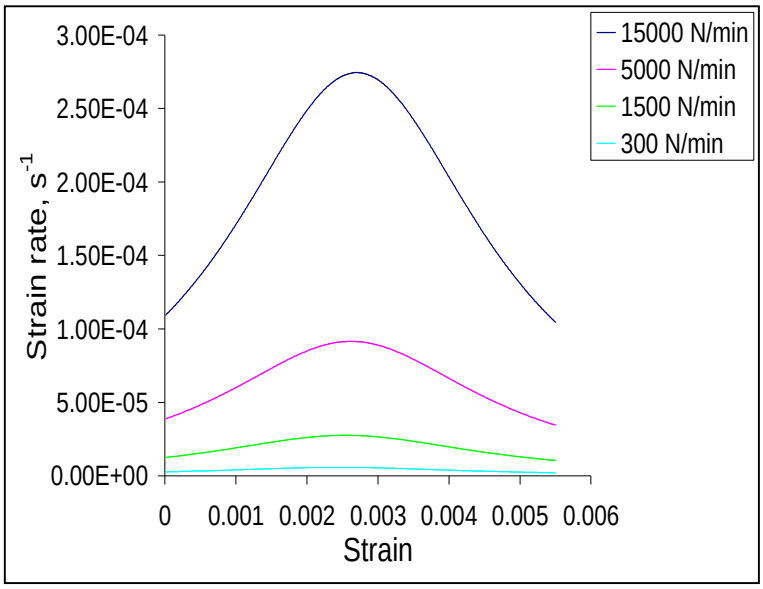

Fig.8.14: strain rate as a function of strain at different loading rates in PZT 5A poled parallel using Procedure 1.

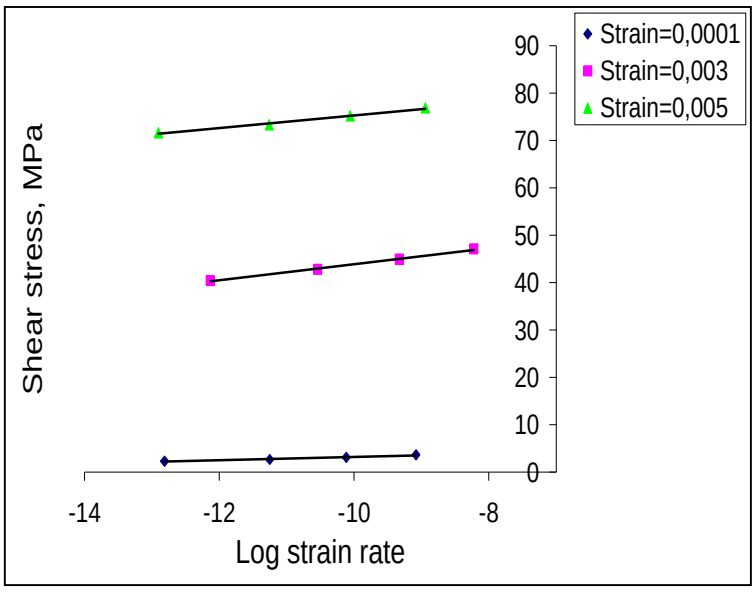

Fig.8.15: examples of $\tau_{app} - \ln \dot{\varepsilon}$ plots at three different strain levels in PZT 5A poled parallel.

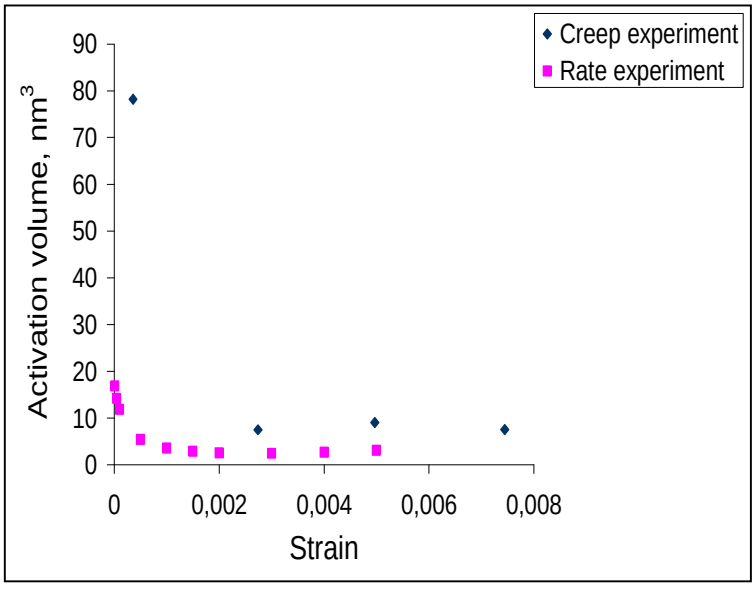

Fig.8.16: activation volume comparison with creep experiment as a function of strain in PZT 5A poled parallel.

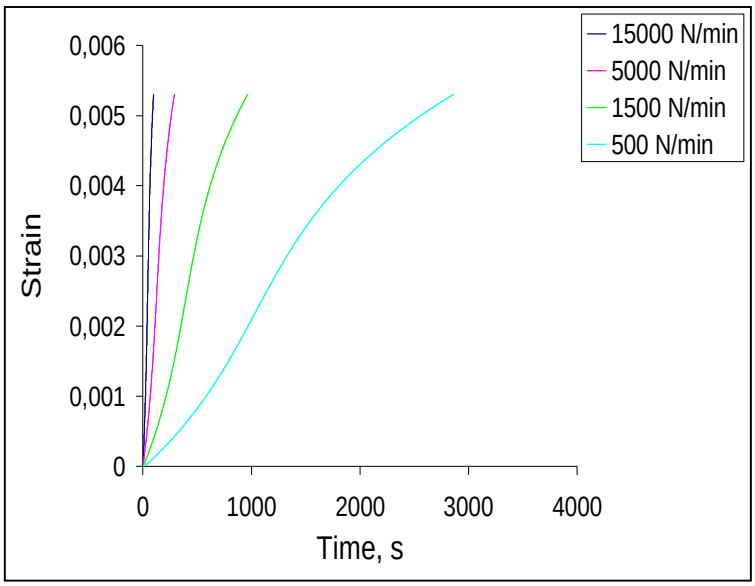

Fig.8.17: strain –time plots at different loading rates in LSFC using Procedure 1.

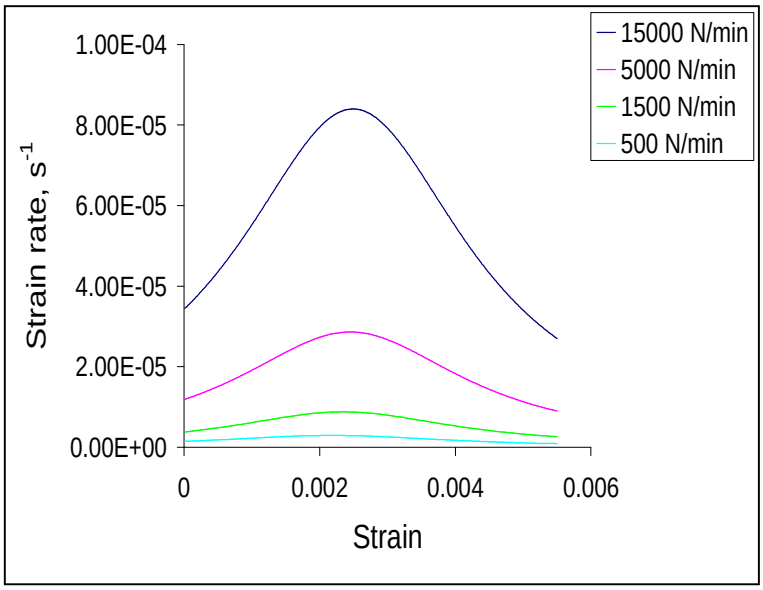

Fig.8.18: strain rate as a function of strain at different loading rates in LSFC poled parallel using Procedure 1.

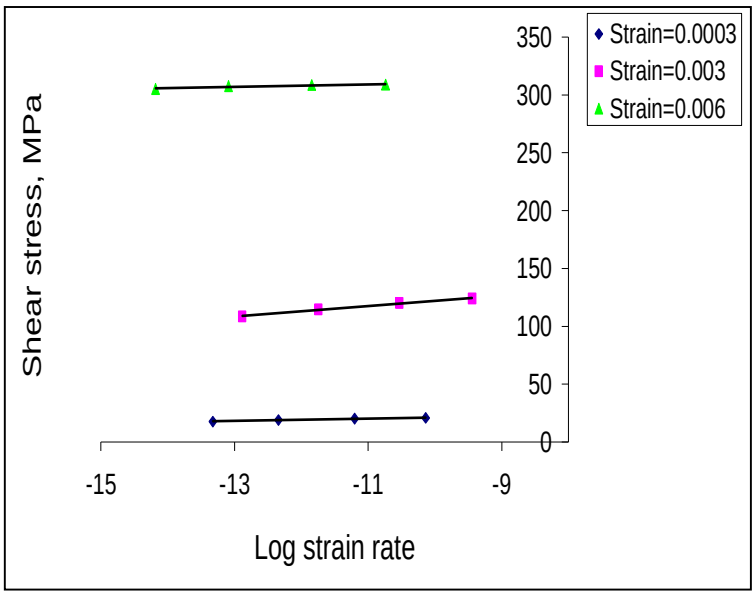

Fig.8.19: examples of $\tau_{app} - \ln \dot{\varepsilon}$ plots at three different strain levels in LSFC.

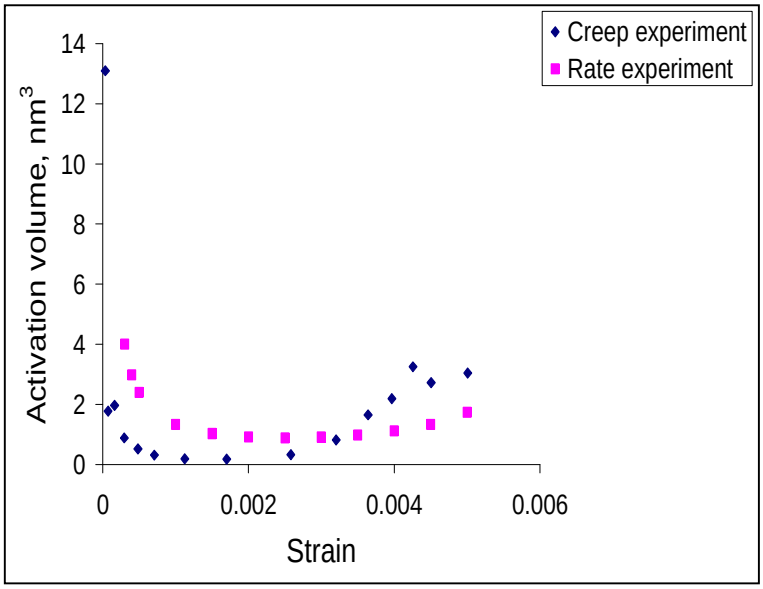

Fig.8.20: activation volume comparison with creep experiment as a function of strain in LSFC.

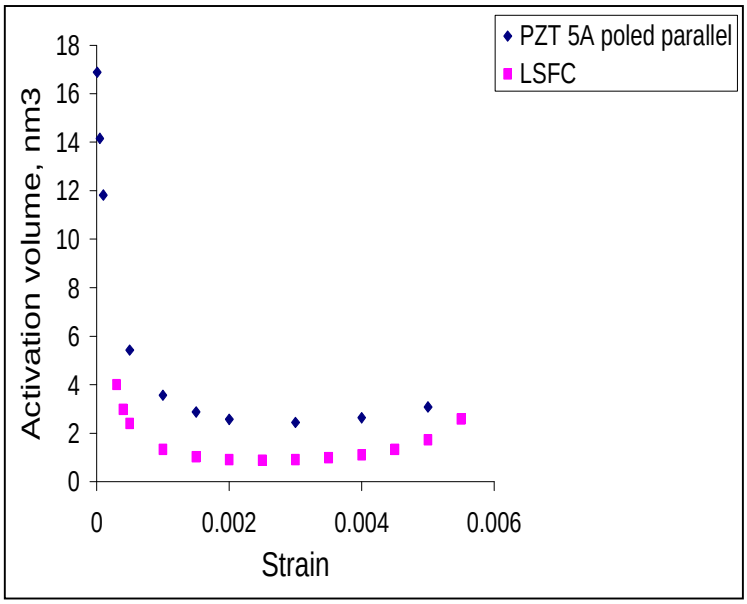

Fig.8.21: activation volume comparison in PZT 5A poled parallel and LSFC.

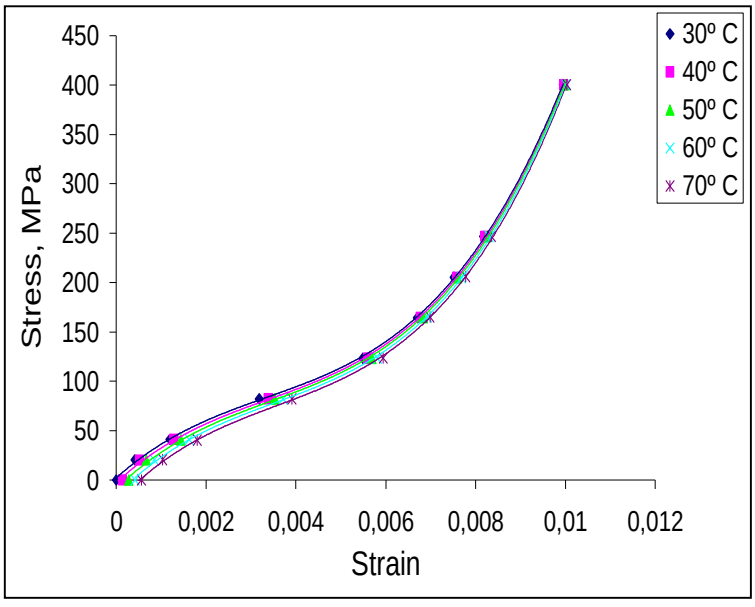

Fig.8.22: stress-strain loading curve at different temperature at 5000 N/min in PZT 5A poled parallel using Procedure 3.

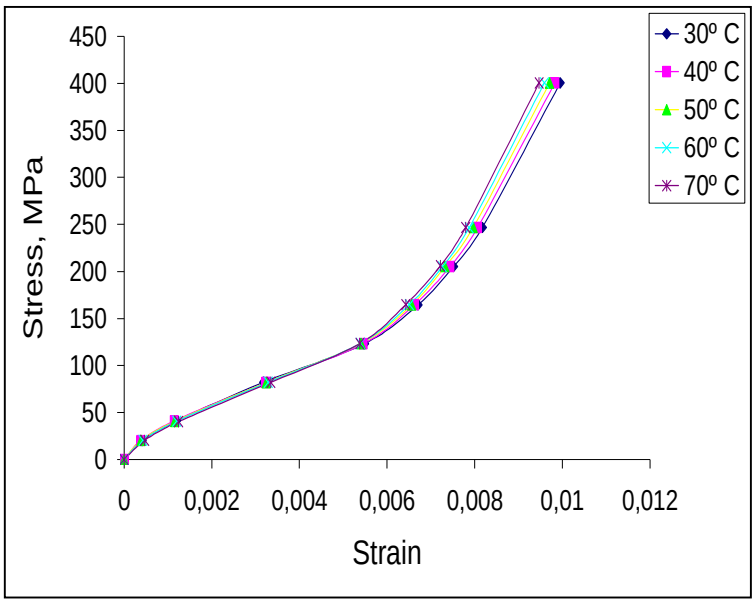

Fig.8.23: stress-strain loading curve at different temperature at 5000 N/min in PZT 5A poled parallel (same origin).

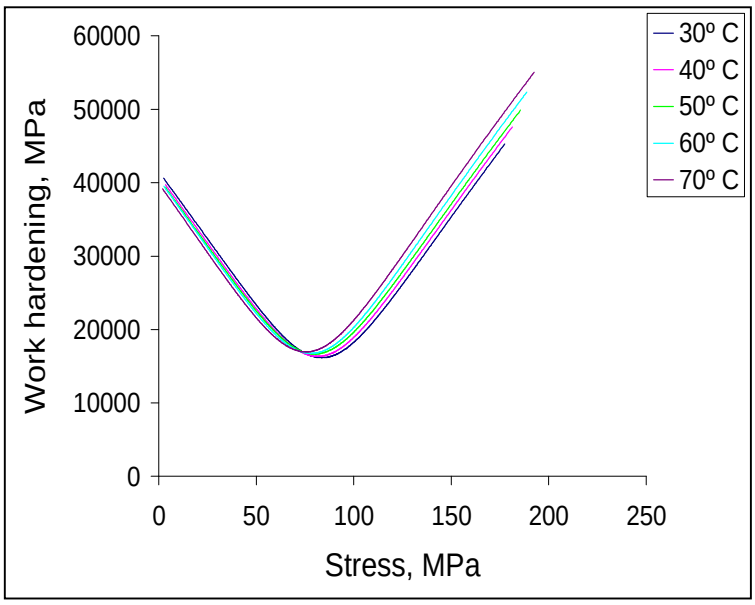

Fig.8.24: work hardening as a function of stress at different temperature in PZT 5A poled parallel (5000 N/min).

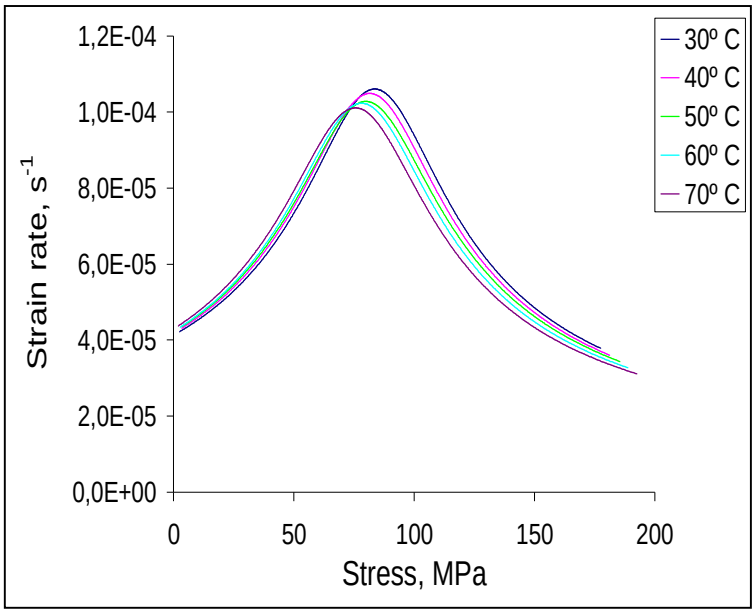

Fig.8.25: strain rate as a function of stress at different temperature in PZT 5A poled parallel (5000 N/min).

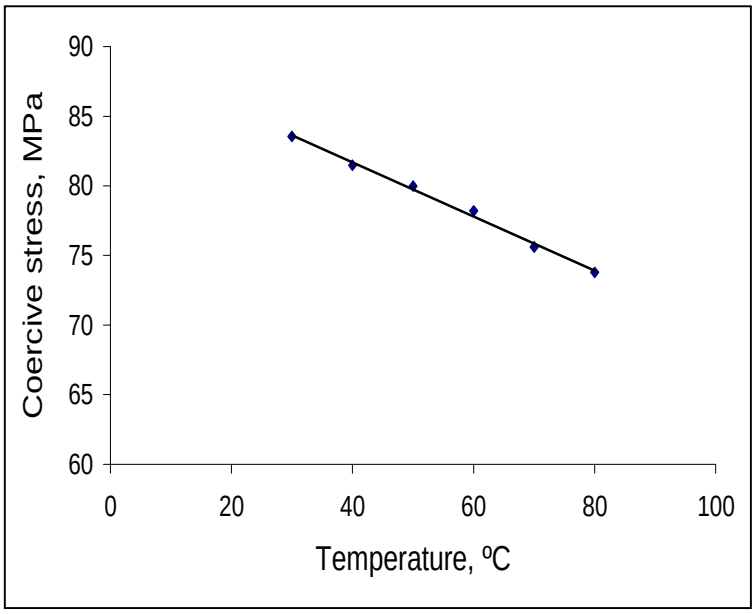

Fig.8.26: coercive stress as a function of temperature in PZT 5A poled parallel.

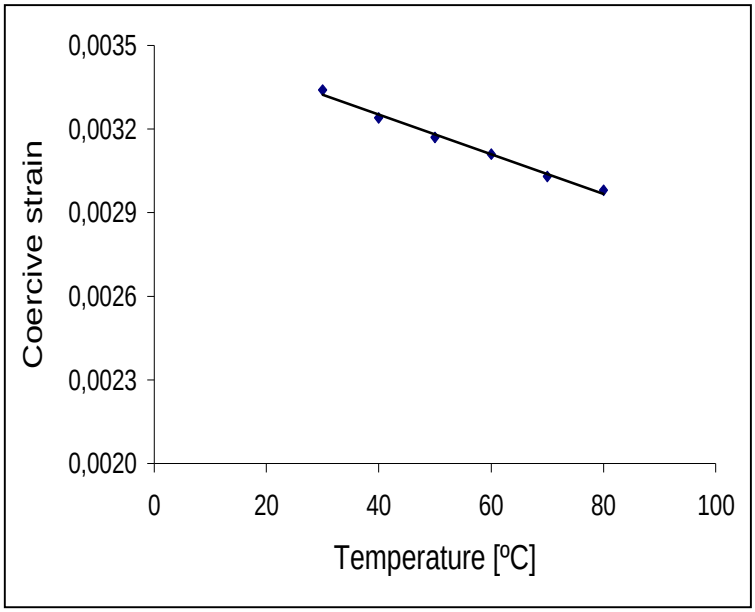

Fig.8.27: coercive strain as a function of temperature in PZT 5A poled parallel.

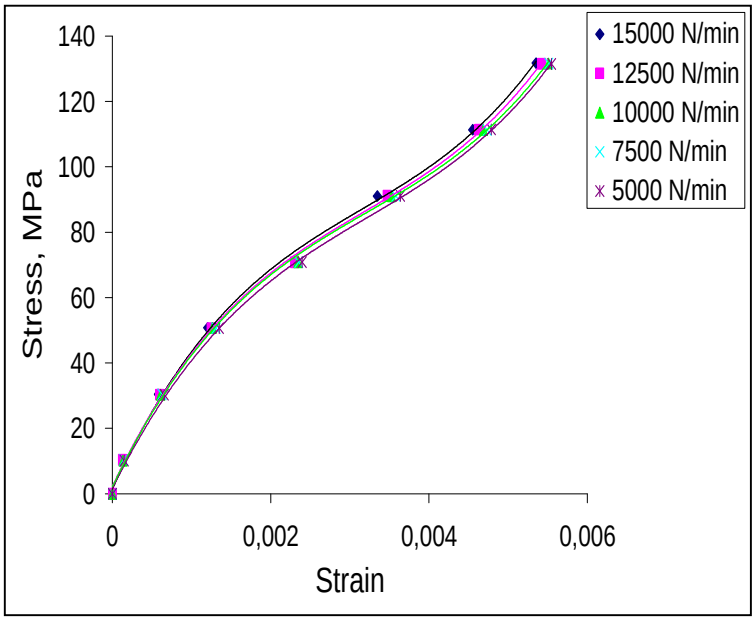

Fig.8.28: stress-strain curve at different loading rate at T=30ºC in PZT 5A poled parallel.

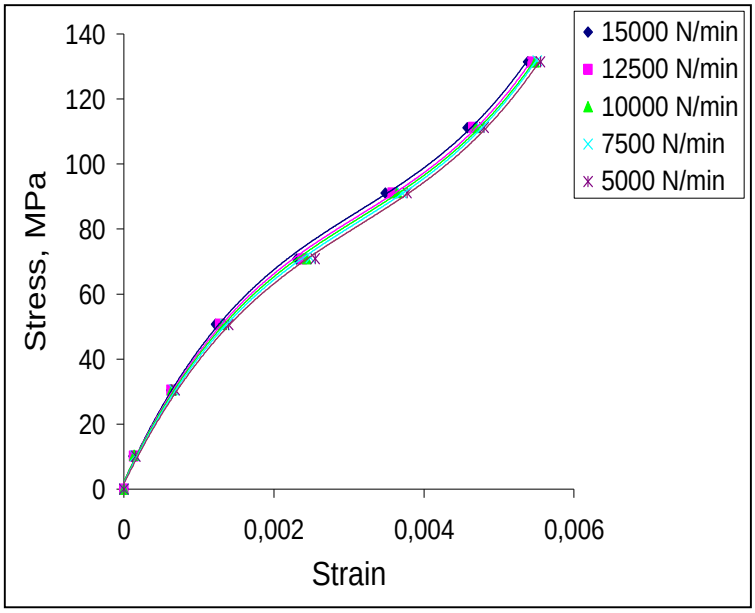

Fig.8.29: stress-strain curve at different loading rate at T=40°C in PZT 5A poled parallel.

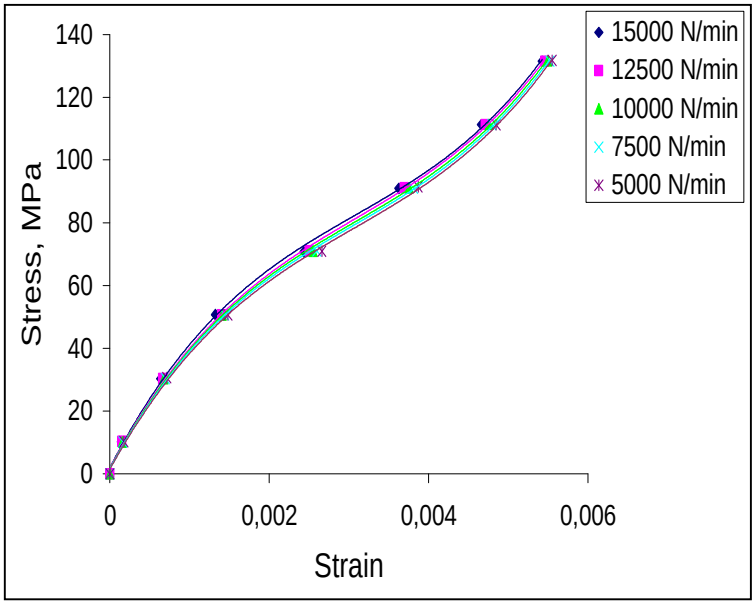

Fig.8.30: stress-strain curve at different loading rate at T=50°C in PZT 5A poled parallel.

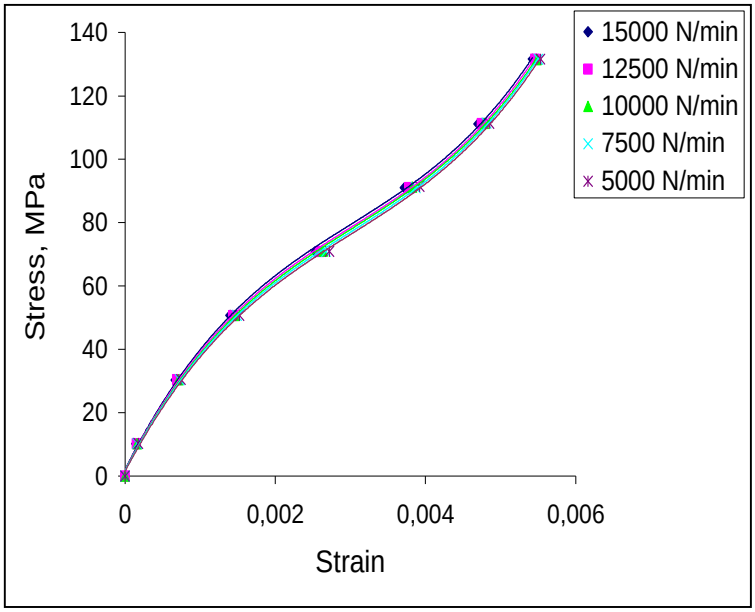

Fig.8.31: stress-strain curve at different loading rate at T=60ºC in PZT 5A poled parallel.

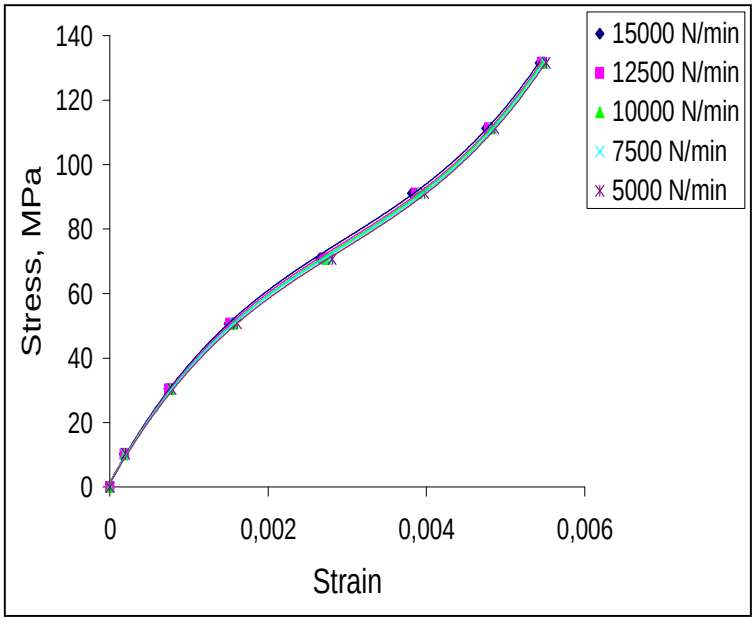

Fig.8.32: stress-strain curve at different loading rate at T=70ºC in PZT 5A poled parallel.

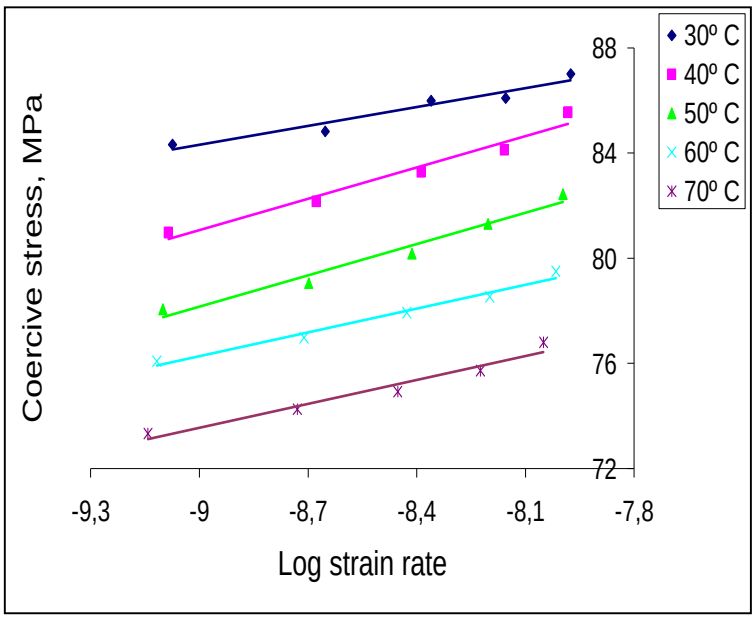

Fig.8.33: master plot in PZT 5A poled parallel.

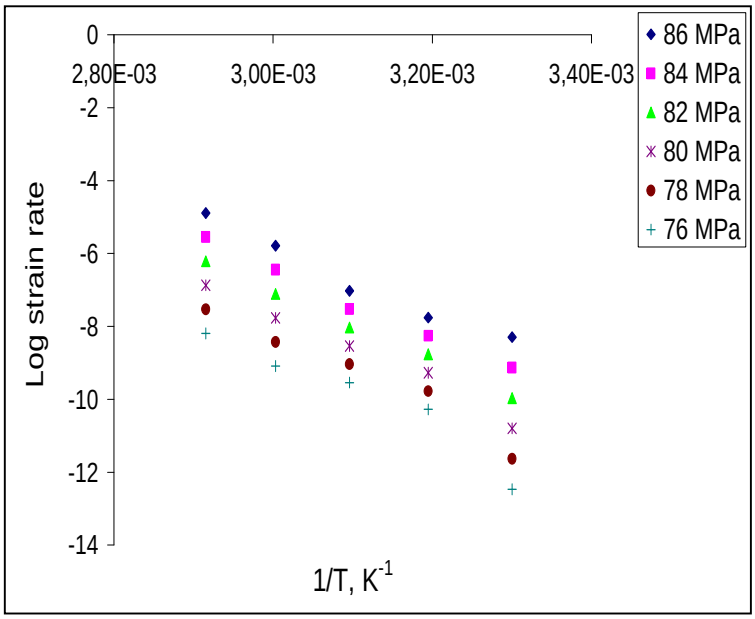

Fig.8.34: plot of Eq. 8.4 for six different coercive stress values in PZT 5A poled parallel.

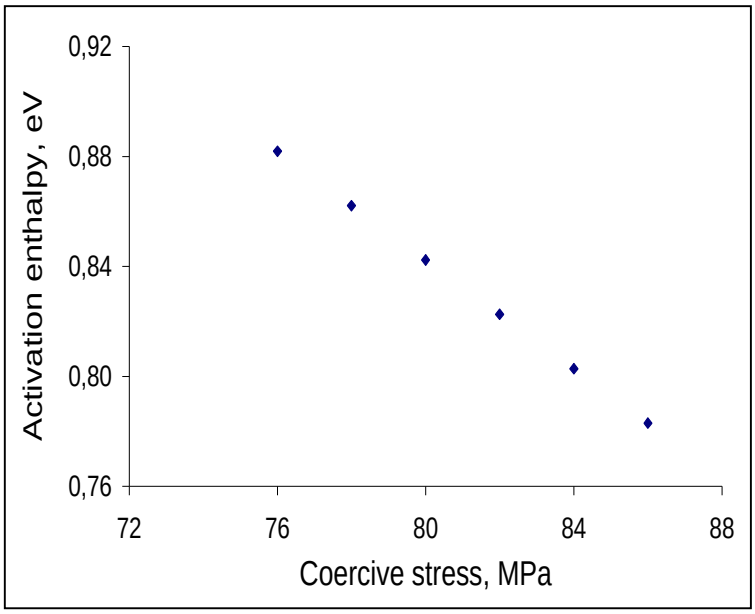

Fig.8.35: activation enthalpy in PZT 5A poled parallel.

Chapter 9: Ferroelectric switching in PZT 5A

9.1 Introduction

Domain switching is responsible for the non-linear and hysteretic behaviour of ferroelectric systems upon the application of an alternating bipolar electric field. The shape of the loops and the magnitude of the hysteresis depend on the amplitude and the rate of the applied field, on the temperature and on various microstructural features such as crystal structure, doping agents, defects and impurities, domain and grain size. Ferroelectric switching has been subject of extensive theoretical and experimental research for decades, but at the present the mechanisms involved are still not completely understood. The main purpose of this work is to understand the evolution of the domain configuration along the P-E and butterfly loops and to clarify the physical mechanisms involved in the domain switching dynamics in the different regions of the hysteresis loops. The experimental approach employed is based on the analysis of the P-E loop, the butterfly hysteresis and creep relaxation curves with the simultaneous measurement of polarization and strain during the application of a constant electric field of different magnitude. In addition P-E and butterfly loops were generated at different frequencies in order to study rate effects, investigating the role of thermal fluctuations in ferroelectric switching.

9.2 P-E loop

Alternating electric field ramps with 1 Hz frequency were applied to PZT 5A samples, using the equipment described in Chapter 4. I-E curves (Fig.9.1), P-E loops (Fig.9.2) and the butterfly loops (Fig.9.3) were generated and studied. In Fig.9.1 the current I represents the polarization rate and it has been plotted as a function of the applied field. The field corresponding to the maximum current represents the coercive field E_C. In the P-E (polarization-electric field) loop (see Fig.9.2) the coercive field coincides with the field at which the polarization is zero (point B in Fig.9.2). Experiments were started with a poled material with a polarization $P=-P_R$ (point A in

Fig.9.2). The application of a positive electric field firstly determines a depoling process of the material, evidenced by the decreasing magnitude of the polarization until the coercive field (point B in Fig.9.2), where the material is completely unpoled, having P=0. Above the coercive field, the material starts to be poled in the opposite direction, displaying a positive value of polarization, which increases in magnitude until the saturation value P_S, which corresponds to the maximum electric field applied (point C, where E=4 kV/mm in Fig.9.2). On decreasing the field (unloading), part of the domains switch back, determining a decrease of the polarization. When the field is completely removed (point D, where E=0 kV/mm in Fig.9.2), the material shows a "*remanent polarization*" (P_R). The process just described is then repeated in the reverse direction if a negative field is applied. The loops and the coercive field are not always symmetrical. In some materials, such as PZT 4D the presence of point defects generates defect dipoles that can produce a bias field. The PZT 5A was chosen for this study because it produces reproducible and symmetrical loops.

9.4 Analysis of the "butterfly loop"

Due to their piezoelectric and electrostrictive properties, ferroelectric materials also experience deformations when subjected to an applied electric field. Unlike the polarization, which has a monotonic dependence on the electric field, the strain shows a non-monotonic trend with the applied field, displaying loops with a characteristic "butterfly shape" (Fig.9.3).

The butterfly loop in Fig.9.3 was generated using the waveform generator HP33120A, software controlled. Two electrical field ramps were applied to the sample and the data during the second ramp (when reproducible loops can be generated) was acquired by the software and plotted as a function of the field (Fig.9.3). In the butterfly loop in Fig.9.3, the values and the sign of the strain have a relative validity as they depend on the settings at the beginning of the tests. In this instance before each test, the strain has been conventionally set at zero as the reference point.

The non-monotonic trend of the strain with the field in the loading part of the loop, suggests that the material experiences shrinkage and elongation under the action of

the applied field, as also explained in [49,127]. For the relative validity of the magnitude of the strain values and of their sign, from the butterfly loop itself, is not easy to distinguish in which range of the applied field shrinkage and elongation take place. This can be addressed by studying the sign of the strain rate as a function of the electric field (Fig.9.4) as it depends only on the changes in strain during the ramps and not on the initial settings of the tests. The strain rate was obtained by the first numerical differentiation of the plot strain-time and plotted against the electric field (Fig.9.4).

As previously mentioned, the experiments were performed on a poled PZT 5A sample. The sample tested had a prevalence of tetragonal structure [44] and therefore, in the poled state, the samples are elongated along the poling direction. By applying the field, domain switching takes place, producing initially a depoling and a shrinkage process in the material, through 90° domain switching which reduces its elongation along the poling direction. Shrinkage is consistent with the initial negative sign of the strain rate plot in Fig.9.4. In correspondence of $E=E_1=1.2$ kV/mm, a maximum in the shrinkage rate can be observed.

In the range $E_1<E<E_2$ the shrinkage rate reduces, until it becomes zero at $E=E_2=1.5$ kV/mm (Fig.9.4). For $E>E_2$, the strain rate changes sign indicating that the material begins to elongate.

In the range $E_2<E<E_C$, the material recovers the shrinkage until $E=E_C$, where the material is unpoled. In the butterfly loops presented in [49] the overall strain of the material was zero at the coercive field. In Fig.9.3 the butterfly loop was not shifted, having as zero strain, the strain at the beginning of the each test, as already mentioned above. At $E>E_C$ the overall polarization changes sign, the material starts to elongate in the direction of the field, with a rate that decreases with increasing the field.

In order to understand the trend of the overall strain in correspondence of E_1, E_2 and E_C, the slope of the butterfly loop was numerically calculated and plotted as a function of the electric field (Fig.9.5). It can be observed that at $E=E_1$, the plot presents a local minimum and it corresponds to an inflection point in the butterfly loop (see also Fig.9.3). At $E=E_2$ the slope is zero reflected in a minimum in the butterfly loop (see

also Fig.9.3). At $E=E_C$ the slope of the butterfly loop assumes a local maximum, indicating another inflection point in the butterfly loop (see also Fig.9.3). According to the strain rate and the butterfly loop slope, four regions can be identified:

1) $E<E_1$
2) $E_1<E<E_2$
3) $E_2<E<E_C$
4) $E>E_C$

9.4 Ferroelectric switching mechanisms

Differently from the mechanical case, where domain switching occurs only through the movement of non-180° domain walls, ferroelectric switching is believed to occur through a combination and a succession of non-180° and 180° domain switching events. It was proposed that in the tetragonal phase, domain switching occurs through two 90° switching steps and in rhombhohedral phase through a first step of 70.5° and a second step of 109.5° [49]. The idea of multiple steps switching process is supported also by other previous studies [127]. Based on the present analysis of the P-E and butterfly loops, it is proposed that polarization reversal involves two consecutive steps of 90° or multiple consecutive steps of the more general non-180°, as follows. In the region $0<E<E_1$, the domains more favourably oriented with the applied field start to switch in direction of the field, performing the first step of non-180° switching. This produces a shrinkage of the material until $E=E_1=1.2$ kV/mm. The predominance of non-180° domain switching of domains favourably oriented with the external electric field in this region is confirmed by small variation in the polarization as a function of the electric field (see P-E loop).

In the region $E_1<E<E_2$, even though the material continues to experience shrinkage (strain rate still negative), the strain rate starts to decrease in magnitude (see Fig.9.4), indicating the exhaustion of the first step of non-180°, with also the possibility that some of the domains are able to complete their total 180° switching, or at least are capable of performing multiple switching steps, with an overall switching higher than 90°, producing a reduction in the shrinkage rate. This is also suggested by an increase in the P-E loop slope, in that region.

At $E=E_2$, the strain rate and the butterfly loop slope are both zero. This indicates that the material at that point has finished shrinking and it is about to recover the shrinkage and then to elongate along the direction of the applied field.

In the region $E_2<E<E_C$, massive variation of polarization upon small variation of the electric field can be observed in the P-E loop (Fig.9.2). A significant amount of domains are able to perform a domain switching higher than 90°, producing also a complete recovery of the shrinkage previously produced. At $E=E_C$ the material is depoled and undeformed. In the region $E>E_C$, most of the domain complete their 180° domain switching, producing an opposite poling state.

9.5 Analysis of creep-relaxation curves

Further insight regarding the switching mechanisms in the different regions of the loops can be gained with an accurate analysis of the creep-relaxation curves (Fig.9.6-9.9). The simultaneous monitoring of polarization and strain during the application of a constant field gives the possibility of observing the domain switching evolution in different regions of the hysteresis loops in a longer time scale compared with the simple monotonic loading at finite rate. Furthermore, creep experiments allowed the study of the combined effect of the constant applied field and the thermal fluctuation on the domain switching process during the dwell time.

Experimental results showed that the creep magnitude for both polarization and strain strongly depends on the level of the applied electric field (Fig.9.6-9.9), in agreement with previous studies [68-70] and analogously to the mechanical case (see Chapter 6). In Fig.9.6, 9.7, the polarization and the strain during creep were normalized using their respective initial values at the beginning of the dwell period, when the electric field was held constant. It can be observed that during the dwell time the polarization is always a monotonic function of the time, while the strain shows a more complicated trend (Fig.9.6, 9.7).

In the range $0<E<E_1$ (with $E_1=1.2$ kV/mm), the strain during creep is always monotonic with time. During dwell at $E=E_1=1.2$ kV/mm the strain starts to display a

non-monotonic trend. Such inversions of trend was only measured only in the range $E_1<E<E_2$ (with E_2=1.5 kV/mm) as shown in Fig.9.7. For $E>E_2$ no more inversions were observed.

Referring to the creep strain curve at $E=E_1$=1.2 kV/mm, a visible turning point can be observed (see Fig.9.7). Before the turning point the material experiences shrinkage and beyond the turning point, the shrinkage starts to be recovered. It is likely that at the field where the strain inversion starts ($E=E_1$), thermal energy helps some of the domains to complete their total 180° switching, or at least thermal fluctuations promote multiple switching steps with an overall switching higher than 90°. Besides, a comparison between all the creep strain curves in the range $0<E<E_1$ confirms that at $E=E_1$ the material has the highest shrinking rate, as previously observed from the analysis of the strain rate plot in Fig.9.4. In fact, it can be noticed that the creep strain measured until the turning point in the creep curve (approximately after 1.3 seconds) is higher than the creep strain produced at lower fields in the entire dwelling time (3 seconds).

Considering the three curves at E=1.2, 1.4 and 1.5 kV/mm (Fig.9.7), it can be noticed that by increasing the field, the turning point occurs in a shorter time range. By holding the field at E=1.4 kV/mm and E=1.5 kV/mm, the material changes poling state and the overall polarization changes sign, from negative values to positive (see Fig.9.8). It is now clear that thermal fluctuations have significant effects under static condition and minor ones in dynamic conditions, as also observed in the mechanical case. In fact, it should be noted that by applying a monotonic loading the material depoles at E_C=1.68 kV/mm and creep results show that the depoled state could be achieved by statically applying a smaller field (for instance E=1.4 kV/mm or E=1.5 kV/mm).

At $E=E_2$=1.5 kV/mm the highest creep polarization was observed (Fig.9.6). By holding the field at $E=E_C$, the magnitude of the creep polarization reduces compared to E=1.5 kV/mm (Fig.9.6), probably because in the range $E_2<E<E_C$, part of the domains that are able to perform the complete 180° switching degree, exhaust. The highest polarization rate at this field (Fig.9.1) is reflected in the highest initial slope of the polarization-time curve at $E=E_C$ (see Fig.9.6).

At the coercive field, the creep strain is monotonic because the material experiences only elongation. At $E=E_C$ the material shows the maximum amount of creep strain, as at this field the material has the highest elongation rate (maximum in the strain rate plot in Fig.9.4) and does not experience any shrinkage, like it does at lower applied fields. In the range $E>E_C$ both the creep polarization and creep strain reduce compared to lower fields, due to the exhaustion of the switching sites at increasing field (Fig.9.6, 9.7).

By analysing the unloading part after the creep (Fig.9.8, 9.9), it can be noticed that for the polarization, the unloading part has the same curvature at any applied field (see Fig.9.8). For the strain this is valid until E=1.2 kV/mm. By holding fields above E=1.2 kV/mm, the material changes poling state as previously mentioned and the unloading part of the strain changes curvature (see Fig.9.9). So, it is likely that during the unloading after dwelling at a field in the range $0<E<E_1$ the material recovers the shrinkage. In the unloading process after dwelling at fields higher than E_1, the material recovers the elongation produced during the creep.

Creep experiments were performed also in the unloading branches of the loops, in order to obtain further information regarding the back switching process. Results show a higher recovery in polarization (back creep) and practically no back creep in the strain at high field (Fig.9.10-9.13). This might suggest that the beginning of the unloading process is dominated by the process 180° back switching, which does not produce strain recovery. Having a poled state at the beginning of the unloading, the strain mismatch between adjacent domains is minimized, as most of the domains are aligned along the same direction (like in textured structures). At smaller fields, the back creep in the strain increases and the back creep of the polarization decreases, meaning that the last stage of the unloading process is probably dominated the 90° back switching. At the end of the unloading process when E=0, the material remains poled, showing significant remanent polarization, which implies a limited back switching process.

9.6 Mechanically and electrically induced domain switching

A comparison between stress-strain curves, P-E loop, butterfly loop and mechanical and electric creep, gives the possibility of a more detailed understanding of domain switching process, stress and electric field induced.

In the mechanical case, the stress-strain and electrical displacement-stress curves of ferroelastic/ferroelectric compositions present an inflection point both at the coercive stress [44]. P-E loop presents one inflection point at the coercive field, while the butterfly loop shows two inflection points, one below the coercive field and one at the coercive field. This is due to the fact that by applying a mechanical compression, only 90° domain switching can be driven, producing only a depolarization process on samples initially poled. The depoling process consequent to the application of mechanical compression on poled samples causes the development of internal stresses due to the increase of strain mismatch between domains [128]. The application of an electric field on a poled sample, instead, firstly produces a depoling of the material and then a poling process in the opposite direction, through a succession non-180° switching events. Due to the occurrence of two processes (depoling and poling), the evolution of the back fields in the electrical case is more complicated and it is still object of ongoing discussion [127].

Remarkable difference can be noticed also between mechanical and electric creep. In the mechanical case, strain and electrical displacement have monotonic time dependence during creep at every level of applied stress [44]. In the electrical case, instead, the polarization is monotonic with time at every field applied, while the strain shows also non-monotonic trend, at certain electric field level, as previously discussed. The magnitude of the creep polarization in the electric case and of the creep strain in the mechanical case could be evaluated with respect to the polarization at saturation and the strain at saturation respectively. Considering the electric field $E=E_2$ where the creep polarization is maximum, it can be noticed that it represents a very high percentage of the polarization of saturation. The creep strain at the coercive stress (maximum in the creep strain) instead, represents a much lower percentage of the saturation strain.

The rate decay of the creep strain upon compression loading in poled samples along the poling direction has been mainly attributed to the build up of the internal stresses, which represent the major obstacle to the domain reorientation and to the depoling process, at every stress applied. In the electric case, it has been shown that at certain levels of the applied electric field, the material can reverse its poling state during creep (see curves at E=1.4 kV/mm and E=1.5 kV/mm in Fig.9.8), evidencing a more complicated evolution of the back fields, also in static condition, compare to the mechanical case.

9.7 Rate dependence

P-E loop and butterfly hysteresis curves were generated at different frequencies in order to analyse the rate sensitivity of ferroelectric switching in PZT 5A. The possibility of applying a bipolar field allowed the microstructure to be recovered, generating reproducible and stable loops. Four different frequencies (f=0.1, 0.5, 1, 5 Hz) were chosen in a range that allows nearly constant microstructure and that at the same time ensures significant effects that can be sensibly measured.

P-E and butterfly loops at different frequencies are shown in Fig.9.14 and Fig.9.15 respectively. By observing the P-E loops (Fig.9.14) it can be noticed that by increasing the frequency the coercive field increases and that the saturation polarization P_S and the remanent polarization P_R both decrease at higher frequencies. The reduction in P_S and P_R is more pronounced in correspondence of the highest frequency used (5 Hz). The frequency effects are more significant in the region of high electric field, where the curves evidenced higher rate dependence (Fig.9.14). Opposite trend can be observed in the butterfly loops, quite rate sensitive at small applied fields and weakly frequency dependent at higher fields (see Fig.9.15).

The described rate effects arise from the thermally activated nature of the ferroelectric switching process, where thermal fluctuations contribute to the formation of new nuclei with polarization favourably oriented with the applied field. In order to produce increments of polarization switching, energy barriers have to be overcome. Energy barriers are produced by long and short range interactions (see also Chapter 3), where

the former act throughout the material and the latter are superimposed on the former ones and have only local effects. Thermal fluctuations supply an additional amount of energy to overcome short range interactions. At high frequency the contribution of the thermal fluctuation to the switching process is negligible and most of the energy required is provided by the applied field. On the other hand, when the frequency of the applied field is low, thermal fluctuations have more time to accumulate energy having more significant contributions to the switching process.

There is a general agreement in the literature that ferroelectric switching occurs through the nucleation and the subsequent expansion of critical nuclei. The rate limiting step is here assumed to be the nucleation of activated nuclei, having the domain walls as the preferred sites for the nucleation event, as also mentioned in previous studies [45]. If thermal activation is taken into account, the polarization rate can be expressed as [45]:

$$\dot{P} = A\exp\left(-\frac{\Delta U - E_{eff} P_0 V_a}{k_B T}\right) \tag{9.1}$$

$\dot{P}$ is the polarization rate, A is the pre-exponential term which depends on complex structural factors, such as the density of nucleation sites, the volume swept by nuclei, the entropy variation during domain wall movement. The term ΔU represents the variation of the internal energy, $E_{eff} P_0 V_a$ is the work done by the electric field to produce activated nuclei, with E_{eff} being the effective electric field acting on the domain walls, P_0 the spontaneous polarization and V_a the activation volume. With an analogous procedure used in the mechanical case, from Eq.9.1 it follows that:

$$\ln \dot{P} = \ln A + \frac{E_{eff} P_0 V_a}{k_B T} \tag{9.2}$$

The previous equation predicts a linear variation of the logarithm of the polarization rate with the effective field E_{eff}. In order to study the effect of rate in ferroelectric switching, the coercive field was chosen as the reference point to perform the rate analysis. The choice is justified by the fact that in correspondence of the coercive field, the same value of polarization (P=0) is produced at every frequency,

guaranteeing constant microstructure conditions. In addition, at the coercive field, the highest polarization switching rate is produced at every frequency, determining the most appropriate thermodynamical conditions to analyze rate effects compared with other regions along the loops. By assuming that at the coercive field the microstructure remains constant when the frequency is changed and that a variation in the frequency does not produce significant changes in the back fields, the rate sensitivity in ferroelectric switching can be defined from Eq.9.2 as:

$$\lambda = \frac{k_B T}{P_0 V_a} = \frac{\partial E_C}{\partial \ln \dot{P}} \tag{9.3}$$

It should be noted that the best way of quantifying the rate sensitivity would have been by generating the P-E loops in polarization control. Due to the absence of an adequate equipment for such measurements, the electric field was chosen as the independent variable and the polarization rate was calculated as the numerical differentiation of the polarization respect with time.

Fig.9.16 shows a linear variation of the coercive field with $\ln \dot{P}$. In order to estimate the activation volume V_a from Eq.9.3, the value of the spontaneous polarization P_0 was calculated from the saturation polarization P_S at the smallest frequency multiplied by the geometrical factor 1/0.83 used in tetragonal structure, to take into account the fact that in polycrystalline materials P_S is smaller than P_0 [45]. From the slope of the plot in Fig.9.16 the activation volume V_a was estimated to be 77 nm^3, which is around half of the value calculated in PZT 5H (162 nm^3) with a similar method [121]. This suggests that the PZT 5A has greater rate dependence than PZT 5H and confirms that domain switching in soft compositions involves large activated nuclei. Large activated volume is also consistent with the idea that domain wall boundaries in PZTs are broad and diffuse regions of finite thickness, representing the most preferred site for the nucleation to take place [45,121].

The activation volume calculated at the coercive stress from rate experiments in the mechanical case (3 nm^3) in PZT 5A is around twenty-five times smaller than the one calculated in the electrical case (77 nm^3). The difference is attributed to the different experiments performed, to the different domain configuration in the two cases and to

the different domain switching mechanisms (only non-180° domain switching in the mechanical case and non-180° and 180° in the electrical case). Other sources of discrepancy might come from the validity of the model assumptions in the mechanical case.

9.4 Conclusions

Ferroelectric switching dynamics has been studied in dynamic (electric field ramps) and static (creep) conditions. Analysis of the P-E and butterfly loop allowed identifying the ranges of the applied field where the material experience shrinkage and elongation. A domain switching mechanism has been proposed based on successive non-180° steps, clarifying the evolution of the domain configuration in the different regions of the hysteresis loops. The domain switching dynamics depicted is also supported by the analysis of creep relaxation curves, which allowed the switching kinetic under constant electric field of different magnitudes to be studied. The creep trends also revealed analogies and differences between domain switching induced by a mechanical stress and by an electric field. It was noticed that by holding a static electric field of certain magnitude, the material experiences a poling state change, determining a complex evolution of the back fields. Due to this additional complication and due to the non-monotonic trend of the creep strain during the electrical creep, the rate model proposed to describe the creep strain in the mechanical case could not be applied in the electrical case. Modifications of the rate model proposed in the mechanical case are required to model the time evolution of creep polarization and strain, during the application of a constant electric field. A more detailed knowledge of the changes in the internal stresses during creep at different stages based on in situ analysis could represent a significant progress for the implementation of a sensible model. Rate effects were studied by generating P-E loops at different frequencies, denoting that the coercive field increases and P_S and P_R decrease with increasing frequency. The rate dependence was modelled by applying rate theory and the activation volume was estimated as 77 nm^3. Its relatively large value indicate a quite small rate dependence and confirms the idea that domain walls are the favourite sites for the nucleation of activated nuclei, being a region highly diffused and mobile.

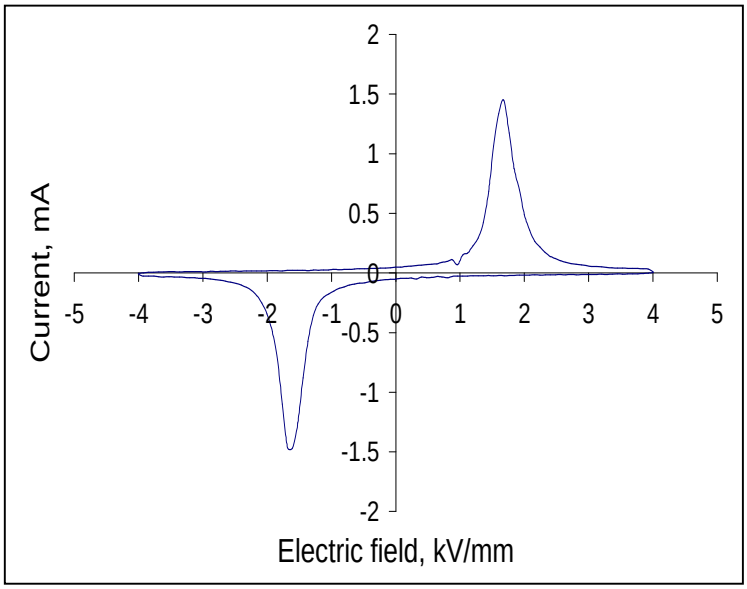

Fig.9.1: I-E plot in PZT 5A at 1 Hz.

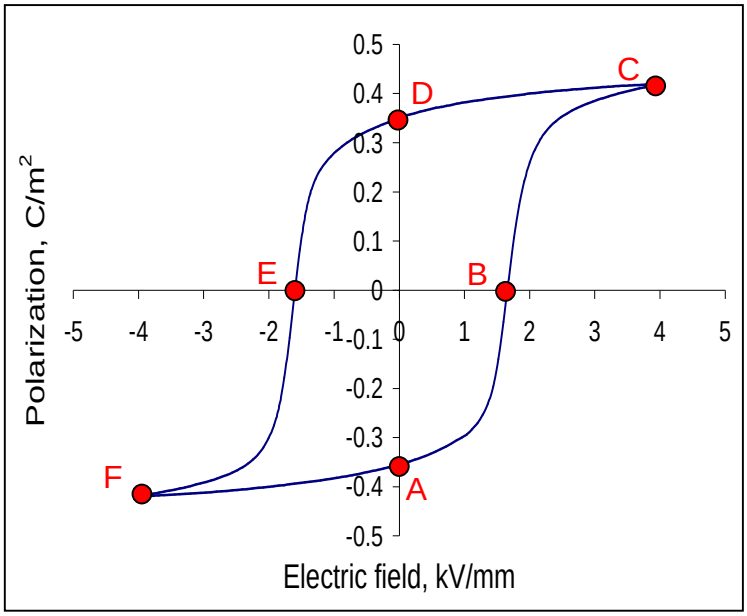

Fig.9.2: P-E loop in PZT 5A at 1 Hz.

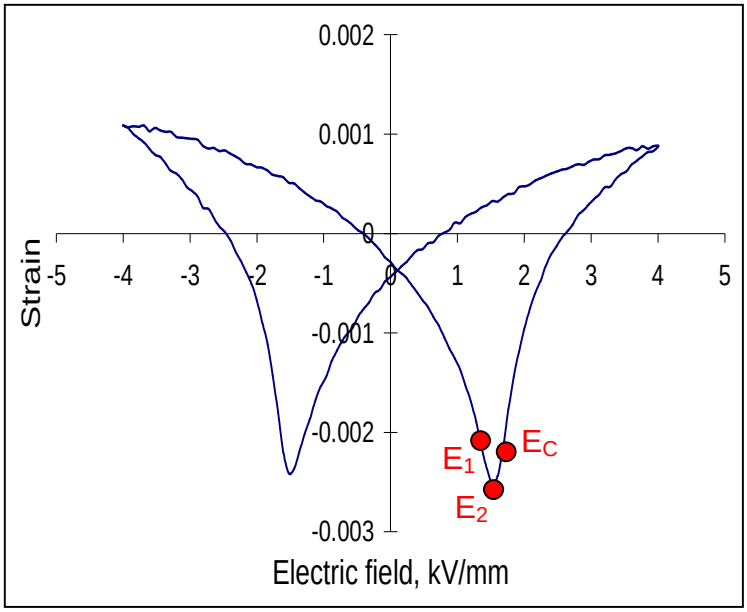

Fig.9.3: butterfly loop in PZT 5A at 1 Hz.

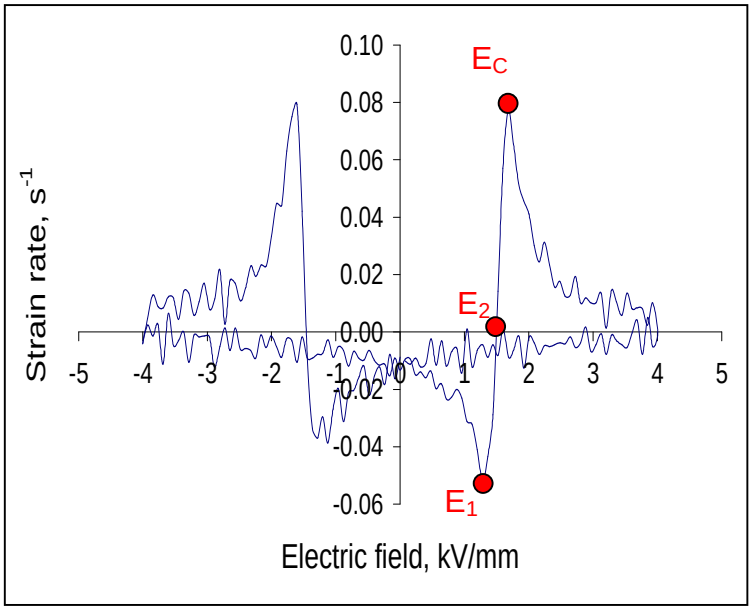

Fig.9.4: strain rate as a function of the electric field in PZT 5A at 1 Hz.

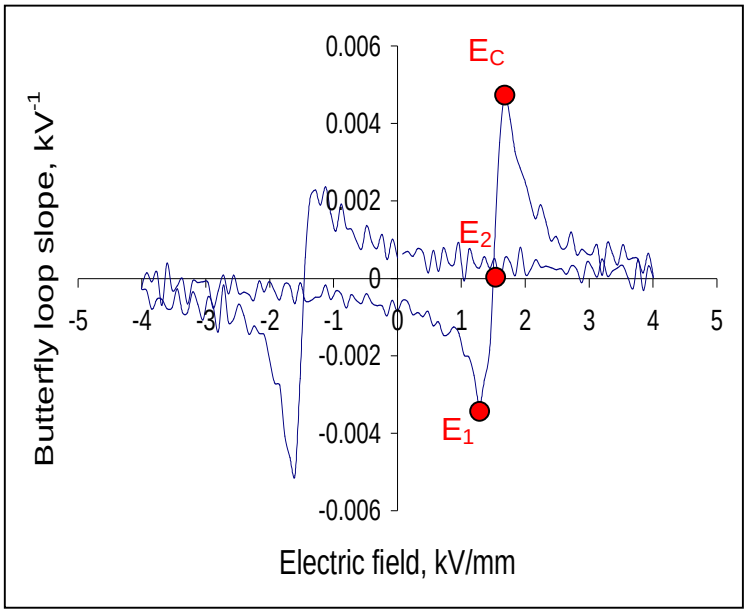

Fig.9.5: butterfly loop slope as a function of the electric field in PZT 5A at 1 Hz.

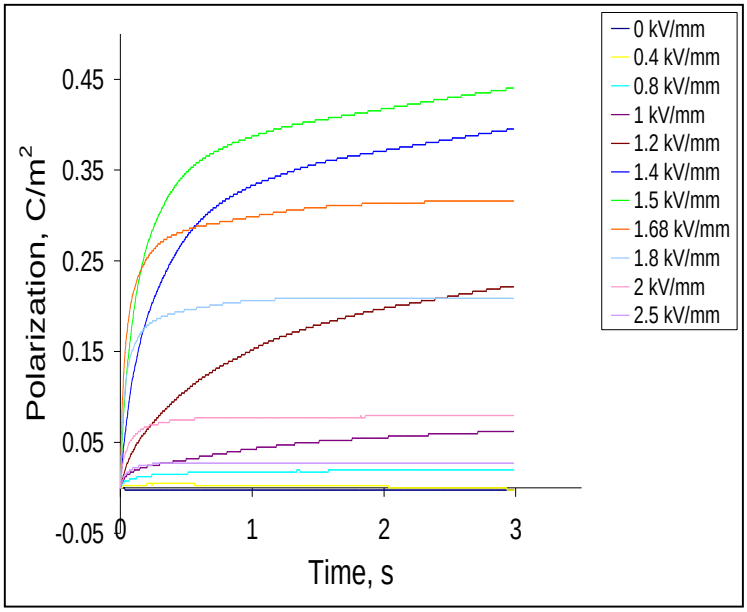

Fig.9.6: creep polarization as function of time in PZT 5A in the loading part of the hysteresis loops.

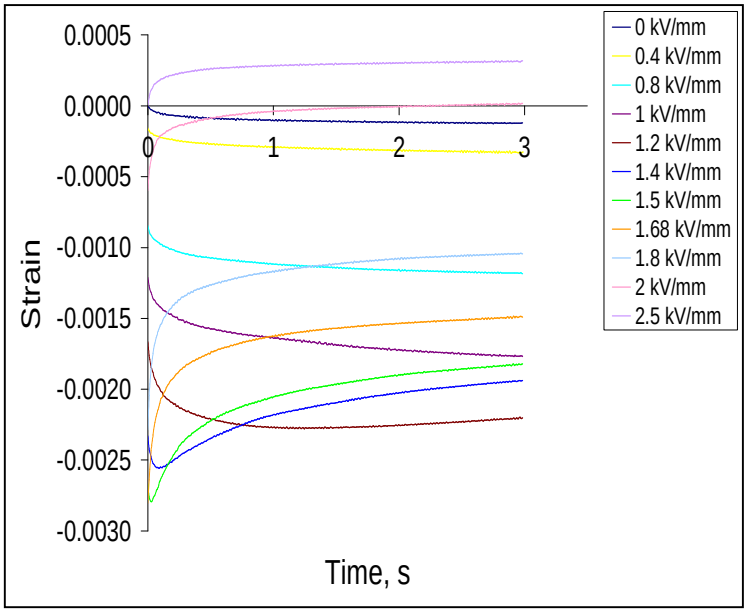

Fig.9.7: creep strain as function of time in PZT 5A in the loading part of the hysteresis loops.

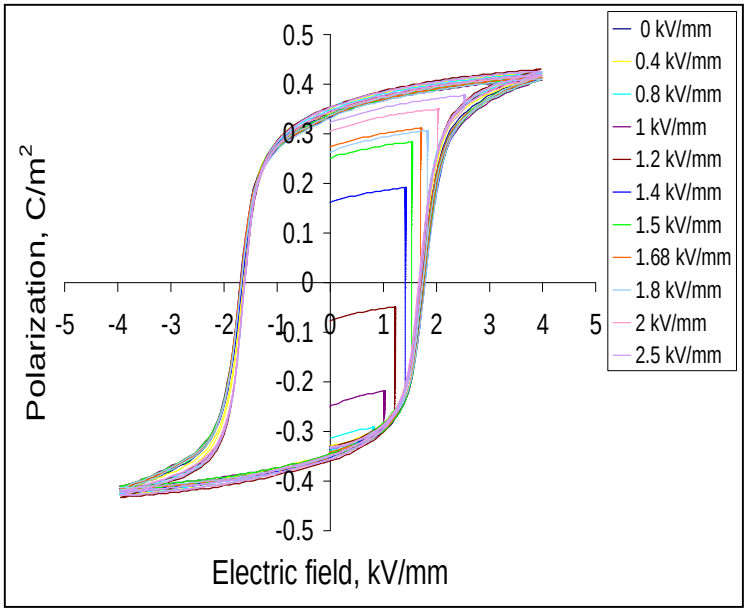

Fig.9.8: creep at different electric field in the loading part of the P-E loop in PZT 5A at 1 Hz.

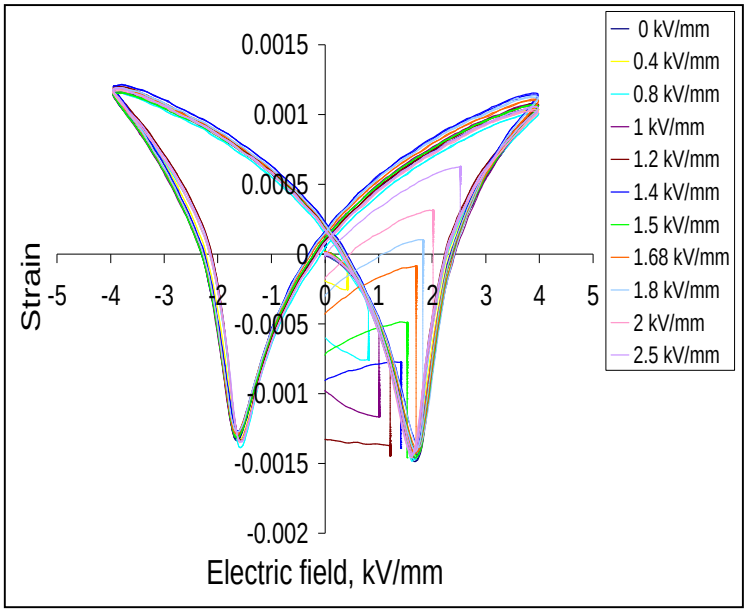

Fig.9.9: creep at different electric field in the loading part of the butterfly loop in PZT 5A at 1 Hz.

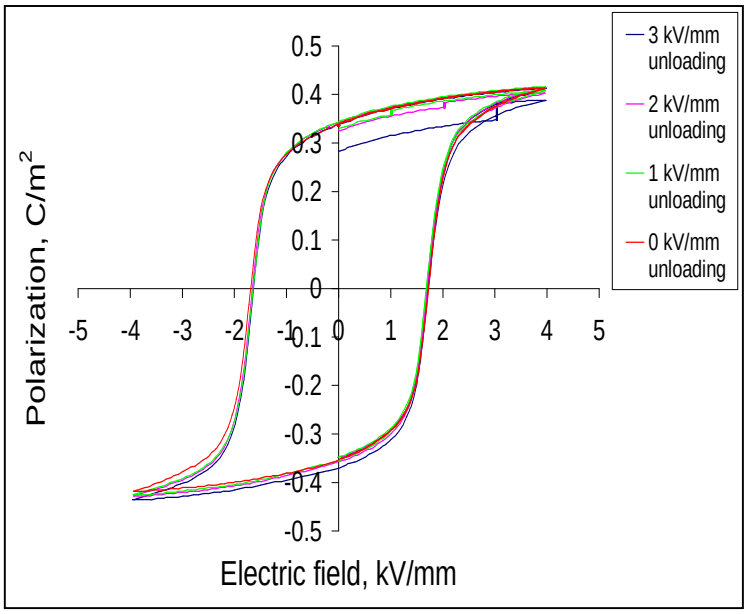

Fig.9.10: creep at different electric field in the unloading part of the P-E loop in PZT 5A at 1 Hz.

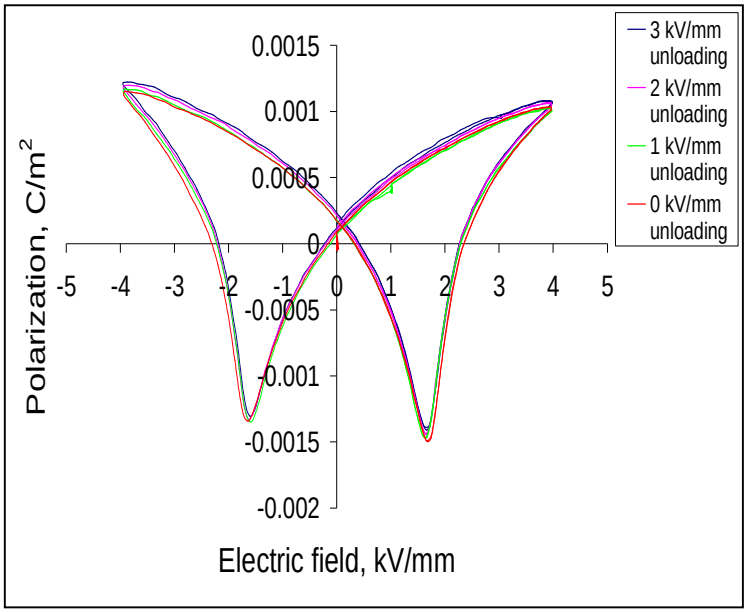

Fig.9.11: creep at different electric field in the unloading part of the butterfly loop in PZT 5A at 1 Hz.

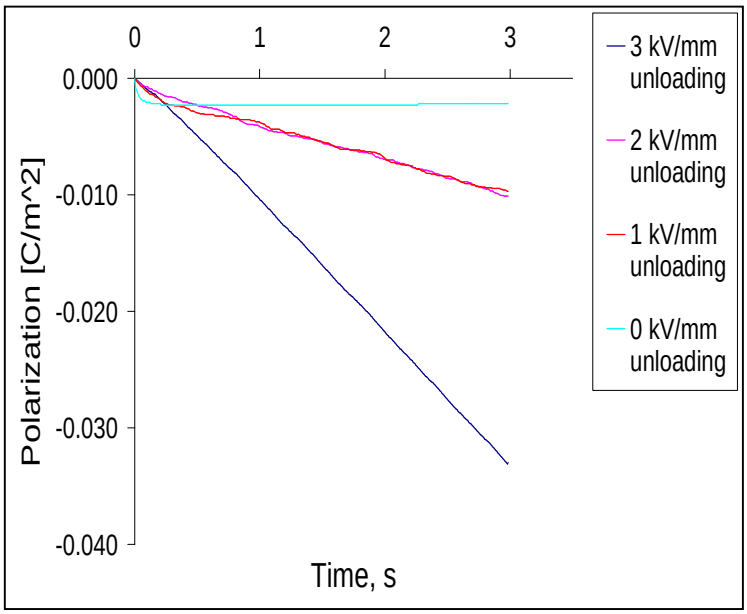

Fig.9.12: creep polarization as function of time in PZT 5A in the unloading part of the hysteresis loops.

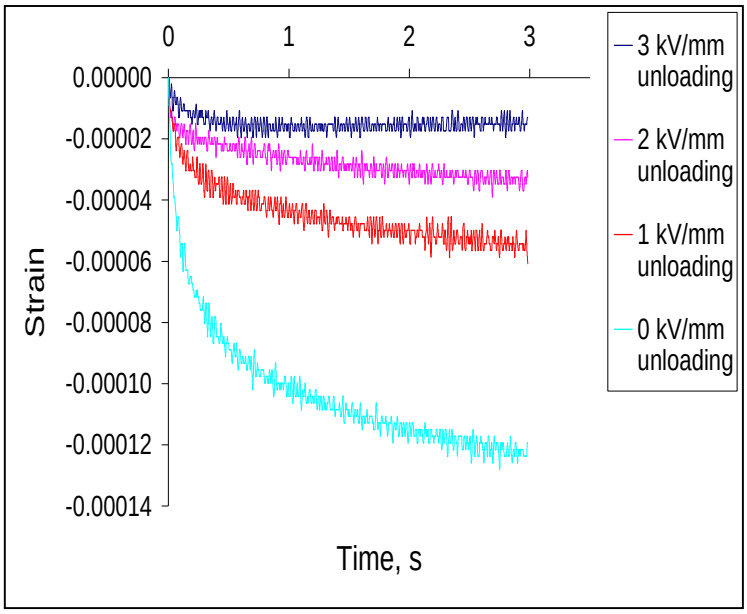

Fig.9.13: creep strain as function of time in PZT 5A in the unloading part of the hysteresis loops.

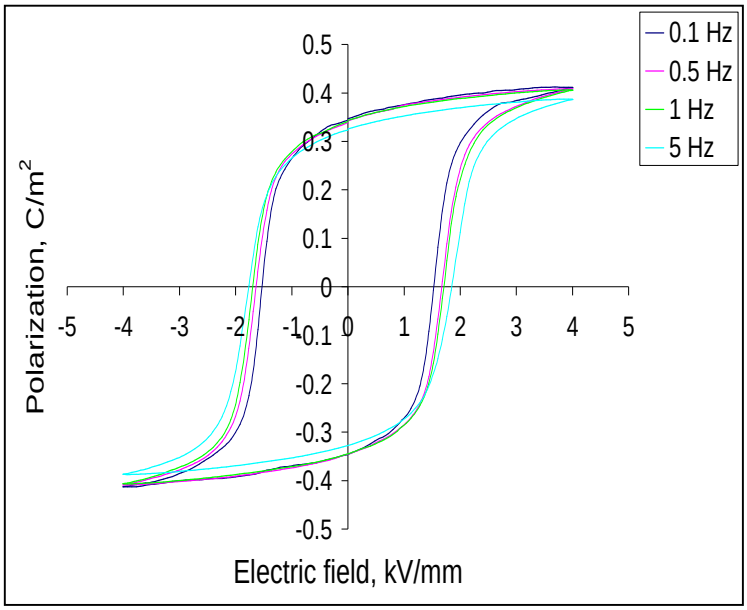

Fig.9.14: P-E loops at different frequencies in PZT 5A.

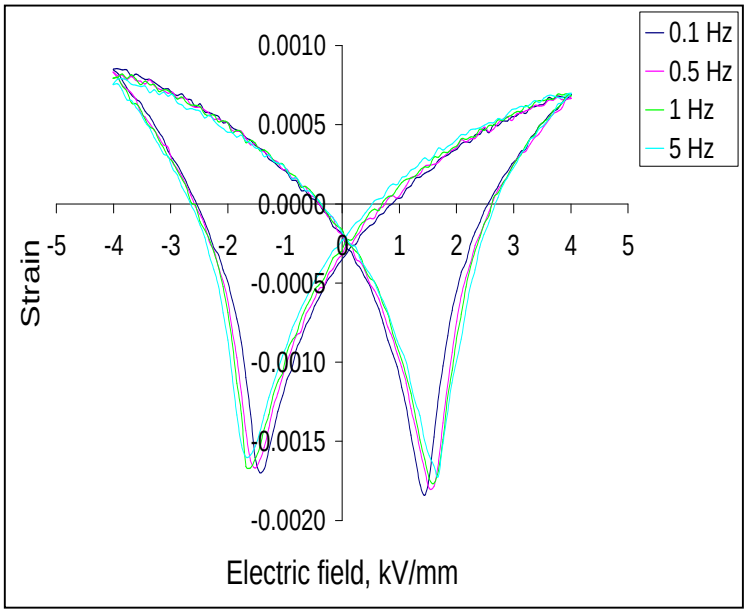

Fig.9.15: butterfly loops at different frequencies in PZT 5A.

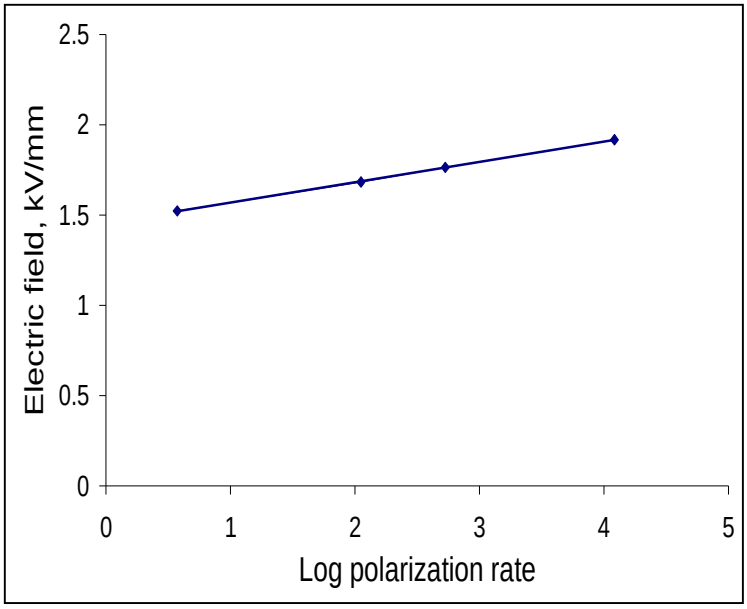

Fig.9.16: $E_C - \ln \dot{P}$ **plot in PZT 5A.**

Chapter 10: General conclusions and future work

10.1 Conclusions

The present thesis contains several novel aspects which are listed below:

- The effect of thermal fluctuation on domain switching process was taken into account by developing a rate model based on Arrhenius rate theory. It was shown that the model can be used to estimate the activation parameters of ferroelastic switching, to quantify the rate sensitivity of ferroelastic materials and to predict the effect of loading rate on the Rayleigh-type behaviour.
- Different novel experimental techniques have been developed to study rate dependence in ferroelastic switching.
- Novel and original aspects include also the study of the influence of acceptor doping on the ferroelastic properties of $LaCoO_3$ based perovskites.
- Rayleigh-type relationship were proposed to describe the Rayleigh-type behaviour in ferroelasticity, proving that hysteretic behaviour of ferroic materials upon weak fields can be described using analogous models.
- A comparison between domain switching mechanically and electrically induced was performed evidencing analogies and differences.

The main conclusions of the present thesis can be summarized as follows:

- **The role of thermal fluctuations in ferroelastic switching**

Thermal fluctuations assist the domain switching process, supplying additional energy to produce activated nuclei. The effect of thermal fluctuations is more significant in hard compositions that show greater rate dependence and greater creep effects than soft compositions. In hard materials domain switching occurs through the nucleation and the expansion of small activated nuclei, compared to the soft compositions that have shown higher activation volume and therefore a faster domain switching kinetic.

- **The role of dopants in ferroelastic switching**

Doping agents dramatically influence the ferroelastic switching properties. In particular, it was noticed that calcium doping of $LaCoO_3$ increases the coercive stress, the hysteresis area and the irreversible strain. Hard ferroelasticity generated by calcium doping could arise from the oxygen vacancies equivalent to the acceptor doping which have a clamping effect on domain walls.

- **Characterization of rate and temperature dependence of ferroelastic switching**

Different experimental techniques were successfully developed to study the rate and temperature effects on domain switching mechanical stress induced. Rate and temperature dependence of ferroelastic switching were systematically studied via Rayleigh-type analysis and with newly developed methods. It can be generally concluded that:

Rayleigh-type analysis represents a powerful technique to study the rate dependence under weak mechanical stress applied, enabling testing one sample under dynamic loading at different frequency/loading rate, through the generation of reproducible stress-strain loops. Rayleigh-type analysis can be also regarded as an efficient methodology in studying the effect of composition on the rate dependence of ferroelastic switching. In addition it allows the study of the influence of temperature during the application dynamic load of small amplitude, with the possibility of evaluating mechanical and thermal contribution to domain switching, when the stress amplitude is kept constant and the temperature varied.

By analysing the mechanical compliance in the Rayleigh loops it is possible to estimate intrinsic and extrinsic contribution to the strain. It was found that under the application of a weak field the intrinsic contribution is higher than the extrinsic in the Rayleigh loops generated.

Stress-strain Rayleigh loops and mechanical compliance can be successfully described with Rayleigh empirical relationships analogous to the expressions used in ferromagnetic and ferroelectric systems, providing valid constitutive relationships for

the response of ferrolastic solids to cyclic weak loads of different amplitudes and frequencies.

The novel methodologies developed to study the loading rate and the temperature sensitivity of ferroelastic switching along the entire stress-strain curve on only one sample prevented data scattering that would arise from the use of different specimens. The set of data provided prove that the developed techniques represent a promising experimental tool for such studies.

Based on the experimental results, it was found that the coercive stress region has the highest rate sensitivity. Furthermore it was observed that the coercive stress increases logarithmically with increasing the rate of the applied load and it linearly decreases with increasing the temperature.

- **Rate theory model**

The rate model developed is able to describe the thermal activated nature of ferroelastic switching. According to rate theory, the rate decay of creep deformation arises from the development of internal stresses, due to the rearrangement of the domain configuration during the switching. Applying rate theory, the volume of activated nuclei was identified as a key parameter in controlling the domain switching kinetic and estimated.

Rate theory allowed quantification of the effect of the loading rate on the extrinsic strain in the Rayleigh loops. The model predicts that for constant stress amplitude the product between extrinsic strain and loading rate is constant for every loading rate applied. The accuracy of the prediction is higher for small stress amplitudes, where the assumptions of the model hold more reasonably.

Rate theory model enables quantification of the loading rate sensitivity of ferroelastic switching at different temperatures and to produce a first rough estimation of the activation enthalpy of ferroelastic switching.

- **Ferroelectric switching**

Based on an accurate analysis of the P-E loop, butterfly loop and creep relaxation curves, further insights on the evolution of the domain configuration under the application of an electric field were obtained. It is proposed that polarization reversal is achieved through multiple steps of non-180° domain switching, which in turn determine a complex strain evolution, with a succession of shrinkage and elongation events, whose stages were identified and distinguished.

Ferroelectric switching kinetics was studied via creep tests at different electric field levels, which allowed the comparison with mechanical creep. In the mechanical case creep strain and electrical displacement are monotonic functions of time during creep. In the electrical case, polarization has monotonic time dependence, while the creep strain showed non-monotonic trends. This confirms that in poled compositions, domain switching mechanically induced occurs through the movement of non-180° domain walls, while the application of an electric field produces the complete 180° domain switching.

It was observed that if the applied electric field is sufficiently large a change in the poling state can be produced with the application of a constant field (during creep). Since the material can go through different poling states during creep, the evolution of the back fields is very complex and cannot be estimated without more specific investigations.

The effect of thermal fluctuations in ferroelectric switching was investigated by generating P-E and butterfly loops at different frequencies. By applying rate theory the rate sensitivity and the activation volume were estimated, whose values suggest small rate dependence and a nucleation event taking place at the domain walls, which can be thought as mobile region with broad and finite thickness.

10.2 Future work

- **The effect of calcium doping on $LaCoO_3$**

In order to clarify the role of calcium doping on the ferroelastic properties of $LaCoO_3$, a systematic study could be carried out, by testing compositions with different calcium contents. Unit cell distortion and grain size could be estimated and compression stress-strain measurements and creep tests could be performed to clarify the relationships microstructure-dopants-ferroelastic properties.

- **Rayleigh-type analysis**

Future investigations could attempt the prediction of the dependence of the Rayleigh parameters α_R and S_{Init} on loading rate and/or frequency. Furthermore, the temperature effects could be analyzed using dynamic loads of different amplitudes. The rate model developed could be then applied to describe the temperature effects, by estimating the activation enthalpy of the Rayleigh-type deformations.

- **Effects of temperature on ferroelastic switching**

In Chapter 8 it was found an interesting trend of the strain rate as a function of stress at different temperature. At higher temperature the strain rate increases until a certain value of the stress applied σ_{cross}, while at higher stresses the strain rate reduces if the temperature increases. Further investigations may try to clarify the reason behind the described trend, opening new research perspectives, which would provide a clearer picture of domain switching kinetic, with the possibility of extending the findings to other types of ferroelastic/ferroelectric systems and also to other types of ferroic materials.

- **Evolution of internal stresses during polarization reversal**

In order to quantify the evolution of the internal stresses during the application of an electric field, in-situ neutron diffraction analysis is suggested. Neutron diffraction experiments would enable to monitor the lattice parameters change during the domain switching process, determining the lattice strain and consequently the internal stresses developed. Similar analysis would be indicative also in the mechanical case.

- **Development of a rate model to describe ferroelectric creep**

The evolution of the back fields could be determined in static and dynamic conditions. Once the evolution of the back fields in the static case is known, an implementation of a rate model to describe the electrical creep behaviour could be attempted and the microstructural parameters controlling the rate decay during the application of a constant electric field could be estimated.

References

[1] E.K.Salje "*Phase transitions in ferroelastic and co-elastic crystals*" Cambridge University Press, 1993.

[2] K.Aizu: *Physical Review B*, 1970, **2**, 754-772.

[3] K.Aizu: *Journal of the Physical Society of Japan*, 1969, **27**, 387-396.

[4] V.Wadhawan "*Introduction to ferroic materials*" CRC Press, Amsterdam, 2000.

[5] O.Prytz "*Phase separation, transformation and domain formation in $LaNbO_4$ supersatured with Sr"* PhD thesis, University of Oslo, 2003.

[6] E.K. Salje, S.A. Hayward, W.T. Lee: *Acta Crystallographica,* 2004, **A61**, 3-18.

[7] J.Sapriel: *Physical Review B*: 1975, **12**, 5128-5140.

[8] E.Salje, A.Buckley, G.Van Tendeloo, Y.Ishibashi, G.L.Nord Jr.: *American Mineralogist*, 1998, **83**, 811-822.

[9] E.Little: *Physical Review*, 1955, **98**, 978-988.

[10] D.Damjanovic: "*Hysteresis in Piezoelectric and Ferroelectric Materials*", The Science of Hysteresis, Volume 3; I. Mayergoyz and G.Bertotti (Eds.); Elsevier (2005).

[11] W.J.Merz: *Physical Review*, 1954, **95**, 690-704.

[12] W.J.Merz: *Journal of Applied Physics*, 1956, **27**, 938-943.

[13] E.Little: *Physical Review*, 1955, **98**, 978-988.

[14] H.L.Stadler: *Journal of Applied Physics*, 1958, **29**, 1485-1487.

[15] V.Gopalan, T.E.Mitchell: *Journal of Applied Physics*, 1998, **83**, (2), 941-954.

[16] V.Gopalan, M.C.Gupta: *Journal of Applied Physics*, 1996, **80**, (11), 6099-6106.

[17] T.J.Yang, V.Gopalan, P.J.Swart, U.Mohideen: *Physical Review Letters*, 1999, **82**, (20), 4106-4109.

[18] T.Tybell, P.Paruch, T.Giamarchi, J.M.Triscone: *Physical Review Letters*, 2002, **89**, (9), 097601.

[19] P.Paruch, T.Giamarchi, J.M.Triscone: *Physical Review Letters*, 2005, **94**, 197601.

[20] A.Gruverman, B.J.Rodriguez, C.Dehoff, J.D.Waldrep, A.I.Kingon, R.J.Nemanich, J.S.Cross: *Applied Physics Letters*, 2005, **87**, 082902.

[21] S.Jesse, B.J.Rodriguez, S.Choudry, A.P.Baddorf, I.Vrjoiu, D.Hesse, M.Alexe, E.A.Eliseev, A.N.Morozovska, J.Zhang, Long-Qing Chen, S.V.Kalinin: *Nature Materials*, 2008, **7**, 209-215.

[22] Y.Ishibashi, Y.Takagi: *Journal of the Physical Society of Japan*, 1971, **31**, 506-510.

[23] V.Shur, E.Rumyantsev, S.Makarov: *Journal of Applied Physics*, 1998, **84**, (1), 445-451.

[24] A.K.Tagantsev, I.Stolichnov, N. Setter, J.S.Cross, M.Tsukada: *Physical Review B*, 2002, **66**, 214109.

[25] D.Viehland, J.F.Li: *Journal of Applied Physics*, 2001, **90**, (6), 2995-3003.

[26] S.A.Kukushkin, AV.Osipov: *Physical Review B*, 2002, **65**, 174101.

[27] S.A.Kukushkin, M.A.Zakharov: *Physics of the Solid State*, 2002, **44**, (12), 2193-2203.

[28] J.Shieh, J.E.Huber, N.A.Fleck: *Acta Materialia*, 2003, **51**, 6123-6137.

[29] C.Landis: *Current Opinion in Solid State and Materials Science*, 2004, **8**, 59-69.

[30] A.C.F.Cocks, R.M.McMeeking: *Ferroelectrics*, 1999, **228**, 219-228.

[31] C.Landis: *Journal of the Mechanics and Physics of Solids*, 2002, **50**, 127-152.

[32] T.Nattermann, Y.Shapir, I.Vilfan: *Physical Review B*, 1990, **42**, 8577-8586.

[33] T.Nattermann: *Physical Review Letters*, 1990, **64**, (20), 2454-2457.

[34] S.Brazovkii, T.Nattermann: *Advances in Physics*, 2004, **53**, 177-253.

[35] W.Kleeman: *Annual Review Materials Research*, 2007, **37**, 415-448.

[36] P.Paruch: "Atomic force microscopy studies of ferroelectric domains in epitaxial PbZr0:2Ti0:8O3 thin films and the static and dynamic behavior of ferroelectric domain walls" PhD thesis, University of Geneve, 2003.

[37] W.Schranz, A.Troster, A.V.Kityk, P.Sondergeld, E.K.H.Salje: *Europhysics Letters*, 2003, **62**, 512-518.

[38] F.D.A.A.Reis: *Brazilian Journal of Physics*, 2003, **33**, 501-513.

[39] S.F.Edwards, D.R.Wilkinson: *Proceedings of the Royal Society A*, 1982, **381**, 17-31.

[40] S.Lemerle, J. Ferré, C.Chappert, V.Mathet, T.Giamarchi, P. Le Doussal: *Physical Review Letters*, 1997, **80**, (4), 849-852.

[41] D.Damjanovic: *Reports on Progress in Physics*, 1998, **61**, 1267-1324.

[42] D.Damjanovic: *Physical Review B*, 1997, **55**, 649-652.

[43] Y.Estrin, P.G.McCormick, R.Street: *Journal of Physics: Condensed Matter*, 1989, **1**, 4845-4851.

[44] D.Hu:"Domain wall dynamics in ferroelectric ceramics under mechanical stress", PhD thesis, Queen Mary University, London, UK, 2005.

[45] K.B.Chong, F.Guiu, M.J.Reece: *Journal of Applied Physics*, 2008, **103**, 014101.

[46] D.Fang, C.Li: *Journal of Materials Science*, 1999, **34**, 4001-4010.

[47] A.B.Schaufele, K.H.Hardtl: *Journal of the American Ceramic Society*, 1996, **79**, (10), 2637-2640.

[48] J.M.Calderon-Moreno, F.Guiu, M.Meredith, M.J.Reece, N.McN.Alford: *Journal of the European Ceramic Society*, 1999, **19**, 1321-1324.

[49] C.S.Lynch: *Acta Materialia*, 1996, **44**, (10) 4137-4148.

[50] J.Fan, W.A.Stoll, C.S.Lynch: *Acta Materialia*, 1999, **47**, (17), 4415-4425.

[51] D.Zhou, M.Kamlah, D.Munz: *Journal of the American Ceramic Society*, 2005, **88**, (4), 867-874.

[52] J.M.Calderon-Moreno, M.Popa: *Materials Science and Engineering A*, 2002, **336**, 124-128.

[53] S.Pojprapai (Imlao), J.L.Jones, M.Hoffman: *Journal of the American Ceramic Society*, 2006, **89**, (11), 3567-3569.

[54] N.Orlovskya, H.Anderson, M.Brodnikovskyy, M.Lugovy, M.J.Reece: *Journal of Applied Physics*, 2006, **100**, 026102.

[55] A.Fossdal, M.A.Einarsrud, T.Grande: *Journal of the European Ceramic Society*, 2005, **25**, 927-933.

[56] N.Orlovskaya, Y.Gogotsi, M.J.Reece, B.Cheng, I.Gibson: *Acta Materialia*, 2002, **50**, 715-723.

[57] P.E.Vullum, J.Mastin, J.Wright, M.A.Einarsrud, R.Holmestad, T.Grande: *Acta Materialia*, 2006, **54**, 2615-2624.

[58] J.S.Forrester, E.H. Kisi, A.J.Studer: *Journal of the European Ceramic Society*, 2005, **25**, 447-454.

[59] T.Fett, S.Muller, D.Munz, G.Thun: *Journal of Materials Science Letters*, 1998, **17**, (4) 261-265.

[60] O.Guillon, F.Thiebaud, P.Delobelle, D.Perreux: *Materials Science Letters*, 2004, **58**, (6), 986-990.

[61] T.Fett, S.Muller, D.Munz, G.Thun: *Journal of Materials Science Letters*, 1999, **18**, 1895-1898.

[62] O.Guillon, F.Thiebaud, D.Perreux: *International Journal of Fracture*, 2002, **117**, 235-246.

[63] E.C.Subbarao, M.C.McQuarrie, W.R.Buessem: *Journal of Applied Physics*, 1957, **24**, (10), 1194-1200.

[64] T.Fett, D.Munz: *Journal of Testing and Evaluation*, 2000, **28**, (1), 27-35.

[65] M.D.Hill, S.White, C.S.Hwang: *Journal of the American Ceramic Society*, 1996, **79**, (7), 1915-1920.

[66] T.Fett, D.Munz: *Advanced Engineering Materials*, 2003, **5**, (10), 718-722.

[67] A.S.Nowick, E.S.Machlin: *National Advisory Commitee for Aeronautices*, Report No. **845**, 169-178.

[68] D.Zhou, M.Kamlah: *Acta Materialia*, 2006, **54**, (10), 1389-1396.

[69] D.Zhou, M.Kamlah: *Journal of Applied Physics*, 2005, **98**, 104107.

[70] Q.D.Liu, J.E.Huber: *Journal of the European Ceramic Society*, 2006, **26**, 2799-2806.

[71] J.S.Forrester, E.H.Kisi: *Journal of the European Ceramic Society*, 2004, **24**, 595-602.

[72] O.Guillon, F.Thiebaud, P.Delobelle, D.Perreux: *Journal of the European Ceramic Society*, 2004, **24**, 2547-2552.

[73] M.Lugovy, V.Slyunyayev, N.Orlovskya, M.J.Reece: *Physical Review B*, 2008, **78**, 024107.

[74] L.Rayleigh: *Phylosophical Magazine*, 1887, **23**, 225.

[75] G.Bertotto "*Hysteresis in Magnetism*" (Academic Press, San Diego, 1998)

[76] L.Neel: *Cahiers Phys*ics, 1942, **12**, 1-20

[77] F.Colaiori, A. Gabrielli, S.Zapperi: *Physical Review B*, 2002, **65**, 224404-1/224404-7

[78] S.Zapperi, A.Magni, G.Durin: *Journal of Magnetism and Magnetic Materials*, 2002, **242-245**, 987-992.

[79] D.Damjanovic: *Journal of Applied Physics*, 1997, **82**, (4), 1788-1797.

[80] D.Damjanovic, M.Demartin: *Journal of Physics D: Applied Physics*, 1996, **29**, 2057-2060

[81] D.Damjanovic, M.Demartin: *Journal of Physics: Condensed Matter*, 1997, **9**, 4943-4953.

[82] D.A.Hall: *Journal of Materials Science*, 2001, **36**, 4575-4601.

[83] O.Boser: *Journal of Applied Physics*, 1987, **62**, (4), 1344-1348.

[84] S.S.N. Bhadarawaja, A. Laha, S. Halder, S.B. Krupanidhi: *Materials Science and Engineering B*, 2002, **94**, 218-222.

[85] D. Bolten, U. Bottger, T.Shneller, M.Grossmann, O.Lohse, R. Waser: *Applied Physics Letters*, 2000, **77**, (23), 3830-3832.

[86] S.T.McKinstry, N.B.Gharb, D.Damjanovic: *Applied Physics Letters*, 2006, **88**, 202901-1/202901-3.

[87] D. Bolten, U. Bottger, R. Waser: *Journal of Applied Physics*, 2003, **93**, (3), 1735-1742

[88] A.Stancu, D.Ricinshi, L.Mitoseriu, P.Postolache, M.Okuyama: *Applied Physics Letters*, 2003, **83**, (18), 3767-3769.

[89] J.E.Garcia, R.Perez, A.Albareda: *Journal of Physics: Condensed Matter*, 2005, **17**, 7143-7150.

[90] J.E.Garcia, R.Perez, A.Albareda: *Journal of European Ceramic Society*, 2007, **27**, 4029-4032.

[91] Q.M.Zhang, H.Wang, N.Kim, L.E. Cross: *Journal of Applied Physics*, 1994, **75**, (1), 454-459

[92] D.Damjanovic, Demartin, H.S. Shulman, M.Testorf, N.Setter: *Sensor and actuators*, 1996, **53**, 353-360.

[93] Chae-Ryong Cho, Won-Jae Lee, Byoung-Gon Yu, Bo-Woo Kim: *Journal of Applied Physics*, 1999, **86**, (5), 2700-2711

[94] M.Alguero, B.Jimenez, L.Pardo: *Applied Physics Letters*, 2003, **83**, (13), 2641-2643.

[95] Young-Han-Shin, Ilya Grinberg, I-Wei Chen, Andrew M. Rappe: *Nature Letters* 2007, **449**, 881-884

[96] S.V. Kalinin, B.J. Rodriguez, S.Jesse, Y.H.Chu, T.Zhao, R.Ramesh, S.Choudhury, L.Q.Chen, E.A. Eliseev, A.N. Morozovska: 2007, 104, (51), 20204-20209.

[97] C.F.Pulvari, W.Kuebler: *Journal of Applied Physics*, 1958, **29**, (9), 1315-1321.

[98] H.H.Wieder: *Journal of Applied Physics*, 1957, **28**, (3), 367-369.

[99] T.K.Song, S.Aggarwal, A.S.Prakash, B.Yang, R.Ramesh: *Applied Physics Letters*, 1997, **71**, (15), 2211-2213.

[100] M.H.Lente, A.Picinin, J.P.Rino, J.A.Eiras: *Journal of Applied Physics*, 1958, **29**, (9), 1315-1321.

[101] J.Yin, W.Cao: *Applied Physics Letters*, 2002, **80**, (6), 1043-1045.

[102] M.H.Lente, J.A.Eiras: *Journal of Applied Physics*, 2004, **95**, (5), 2646-2653.

[103] D.Viehland, Yun-Han Chen: *Journal of Applied Physics*, 2000, **88**, (11), 6696-6707

[104] A.Savage, R.C.Miller: *Journal of Applied Physics*, 1960, **31**, (9), 1546-1549

[105] A.R.Lim, J.H.Chang, S.Y.Jeong: *Journal of Applied Physics*, 1998, **83**, (3), 1296-1298

[106] R.A.Wolf, S. Trolier-McKinstry: *Journal of Applied Physics*, 2004, **95**, (3), 1397-1406

[107] J.Y.Hwang, S.A.Lee, S.Y.Jeong, C.R.Cho: *Europhysics Letters*, 2006, **76**, (1), 88.

[108] S.T.Zhang, G.L.Yuan, J.Wang, Y.F.Chen, G.X.Cheng, Z.G.Liu: *Solid State Communications*, 2004, **132**, 315-318.

[109] A.S.Krausz: *Materials Science and Engineering*, 1969, **4**, (4), 193-197.

[110] A.S.Krausz: *Acta Metallurgica*, 1968, **16**, (7), 897-902.

[111] B.L.Cheng, M.J.Reece: *Bullettin of Materials Science*, 2001, **24**, (2), 165-167.

[112] J.C.Walmsley, A.Bardal, K.Kleveland, M.A.Einarsrud, T.Grande: *Journal of Materials Science*, 2000, **35**, 4251-4260.

[113] N.Orlovskaya, N.Browning, A.Nicholls: *Acta Materialia*, 2003, **51**, 5063-5071.

[114] N.Orlovskaya, Y.Gogotsi, A.Nicholls: *Electrochemical Society Proceedings*, 2001, **2001-16**, 624-632.

[115] N.Orlovskaya, Kjersti Kleveland, Tor Grande, Mari-Ann Einarsrud: *Journal of European Ceramic Society*, 2000, **20**, 51-56.

[116] D.L.Meixner, R.A.Cutler: *Solid State Ionics*, 2002, **146**, 273-284.

[117] D.L.Meixner, R.A.Cutler: *Solid State Ionics*, 2002, **146**, 285-300.

[118] C.M.D'Souza, N.M.Sammes: *Journal of the American Ceramic Society*, 2000, **83**, (1), 47-52.

[119] N.Orlovskaya, M.Lugovy, V.Slyunyayev, D.Verbylo, M.J.Reece: *Scripta Materialia*, 2009 in press.

[120] F.S.Baumann: "Oxygen reduction kinetics on mixed conducting SOFC model cathodes" PhD thesis, Max Plank Institute, Stuttugart, Germany, 2006.

[121] K.B.Chong: "An alternative interpretation for domain wall dynamics in ferroelectric switching: thermal activation approaches" PhD Thesis, Queen Mary University, London, UK, 2007.

[122] H.L.Lein, O.S.Andersen, P.E.Vullum, E.Lara-Curzio, R.Holmestad, M.A.Einarsrud, T.Grande: *Journal of Solid State Electrochemistry*, 2006, **10**, 635-642.

[123] P.Paruch, T.Giamarchi, J.M.Triscone: *Physical Review Letters*, 2005, **94**, 197601.

[124] J.Wang, G.Liu, G.Ni, Y.Du: *Journal of Magnetism and Magnetic Materials*, 2004, **280**, 316-321

[125] M.Davis, D.Damjanovic, N.Setter: *Journal of Applied Physics*, 2006, **100**, 084103.

[126] N.B.Gharb, I.Fujii, E.Hong, S.T.McKinstry, D.V.Taylor, D.Damjanovic: *Journal of Electroceramics*, 2007, **19**, 47-65.

[127] A.Achuthan, C.T.Sun: *Journal of Applied Physics*, 2005, **97**, 114103.

[128] Q.Wan, C.Chen, Y.P.Shen: *Journal of Materials Science*, 2006, **41**, 549-555.